The Application of Image Analysis Extensions to Processes of Relevance to Drug Development

A Thesis Submitted to the University of Manchester for the Degree of Doctor in Philosophy in the Faculty of Medical and Human Sciences

2013

Zahra Hamrang

Supervised by Dr Alain Pluen and Professor David Clarke

The University of Manchester

School of Pharmacy and Pharmaceutical Sciences

Table of Contents

CHAPTER 6:

THE ASSESSMENT OF CELLULAR UPTAKE USING BIOIMAGING AND CONVENTIONAL ASSAYS

LIST OF APPENDICES

APPENDIX 1:

QUANTIFICATION OF THE LASER BEAM WAIST AND DETERMINATION OF PMT SHOT NOISE

APPENDIX 2:

COMPARING GAUSSIAN MIXTURE MODELS USING THE F-TEST

APPENDIX 3:

SUPPLEMENTARY INFORMATION FOR VALIDATION OF RICS AS A NOVEL TOOL FOR THE ASSESSMENT OF PROTEIN DIFFUSIONAL BEHAVIOUR IN SOLUTION

Appendix 4:

SUPPLEMENTARY INFORMATION FOR THE APPLICATION OF IMAGE ANALYSIS TO THE QUANTIFICATION OF MONOMER LOSS AND AGGREGATION IN SOLUTION

Appendix 5 (Part A):

SUPPLEMENTARY INFORMATION FOR THE QUANTIFICATION AND ANALYSIS OF P-GLYCOPROTEIN EXPRESSION AND INHIBITION USING LIVE CELL IMAGING

Appendix 6:

SUPPLEMENTARY INFORMATION FOR THE ASSESSMENT OF CELLULAR UPTAKE USING BIOIMAGING AND CONVENTIONAL ASSAYS

Word Count: 66,792

List of Tables

Chapter 1

Chapter 3

Chapter 4

Chapter 5

List of Figures

Chapter 1

Chapter 3

Chapter 4

Chapter 5

Chapter 6

List of Abbreviations

ABC	ATP-Binding Cassette
ACF	Autocorrelation Function
ANOVA	Analysis of Variance
APD	Avalanche Photodiode
ATP	Adenosine Triphosphate
AUC	Analytical Ultracentrifugation
BAECS	Bovine Aortic Endothelial Cells
BBB	Blood-Brain Barrier
BCRP	Breast Cancer Resistance Protein
BSA	Bovine Serum Albumin
BSA-AF488	BSA-Alexa Fluor® 488
Caco-2	Colorectal Carcinoma Cells
CD	Circular Dichroism
CD	*Cluster of Differentiation*
cDNA	Circular Deoxyribonucleic Acid
CLSM	Confocal Laser Scanning Microscopy
CNS	Central Nervous System
CO_2	Carbon Dioxide
Da	Daltons
DAPI	4',6-diamidino-2-phenylindole

DLS	Dynamic Light Scattering
DMEM	Dulbecco's Modified Eagle Medium
DMSO	Dimethyl Sulfoxide
DNA	Deoxyribonucleic Acid
DSC	Differential Scanning Calorimetry
ELISA	Enzyme-Linked Immunosorbent Assay
FBS	Foetal Bovine Serum
FCS	Fluorescence Correlation Spectroscopy
FDA	Food and Drug Administration
FI	Fluorescence Intensity
FIDA	Fluorescence Intensity Distribution Analysis
FIGMMA	Fluorescence Intensity Gaussian Mixture Model Analysis
FRAP	Fluorescence Recovery After Photobleaching
FRET	Forster (Fluorescence) Resonance Energy Transfer
FT	Fourier Transform
FTIR	Fourier Transform Infrared Spectroscopy
GFP	Green Fluorescent Protein
HBSS	Hank's Balanced Salt Solution
HeLa	Henrietta Lacks
HEPES	4-(2-hydroxyethyl)piperazine-1-ethanesulfonic acid)
IC_{50}	Half Maximal Inhibitory Concentration
ICS	Image Correlation Spectroscopy

IDV	Integrated Density Value
IF	Immunofluorescence
IgA	Immunoglobulin A
IgG	Immunoglobulin G
i.m.	Intramuscular
i.v.	Intraveneous
***k*ICS**	k-space Image Correlation Spectroscopy
Laser	Light Amplification by Stimulted Emission of Radiation
LC	Liquid Chromatography
LC-MRM	Liquid Chromatography-Multiple Reaction Monitoring
LDL	Low Density Lipoprotein
LQR	Lower Quartile Range
LY	Lucifer Yellow
MALLS	Multi-Angle Laser Light Scattering
MDCK	Madin-Derby Canine Kidney Cells
MDR	Multi-drug Resistant
***m*RNA**	Messenger Ribonucleic Acid
MRP	Multidrug resistance-Related Protein
MS	Mass Spectrometry
NA	Numerical Aperture
NaCl	Sodium Chloride

NADH	Nicotinamide Adenine Dinucleotide
NCI	National Cancer Institute
NMR	Nuclear Magnetic Resonance
P_{app}	Apparent Permeability
PAT	Process Analytical Technology
PBS	Phosphate-Buffered Saline
PCH	Photon Correlation Histogram
PCR	Polymerase Chain Reaction
PD	Pharmacodynamics
p-gp	p-glycoprotein
PICS	Particle Image Correlation Spectroscopy
PK	Pharmacokinetics
PMT	Photomultiplier Tube
PSF	Point Spread Function
PVDF	Polyvinylidine Difluoride
QB	Quantal Brightness
QIF	Quantitative Immunofluorescence
RICS	Raster Image Correlation Spectroscopy
RMT	Receptor-Mediated Transcytosis
ROI	Region of Interest
RT-PCR	Reverse Transcription- Polymerase Chain Reaction
s.c.	Subcutaneous

St. dev.	Standard Deviation
SDS	Sodium Dodecyl Sulphate
SE	Sedimentation Equilibrium
SEC	Size Exclusion Chromatography
SLS	Static Light Scattering
SNR	Signal to Noise Ratio
SpIDA	Spatial Intensity Distribution Analysis
SPT	Single Particle Tracking
STICS	Spatiotemporal Image Correlation Spectroscopy
SV	Sedimentation Velocity
TAMRA	Tetramethylrhodamine
TDA	Taylor Dispersion Analysis
TEM	Transmission Electron Microscopy
TER	Transcellular Electrical Resistance
Tf	Transferrin
TfR	Transferrin receptor
TICS	Temporal Image Correlation Spectroscopy
Trp	Tryptophan
UQR	Upper Quartile Range
UV	UltraViolet
Wt	Wild-type
2D	Two Dimensional

3D	Three Dimensional

General Abstract

In the past forty years advancements in fluorescence-based methods including imaging (e.g. confocal and multi-photon) and quantitative spectroscopies (e.g. Fluorescence Correlation Spectroscopy) have been applied to systems ranging from solutions to *in vivo* models: such methods possess the ability to monitor fluorescence intensity fluctuations and offer the potential to unravel biophysical and biochemical phenomena. A major disadvantage associated with these methods is their ever-increasing cost resulting in the development of image analysis tools that offer the potential to exploit hidden information contained in confocal images.

The hypothesis pertaining to this thesis is that image analysis tools developed in recent years exemplified by Raster Image Correlation Spectroscopy (RICS), Spatial Intensity Distribution Analysis (SpIDA) and Fluorescence Intensity Gaussian Mixture Model Analysis (FIGMMA) will provide a new insight into current pharmaceutical problems. The application of these methods to the quantification of protein aggregation, monomer/dimer equilibria, p-glycoprotein efflux activity and transcytosis are presented in this thesis.

Protein aggregation poses a major challenge to the biotechnology industry which currently lacks analytical capabilities to profile broad particle size ranges. An in-house RICS (ManICS) software was validated against Dynamic Light Scattering and Fluorescence Correlation Spectroscopy (FCS) to determine Bovine Serum Albumin (BSA) aggregate population distributions under accelerated stability conditions. Initial stages implicated in the growth of aggregates are vital to the mechanistic assessment of protein aggregation. Hence, real-time *in situ* examination of monomer loss and aggregation of BSA was performed at 50 °C to enable continuous assessment with imaging and subsequent SpIDA analysis. Results obtained from this study suggested reversible fluctuation between monomers and dimers for up to four hours.

To correlate membrane receptor and transporter expression with activity and enable the comparison of expression in multiple cell lines, population densities of p-glycoprotein transporters and transferrin receptors were determined using SpIDA in samples subjected to immunofluorescence labelling.

The Calcein retention assay is a routine approach to determining multidrug resistance associated with p-glcoprotein efflux and the traditional plate reader approach omits microscopic aspects of p-glycoprotein Calcein-AM uptake and efflux. Confocal microscopy and data obtained from image analyses supported the subcellular and intercellular assessment of Calcein accumulation in *MDR1*-transfected and control cell lines as a function of time and verapamil concentration. Finally, live cell imaging of transferrin vesicular transport and Cell Trace™ Calcein red-orange AM internalisation in combination with traditional Transwell® assays were assessed to compare their transcellular transport and intracellular concentrations in multiple cell lines. Images obtained enabled visualisation of internalisation and following analysis using SpIDA, RICS and FIGMMA the number of intracellular vesicles and dynamic parameters of Cell Trace™ Calcein red-orange diffusion and intracellular concentration were determined.

In conclusion, image analysis tools were applied to providing new parametric insights into a number of pharmaceutically-relevant processes and in some instances this is the first example of such studies. Despite current phenomenal advances in image acquisition capabilities, there remains a broad scope for the validation of image analysis tools and their application to a multitude of areas of interest to pharmaceutical and biomolecular research.

Declaration

No portion of the work referred to in the thesis has been submitted in support of an application for another degree or qualification at any other university or institute of learning.

All experimental data and corresponding analysis reported in this thesis has been performed by the author unless otherwise stated.

Copyright Statement

Acknowledgements

Many thanks to my supervisors Alain and David who have guided and supported me throughout my training towards refining both my character and perspective on research and life as an academic; I will forever be indebted to you.

I would also like to thank Dr Egor Zindy for all those evenings, weekends and nights of programming and the many troubleshooting discussions we shared; I couldn't have possibly survived this image analysis PhD without your endless support.

A special thanks to my colleagues and dear friends Yamini, Carina, Louise, Soheyla, Saeideh, Fariba, Aled, Cat 1, Cat 2, Shohreh, Bahareh, Chantelle, Jennifer, Wadia, Jureerat, Mani, Kanin, Korakoch, Natalie, Samaneh, Myasar, Christopher, Ghislaine, Tejal, Alessandro and Danimal you have all been so kind and supportive to me throughout the years.

My gratitude goes to Professor John Collett, Dr David Allison, Dr Elena Bichenkova, Dr Sally Freeman, Dr David Berk, Dr Harmesh Aojula, Dr Jeff Penny, Professor Mary Tully, Dr Francesco Cellesi, Dr Aleksandra Galetin, Professor Ian Stratford, Dr Costas Demonacos, Professor Brian Lockwood and Mr Mike Harrison for their continued encouragement, support and inspiration throughout the years; be it through allowing me to work in their lab, providing invaluable life advice, or getting my hands dirty with calamine powder…every little counts.

Many thanks to the Brents, Rhonas, Harries, Farhanas, Louises, Terries, Fredas, Donalds, Tracies, Carmelles and Gordons; you truly make everything happen.

I would like to thank my mother, Tracy for always being the caring mum on the other end of the phone, and my baby brother, Ali, I wish you the best of success on your quest to discovering science. Thanks to the Rattray clan (Wilma, John and Jayne), Markus, Milou and Joni-Rose for always putting a smile on my face.

To Leila, my sister, for all those days that I felt challenged and inadequate, your constant courage and battle for life rendered any problems I had small and insignificant; for this you helped me pull through and I will always view you as a true inspiration.

To Violet, my deceased grandmother who lost her battle to cancer, I know that you would be proud of what I have achieved and you will always live in my heart.

Last but not least, to someone special who has always been there, a shoulder to cry on, a friend, technical assistance, a career advisor and a soulmate…

Nicholas John William Rattray to you I dedicate this thesis.

About the Author

In 2008 the Author graduated from The University of Manchester with an Undergraduate Master's degree in Pharmacy with first class honours. In order to qualify as a pharmacist, during the pre-registration year, the author undertook a split industrial and hospital placement at AstraZeneca Pharmaceuticals based in the Macclesfield PAR&D facility in Cheshire and the University Hospital of South Manchester, respectively.

Work undertaken at AstraZeneca pharmaceuticals entailed the validation of *in silico* models for powder compaction in the formation of solid dosage forms, emulsion formulation, characterisation of liquid crystals of an API and optimisation of the freeze-drying procedure for a product in the pipeline.

During the hospital placement, the author was involved in the supervised pharmaceutical care of patients during medical rotations and subsequently qualified as a pharmacist in August 2009.

In September 2009 the author joined the School of Pharmacy and Pharmaceutical Sciences at the University of Manchester, on registration for the PhD programme which was completed in 2013.

Chapter 1

INTRODUCTION

Introduction

In this thesis four very different elements of the drug development process will be considered of relevance to small molecule (e.g. p-glycoprotein efflux) or biomolecular therapeutics (e.g. protein aggregation and transcytosis). The concept of fluorescence and image analysis extensions, a common theme to this thesis, will initially be introduced followed by a brief overview of the topics studied in this thesis. It is envisaged that the potential scope for image analysis contribution to each of these disciplines will become apparent to the reader throughout the thesis.

1.1 The Concept of Fluorescence

Fluorescence may be broadly defined as the emission of light following excitation by a source of higher energy and fluorophores may simply be described as molecules that possess fluorescent characteristics. A transition in the vibrational, electronic and rotational configurations of a fluorophore results from absorption of photons at the electronic ground state. This transition to an excited state takes place on a femtosecond timescale and following loss of energy, in the form of fluorescence emission, and vibrational relaxation (i.e. 10^{-9}-10^{-7} seconds), the fluorophore returns to the ground state, S_0 (See Figure 1.1).[1]

The absorption maxima of a fluorophore normally occurs at a much shorter wavelength than the emission spectra following excitation, due to energy dissipation at excited vibrational states. Energy levels have been utilised to describe this shift in wavelength, termed the Stoke shift, allowing the detection of emitted photons and their differentiation from excited photons.[2]

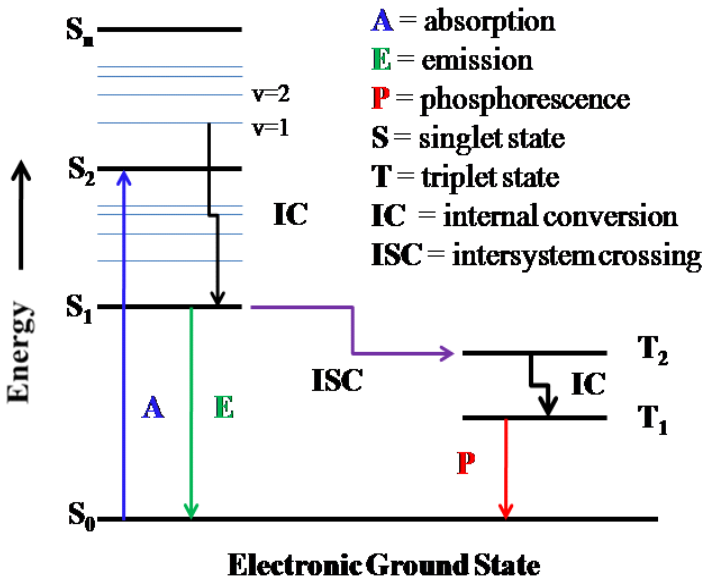

Figure 1.1 *Schematic depicting the Jablonski diagram of energy levels of a molecule. S_0, is the ground state where non-excited fluorophores remain, whilst S_1 and S_2 are electronic excited states following optical absorption, as illustrated in the diagram.*[1]

1.1.1 Fluorescence-Based Approaches

Since the discovery of fluorescence, several fluorescence-based methodologies have been developed that generally utilise multiple components for detection including an excitation source (a laser or lamp), a fluorophore, mirrors or filters in order to differentiate between emitted and excited photons, and a detector that yields recordable output acquired from the emitted photons. Instruments using the above-mentioned components are flow cytometers, fluorescence microscopes, fluorescence scanners, microplate readers and spectrofluorimeters.

1.1.1.1 Confocal Laser Scanning Microscopy (CLSM)

This section aims to introduce and review the underpinning aspects concerning the application of CLSM, image analysis tools and measurement conditions requiring consideration during image acquisition and subsequent analysis.

Images in confocal microscopes are either formed by reflection of excited light off the specimen or excitation of fluorophores, the latter most commonly used in biological applications. Characteristics of a confocal setup include point illumination of the specimen and removal of out-of-plane light.

A typical modern confocal setup shown in Figure 1.2 consists of a laser excitation source that illuminates the fluorescent dye molecule. Dichroic mirrors controlled by a computer reflect light of lower wavelengths than a specific threshold and allow the passage of longer wavelengths so that emitted fluorescence passes through the objective lens.[3] The emitted light is then passed through an adjustable pinhole, excluding any out of plane light and refocusing the photons in the objective plane. This process ultimately results in optical sectioning of the specimen, thereby, creating a background-free image. A reduction in the diameter of the pinhole whilst reducing the amount of light collected, increases the thickness of the optical sectioning resulting in a better definition of the image derived from the specimen.[4] Emitted photons are most commonly detected using a photomultiplier tube (PMT) in commerically available confocal microscopes.

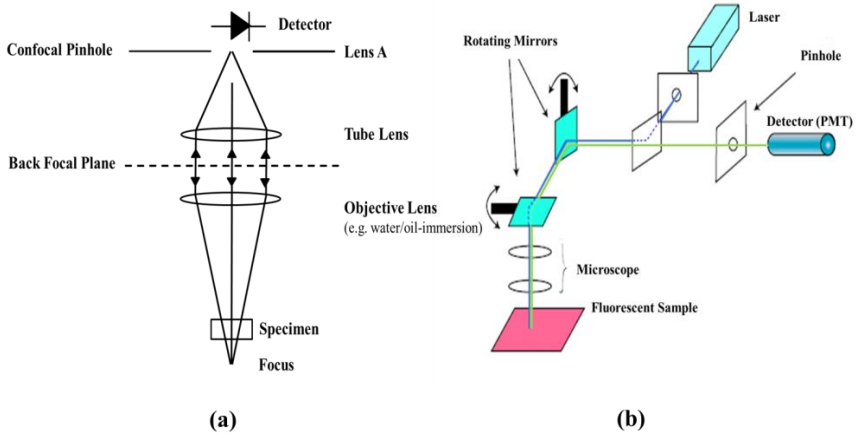

Figure 1.2 (a) *Basic schematic of a confocal optical setup, and* ***(b)*** *the general setup in a confocal laser scanning microscope with a laser excitation source. Light from the laser excitation source is moved over the sample with rotating mirrors and focused through a pinhole onto a detector.*[3]

Both the excitation and resolution of a microscope are limited by diffraction of the excitation source. Disc-like Airy diffraction patterns formed on the image plane consist of a central bright circle (See Figure 1.3) surrounded by outer darker rings that ultimately define the resolution of a point illumination source.

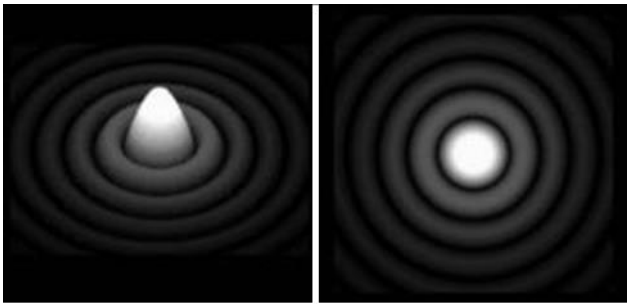

Figure 1.3 *A diffraction pattern for a circular aperture (Airy disc) in the axial (right) and lateral (left) direction, taken from LaFreniere.*[5]

The Airy radius of the central bright circle is defined by the following equation;

$$r_{airy} = \frac{0.61\lambda}{NA} \qquad \textit{Equation 1.1}$$

Where λ is the wavelength of the incident light from the excitation source and NA represents the numerical aperture of the objective lens.[6]

Images acquired through confocal microscopy are a convolution of the PSF with the point source emission spreading over a number of neighbouring pixels arising from diffraction.[7] Emitted light from each point within the detected fluorescence emission is convolved with the PSF to form an image containing blurred regions. Since the PSF is a three-dimensional phenomenon, blurring is existent in three dimensions. Deconvolution performance reconstructs the image through reversal of the process leading to blurring.[8]

Knowledge of the PSF provides an overall perspective of images that would be formed with an optical system in terms of brightness, resolution and deformations conferred through the optics.[9]

As a consequence of its design, the confocal microscope suffers from resolution limitations (i.e. the approximate axial and lateral resolutions for a 63 x 1.4 NA oil immersion objective of a confocal microscope at 500 nm are 0.38 and 0.4 μm, respectively), diffraction limitations, photodamage of the specimen and photobleaching caused by the incident light. In biological applications often a compromise between cell viability and sensitivity of the procedure must be met.[3,10]

In summary, there are numerous advantages associated with the use of confocal microscopy that include (i) optical sectioning (ii) reduced blurring due to collection of out of plane light (iii) electronic adjustment of the magnification (iv) the clear

examination of thick and light scattering objects (v) *xy* scans over large areas of a specimen (vi) increased effective resolution and (vii) a reasonable signal to noise ratio (SNR).[11]

The aforementioned features render the confocal microscope a simple tool appropriate for quantitative studies of the optical properties of a specimen, controlling the amount of light to which the specimen is exposed and requires objectives with long working distances.[11]

1.1.1.2 Practical Aspects in Live Cell Imaging and Appropriate Probe Selection

The principles of confocal microscopy were discussed in the previous section. Considerations in the experimental design of fluorescence-based experiments and routinely encountered problems will be briefly highlighted in this section.

Fluorophore Selection

Fluorescence intensity (FI) is dependent on a number of parameters including quantum yield, intensity of the excitation source, concentration of fluorophore, path length, the molecular extinction coefficient of the fluorophore[12,13], the absorption coefficient (brightness), spectral match of the probes utilised and photostability of the dye. All of these factors require careful consideration during experimental design.[14]

Quantum efficiency (or quantum yield) relates to the efficiency of a fluorophore in absorption and emission of photons and its ability to undergo repeated excitation and emission cycles that ultimately influence fluorescence output under specific environmental conditions.[15] Dye-induced problems commonly encountered with the use of fluorophores include transient dark triplet states[16] and fluctuations due to environmental factors such as pH, proximity to quenchers, dyes or laser light.[17]

Background fluorescence, a result of autofluorescence and free dye molecules compromises fluorescence measurements and must be subtracted from any fluorescence-based analysis.

Photobleaching is a commonly encountered phenomenon, where the emitted fluorescence fades as a consequence of irreversible destruction of a fluorophore in its excited state following excitation by high intensity illumination sources adding further complexity to live cell measurements.[18] Photobleaching effects may be counteracted by

reducing the laser power (i.e. intensity of the illumination source) and increasing the detector gain.[19] Rhodamine derivatives (e.g Rhodamine green), Cy-5 (far red), and photostable far red Alexa dyes (e.g. Alexa Fluor® 647) are standard fluorophores commonly utilised in fluorescence correlation spectroscopy (FCS) experiments performed in aqueous environments introduced later in this thesis.[20]

Autofluorescence

A phenomenon encountered in fluorescence-based live cell imaging methods at short excitation wavelengths (i.e.< 500 nm) is autofluorescence arising from the presence of intrinsic autofluorescent biomolecules such as porphyrins, NADH and flavins in plasma membranes and various cellular compartments.[21,22] The SNR is reduced as a consequence of autofluorescence and may be counteracted by use of orange to red emission dyes. Uncorrelated fluorescence signals arising from slow-moving or immobile sources of autofluorescence can be mathematically corrected or photobleached following exposure to the excitation laser beam.[23] This phenomenon encountered in the imaging of cells and tissues has contributed to the development of autofluorescence-based imaging methods.[24]

1.1.1.3 Fluorescence Correlation Spectroscopy (FCS)

FCS was first developed over 40 years ago to study the reversible binding of ethidium bromide to DNA.[25] Since then FCS has been utilised to profile a diversity of kinetic processes (e.g. translational diffusion) through the detection of temporal fluorescence intensity (FI) fluctuations arising from the diffusion of molecules and subsequent autocorrelation statistical analysis. Fluctuations in the concentration of fluorophores are sampled over a milisecond to second timescale through focusing the laser beam on a single point using a high NA objective (See Figure 1.4) within the sample (i.e. sampling volume ≈ 0.25 fL). Whilst this technique possesses a high temporal resolution in the quantification of small volume concentrations, it is slow for application to sampling larger volumes in order to monitor spatiotemporal changes in local concentrations.[26]

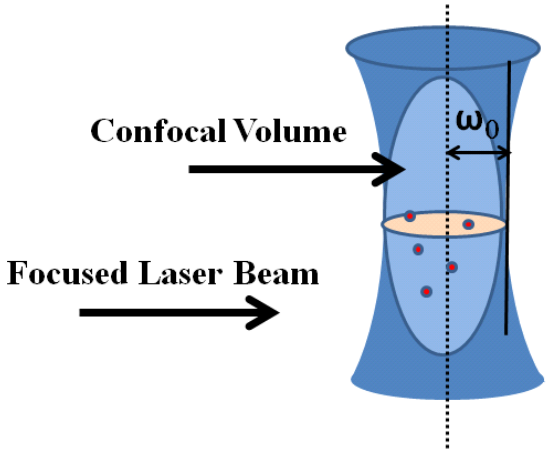

Figure 1.4 *A schematic representing a typical confocal volume within a focused laser beam used in FCS measurements. When a fluorophore diffuses within this volume it is excited followed by emission of fluorescence.*

The temporal autocorrelation functions (ACF) calculated from measuring similarities in the fluorescence fluctuations throughout the sample, provides information concerning the number of molecules within the observation volume and their corresponding diffusion times. The normalised ACF is determined using:

$$G(\tau) = \frac{\langle \delta F(\tau) \delta F(t+\tau) \rangle}{\langle F(t) \rangle^2} \qquad \textit{Equation 1.2}$$

Where, $G(\tau)$ is the correlation function, $\delta F(t)$ is the difference in fluorescence intensity between time t and the mean value and $t+\tau$ represents a later time.

Parameters normally derived from an ACF include (i) the sample concentration (inversely proportional to the amplitude of the ACF) (ii) the decay shape that demonstrates the nature of the transport process occurring and (iii) the diffusion time. Common sources of error introduced into the ACF arise from solvent steady background, photobleaching, laser power or fixed particles. A typical ACF and the corresponding derived parameters are presented in Figure 1.5.[22,27]

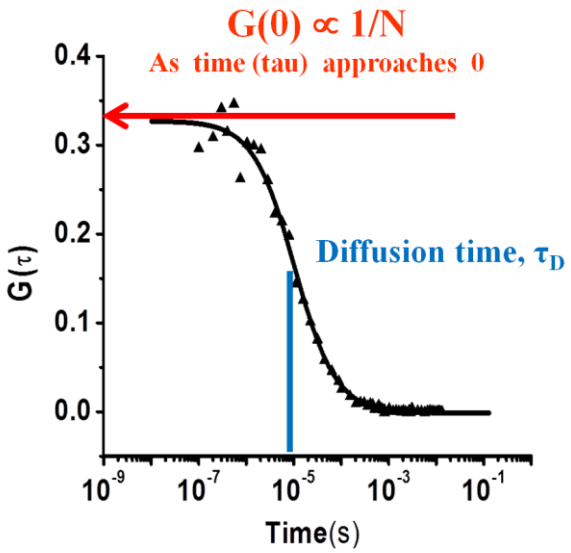

Figure 1.5 *A typical autocorrelation function and the corresponding parameters derived following analysis (number of particles and diffusion time).*

Certain limitations and artifacts have been encountered in the application of FCS measurements to living cells some of which have been described as follows. FCS has been proven to be effective for experiments performed on rapidly occurring processes (i.e. microseconds to milliseconds) with a high degree of sensitivity due to the use of an avalanche photodiode detector (APD) in comparison to confocal micrscopes that utilise PMTs.[28,29]

For immobile or slow-moving components alternative complementary techniques such as fluorescence recovery after photobleaching (FRAP)[30], particle tracking[31], image correlation spectroscopy (ICS)[27,32-34] or fluorescence intensity distribution analysis (FIDA) have been reported.[26,35,36]

FCS measurements are susceptible to instabilities in the laser beam focus and membrane structural changes are known to contribute to transformation in the amplitude of the ACF (i.e. a higher amplitude).[22] FCS studies are amenable to artifacts associated with the use of fluorophores as previously described when applied to intracellular studies.[22]

To date FCS has been utilised in studies aiming to establish the nature of interactions between hormones, proteins and plasma membrane components, aggregation, flow, reactions and diffusion of small proteins in the cytoplasm, within the plasma membrane of live cells, gels and solutions.[22,37]

1.1.1.4 Image Analysis Extensions

Historically, microscopy has been identified as a predominantly qualitative technique. However, digitalisation of microscopy and recent advances in labelling, detectors and camera technologies have improved its ability to be used as a quantitative tool in the elucidation of biophysical and biochemical processes.

In order to facilitate the extraction of meaningful quantitative parameters from high resolution microscopy images, collaboration between microscope users and computational tool developers (i.e. bioimage informatics) has precipitated the formation of open-source communities that have contributed to the emergence of a diverse range of image analysis tools. Numerous projects have contributed to the development of open-source platforms that rely on plug-ins for the performance of specific measurements ranging from routine fluorescence intensity measurements to particle tracking applied to an image time series. Some examples of such software include Image J®,[38] Fiji,[39] ICY[40] and Kalaimascope.[41]

Computational algorithms remain to be the limiting step in achieving localisation of individual molecules (i.e. fluorophores) within images and many such applications remain in their infancy.

The discovery and application of FCS in live cell studies precipitated the development of image analysis methods with a high degree of spatial resolution. In this section the concept of image correlation spectroscopies and intensity distribution analysis techniques will be introduced.

Image Correlation Spectroscopies

Since the advent of FCS, numerous image analysis extensions have been developed with a wide scope for application to a variety of intracellular and biochemical processes. Image correlation spectroscopy (ICS) was developed by Petersen *et al.* as a mathematical image analysis approach that could be applied to images acquired by any microscope and all images types. The basis of ICS included solving two-dimensional fast Fourier-transform algorithms to permit the determination of particle sizes (i.e. aggregation) and their concentrations within an image.[32]

ICS approaches were developed as imaging analogues of FCS where the spatial autocorrelation function is determined from images or image sequences (i.e. time series) acquired on microscopes through scanning adjacent pixels and lines. Compared to FCS, ICS is more sensitive to analysis of fluctuations arising from slower processes, and thus can provide statistical intensity information on longer timescales (i.e. seconds to minutes).[36]

Generally, the timescale of the procedure is microseconds for neighbouring pixels, a few milliseconds across a single frame, and seconds between successive frames. Information concerning molecular dynamics contained within the image thus expands to a larger timescale and provides a higher degree of information relating to the spatial distribution of studied entities compared to FCS.[29,36] For further information on the dynamic timescales quantified by ICS see Figure 1.6 as follows;

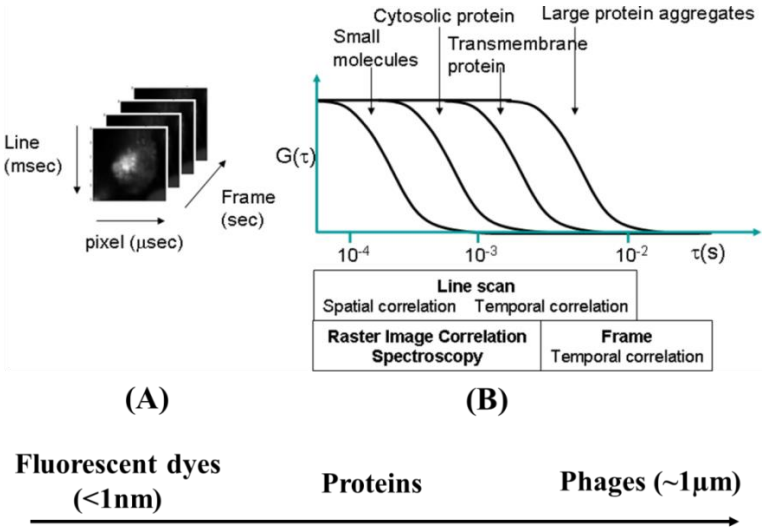

Figure 1.6 *Graphical representation of* ***(A)*** *image time series and* ***(B)*** *autocorrelation curves obtained from various image correlation spectroscopies and the corresponding diffusion times quantified by these methods, adapted from Digman et al.*[34]

Other variations of image correlation spectroscopy to date, their relative merits and applications may be exemplified by;

Temporal Image Correlation Spectroscopy (TICS) operates on image stacks to provide spatial maps of intermolecular interactions with a spatial resolution equal to that of the image and a temporal resolution dependent on the frame rate of the acquired image. To date reports of TICS applications have included assessment of membrane protein aggregation statuses,[42] quantification of number densities and dynamics.[43,44]

Space-Time Image Correlation Spectroscopy (STICS) is an extension of TICS that in contrast to ICS does not separately calculate temporal changes from spatial fluctuations.[45] Overall, STICS is an ideal method for determining mobile sub-populations within a sample and has been demonstrated as a powerful tool in the assessment of macromolecular directional flow.[45]

Particle Image Correlation Spectroscopy (PICS) is a technique containing aspects of both ICS and particle tracking. A principle ICS limitation includes a lack of sensitivity to particle movements as a consequence of diffraction limitations relating to the imaging setup. In the case of particle tracking a high density of particles may contribute to difficulties in assessing particle trajectories and co-ordinates in an image time series. However, PICS circumvents the limitations of both approaches and enables the quantification of high diffusion coefficients in dense samples provided that particles are detected and identified in each frame within an image stack or time series.[43]

k-space Image Correlation Spectroscopy (kICS) was initially developed for blinking or photobleaching fluorophores. The principle advantage of *k*ICS is the unbiased estimation of movement within a sample without the prior need for PSF calibration or alignment of the optical setup. Therefore, *k*ICS is capable of dynamic profiling with non-Gaussian PSFs and misaligned optical systems. However, the major limitation in the application of this approach is that regions of interest (ROIs) smaller than 32 x 32 pixels cannot be selected for analysis.

Raster Image Correlation Spectroscopy (RICS) originally described by Digman *et al*. in 2005,[34] is an image correlation spectroscopy analogue possessing the ability to spatially and temporally map intracellular concentrations, flow and interactions.[7]

A disadvantage typically reported with the use of TICS and kICS has been limitations imposed by the imaging rate that ultimately dictates the maximum diffusion coefficient determined with a particular microscope (i.e. 10^{-9} cm^2/sec for a typical commercial confocal setup) which can render the assessment of some membrane protein components impossible using these techniques. Small and rapidly diffusing fluorophores may also go undetected using these approaches and are often uncorrelated.[7]

Using RICS it is possible to measure the dynamic parameters of rapidly diffusing species with the added advantage of utilising a commercial confocal laser scanning microscope for image acquisition with a raster scan (See Figure 1.7). Spatial resolution at pixel level for raster images and dynamic processes can only be obtained for millisecond dynamics.[27,34] The correlation function utilised in RICS is identical to ICS with the exception of the manner in which the data is acquired that entails raster scanning of an image using a confocal setup. As with STICS slowly moving species may mask the spatiotemporal distribution of diffusion coefficients from species of interest. However, in the case of RICS it is possible to apply a mean contribution filter from either mobile or immobile species present within the sample.[7]

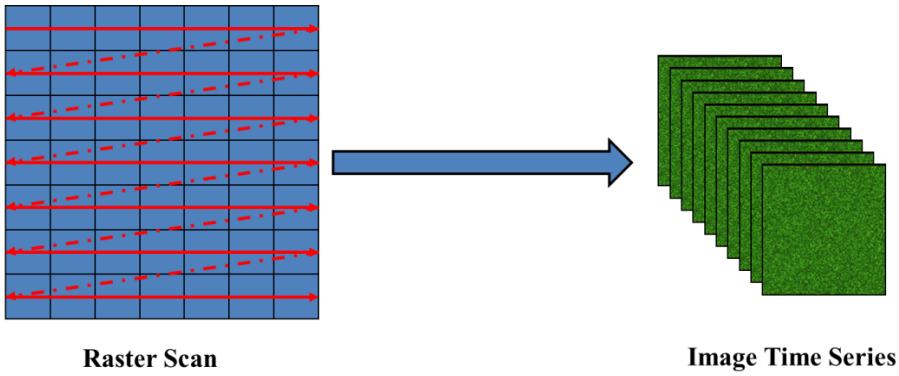

Figure 1.7 *Schematic representing a classic raster scan occuring from line to line and the subsequent acquisition of image time series following repetition of the same process for several frames.*

The pixel dwell time (i.e. a few microseconds), frame size, number of frames (i.e. 50-100) and pixel size (i.e. 3-5 times smaller than the waist beam) require optimisation when performing RICS as previously highlighted since the spatial resolution of RICS is dependent on the diffusion time of the molecules studied.[46] For example, the selection of a rapid pixel dwell time for a slow moving species may give rise to a diffusion coefficient slower than the real parameter. On the contrary, a slow pixel dwell time for rapidly diffusing entities may give rise to their exclusion from correlation arising from the difficulty in their localisation during image acquisition.[34]

In summary, image correlation spectroscopies have been applied to the characterisation of various processes including cell adhesion and migration, studying receptor interactions with their respective ligands, uptake of gene delivery systems into cells,[36] receptor quantification[32] and studying vesicle dynamics.[47]

Overall, ICS analyses offer the potential to monitor and assess quantitative dynamic parameters with the added capability of mapping temporal distributions and retrospective assessment of ROIs following image acquisition. Further advantages of such correlation-based studies is rapid data analysis, broad analyte concentration (density) range and the possibility to apply ICS to slowly moving or immobile components, a feature that is not possible in the FCS assessment of biochemical and intracellular phenomena.

Spatiotemporal Intensity Distribution Analysis (SpIDA)

SpIDA, a novel fluorescence-based image analysis tool, measures quantal brightness and the absolute number of particles as a function of the photon correlation histogram (PCH) through space allowing for the spatial assessment of aggregation and kinetic behaviour intracellularly, and in solution for an image time series. SpIDA assumes linearity in the relationship between the fluorescence intensity detected and the signal obtained from the number of photons collected by the PMT. To date, applications of SpIDA have included quantitative assessment of receptor oligomerisation as a consequence of the activation of signal transduction pathways exemplified by the tryosine kinase receptor.[48,49]

SpIDA is able to detect protein-protein interactions and associations occuring at a distance of >10 nm and differentiate between signals detected from monomeric and oligomeric species at high densities (i.e. >10,000 particles per μm^3) and in random heterogeneous particle distributions. A high spatial resolution is a distinct attribute of SpIDA therefore enabling application to the oligomerisation of receptors, dynamics of intracellular trafficking or monomers in pre-defined regions or subcellular compartments.[48] Compared to image correlation spectroscopies that can be roughly applied to the determination of particle size distributions, SpIDA is able to resolve monomer to dimer ratios accurately.[48]

A potential source of error arising from the use of SpIDA may be bias in measurements arising from subdomains as a consequence of heterogeniety in samples. In order to minimise the impact of this artifact through sampling strategies it is possible to select and mask specific regions and perform separate measurements. If constant bleaching is found to occur within a time series, then the density of particles reduces with no influence on the detected brightness parameter.

1.2 Protein Aggregation and the Biopharmaceutical Lifecycle: Factors Influencing Aggregation and Considerations During Early Product Development

Over the recent decades medical and pharmaceutical sciences have made significant advances as a consequence of the emergence of powerful biochemical and biophysical instrumentation. The development of such technologies has enabled high-throughput assessment of compounds, the implementation of recombinant DNA technology and large scale manufacture of monoclonal antibodies resulting in the biopharmaceuticals/biologics stronghold in the therapeutic market.

Aggregation in biopharmaceuticals remains a challenge in the formulation and administration of biopharmaceutical preparations due to adverse clinical effects associated with immunogenicity and loss of therapeutic activity. This in turn has stimulated the definition of minimum acceptable standards that guarantee safe and efficacious administration of a product in the clinic by regulatory bodies.

A recognised fact is that an understanding of molecular interactions governing aggregation is of paramount importance to controlling biopharmaceutical product stability and currently no single analytical technique can be applied to the characterisation of aggregation over broad concentration and particle size ranges.

Since the approval of Humulin I for marketing in 1982, there has been an ever-increasing application of biopharmaceutical preparations in clinical practice owing to the higher potency and target selectivity of protein-based formulations compared to their small molecule counterparts.[50] Due to the ever-growing pipeline of protein-based biopharmaceutical preparations and aggregation posing the most significant challenge to product development, an increasing demand has been placed on research into novel technologies enabling characterisation of product stability over a diverse range of concentrations and particle sizes during early product development.

Indeed, macromolecular therapeutics are generally recognised as exhibiting a higher degree of target selectivitiy and lower toxicity compared to small molecule synthetic drugs, resulting in the rapid development and marketing of such products. However, caveats such as under-analysis of degradation mechanisms during shelf-life, limitations in the number of analytical approaches utilised in product characterisation and changes in protein native structure during shelf life often present a challenge to the formulation scientist and may result in sub-optimal formulation of such products.[51]

Biotechnological processes contributing to aggregation as well as current emerging trends in technologies applied to the prediction and assessment of aggregation during various stages of the biopharmaceutical product lifecycle will be discussed in the following section.

1.2.1 Aggregation

Aggregates are generally referred to as high molecular weight protein moieties that are oligomers of the monomeric form (i.e. native protein). One of the most common challenges faced in the maintenance of stability during a biopharmaceutical product lifecycle is the prevention and removal of large aggregates (i.e. ≥ 10-mers) from the formulation.[52] Despite extensive characterisation of the propensity of a protein to aggregate over time during product development, significant monomer loss may occur over pharmaceutically-relevant timescales and stress conditions during product shelf life.[53] Whilst potential aggregation in these preparations is often aesthetically undesirable, there is an associated higher risk of poor clinical outcome in terms of reduced efficacy and immunogenicity resulting from the formation of large aggregates. Such clinical outcomes have resulted in pharmacopoeial definitions of maximum acceptable limits of aggregate presence and their corresponding sizes within a biopharmaceutical preparation.[54]

Protein biopharmaceuticals should essentially be particle-free and this refers to visible particles (i.e. > 100 μm) that are inspected using visual assessment or light obscuration methods described in pharmacopoeial monographs.[54]

To date several models have been proposed to describe the underlying mechanism of protein aggregation and self-association that are reviewed by Wang *et al*.[55] The classic and most widely-accepted model considers association of unfolded species as a mechanism of protein aggregate formation that has been represented as a schematic (See Figure 1.8);[55]

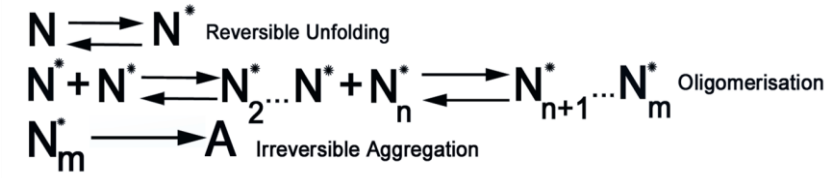

Figure 1.8 *A schematic representation of protein unfolding and subsequent formation of irreversible aggregates from native species. (N denotes the native protein, N* denotes the unfolded state, N^*_m represents oligomers).*

1.2.1.1 Aggregate Classification and Regulatory Limits on Aggregate Presence

Aggregates may form during any stage of the biopharmaceutical product lifecycle and reported classifications have considered size, reversibility, chemistry, solubility, morphology and conformation as descriptors of aggregate types.[56]

Size is a well recognised characteristic used in pharmacopoeial monograph specifications to assess the quality and safety of a product. The terminology used to refer to such species and their corresponding size has been listed in Table 1.1.

Table 1.1 *Representation of aggregate classsification according to size and the associated descriptors.*[57]

Description	Particle Size (*μm*)
Oligomers/Soluble	<0.1
Sub-micron	0.1-1
Sub-visible	0.1-100
Visible	>100

Solubility of aggregates has often been used as a descriptor for sub-visible (i.e.<100μm) species that may not be observed with the naked eye but are eliminated during size exclusion chromatography (SEC) (i.e. > approximately 0.1 μm).[56,57]

Morphologically aggregates may be classified as fibrillar or amorphous in nature. Fibrillar species are identified by a characteristic length of a few microns and diameter of a few nanometers. However, amorphous aggregates may range from tens of nanometers up to a few hundred microns in size. Fibrillar species are generally not observed under ambient conditions and are formed as a function of extreme conditions

of temperature, low protein concentration and net surface charge (i.e. pH and ionic strength). Mechanisms contributing to the formation of amorphous or fibrillar species remain largely unknown but specific analytical methodologies can be implemented to profile both aggregate types. Other parameters exemplified by "*aspect ratio*", "*transparency*", "*roughness*" and "*regularity*" may also be used to describe the appearance of a protein aggregate. Knowledge of the expected morphology of aggregates may be used to differentiate between proteinaceous particles (i.e. aggregates) and foreign particulate contaminants in a product during quality control.[57]

Reversiblility has often been utilised as a measure for the classification of aggregates. Principle interactive forces responsible for their formation, lack of elimination following the application of separative methods (e.g. filtration) and the nature of adverse responses elicited as a consequence of their administration are often indicators applied as measures of aggregate reversibility.[56]

Non-covalent (i.e. reversible) aggregates often occur as a result of pH and protein concentration variations leading to an equilibrium that exists between the monomer and higher order oligomers *via* weak interaction forces (e.g. hydrophobic, Van der Waals, electrostatic and hydrogen bonding).[56] Reversal of solution conditions following such changes may favour reversion to the monomeric form. In most cases the reversible association of an aggregate may be used as an indicator of its reversibility.[57]

Irreversible aggregates are normally formed by covalent association and may be isolated using chromatographic methods (e.g. size exclusion chromatography) with charactersitic elution times. A protein solution may contain a combination of both reversible and irreversible aggregates.[57]

Conformation has been used extensively in the reported literature to differentiate between aggregates. Terms such as "*native*", "*unfolded*", "*partially-unfolded*", "*amyloid*" or "*misfolded*" are typical descriptors that carry a wealth of information contained within a single word from which the secondary or tertiary state of the proten can be inferred. For example, "*native*" refers to a protein in its monomeric state, with an intact secondary and tertiary structure.

Chemical modification occuring in specific amino acid residues promote irreversible cross-linked aggregates (e.g. dityrosines). In some case deamidation and oxidation

(cysteines) can lead to chemical modification of amino acids and precipitate aggregate formation.[56,57]

In summary, the classification of aggregates using any of the terminology described above can often be misleading and lead to ambiguity in the interpretation of the species being described. Many formulation scientists have attempted to apply a common nomenclature mainly utilising particle size ranges and their origin in a bid to improve the simplicity in differentiating between aggregate types.

Despite the classification of larger aggregates as sub-visible particles, smaller aggregates (i.e. 1-10 µm) are often not subjected to quantification in pharmacopoeial monographs and limited restrictions have been placed on their concentrations in biopharmaceutical preparations for intended routes of administration. Whilst the exclusion limits of such aggregates have not been clearly defined, there is a clear association between their presence and adverse clinical outcomes.[53]

1.2.1.2 Consequences of Aggregate Presence within Biopharmaceuticals

Immunogenicity

Published literature has established that repetitive antigen arrays occurring on large aggregate surfaces present in vaccine products are most potent at eliciting immune responses. Immunogenicity arising as a result of protein aggregation is a well-recognised aspect in biopharmaceutical safety and remains to be significant to the assurance of biopharmaceutical safety.

For example, monomeric native proteins do not elicit an antibody response, but in the presence of native oligomerisation following unfolding an immune response may be mounted. Hence, multimerisation (i.e. loss of native structure) is key to immunogenicity and such aggregates may be removed by antigen-presenting cells *via* endocytic mechanisms.[58]

Furthermore, limited studies have considered comprehensive characterisation of parameters contributing to aggregate-induced immunogenicity to date. Patient-related parameters such as route of administration, co-morbidities and immuno-competence have also been identified as factors requiring consideration due to their implication in

patient response and adverse effects in the clinical assessment of biopharmaceutical product safety.[53,58]

Effective clinical evaluation of aggregate immunogenicity (i.e. product safety) may not be achieved without correlation of clinical effects with the presence of specific aggregate size ranges and concentrations that may be elucidated utilising a combination of analytical approaches. The range of available analytical methods applied in aggregate profiling will be introduced later alongside therapeutic examples.[53,59]

Assessing Immunogenicity in Pre-clinical Studies

Changes in the immunogenicity of a product may occur following modification of the manufacture process at any stage. Though knowledge of higher order structural changes and their association with immunogenicity remains limited, there is currently a better understanding of the link between a native primary sequence and the existence of epitopes that elicit immune responses.[60,61]

Classically, immunogenicity has been assessed through antibody production in animal subjects and in some instances a poor correlation has been observed between animal models and immunogenic responses in humans, rendering the application of such studies species-specific.[61]

Various immunoassays can be utilised to detect the presence of antibodies raised against a protein drug product. Such methods include surface plasmon resonance,[62] radio-immunoprecipitation antibody detection assays and ELISA.[63] Previous recommendations have included case-by-case assessment of the suitability of each immunoassay for a specific protein. For example, a reduced performance was noted in the ELISA assay with an observed lower affinity of antibodies raised as a consequence of epoetin alpha-induced red cell aplasia in patients.[64-66]

Loss of Therapeutic Bioactivity

Interaction of protein in its native structure with the desired target site of action is a pre-requisite for retention of therapeutic bioactivity. Processes leading to loss of native protein structure or neutralisation of proteins (e.g. unfolding) as a result of antibody production in response to larger aggregates are responsible for loss of potency and a poor clinical response.[59]

The recruitment and design of reproducible and appropriate bioassays is essential to the quantification of bioactivity or any neutralising antibody responses. *In vitro* assays of bioactivity may be exemplified by cell proliferation, apoptosis and inhibition of cell proliferation, all of which are downstream events of ligand interaction with target receptors. In order to ensure effective profiling of bioactivity, it is essential to possess an understanding of the fundamental molecular signalling pathways recruited following association of a protein with the target receptor so that the appropriate response (i.e. effect) can be measured. For example, application of the kinase receptor activation assay (quantifying the amount of activated phosphotyrosines) though more time consuming would be a more appropriate measure of response to a cytokine rather than a cell proliferation assay.[67]

1.2.2 Contributory Factors to Protein Aggregation During the Product Lifecycle

As highlighted previously, an appreciation of underlying processes resulting in the loss of protein native strucutre is of significance to the maintenance of native protein during manufacture, storage and administration of biotherapeutics. During product development, the specific aggregation pathway for a protein may be characterised with the recruitment of accelerated stability tests that utilise stress conditions (i.e. formulation and environment) to which a product may be exposed during its lifecycle.

1.2.2.1 Cell Culture

Cell culture remains to be the routine commercial option in the large scale production of a diverse range of therapeutic proteins though stability issues arising from the formation of inclusion bodies routinely present challenges to the biotechnologist. Inclusion bodies refer to the intracellular accumulation (and aggregation) of proteins in expression systems that may occur as a consequence of protein over-expression and macromolecular crowding within subcellular compartments where a constant competition between unfolded and refolded states exists.[68,69]

Inclusion bodies have been extensively characterised over the past few decades utilising a diversity of biomolecular,[70-73] crystallographic,[74,75] spectroscopic,[73,75-78] computational[79] and microscopic approaches[72-76] to assess the interplay between cell culture media conditions and expression systems. An early example of one such study is a report by Hart *et al*. in which a combination of phase contrast microscopy, western

blots and gel electrophoresis were utilised to assess the morphology and thermodynamic stability of *Vitreoscilla* inclusion bodies in *Escherichia coli* expression systems. The authors concluded that solubility was the principle feature contributing to inclusion body structure as opposed to folding transitions.[71]

Fourier transform-infrared (FTIR) spectroscopy analysis of isolated and purified inclusion bodies to date has revealed common structural features among such moieties. Such features included a high degree of secondary native structure, suggesting the formation of inclusion bodies from partially-unfolded native species. Similar structures were observed in protein solutions at elevated temperatures leading to the conclusion that an intermediate unfolded state exists for each protein that is prone to aggregation.[77,80]

The rich secondary structure in inclusion bodies has rendered them attractive for the mechanistic assessment of amyloid fibril formation. For example, Wang *et al*. assessed the secondary structure of *E. coli* inclusion bodies utilising a combination of X-ray diffraction studies, nuclear magnetic resonance (NMR) and far-UV circular dichrosim. Data obtained was utilised in combination with morphological and spectroscopic data obtained following electron microscopy and spectrofluorimetric assessment (fibril-labelling dyes).[74] Atomic force microscopy and electron microscopies have been applied in an attempt to ascertain the surface morphology characteristics of inclusion bodies at sub-nanometer scales. Despite the appeal of utilising such approaches, the invasiveness of these methods limits their *in vivo* application.[81]

Whilst each of these analytical approaches provided valuable structural data, they have required *ex situ* assessment of inclusion body formation (i.e. isolation and purification) that may often induce structural changes.

Over the recent years numerous fluorescence-based methods and bio-imaging analyses have been applied to determine *in vivo* aggregation through the formation of fluorescent fusion proteins (e.g. GFP analogues and thermolabile reporter molecules). Such studies have involved non-invasive examination of the spatiotemporal intracellular sequestration of inclusion bodies[70,82] and changes in the detected fluorescence intensity as a function of GFP exposure linked to the loss of protein activity due to intracellular aggregation.[72,81]

Real-time characterisation of inclusion body formation was achieved through mutagenesis and ligation with a fluorescein analogue.[76] The application of fluorescence resonance energy transfer (FRET) has been reported for determining dipole-dipole interactions between GFP-labelled fusion proteins within the 1-10 nm distance range.[73]

The introduction of novel image analysis extensions (i.e. ICS and SpIDA) over the recent decade exploiting fluorescence intensity fluctuations at pixel level (>40 nm) coupled to high resolution imaging with particle tracking has introduced the scope for both qualitative and quantitative real-time examination of intracellular oligomerisation and aggregate growth profiling at a molecular scale.

Numerous models have previously proposed intermediates or conformations contributing to inclusion body formation that vary from unfolded states to partially folded and over-crowded states of intracellular native protein.[68] Despite acknowledgement of inclusion body contribution to aggregation and the implication of numerous physicochemical parameters (e.g. concentration, folding state and charge) in their formation, little is known concerning the underlying molecular mechanisms contributing to their formation.[68]

Interaction of secreted protein with cell culture media as a consequence of macromolecular crowding has also been recognised to catalyse aggregation. Hence, a consideration of the expression system and cell culture media composition is crucial to the manufacture of therapeutic proteins to ensure no loss of activity as a result of denaturation, unfolding and refolding.[83]

1.2.2.2 Manufacture

The manufacture of biotherapeutics is a complex process involving continual refinement and profiling throughout the biopharmaceutical product lifecycle. Constant evolution of process engineering in the context of product development may extend to manufacturing technologies, scale-up, novel analytical technologies and formulation delivery systems all of which may influence characteristics of the end product.

Hence, it is essential to assure that product design and any subsequent changes in the processing and formulation of a protein do not adversely impact on its safety and efficacy through comparison of the product prior to and following implementation of a new process. Companies are required to provide comparability data demonstrating sufficient similarity between the product following changes in a single process. If significant differences are deteced the performance of further toxicity and safety studies is warranted prior to continuation with the clinical development plan.[84]

Prior to the marketing of the first biopharmaceutical preparation (Humulin I), the assessment of protein physicochemical parameters was limited to UV-vis spectroscopic methods, electrophoretic analysis[71] alongside chemical and protein content assays. A growth in the biopharmaceutical market stimulated the development of novel assays to assess consistency, safety and efficacy of protein products such that by the early 1990's mass spectrometry,[78,85] chromatography,[85-88] peptide mapping and NMR[89-92] had been reported as methods for physicochemical profiling of proteins.

Purification- Following cellular protein expression, the product and metabolites are either secreted into the culture environment or extracted through mechano-chemical processes. Purification based on charge, size and affinity (e.g. ion-exchange chromatography) of the protein of interest is then performed to yield the desired protein product. However, this process due to fluctuations in protein concentration, shear stress, changes in pH (acidic during affinity chromatography purification) and ionic strength may contribute to the aggregation process depending on the purification method implemented. Following cell culture or purification, aggregates may be removed through exploitation of their physicochemical characteristics e.g. size, surface charge or hydrophobicity.[52]

Formulation of biopharmaceutical products may entail procedures such as diafiltration, chromatography and freeze-drying all of which are used to both increase product yield and concentration, or improve shelf life. Incompatibilities arising as a function of interplay between specific excipient combinations and manufacturing approaches may induce aggregation in the end product and require consideration during product design. For instance mechanical agitation during filling, transport and other procedures may change flow conditions resulting in the formation of local temperature, pressure and concentration pockets, thereby, facilitating aggregation through the formation of hydrogen and hydroxyl radicals.[56,93]

Parameters such as pH, ionic strength, buffer composition and protein concentration are all recognised to influence the stability of biopharmaceutical preparations:

Buffer Composition and pH- Adequate pH control during shelf life is a pre-requisite for product stability. Significant changes in pH may result in the ionisation of residues and subsequent instabilities. A survey of commercial protein-based products by Meyer *et al*. indicated that buffer components may be associated with storage-related issues: for example, phosphate buffer has been considered responsible for pH shifts observed following freezing of protein-based formulations.[94-96] The addition of stabilisers such as glycine and arginine has been observed to mediate the pH effects observed in systems containing phosphate.[97]

Ionic Strength- Buffers and salts are utilised in formulation to stabilise biopharmaceutical preparations to thermal stresses,[98] aggregation[99] and solubility issues depending on the interactive forces responsible.

Concentration- Increased patient compliance and more attractive administration routes (i.e. *i.m.* and *s.c.*) have precipitated formulation of monoclonal antibody preparations at higher concentrations (i.e. >100 mg/mL) sufficient to promote interactions between native monomers.[100] Whilst formulation of these solutions is advantageous in these respects, significant problems in formulation development arise due to solubility issues or the intrinsic stability of a protein product in a particular formulation. Prolonged storage of high concentration formulations contributes to the formation of larger aggregates over time. Conversely, the dilution of protein solutions containing reversible aggregates has been shown to be responsible for the their subsequent degradation.[101]

1.2.2.3 Shelf Life

Environmental, packaging and formulation-related factors such as pH, temperature, salt type, protein concentration and ionic strength dictate the rate and extent of native structure loss and subsequent aggregation in protein biopharmaceuticals during transport and storage.

Freeze-thaw cycling has been deemed responsible for aggregation through a combination of physicochemical and interfacial factors during storage. Unfolding at low temperatures contributes to the formation of new interfaces facilitating intermolecular interactions and adsorption to container surfaces. Protein, salt and excipient changes in concentration at very low temperatures may contribute to effects similar to that observed following variation in protein concentration.[102]

1.2.2.4 Administration

Herceptin (trastuzamab), clinically utilised in the treatment of breast cancer, when reconstituted in dextrose is known to form aggregates. Demeule *et al*. compared the influence of diluents (i.e. 0.9% *w/v* NaCl and 5% *w/v* dextrose) on aggregate presence per microlitre of sample. This study represents one of the first fluorescence microscopy-based approaches in the determination of fluorescent aggregate particle size distributions.[103]

Most commonly utilised diluents in the formulation of biopharmaceuticals include 0.9% *w/v* sodium chloride, 5% *w/v* dextrose, Ringer's solution and lactated Ringer's solution. They are used to render solutions iso-osmotic but their inability to buffer formulations results in pH changes upon reconstitution. Compatability information may be obtained following pre-formulation studies with various diluents and packaging materials. The storage time between reconstitution and administration, packaging (i.e. *i.v.* bags) compatability, administration flow rates and in-line filters are examples of factors that require due consideration for administration in the clinic.

In summary, a knowledge of factors contributing to aggregation in formulations is of vital importance to the elimination or reduction of any incompatabilities arising from the manufacture process, packaging or storage conditions that may lead to loss of product stability.[104]

1.2.3 Analytical Approaches Utilised in the Assessment of Protein Aggregation

Since recognition of aggregation-induced adverse events, the pharmaceutical industry and academia have focused on the development and implementation of qualitative and quantitative aggregation assays. The result of decades of research has been the validation of a diverse range of bulk or microscopic analytical approaches to assess parameters of aggregation. To date, no single method has been capable of aggregate profiling over the entire size spectrum. In this section some analytical approaches utilised in the characterisation and quantification of protein aggregation will be discussed.

1.2.3.1 Mass Spectrometry

Due to its versatility in protein structure determination, mass spectrometry has been a valuable analytical tool for all stages of biopharmaceutical product development. Structural information obtained from mass spectrometry analyses include post-translational modifications (i.e. during cell culture, manufacture and storage), amino acid sequencing, carbohydrate profiling (i.e. glycosylation) and location of disulphide linkages (peptide mapping).[78,105]

The use of LC-MS in process optimisation has often been reported to entail the determination of appropriate combinations of process conditions (e.g. pH, feed, temperature) in an attempt to maximise product yield and minimise the presence of any potential undesirable post-translational modifications, aggregates or by-products of degradation. Mass spectrometry is often utilised during accelerated stability tests (during product formulation) to determine sequences, post-translational modifications and chemical modifications that contribute to conformational changes precipitating product loss.[85]

1.2.3.2 Fluorescence-Based Approaches

Intrinsic Fluorescence

Aromatic amino acid residues (i.e. tryptophan, phenylalanine and tyrosine) render proteins fluorescent and absorb light in the UV region of the electromagnetic spectrum whilst emitting fluorescence in the 250-450 nm range.[106] For most proteins tryptophan (Trp) is the major contributor to fluorescence emission when excited at 295 nm.[107]

Whilst the prospects of label-free characterisation of protein aggregation and conformation appears attractive, certain factors limit their exploitation in the characterisation of aggregation and conformation.

Fluorescent aromatic residues have a smaller absorption peak at 220 nm and a major absorption peak at around 280 nm. The smaller absorption peak occurs at 220 nm as a consequence of aromatic amino acid residue presence, charge and peptide bonds. Tyrosine residue existence within the protein structure often complicates intrinsic fluorescence measurements to the extent that excitation at 270 nm is used to eliminate tyrosine contribution. The fluorescence of tryptophan (i.e. indole chromophore) is dependent on its local environment and proximity to polar groups/components that may be used to infer information concerning protein conformation (i.e. unfolding).[108]

This concept may be further illustrated with BSA that possesses two tryptophan residues contributing to two spectral contributions: the larger contribution is from Trp-134 present in the hydrophobic pocket in proximity to the domain *I* surface and the Trp-213 residue concealed in domain *II* contributing to a smaller second emission band.[109]

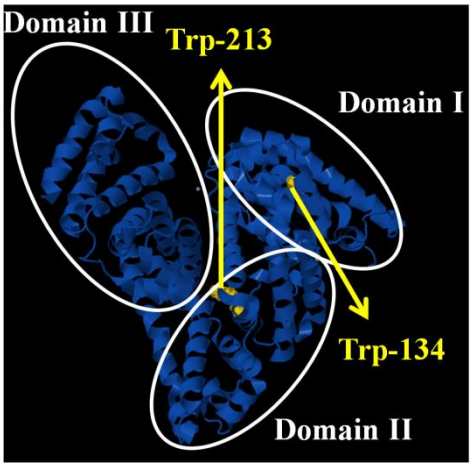

Figure 1.9 *Three dimensional structural representation of BSA crystal structure, domains and the location of tryptophan residues, extracted from the RSCB protein databank.*[110]

Due to the absence of a requirement for extrinsic dyes, the exploitation of intrinsic fluorescence emission changes has become ever increasingly favourable over recent years owing to the probeless nature of the method. A recent study has reported the application of two photon fluorescence correlation spectroscopy and steady state tryptophan fluorescence measurements as a reliable tool to assess changes in BSA conformation and fibril formation.[111]

Whilst intrinsic fluorescence measurements may be used in combination with time-resolved and steady-state measurements, assessment of peptide sequences containing one or two tryptophan residues renders intrinsic fluorescence-based assessment of aggregation and conformation complex in sequences containing several tryptophan and tyrosine residues.[108]

Fluorescence Microscopy

To date the application of confocal microscopy to the analysis of protein aggregation in solution has been performed using a combination of hydrophobic pocket binding dyes (e.g. Thioflavin T, ANS and Nile red) and covalently-labelled proteins (e.g. Alexa Fluor® 488). Demeule *et al*. have reported the use of confocal imaging in assessing protein aggregation and stability in herceptin to assess diluent compatibility during reconstitution[103] and antibody A[112] as therapeutic examples (See Table 1.2).

Table 1.2 *A summary of fluorescence microscopy-based studies performed to date in pharmaceutically-relevant preparations.*

Protein	Dye	Image Analysis Software	Factor Examined
Herceptin[103]	Nile Red Thioflavin T	Image J®	Diluent (5% dextrose)
Salmon Calcitonin[113]	Nile Red	Openlab	Pegylation
Serum IgG[114]	Alexa Fluor® 488	Particle Tracking	
Antibody A (recombinant IgG1)[115,116]	Nile Red Congo Red Thioflavin T	Image J®	Formulation (acetic acid, $MgCl_2$)
Human G-CSF[117]	ANS	Image J®	Mixing

Analysis of confocal micrographs has often entailed the use of image analysis software (i.e. Image J®) to detect particles and determine their corresponding size distributions.

Unfortunately, in the case of oligomeric species smaller than the selected pixel size, lack of detection or contribution to increased fluorescence within the image background is common. Filipe *et al*. demonstrated the application of single particle tracking to the detection of large labelled IgG aggregates (i.e. >50 *nm*).[114]

The introduction of image analysis extensions exemplified by image correlation spectroscopies[34,118,119] and photon correlation histogram-based methods[48,120,121] in conjunction with aggregate-labelling capabilities, has rendered the mechanistic assessment of protein oligomerisation and assembly into high molecular weight aggregates, and their direct visualisation at high spatiotemporal resolutions within reach.[122]

With advances in imaging and small sample volume requirements, the application of confocal microscopy in aggregate detection following exposure to stress conditions is increasingly being reported in the literature. The pre-requisite for fluorescent aggregate

labelling has often been considered an obstacle in the application of microscopy to aggregate analysis. However, increasing numbers of commercial hydrophobic pocket-associating dyes are becoming available that allow specific labelling of components of interest (i.e. amorphous or fibrillar species). A summary of currently available commercial aggregate-labelling extrinsic dyes are presented in Table 1.3 based on Hawe *et al*.[123]

Table 1.3 *Routine extrinsic aggregate labelling dyes, their applications and reported examples of their use in the literature.*

Dye	Excitation (nm)	Emission (nm)	Applications	Reported methods*
ANS	350-380	505	Unfolding/refolding Surface hydrophobicity Aggregate conformation	Fluorescence microscopy Steady state Fluorescence
SYPRO Orange[124,125]	488	500-600	Surface hydrophobicity Conformational transition	High throughput fluorescence
Congo Red[126,127]	530-585	>600 nm	Fibrillation	Microscopy
Thioflavin T[128]	450	480-490	Fibrillation	Steady state fluorescence Fluorescence anisotropy Fluorescence microscopy
Proteostat[119]	~550	~600	Aggregation/fibrillation	Fluorescence plate reader
Nile Red[115,116]	540-580	660	Unfolding/refolding Surface hydrophobicity Aggregate conformation	Steady-state fluorescence Fluorescence anisotropy Fluorescence microscopy
DCVJ[129]	450	470-530	Viscosity of protein microenvironment	Steady state fluorescence Time-resolved fluorescence
Bis-ANS	385-400	470-530	Unfolding/refolding Surface hydrophobicity Aggregate conformation	

*Denotes the reported methods by which these extrinsic dyes have been characterised.

1.2.3.3 Light Scattering Approaches

Scattering approaches are based around deflection of incident radiation due to movement of the particles through the incident light beam, the intensity of which may be quantified as an interplay between particle size, shape, wavelength of the incident light and the angle of observation.[130] Generally, light scattering instruments consist of a light source (i.e. laser beam), a spectrometer (defining the scatter angle volume), a detector (i.e. PMT) and an analyser or correlator (for dynamic measurements) connected to a computer (Figure 1.10).

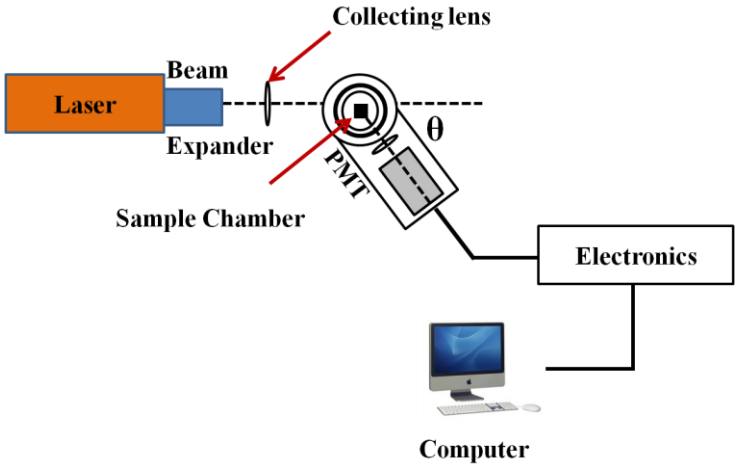

Figure 1.10 *Schematic depicting the components of a typical light scattering setup from the top view, adapted from Hiemenz et al.*[130]

Currently in the characterisation of protein aggregation one of the three following light scattering methods may be applied;

Static Light Scattering (SLS) and Multi-angle Laser Light Scattering (MALLS), used in the determination of molecular weight and molar masses, can aid the elucidation of oligomer and higher order aggregate formation. For smaller globular proteins (i.e. <500 *kDa*), a single detection angle of 90° may suffice, whereas, for larger aggregates of irregular morphologies scattering may be observed at multiple angles (i.e. MALLS) and the absolute molecular weight determined.[130]

Dynamic Light Scattering or Quasi-Elastic Light Scattering involves the analysis of temporal fluctuations in intensity arising from light scattered by moieties undergoing Brownian motion (i.e. diffusion). The scattering of light by species undergoing

diffusion is measured (as a function of their size and shape) using an ACF, the exponential decay of which may be described using the following equation;

$$G(\tau) = A\exp\left(-2DQ^2\tau\right) + B \qquad \textit{Equation 1.3}$$

Where Q is the wave vector, D represents the diffusion coefficient , A and B are constants.

In the case of homogenous samples it is possible to determine the hydrodynamic radius (R_H) of proteins using the Stokes-Einstein equation;

$$D = \frac{kT}{6\pi\eta R} \qquad \textit{Equation 1.4}$$

Parameters utilised in the Stokes-Einstein equation include k representing the Boltzmann constant, T the temperature, η the viscosity of the solution and R the hydrodynamic radius of the diffusing species determined from the diffusion coefficient.

For multimodal samples it is possible to apply one of two approaches:

(i) Fitting the data to the sum of exponential functions to yield a multimodal distribution of particle sub-populations.

(ii) Fitting the data to a function resembling $ln[g(\tau)\text{-}k]$ to determine the polydispersity parameter and the weight average mean diameter (i.e. the cumulant method).

Since the quantification of particle size distributions within biopharmaceutical preparations is of importance in the characterisation of product stability, DLS has traditionally been utilised for this purpose.

Raman or inelastic scattering, occuring less commonly than Rayleigh or Mie scattering, refers to a two photon process in which the energy of the emitted photon is weaker than that of the excitation source, leading to an energy gain of the molecule from the photon and subsequent promotion to an excited state. This results in Stokes Raman scattering which is the principle characteristic profiled in a Raman experiment.[131]

Previous pitfalls in the application of Raman scattering-based methods had included the weakness of the Raman signal (i.e. one out of every million incoming photons interacted with the analyte molecules and subsequently made one scattered Raman

photon available for analysis) and the requirement for enhancing detected signals that ultimately rendered the method prone to interference from fluorescence effects in the visible light region. However, to circumvent these caveats recent advances in Raman instrumentation and performance of measurements at sufficient spectral separation from visible light (e.g. the use of wavelengths above 1064 nm in FT-Raman) have increased the scope for Raman-based methodology application to a range of protein products.

Reports of Raman scattering-based approaches to date have included profiling protein composition and aggregation, real-time monitoring of freeze-drying,[132] protein stability during shelf-life,[133] the use of Raman confocal microscopy in profiling the identity of proteinaceous and non-proteinaceous particles,[134,135] conformation analysis[136] and monitoring post-translational modifications (i.e. glycosylation) that are ultimately recognised as components contributing to the overall stability of a protein structure.[137]

Other applications currently being explored for Raman spectroscopic methods include the integration of such technologies as a process analytical technology (PAT) method in bioreactors and particulate detection in formulations.[134,135,138]

1.2.3.4 Size Exclusion Chromatography (SEC)

SEC, a versatile analytical instrument, has been utilised to assess changes in self-associated monomeric species through their separation as a function of permeation into the stationary phase pores according to size. Larger molecules (i.e. large aggregates) are normally excluded and elute rapidly while smaller molecules passing through resin pores elute at later times. SEC is often connected to a further analytical instrument (e.g. UV-vis spectrometer, MALLS and DLS) as a detector; thus permitting characterisation of the separated size fractions.[139]

Factors that limit the use of analytical SEC in biopharmaceutical aggregation profiling entail retention of larger aggregates (i.e. size fractions), changes in the concentration of the eluent (resulting in a reduction in the concentration of soluble reversible aggregates with dilution effects)[140] and interaction with the column resin. In the case of protein complexes containing carbohydrate moieties a significant change has been previously noted in the elution position.

However, SEC remains a routinely implemented method and may be applied to the preliminary quantitative assessment of aggregate presence in a sample with the ability to

resolve monomers from dimers. One of the principle advantages of utilising SEC in combination with light scattering is that absolute molecular weights are determined for the fractions irrespective of their elution position.[141]

1.2.3.5 Analytical Ultracentrifugation (AUC)

AUC, based around sedimentation velocity, aids determination of protein hydrodynamic radii, their binding and association.[142] Advantages associated with this technique include minimal sample preparation and a broad analyte concentration range allowing analysis of aggregation under a diverse range of solvent conditions. Following application of a centrifugal force, concentration boundary layers are formed between the macromolecular aggregates and smaller particles as time progresses that facilitates their separation.[143]

Methods utilised in AUC may be exemplified by boundary sedimentation velocity (SV) and sedimentation equilibrium (SE),[88] analytical band sedimentation and tracer sedimentation equilibrium. SE yields aggregate molecular weights, mass and association constants in both homogenous and heterogenous systems, whilst SV provides hydrodynamic information concerning molecular shape and size.[56,143] To date AUC has been used to assess a diverse range of protein-based biopharmaceuticals and while mass spectrometry and static light scattering are proving to be more accurate tools in molecular weight determination, AUC remains to be recognised as a valuable method in profiling protein aggregation particularly in the determination of oligomeric fractions.[142]

1.2.3.6 Circular Dichroism (CD)

Analysis of protein aggregation and conformation entails measurement of the differential absorption of clockwise and counter-clockwise components of polarised light by optically active chromophores (i.e. the amide backbone) in the protein structure. If the left- and right-handed components are absorbed to differing extents, the absorption is eliptically polarised hence the output parameter is referred as elipticity (θ) expressed in degrees (See Equation 1.5).

$$\theta = \tan^{-1}\frac{b}{a}$$ *Equation 1.5*

Where *b* and *a* are the size of the minor and major semi-axes of the resulting ellipse.

The presence of optically active components arising from alpha helical, beta sheet and higher order structure arrangement contribute to the detection of structural and conformational changes by CD.[144]

Far-UV CD (i.e. 180-260 nm) is the most common analytical approach used for elucidation of protein secondary structure and is highly sensitive to conformational changes. In the case of near-UV CD (i.e. 240-320 nm) utilised for the assessment of protein tertiary structure, assymetry in the environment in which aromatic side chain residues (absorption ~250-350 nm) and disulphide bonds reside (broad weak signal ~260 nm), gives rise to a signal of lower intensity than far-UV CD.

Whilst the two methods characterise different elements of the protein structure/conformation, they can be applied to yield complementary information concerning changes following denaturation or fibril formation.[145,146]

1.2.3.7 Taylor Dispersion Analysis

Taylor Dispersion Analysis (TDA) is a rapid and absolute method that measures the diffusion coefficient and hydrodynamic radii of molecular species *via* the dispersion of solute under laminar Poiseuille flow through a cylinder. Solute is injected into a moving stream of solvent through a column dispersed by a combination of cross-sectional velocity and radial diffusion. The detector in a TDA setup records the band broadening of an injected specimen driven through a capillary tube and imaged at two windows upon entry and exit from the tube. To date the reported applications of TDA have been the characterisation of nanoparticles,[147] biopolymers[148] and small molecules.[149] However, TDA remains under-utilised in profiling protein-based biopharmaceuticals such that Hawe *et al*. evaluated TDA for the analysis of protein aggregation in formulations subjected to stress and compared the resultant data against that of DLS to extend the application of this method to biopharmaceutical aggregate profiling.

The application of TDA offers advantages such as small sample volumes, no requirements for internal standards and increased sensitivity in differentiating monomers from dimers compared to dynamic light scattering.[150-152]

1.2.4 The Current Role of Imaging in the Assessment of Protein Aggregation

To date limited applications of imaging in the determination of aggregate particle counts and their corresponding size distributions have been reported using routine image analysis software.[103,116] However, despite the recent ever-growing implementation of fluorescence-based imaging, little has been done to apply automated correlation and histogram-based image analyses to the determination of early aggregation processes and particle size distributions at a higher resolution with little operator intervention. The validation and application of such image analysis methods for the analysis of protein aggregation is reported in this thesis.

In summary, currently several analytical technologies exist that enable biopharmaceutical profiling during product development. Despite the diverse arsenal of methodologies, each technology is known to possess limitations in providing multi-parametric output concerning bioactivity, structural chemistry, conformational stability and aggregate size distributions.

Furthermore, challenges in the analysis of protein aggregation often relate to the nature of analyte aggregate species and their corresponding heterogeneities in size (a few nanometers to hundreds of microns), an aspect that no current existing methodology is able to address. This is further complicated by the recruitment of several orthogonal approaches that whilst enabling the quantification of aggregate size ranges over a diverse spectrum require sample handling and ultimately result in physical modifications of the aggregate structure (e.g. non-specific adsorption to column matrices and dilution effects in SEC) that may present further technical artifacts in the form of misleading data. To address this issue, common practice in product development entails the systematic selection of several orthogonal approaches that generate complementary output parameters in a timely fashion with sufficient resolution for the intended experiment.

Hence, rational structure-activity assessment of a novel protein therapeutic may require the recruitment, validation and implementation of several orthogonal approaches (i.e.

novel and existent) in order to enable a multi-faceted approach in the accurate prediction and determination of product safety and efficacy. This may only become a reality through collaboration of regulatory bodies, academic organisations and the biotechnological industry in a bid to direct a data-driven approach to the prediction of biopharmaceutical safety and efficacy matters during the biopharmaceutical product lifecycle. Whilst the assessment of protein aggregation is essential to product safety, a consideration of membrane permeation mechanisms and their relative relevance are of equal importance in the efficient and targetted delivery of macromolecular therapeutics. P-glycoprotein-mediated efflux and receptor-mediated transcytosis will be discussed as such an entry route in Sections 1.4 and 1.5, respectively.

1.3 The Plasma Membrane

A physical and chemical barrier to the permeation of xenobiotics is the plasma membrane that is implicated in the maintanence of homeostasis and uptake of endogenous ligands from the environment vital to cell survival and growth. The implications of manufacturing conditions, formulation and profiling instabilities were emphasised earlier in this thesis (See Section 1.2).

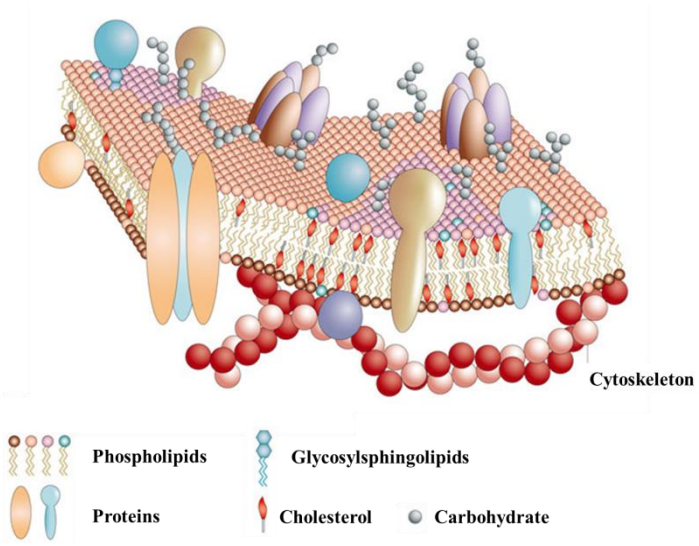

Figure 1.11 *Simplified representation of the fluid-mosaic structure of the plasma membrane and its components, adapted from Pietzsch.*[153]

In the case of small molecule drugs, efflux activity remains to pose a challenge hence determining the susceptibility of a lead compound to p-glycoprotein efflux activity is a subject area of interest to the pharmaceutical industry.

The presence of efflux transporters at the site of absorption or pathology can significantly impair the efficacy of a therapeutic and lead to multidrug resistance or drug-drug interactions. In this section the concept of p-glycoprotein efflux and transcytosis uptake as two significant membrane-related phenomena to the pharmaceutical industry will be introduced and discussed. Figure 1.12 is a simplified representation of such transmembrane/transcellular transport processes and illustrates p-glycoprotein efflux and transferrin-receptor mediated transcytosis.

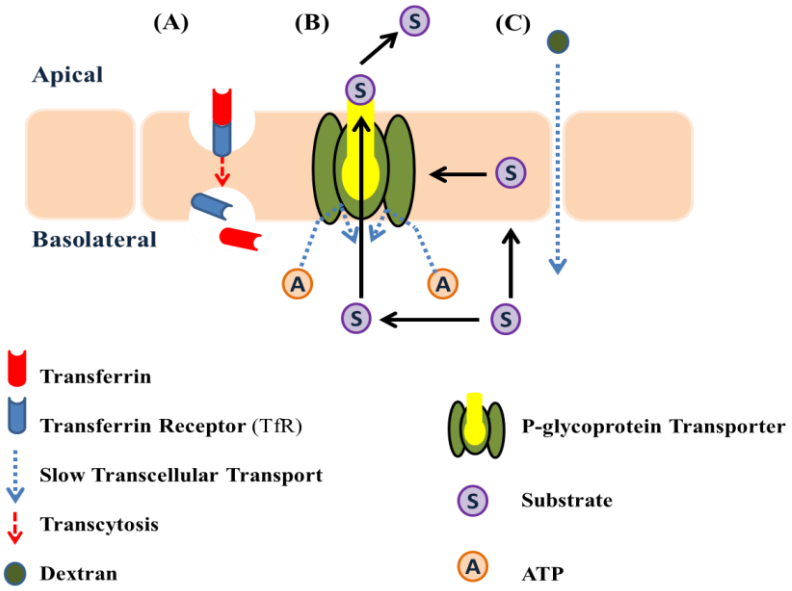

Figure 1.12 *Schematic depicting the transmembrane transport processes across a monolayer* ***(A)*** *receptor-mediated transcytosis and* ***(B)*** *p-glycoprotein transporter efflux discussed in this thesis and* ***(C)*** *paracellular permeability.*

1.4 P-glycoprotein

P-glycroprotein, encoded by the human MDR1 gene, is responsible for the efflux of a structurally diverse range of xenobiotics and the observed poor therapeutic activity (i.e. drug resistance) of drugs and drug-drug interactions.

Knowledge of the constitutive expression of p-glycoprotein in a diverse range of tissues (e.g. the gastrointestinal tract and the central nervous system (CNS)) and the associated poor prognosis in the treatment of malignancies has presented a challenge to the pharmaceutical industry in the context of discovery and development of novel p-glycoprotein inhibitors or small molecule therapeutics that do not exhibit inhibitory or substrate activity.

Structurally, the p-glycoprotein efflux transporter is a transmembrane protein possessing two membrane-bound cassettes consisting of six transmembrane helices that gives rise to a large internal cavity accessible through both the cytoplasmic and inner membrane compartment (See Figure 1.13). As illustrated in Figure 1.12, ATP binds to the two nucleoside binding domains in the cytoplasmic compartment, the hydrolysis of which results in the conformational change of p-glycoprotein that ultimately exposes drug molecules bound to the drug binding pocket to the extracellular environment.[154]

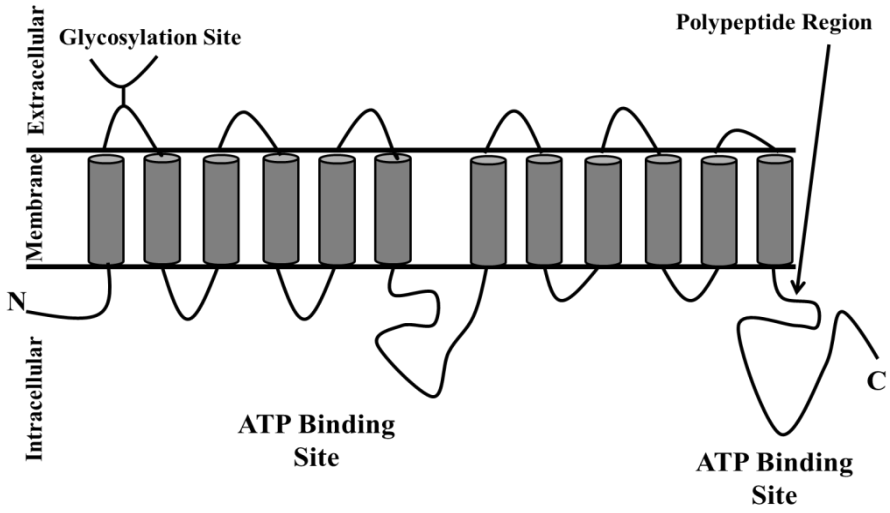

Figure 1.13 *A simplified two-dimensional schematic representing the structure of the p-glycoprotein transporter, its location in the plasma membrane and nucleoside-binding domains-ATP binding sites are highlighted in the intracellular compartment, adapted from Ambudkar et al.*[155]

1.4.1 Therapeutic Implications of P-glycoprotein Expression and Activity

P-glycoprotein, a member of the ATP-binding Casette family (ABC), has been implicated in numerous drug-drug interactions (e.g. quinidine and digoxin) and the poor therapeutic activity observed with some CNS[156] and anti-cancer agents.[157-159] Despite the diversity of structures susceptible to p-glycoprotein efflux, studies have attempted to predict pharmacophores responsible for the association of compounds with the drug binding pocket in the MDR1 transporter. Such attempts have been performed in a bid to reduce drug-drug interactions and multidrug resistance, both phenomena associated with p-glycoprotein activity.[160]

Drug-drug interactions resulting from induction, inhibition or substrate activity exhibited by chemical compounds often give rise to serious adverse events with drugs possessing a narrow therapeutic window (e.g. digoxin) when administered concomitantly.[161,162] Such interactions may be exemplified by the well-documented observed digoxin toxicity observed with the co-administration of digoxin and quinidine arising from the elevation of serum digoxin levels as a consequence of p-glycoprotein inhibition by quinidine.[163,164] Following documentation of similar effects following administration of antibiotics, antimycotics and a range of other drugs, researchers found that the principle sites at which quinidine inhibited p-glycoprotein activity were located

in the small intestine[165] and the kidney.[165] Since then p-glycoprotein has been detected in tumours, at the blood-brain barrier (BBB) and many other tissues and has been observed to play a significant role in the ADME of small molecule drugs.[166]

Multidrug resistance arising from the efflux of chemotherapeutics is a phenomenon more commonly associated with p-glycoprotein expression in leukaemias and tumours.[167-169] However, multidrug resistance has also been observed in epilepsy and some psychiatric conditions presenting an additional challenge to the successful management of these clinical conditions and discovery of novel therapeutics that are not effluxed through the BBB.[170] Much effort over the recent decades has been directed to combating the poor prognosis observed in the clinic associated with multidrug resistance and several approaches have been applied to shedding more light on the expression and functionality of efflux transporters.

1.4.2 P-glycoprotein Expression

P-glycoprotein is known to be expressed in most tissues exemplified by the gastrointestinal tract mucosa,[162,171,172] blood brain barrier[156,170,172] and the kidney.[173] Expression of p-glycoprotein in polarised tissue plasma membranes (e.g. gastrointestinal tract) occurs on the apical side of polarised cells suggesting a detoxifying role for this efflux transporter with respect to xenobiotic access to susceptible tissues.[156]

1.4.2.1 Qualitative and Quantitative Characterisation of P-glycoprotein Expression

Quantification of protein expression, in particular functional p-glycoprotein, is essential to the determination of the extent of MDR1 activity and its influence on intracellular drug retention and efflux. Despite the existence of a multitude of technologies for the quantification of transporter expression, fewer studies have compared two or more routine methods, the results of which have exhibited a high degree of variability depending on the secondary detection systems and antibodies utilised.

Reverse-Transcription Polymerase Chain Reaction (RT-PCR)

In vitro transcription and translation data are useful in the interpretation of protein expression levels within biological systems. To date the application of RT-PCR has been reported in numerous studies profiling transmembrane transporter expression using RT-PCR in sandwich cultured hepatocytes[171,174] or the determination of p-glycoprotein expression in tumours and various cell lines.[171,175,176] Whilst the data obtained from PCR experiments allows the quantification of mRNA levels involved in the expression of p-glycoprotein transporters within a tissue or tumour cell line through the generation of a large number of cDNA copies, there is little indication as to whether expressed transporters are indeed functional.

Mass Spectrometry

As a powerful analytical tool in the proteomics arena mass spectrometry has been applied over the recent years in conjunction with separative methods (i.e. chromatographies) to yield information concerning the amount of protein expression per unit weight of tissue analysed.[177] Liquid chromatography-tandem mass spectrometry has been reported increasingly in the literature over the recent decade in the quantitative evaluation of transporter expression in tissues.[178,179] Whilst mass spectrometry is ever-increasingly being reported as a valuable tool in the quantification of transporter distributions in tissues, the method is invasive and does not allow direct visualisation of transporters in their native environment and spatial assessment of their densities.

Immunochemistry is a widely used method in clinical pathology to characterise protein expression and disease prognosis. Procedures utilising this concept are immunofluorescence staining,[180] immunoblotting[181] and immunohistochemical studies. These methods suffer from disadvantages revolving around interlab differences in

protocols, requirement for standardisation of these methods and subjectivity in the analysis of protein expression utilising these approaches.

Immunofluorescence and immunohistochemistry normally entail imaging tissue incubated with a primary antibody directed against the protein of interest and subsequent incubation with a secondary conjugated antibody system to allow the detection of labelled moieties.[181,182]

Over the recent years, quantitative immunofluorescence and morphometric analysis of labelled punctate species have increasingly been reported in the literature using routine image analysis tool exemplified by Image J® to determine integrated density values[180,181] or coupled to flow cytometric analysis to quantify specific fluorescence intensities relative to a control.[183] To date several studies have utilised this procedure to semi-quantitatively characterise expression of receptors or transporters in a diverse range of cell lines.[184,185] Whilst such methods have been successful in the visualisation of protein expression, there remains a requirement for novel image analysis tools that can enable the objective and automated acquisition of quantitative parameters relating to the density and number of transporters expressed in a sample.

Immunoblotting entails cell lysis followed by a subsequent multi-step centrifugation process to prepare a membrane fraction for analysis. Subsequent quantification of protein content in the lysate sample is then utilised to determine the loading amount onto the electrophoresis gel. Proteins are subjected to reducing and denaturing conditions (i.e. in the presence of SDS) that renders the denatured proteins negatively charged and following application of a current on the reducing gel, protein components are separated according to their size and charge. SDS-PAGE is subsequently followed by transfer of the separated protein fractions on the gel to a membrane (i.e. PVDF or nitrocellulose). The application of primary and secondary antibodies allows detection and subsequent assessment of the degree of protein expression within the cell line of interest such that western blots may be utilised as a semi-quantitative method in densitometric analyses.[171]

Protein Microarrays can be applied to the quantification of protein expression and interactions enabling highthroughput multiparametric assessment of a sample following the immobilisation of an analyte on a solid support. Samples prepared in this manner

may be subsequently analysed using a diversity of methods ranging from mass spectrometry to fluorescence-based measurements.[186]

One of the major issues that has emerged in multidrug resistance profiling of tumours and tissues to data has revolved around the quality control and standardisation of methods used to detect p-glycoprotein expression.[187]

1.4.2.2 Functional Assays of P-glycoprotein Activity

In Vitro Assays

Depending on the system implemented, application of numerous cell models to the characterisation of the role of p-glycoprotein as an efflux transporter has been reported.

Colorectal carcinoma (i.e. Caco-2) cells have commonly been utilised as a model for gastrointestinal system absorption and distribution due to the observed functional and morphological similarities to enterocytes.[188] However, due to the expression of multiple efflux transporters (e.g. Breast Cancer Resistance Protein (BCRP) and Multidrug Resistance-Related protein (MRP))[189] and susceptibility to cell culture conditions,[190] this cell line has been rendered difficult for the sole assessment of MDR1 efflux activity and substituted by MDR1-transfected cell lines. Madin Derby Canine Kidney cells (i.e. MDCK) transfected with the human MDR1 gene have been characterised as a potential substitute for the Caco-2 monolayer model due to the formation of columnar epithelia when seeded onto transwell filters and rapid formation of tight junctions compared to Caco-2 cells (i.e. three versus 21 days). Tight junction formation in MDCK cells has been attirbuted to the MDCKI strain whilst in the case of MDCKII cells leaky junctions and consequently lower transcellular electrical resistances are observed.[191] The localisation of the p-glycoprotein transporters in monolayers of the MDCK-*MDR1* cell line has been confirmed to occur on the apical plasma membrane compartment.[192]

Additionally, the passive absorption characteristics of Caco-2 and MDCK cell lines have previously been examined and shown to correlate closely.[193] Factors that should be considered when comparing data obtained from *in vitro* models include interspecific differences resulting from the existence of polymorphs of the gene encoding p-glycoprotein thus influencing the outcome of experiments depending on the *in vitro* model utilised for the study, and a consideration of the changes in the functional expression of transporters across various passages.[194,195]

In this section commonly utilised assays in the assessment of p-glycoprotein function and the inducer, substrate or inhibitory activity of lead compounds will be introduced and contrasted. Each of the methods introduced are known to possess their own relative merits and several studies have compared their ability in determining the nature of p-glycoprotein modulation by various compounds, in some cases leading to conflicting data or overlapping specificities of each assay.[196-199] Such disparities may depend on the standardisation of assay conditions, acceptance criteria, cell culture conditions and in some cases defining efflux ratio thresholds for the classification of compounds as either substrates, inducers or inhibitors. For example in the case of verapamil, transport may not be observed from the monolayer efflux assay but an increase in intracellular calcein fluorescence intensity and changes in inorganic phosphates may be observed with the ATPase assay.[200,201]

Dye Efflux Assays generally benefit from being of high throughput nature to the ability to automate readings that renders their application in pre-screening of p-glycoprotein modulation by lead compounds favourable.

Rhodamine 123 is a well-recognised substrate for the p-glycoprotein transporter and its intracellular retention and uptake has been utilised as a marker of p-glycoprotein activity coupled to fluorescence-based approaches exemplified by flow cytometric analysis.[202] For example, in a study by the National Cancer Institute (NCI) the rhodamine efflux assay was utilised as a means of screening p-glycoprotein substrates.[169]

Calcein acetoxymethyl ester (Calcein-AM) initially developed for intracellular calcium quantification is a substrate for the p-glycoprotein transporter. Calcein-AM is internalised into cells and cleaved by cytoplasmic esterases to yield a fluorescent product that is poorly permeable and not a substrate for p-glycoprotein efflux. Therefore, cells expressing the p-glycoprotein transporter and non-viable cells exhibit a low intracellular cleaved Calcein retention (i.e. a lower fluorescence) and any subsequent increase or reduction in intracellular cleaved Calcein fluorescence intensity can be quantified and attributed to the modulation of p-glycoprotein activity (e.g. inhibition). The fluorescence of Calcein in the presence of specific concentrations of test compound is often measured relative to the fluorescence intensity in the presence of Elacridar (i.e. absolute inhibition).[196,203]

The ATPase Assay quantifies the amount of inorganic phosphate liberated from the hydrolysis of ATP. Hydrolysis of ATP is assumed to accompany all energy-dependent processes and has been used to detect p-glycoprotein-mediated efflux of substrates.[204] Active transport of substances may be identified through the concentration-dependent increases of inorganic phosphate. Drawbacks associated with the use of ATPase assays relate to the requirement for high concentration of substrate, inconsistencies between ATPase activity and transport of drugs leading to false positives and negatives.[205]

Membrane Vesicle Assays rely on inverted membrane vesicles and assess the permeability of substrates through the quantification of the concentration of low permeability substrates that become entrapped in vesicles.[177,206] This assay requires maintenance of constant ATP concentrations to ensure p-glycoprotein activity throughout the duration of the experiment. Non-specific binding of hydrophobic compounds to the membrane preparation may contribute to a higher background measurement in vesicle preparations.[205]

Monolayer Efflux Ratios are determined through the quantification and comparison of bidirectional compound transport across polarised monolayers cultivated on membrane supports. However, in an industrial setting the assay throughput is limited by the labour-intensive nature of the method due to cell culture and analytical requirements. The relative merits of each approach have been summarised in Chapter 5.

In Vivo Studies

In addition to the *in vitro* assays described above, animal models have been utilised to assess the impact of p-glycoprotein efflux on the pharmacokinetics of a range of substrates. Previous studies with transgenic mdr1-knockout and wild-type mice have used the brain/plasma exposure ratio as a tool for the assessment of potential CNS effects of p-glycoprotein efflux on accumulation of drugs in the CNS.[207] Data obtained from animal models coupled to *in vitro* tests can therefore be utilised to ascertain the potential for a compound as a substrate, inhibitor or inducer of p-glycoprotein and the significance of efflux to the therapeutic activity of the compound of interest.

1.5 Transcytosis

Transcytosis is a vesicular transcellular transport mechanism by which macromolecular cargo is transported across the cell. Since the initial postulation of vesicular transport by Palade in the 1950's, a diverse range of approaches have been applied to understanding the molecular machinery and kinetics of transcytosis.

This section will introduce the concept of transcytosis, its relevance to drug delivery and consider studies and methods applied to the assessment of transcytosis to date.

1.5.1 Receptor-Mediated Transcytosis

Transcytosis is a multistage process consisting of endocytosis, exocytosis, recycling, and may be broadly categorised as being receptor-dependent or receptor-independent depending on the nature of cargo association with plasma membrane components: to illustrate the various stages of this transcellular transport mechanism for the receptor-mediated pathway, the transcytosis of transferrin will be used as an example.

Receptor-mediated transcytosis (RMT), a multistage process, is highly dependent on ligand interaction with cell surface receptors: thus, polymerisation or conformational changes may ensue following association of a ligand with its respective receptor.[208] Components constituting the vesicle membrane dictate the fate of the internalised ligand which may either entail degradation by lysosomes, interaction with intracellular receptors or exocytosis *via* sorting pathways.[209,210]

Exploitation of receptor-dependent pathways has been studied extensively in order to aid the development of selectively targeted therapeutics conjugated to ligands that will interact with specific receptors.[211,212] A more detailed account of transferrin receptor (TfR)-mediated transcytosis and expression will be considered in Chapter 6.

1.5.1.1 Transferrin Receptor Expression

The transferrin receptor (TfR) a transmembrane glycoprotein, is involved in iron metabolism and regulation of cell growth.[213,214] Many studies have recognised the TfR as a promising target for drug delivery at sites where over-expression of the TfR is evident.[213-216]

The expression of TfRs has been characterised in various cell lines including HeLa (a cervical cancer cell line),[217] Caco-2[218] and endothelial cell lines rendering them suitable for mechanistic profiling of TfR-mediated transcytosis.[219,220]

1.5.2 Routine Models of Epithelial Transcytosis

Epithelial cells lining the inner cavities of the body are polar, possessing an apical and basolateral face that functionally and compositionally differ in nature. The presence of tight junctions prevents leakage of solutes whilst also maintaining integrity of epithelial tissue.

Delivery of proteins to the apical or basolateral face my take place directly, or *via* indirect transcytotic pathways that possess protein and cell specificity.[221] Two commonly studied and well-characterised epithelial cell lines include Caco-2 and MDCK cells.[222-224] Transcytosis has been considered the sole sorting mechanism existent in all epithelial cell lines studied to date.[225,226]

To date pulmonary and gastrointestinal epithelial barriers have been applied to the characterisation of transcytosis with a view to delivery of novel therapeutics that exhibit enhanced uptake at these barriers. Analysis of transcytosis in these models has often entailed the use of blackbox technologies that deliver little mechanistic information concerning the molecular biology of vesicular transport processes. The design of *in vitro* models has provided a platform for the characterisation of barriers in isolation with the additional capability of monitoring and controlling the cell culture environment. Additionally, the application of these models reduces the need for extensive *in vivo* studies, even though validation of such results is required to be carried out in animal models. Various cell models may be used to study particular transport characteristics.

1.5.2.1 The Gastrointestinal Epithelial Barrier

The small intestinal epithelial barrier is composed of goblet cells, endocrine cells, stem cells, enterocytes, and paneth cells. Goblet and absorptive cells are the most common cells present at this barrier.[227-229] Ascertaining the significance of transcytosis contribution to overall transepithelial transport across polarised cells in the gastrointestinal tract may offer a potential for peroral delivery of peptides and proteins that exploit this uptake mechanism.

Caco-2 cells derived from human colorectal carcinoma cells are the most commonly-studied cells for characterisation of the gastrointestinal barrier and measurement of substance uptake across the gastrointestinal tract owning to their ease of transfection and differentiation.[230]

When cultured to confluence on Transwell® membranes, Caco-2 cells form a highly polarised barrier to the penetration of solutes. Due to their morphological and functional similarity to intestinal epithelial cells, Caco-2 are commonly utilised in the development of *in vitro* transport assays.[216] The polarity and morphology of Caco-2 cells is achieved within two days after confluence whereas, differentiation is a relatively slow process and can take up to 21 days.[216,231,232] To date the receptor-mediated uptake of intrinsic factor-cobalamin complexes,[233] transferrin,[232,234] and toxin uptake has been characterised for the gastrointestinal epithelial model.

1.5.3 The Current Role of Imaging in the Quantification of Vesicular Trafficking

To date numerous imaging acquisition methods and subsequent analysis extensions have been applied to the kinetics and extent of the endocytosis, transcellular transport and efflux of transcytosis substrates.

Currently real-time live cell imaging with confocal microscopy remains a popular option in the visualisation of vesicular internalisation processes owing to the ability to locate various subcellular components (e.g. fluorescently-labelled nuclei and endosomes) relative to the internalised species under examination.[235] Images possessing a sufficient resolution with clear vesicular boundaries can subsequently be analysed using particle tracking or ICS approaches that may be applied to the spatiotemporal determination of intracellular transport dynamics and local concentrations within the image.

1.6 References

1. Lichtman JW, Conchello J-A 2005. Fluorescence microscopy. Nat Meth 2(12):910-919.

2. Jameson DM, Croney JC, Moens PDJ, Gerard Marriott IP. 2003. Fluorescence: Basic concepts, practical aspects, and some anecdotes. Methods in Enzymology, ed.: Academic Press. p 1-43.

3. Semwogerere D, Weeks ER. 2005. Confocal Microscopy. Encyclopedia of biomaterials and biomedical engineering, ed., London: Taylor and Francis.

4. Paddock S 2000. Principles and practices of laser scanning confocal microscopy. Molecular Biotechnology 16(2):127-149.

5. LaFreniere G, 2002. Huygen's principle, http://www.rhythmodynamics.com/Gabriel_LaFreniere/matter.htm, accessed on 12/1/2013.

6. Keller HE. 2006. Objective lenses for confocal microscopy. In Pawley JB, editor Handbook of biological confocal microscopy, Third ed., New york: Springer. p 146.

7. Kolin DL, Wiseman PW 2007. Advance in imaging correlation spectroscopy: measuring number densities, aggregation states, and dynamics of fluorescently labeled macromolecules in cells. Cell Biochemistry and Biophysics.

8. Wallace W, Schaefer LH, Swedlow JR 2001. A working person's guide to deconvolution in light microscopy. Biotechniques 31(5):1076-+.

9. Ellenberger S. 2000. Influence of defocus on measurements in microscope images. ed.: Technical University Delft. p 161.

10. Stelzer EHK. 2006. The intermediate optical system of laser scanning confocal microscopes. In Pawley JB, editor Handbook of biological confocal microscopy, 3rd ed., New york: Springer. p 209.

11. Inoue S. 2006. Foundations of confocal scanned imaging in light microscopy. In Pawley JB, editor Handbook of biological confocal microscopy, 3 ed., New York: Springer. p 5.

12. White NS, Errington RJ 2005. Fluorescence techniques for drug delivery research: theory and practice. Advanced Drug Delivery Reviews 57(1):17-42.

13. Life Technologies. 2010. Molecular probes: The handbook. http://www.invitrogen.com/site/us/en/home/References/Molecular-Probes-The-Handbook.html?CID=fl-handbook, accessed on 12/1/2013.

14. Bacia K, Schwille P 2007. Practical guidelines for dual-color fluorescence cross-correlation spectroscopy. Nature Protocols 2(11):2842-2856.

15. Sugden JK 2004. Photochemistry of dyes and fluorochromes used in biology and medicine: some physicochemical background and current applications. Biotechnic & Histochemistry 79(2):71-90.

16. Widengren J, Mets U, Rigler R 1995. Fluorescence correlation spectroscopy of triplet-states in solution- A theoretical and experimental study Journal of Physical Chemistry 99(36):13368-13379.

17. Widengren J, Mets U, Rigler R 1999. Photodynamic properties of green fluorescent proteins investigated by fluorescence correlation spectroscopy. Chemical Physics 250(2):171-186.

18. Sugden JK 2004. Photochemistry of dyes and fluorochromes used in biology and medicine: some physicochemical background and current applications. Biotechnic and Histochemistry 79(2):71 - 90.

19. Kim SA, Heinze KG, Schwille P 2007. Fluorescence correlation spectroscopy in living cells. Nat Meth 4(11):963-973.

20. Dittrich P, Malvezzi-Campeggi F, Jahnz M, Schwille P 2001. Accessing molecular dynamics in cells by fluorescence correlation spectroscopy. Biological Chemistry 382(3):491-494.

21. Byassee TA, Chan WCW, Nie SM 2000. Probing single molecules in single living cells. Analytical Chemistry 72(22):5606-5611.

22. Schwille P, Haupts U, Maiti S, Webb WW 1999. Molecular dynamics in living cells observed by fluorescence correlation spectroscopy with one- and two-photon excitation. Biophysical Journal 77(4):2251-2265.

23. Kohl T, Schwille P 2005. Fluorescence correlation spectroscopy with autofluorescent proteins. Microscopy Techniques 95:107-142.

24. König K, Ehlers A, Riemann I, Schenkl S, Bückle R, Kaatz M 2007. Clinical two-photon microendoscopy. Microscopy Research and Technique 70(5):398-402.

25. Magde D, Elson E, Webb WW 1972. Thermodynamic fluctuations in a reacting system measurement by fluorescence correlation spectroscopy. Physical Review Letters 29(11):705-708.

26. Ries J, Schwille P 2008. New concepts for fluorescence correlation spectroscopy on membranes. Physical Chemistry Chemical Physics 10(24):3487-3497.

27. Digman MA, Sengupta P, Wiseman PW, Brown CM, Horwitz AR, Gratton E 2005. Fluctuation correlation spectroscopy with a laser-scanning microscope: Exploiting the hidden time structure. Biophysical Journal 88(5):L33-L36.

28. Lawrence WG, Varadi G, Entine G, Podniesinski E, Wallace PK 2008. A comparison of avalanche photodiode and photomultiplier tube detectors for flow cytometry.68590M-68590M.

29. Schwille P, Korlach J, Webb WW 1999. Fluorescence correlation spectroscopy with single-molecule sensitivity on cell and model membranes. Cytometry 36(3):176-182.

30. Tsibidis GD 2009. Quantitative interpretation of binding reactions of rapidly diffusing species using fluorescence recovery after photobleaching. Journal of Microscopy 233(3):384-390.

31. Apgar J, Tseng Y, Fedorov E, Herwig MB, Almo SC, Wirtz D 2000. Multiple-particle tracking measurements of heterogeneities in solutions of actin filaments and actin bundles. Biophysical Journal 79(2):1095-1106.

32. Petersen NO, Hoddelius PL, Wiseman PW, Seger O, Magnusson KE 1993. Quantitation of membrane receptor distributions by image correlation spectroscopy- concept and application. Biophysical Journal 65(3):1135-1146.

33. Wiseman PW, Squier JA, Ellisman MH, Wilson KR 2000. Two-photon image correlation spectroscopy and image cross-correlation spectroscopy. Journal of Microscopy-Oxford 200:14-25.

34. Digman MA, Brown CM, Sengupta P, Wiseman PW, Horwitz AR, Gratton E 2005. Measuring fast dynamics in solutions and cells with a laser scanning microscope. Biophysical Journal 89(2):1317-1327.

35. Gielen E, Smisdom N, De Clercq B, vandeVen M, Gijsbers R, Debyser Z, Rigo J-M, Hofkens J, Engelborghs Y, Ameloot M 2008. Diffusion of myelin oligodendrocyte glycoprotein in living OLN-93 cells investigated by Raster-Scanning image correlation spectroscopy (RICS). Journal of Fluorescence 18(5):813-819.

36. Kulkarni RP, Wu DD, Davis ME, Fraser SE 2005. Quantitating intracellular transport of polyplexes by spatio-temporal image correlation spectroscopy. Proceedings of the National Academy of Sciences of the United States of America 102:7523-7528.

37. Pedersen JS, Dikov D, Flink JL, Hjuler HA, Christiansen G, Otzen DE 2006. The changing face of glucagon fibrillation: Structural polymorphism and conformational imprinting. Journal of Molecular Biology 355(3):501-523.

38. Schneider CA, Rasband WS, Eliceiri KW 2012. NIH Image to ImageJ: 25 years of image analysis. Nat Meth 9(7):671-675.

39. Schindelin J, Arganda-Carreras I, Frise E, Kaynig V, Longair M, Pietzsch T, Preibisch S, Rueden C, Saalfeld S, Schmid B, Tinevez J-Y, White DJ, Hartenstein V, Eliceiri K, Tomancak P, Cardona A 2012. Fiji: an open-source platform for biological-image analysis. Nat Meth 9(7):676-682.

40. de Chaumont F, Dallongeville S, Chenouard N, Herve N, Pop S, Provoost T, Meas-Yedid V, Pankajakshan P, Lecomte T, Le Montagner Y, Lagache T, Dufour A, Olivo-Marin J-C 2012. Icy: an open bioimage informatics platform for extended reproducible research. Nat Meth 9(7):690-696.

41. Collinet C, Stoter M, Bradshaw CR, Samusik N, Rink JC, Kenski D, Habermann B, Buchholz F, Henschel R, Mueller MS, Nagel WE, Fava E, Kalaidzidis Y, Zerial M 2010. Systems survey of endocytosis by multiparametric image analysis. Nature 464(7286):243-249.

42. Wiseman PW, Höddelius P, Petersen NO, Magnusson KE 1997. Aggregation of PDGF-β receptors in human skin fibroblasts: Characterization by image correlation spectroscopy (ICS). FEBS Letters 401(1):43-48.

43. Kolin DL, Costantino S, Wiseman PW 2006. Sampling Effects, Noise, and Photobleaching in Temporal Image Correlation Spectroscopy. Biophysical Journal 90(2):628-639.

44. Wiseman PW, Brown CM, Webb DJ, Hebert B, Johnson NL, Squier JA, Ellisman MH, Horwitz AF 2004. Spatial mapping of integrin interactions and dynamics during cell migration by Image Correlation Microscopy. Journal of Cell Science 117(23):5521-5534.

45. Hebert B, Costantino S, Wiseman PW 2005. Spatiotemporal Image Correlation Spectroscopy (STICS) Theory, Verification, and Application to Protein Velocity Mapping in Living CHO Cells. Biophysical Journal 88(5):3601-3614.

46. Digman MA, Gratton E 2009. Analysis of diffusion and binding in cells using the RICS approach. Microscopy Research and Technique 72(4):323-332.

47. Bove J, Vaillancourt B, Kroeger J, Hepler PK, Wiseman PW, Geitmann A 2008. Magnitude and direction of vesicle dynamics in growing pollen tubes using Spatiotemporal Image Correlation Spectroscopy and Fluorescence Recovery after Photobleaching. Plant Physiol 147(4):1646-1658.

48. Godin AG, Costantino S, Lorenzo L-E, Swift JL, Sergeev M, Ribeiro-da-Silva A, De Koninck Y, Wiseman PW 2011. Revealing protein oligomerization and densities *in situ* using spatial intensity distribution analysis. Proceedings of the National Academy of Sciences 108(17):7010-7015.

49. Swift JL, Godin AG, Doré K, Freland L, Bouchard N, Nimmo C, Sergeev M, De Koninck Y, Wiseman PW, Beaulieu J-M 2011. Quantification of receptor tyrosine kinase transactivation through direct dimerization and surface density measurements in single cells. Proceedings of the National Academy of Sciences 108(17):7016-7021.

50. Walsh G 2005. Biopharmaceuticals: recent approvals and likely directions. Trends in Biotechnology 23(11):553-558.

51. Frokjaer S, Otzen DE 2005. Protein drug stability: A formulation challenge. Nature Reviews Drug Discovery 4(4):298-306.

52. Cromwell MEM, Hilario E, Jacobson F 2006. Protein aggregation and bioprocessing. The American Association of Pharmaceutical Scientists Journal 8(3):E572-E579.

53. Carpenter JF, Randolph TW, Jiskoot W, Crommelin DJA, Middaugh CR, Winter G, Fan Y-X, Kirshner S, Verthelyi D, Kozlowski S, Clouse KA, Swann PG, Rosenberg A, Cherney B 2009. Overlooking subvisible particles in therapeutic protein products: Gaps that may compromise product quality. Journal of Pharmaceutical Sciences 98(4):1201-1205.

54. BPC. 2012. British Pharmacopoeia. ed., London, England.

55. Wang W 2005. Protein aggregation and its inhibition in biopharmaceutics. International Journal of Pharmaceutics 289(1–2):1-30.

56. Mahler H-C, Friess W, Grauschopf U, Kiese S 2009. Protein aggregation: pathways, induction factors and analysis. Journal of Pharmaceutical Sciences 98(9):2909-2934.

57. Narhi LO, Schmit J, Bechtold-Peters K, Sharma D 2012. Classification of protein aggregates. Journal of Pharmaceutical Sciences 101(2):493-498.

58. Rosenberg AS 2006. Effects of protein aggregates: An immunologic perspective. Aaps Journal 8(3):E501-E507.

59. Giezen TJ, Mantel-Teeuwisse AK, Straus SMJM, Egberts TCG, Blackburn S, Persson I, Leufkens HGM 2009. Evaluation of post-authorization safety studies in the first cohort of EU risk management plans at time of regulatory approval. Drug Safety 32(12):1175-1187.

60. Chackerian B, Lenz P, Lowy DR, Schiller JT 2002. Determinants of autoantibody induction by conjugated papillomavirus virus-like particles. The Journal of Immunology 169(11):6120-6126.

61. Chirino AJ, Ary ML, Marshall SA 2004. Minimizing the immunogenicity of protein therapeutics. Drug Discovery Today 9(2):82-90.

62. Takacs MA, Jacobs SJ, Bordens RM, Swanson SJ 1999. Detection and characterization of antibodies to PEG-IFN-alpha 2b using surface plasmon resonance. Journal of Interferon and Cytokine Research 19(7):781-789.

63. Mire-Sluis AR, Barrett YC, Devanarayan V, Koren E, Liu H, Maia M, Parish T, Scott G, Shankar G, Shores E, Swanson SJ, Taniguchi G, Wierda D, Zuckerman LA 2004. Recommendations for the design and optimization of immunoassays used in the detection of host antibodies against biotechnology products. Journal of Immunological Methods 289(1–2):1-16.

64. Casadevall N, Nataf J, Viron B, Kolta A, Kiladjian J-J, Martin-Dupont P, Michaud P, Papo T, Ugo V, Teyssandier I, Varet B, Mayeux P 2002. Pure red-cell aplasia and antierythropoietin antibodies in patients treated with recombinant erythropoietin. New England Journal of Medicine 346(7):469-475.

65. Schellekens H 2002. Bioequivalence and the immunogenicity of biopharmaceuticals. Nat Rev Drug Discov 1(6):457-462.

66. Swanson SJ, Ferbas J, Mayeux P, Casadevall N 2004. Evaluation of methods to detect and characterize antibodies against recombinant human erythropoietin. Nephron Clinical Practice 96(3):c88-c95.

67. Sadick MD, Intintoli A, Quarmby V, McCoy A, Canova-Davis E, Ling V 1999. Kinase receptor activation (KIRA): a rapid and accurate alternative to end-point bioassays. Journal of Pharmaceutical and Biomedical Analysis 19(6):883-891.

68. Fink AL 1998. Protein aggregation: folding aggregates, inclusion bodies and amyloid. Folding and Design 3(1):R9-R23.

69. Ellis RJ 2001. Macromolecular crowding: an important but neglected aspect of the intracellular environment. Current Opinion in Structural Biology 11(1):114-119.

70. Rokney A, Shagan M, Kessel M, Smith Y, Rosenshine I, Oppenheim AB 2009. E. coli transports aggregated proteins to the poles by a specific and energy-dependent process. Journal of Molecular Biology 392(3):589-601.

71. Hart RA, Rinas U, Bailey JE 1990. Protein composition of Vitreoscilla hemoglobin inclusion bodies produced in Escherichia coli. Journal of Biological Chemistry 265(21):12728-12733.

72. Garcia-Fruitos E, Aris A, Villaverde A 2007. Localization of functional polypeptides in bacterial inclusion bodies. Appl Environ Microbiol 73(1):289-294.

73. Morell M, Bravo R, Espargaró A, Sisquella X, Avilés FX, Fernàndez-Busquets X, Ventura S 2008. Inclusion bodies: Specificity in their aggregation process and amyloid-like structure. Biochimica et Biophysica Acta (BBA) - Molecular Cell Research 1783(10):1815-1825.

74. Wang L, Maji SK, Sawaya MR, Eisenberg D, Riek R 2008. Bacterial inclusion bodies contain amyloid-like structure. PLoS Biol 6(8):1791-1801.

75. Wang L, Schubert D, Sawaya MR, Eisenberg D, Riek R 2010. Multidimensional structure activity relationship of a protein in its aggregated states. Angew Chem-Int Edit 49(23):3904-3908.

76. Ignatova Z, Gierasch LM 2004. Monitoring protein stability and aggregation *in vivo* by real-time fluorescent labeling. Proc Natl Acad Sci U S A 101(2):523-528.

77. Oberg K, Chrunyk BA, Wetzel R, Fink AL 1994. Native-like secondary structure in inerleukin-1-beta inclusion bodies by attenuated total reflectance FTIR. Biochemistry 33(9):2628-2634.

78. Kaltashov IA, Bobst CE, Abzalimov RR, Wang G, Baykal B, Wang S 2012. Advances and challenges in analytical characterization of biotechnology products: Mass spectrometry-based approaches to study properties and behavior of protein therapeutics. Biotechnology Advances 30(1):210-222.

79. Hamodrakas SJ 2011. Protein aggregation and amyloid fibril formation prediction software from primary sequence: towards controlling the formation of bacterial inclusion bodies. FEBS Journal 278(14):2428-2435.

80. Doglia SM, Ami D, Natalello A, Gatti-Lafranconi P, Lotti M 2008. Fourier transform infrared spectroscopy analysis of the conformational quality of recombinant proteins within inclusion bodies. Biotechnology Journal 3(2):193-201.

81. Gatti-Lafranconi P, Natalello A, Ami D, Doglia SM, Lotti M 2011. Concepts and tools to exploit the potential of bacterial inclusion bodies in protein science and biotechnology. FEBS Journal 278(14):2408-2418.

82. Winkler J, Seybert A, Konig L, Pruggnaller S, Haselmann U, Sourjik V, Weiss M, Frangakis AS, Mogk A, Bukau B 2010. Quantitative and spatio-temporal features of protein aggregation in Escherichia coli and consequences on protein quality control and cellular ageing. EMBO J 29(5):910-923.

83. Minton AP 2001. The influence of macromolecular crowding and macromolecular confinement on biochemical reactions in physiological media. Journal of Biological Chemistry 276(14):10577-10580.

84. Xie H, Chakraborty A, Ahn J, Yu YQ, Dakshinamoorthy DP, Gilar M, Chen W, Skilton SJ, Mazzeo JR 2010. Rapid comparison of a candidate biosimilar to an innovator monoclonal antibody with advanced liquid chromatography and mass spectrometry technologies. Mabs 2(4):379-394.

85. Eng M, Ling V, Briggs JA, Souza K, CanovaDavis E, Powell MF, DeYoung LR 1997. Formulation development and primary degradation pathways for recombinant human nerve growth factor. Analytical Chemistry 69(20):4184-4190.

86. Corbett RJT, Roche RS 1984. Use of high-speed size-exclusion chromatography for the study of protein folding and stability. Biochemistry 23(8):1888-1894.

87. Moore JM, Patapoff TW, Cromwell ME 1999. Kinetics and thermodynamics of dimer formation and dissociation for a recombinant humanized monoclonal antibody to vascular endothelial growth factor. Biochemistry 38(42):13960-13967.

88. Varley PG, Brown AJ, Dawkes HC, Burns NR 1997. A case study and use of sedimentation equilibrium analytical ultracentrifugation as a tool for biopharmaceutical development. European Biophysics Journal 25(5):437-443.

89. Clore GM, Gronenborn AM 1998. NMR structure determination of proteins and protein complexes larger than 20 kDa. Current Opinion in Chemical Biology 2(5):564-570.

90. Clore GM, Gronenborn AM 1998. Determining the structures of large proteins and protein complexes by NMR. Trends in Biotechnology 16(1):22-34.

91. Muzammil S, Kumar Y, Tayyab S 1999. Molten globule-like state of human serum albumin at low ph. European Journal of Biochemistry 266(1):26-32.

92. Sadler PJ, Tucker A 1993. pH-induced structural transitions of bovine serum albumin. Histidine pK(a) values and unfolding of the N-terminus during the N to F transition. European Journal of Biochemistry 212(3):811-817.

93. Morel MH, Redl A, Guilbert S 2002. Mechanism of heat and shear mediated aggregation of wheat gluten protein upon mixing. Biomacromolecules 3(3):488-497.

94. Vandenberg L, Rose D 1959. Effect of freezing on the pH and composition of sodium and potassium phosphate solutions-The reciprocal system KH2PO4-NA2HPO4-H2O Archives of Biochemistry and Biophysics 81(2):319-329.

95. Murase N, Franks F 1989. Salt precipitation during the freeze-concentration of phosphate buffer solutions. Biophysical Chemistry 34(3):293-300.

96. Pikal-Cleland KA, Rodriguez-Hornedo N, Amidon GL, Carpenter JF 2000. Protein denaturation during freezing and thawing in phosphate buffer systems: Monomeric and tetrameric beta-galactosidase. Archives of Biochemistry and Biophysics 384(2):398-406.

97. Pikal-Cleland KA, Cleland JL, Anchordoquy TJ, Carpenter JF 2002. Effect of glycine on pH changes and protein stability during freeze-thawing in phosphate buffer systems. Journal of Pharmaceutical Sciences 91(9):1969-1979.

98. Foster TM, Dormish JJ, Narahari U, Meyer JD, Vrkljan M, Henkin J, Porter WR, Staack H, Carpenter JF, Manning MC 1996. Thermal stability of low molecular weight urokinase during heat treatment. III. Effect of salts, sugars and Tween 80. International Journal of Pharmaceutics 134(1):193-201.

99. Ahmad F, Bigelow C 1986. Thermodynamic stability of proteins in salt solutions: A comparison of the effectiveness of protein stabilizers. Journal of Protein Chemistry 5(5):355-367.

100. Bhambhani A, Thakkar S, joshi SB, Middaugh CR. 2012. A formulation method to improve the physical stability of macromolecular-based drug products. In Meyer BK, editor Therapeutic protein drug products, ed., Oxford: Biohealthcare. p 14-45.

101. Chi EY, Krishnan S, Randolph TW, Carpenter JF 2003. Physical stability of proteins in aqueous solution: Mechanism and driving forces in non-native protein aggregation. Pharmaceutical Research 20(9):1325-1336.

102. Kueltzo LA, Wang W, Randolph TW, Carpenter JF 2008. Effects of solution conditions, processing parameters, and container materials on aggregation of a monoclonal antibody during freeze–thawing. Journal of Pharmaceutical Sciences 97(5):1801-1812.

103. Demeule B, Palais C, Machaidze G, Gurny R, Arvinte T 2009. New methods allowing the detection of protein aggregates A case study on trastuzumab. Mabs 1(2):142-150.

104. Sharma M, Narasimhan C, Shameem M. 2012. Administration in the clinic. In Meyer BK, editor Therapeutic protein drug products, ed., Oxford: Biohealthcare. p 98-113.

105. Gorman JJ, Wallis TP, Pitt JJ 2002. Protein disulfide bond determination by mass spectrometry. Mass Spectrometry Reviews 21(3):183-216.

106. Teale FW, Weber G 1957. Ultraviolet fluorescence of the aromatic amino acids. Biochem J 65(3):476-470.

107. Teale FW 1960. The ultraviolet fluorescence of proteins in neutral solution. Biochem J 76:381-380.

108. Jiskoot W, Hlady V, Naleway JJ, Herron JN. 1995. Application of fluorescence spectroscopy for determining the structure and function of proteins. In Herron JN, Jiskoot W, Crommelin DJA, editors. Physical methods to characterise pharmaceutical proteins, ed., New York: Plenum Press. p 1-64.

109. Carter DC, Ho JX 1994. Structure of serum albumin. Advances in Protein Chemistry 45:153-203.

110. Majorek KA, Porebski PJ, Dayal A, Zimmerman MD, Jablonska K, Stewart AJ, Chruszcz M, Minor W Structural and immunologic characterization of bovine, horse, and rabbit serum albumins. Molecular Immunology 52(3â€“4):174-182.

111. Sahoo B, Balaji J, Nag S, Kaushalya SK, Maiti S 2008. Protein aggregation probed by two-photon fluorescence correlation spectroscopy of native tryptophan. The Journal of Chemical Physics 129(7):075103-075105.

112. Demeule B, Lawrence MJ, Drake AF, Gurny R, Arvinte T 2007. Characterization of protein aggregation: The case of a therapeutic immunoglobulin. Biochimica et Biophysica Acta (BBA) - Proteins and Proteomics 1774(1):146-153.

113. Mueller C, Capelle MAH, Arvinte T, Seyrek E, Borchard G 2011. Tryptophan-mPEGs: Novel excipients that stabilize salmon calcitonin against aggregation by non-covalent PEGylation. European Journal of Pharmaceutics and Biopharmaceutics 79(3):646-657.

114. Filipe V, Poole R, Oladunjoye O, Braeckmans K, Jiskoot W 2012. Detection and characterization of subvisible aggregates of monoclonal IgG in serum. Pharmaceutical Research 29(8):2202-2212.

115. Demeule B, Gurny R, Arvinte T 2007. Detection and characterization of protein aggregates by fluorescence microscopy. International Journal of Pharmaceutics 329(1–2):37-45.

116. Demeule B, Lawrence MJ, Drake AF, Gurny R, Arvinte T 2007. Characterization of protein aggregation: The case of a therapeutic immunoglobulin. Biochimica et Biophysica Acta (BBA) - Proteins & Proteomics 1774(1):146-153.

117. Roessl U, Wiesbauer J, Leitgeb S, Birner-Gruenberger R, Nidetzky B 2012. Non-native aggregation of recombinant human granulocyte-colony stimulating factor under simulated process stress conditions. Biotechnology Journal 7(8):1014-1024.

118. Brown CM, Dalal RB, Hebert B, Digman MA, Horwitz AR, Gratton E 2008. Raster image correlation spectroscopy (RICS) for measuring fast protein dynamics and concentrations with a commercial laser scanning confocal microscope. Journal of Microscopy-Oxford 229(1):78-91.

119. Hamrang Z, Pluen A, Zindy E, Clarke D 2012. Raster image correlation spectroscopy as a novel tool for the quantitative assessment of protein diffusional behaviour in solution. Journal of Pharmaceutical Sciences 101(6):2082-2093.

120. Sergeev M, Godin AG, Kao L, Abuladze N, Wiseman PW, Kurtz I 2012. Determination of Membrane Protein Transporter Oligomerization in Native Tissue Using Spatial Fluorescence Intensity Fluctuation Analysis. PLoS ONE 7(4):e36215.

121. Sergeev M, Swift JL, Godin AG, Wiseman PW 2011. Ligand-induced clustering of EGF receptors: A quantitative study by fluorescence image moment analysis. Biophysical Chemistry 161(0):50-53.

122. Filipe V, Hawe A, Jiskoot W 2010. Critical Evaluation of Nanoparticle Tracking Analysis (NTA) by NanoSight for the Measurement of Nanoparticles and Protein Aggregates. Pharmaceutical Research 27(5):796-810.

123. Hawe A, Sutter M, Jiskoot W 2008. Extrinsic Fluorescent Dyes as Tools for Protein Characterisation. Pharmaceutical Research 25(7):1487-1499.

124. Mach H, Bhambhani A, Meyer BK, Burek S, Davis H, Blue JT, Evans RK 2011. The use of flow cytometry for the detection of subvisible particles in therapeutic protein formulations. Journal of Pharmaceutical Sciences 100(5):1671-1678.

125. He F, Phan DH, Hogan S, Bailey R, Becker GW, Narhi LO, Razinkov VI 2010. Detection of IgG aggregation by a high throughput method based on extrinsic fluorescence. Journal of Pharmaceutical Sciences 99(6):2598-2608.

126. Holm NK, Jespersen SK, Thomassen LV, Wolff TY, Sehgal P, Thomsen LA, Christiansen G, Andersen CB, Knudsen AD, Otzen DE 2007. Aggregation and fibrillation of bovine serum albumin. Biochimica et Biophysica Acta (BBA) - Proteins & Proteomics 1774(9):1128-1138.

127. Juárez J, Taboada P, Mosquera V 2009. Existence of different structural intermediates on the fibrillation pathway of human serum albumin. Biophysical Journal 96(6):2353-2370.

128. Maas C, Hermeling S, Bouma B, Jiskoot W, Gebbink MFBG 2007. A role for protein misfolding in immunogenicity of biopharmaceuticals. Journal of Biological Chemistry 282(4):2229-2236.

129. Hawe A, Filipe V, Jiskoot W 2010. Fluorescent molecular rotors as dyes to characterize polysorbate-containing IgG formulations. Pharmaceutical Research 27(2):314-326.

130. Hiemenz PC, Rajagopalan R. 1997. Static and dynamic light scattering and other radiation scattering. In Hiemenz PC, Rajagopalan R, editors. Principles of colloid and surface chemistry, 3 ed., New York: Marcel Dekker. p 193-247.

131. Wen Z-Q 2007. Raman spectroscopy of protein pharmaceuticals. Journal of Pharmaceutical Sciences 96(11):2861-2878.

132. De Beer TRM, Vercruysse P, Burggraeve A, Quinten T, Ouyang J, Zhang X, Vervaet C, Remon JP, Baeyens WRG 2009. In-line and real-time process monitoring of a freeze drying process using Raman and NIR spectroscopy as complementary process analytical technology (PAT) tools. Journal of Pharmaceutical Sciences 98(9):3430-3446.

133. Sane SU, Wong R, Hsu CC 2004. Raman spectroscopic characterization of drying-induced structural changes in a therapeutic antibody: Correlating structural changes with long-term stability. Journal of Pharmaceutical Sciences 93(4):1005-1018.

134. Cao X, Wen Z-Q, Vance A, Torraca G 2009. Raman microscopic applications in the biopharmaceutical industry: *in situ* identification of foreign particulates inside glass containers with aqueous formulated solutions. Appl Spectrosc 63(7):830-834.

135. Zolls S, Tantipolphan R, Wiggenhorn M, Winter G, Jiskoot W, Friess W, Hawe A 2012. Particles in therapeutic protein formulations, Part 1: Overview of analytical methods. Journal of Pharmaceutical Sciences 101(3):914-935.

136. Wen Z-Q, Cao X, Vance A 2008. Conformation and side chains environments of recombinant human interleukin-1 receptor antagonist (rh-IL-1RA) probed by Raman, Raman optical activity, and UV-resonance Raman spectroscopy. Journal of Pharmaceutical Sciences 97(6):2228-2241.

137. Brewster VL, Ashton L, Goodacre R 2011. Monitoring the glycosylation status of proteins using Raman spectroscopy. Analytical Chemistry 83(15):6074-6081.

138. Lankers M, Munhall J, Valet O 2008. Differentiation between foreign particulate matter and silicone oil induced protein aggregation in drug solutions by automated Raman spectroscopy. Microscopy and Microanalysis 14(SupplementS2):1612-1613.

139. Gabrielson JP, Brader ML, Pekar AH, Mathis KB, Winter G, Carpenter JF, Randolph TW 2007. Quantitation of aggregate levels in a recombinant humanized monoclonal antibody formulation by size-exclusion chromatography, asymmetrical flow field flow fractionation, and sedimentation velocity. Journal of Pharmaceutical Sciences 96(2):268-279.

140. Kunitani MG, Cunico RL, Staats SJ 1988. Reversible subunit dissociation of tumor necrosis factor during hydrophobic interaction chromatography. Journal of Chromatography A 443(0):205-220.

141. Hongping Y 2006. Simultaneous determination of protein aggregation, degradation, and absolute molecular weight by size exclusion chromatography–multiangle laser light scattering. Analytical Biochemistry 356(1):76-85.

142. Demeule B, Shire SJ, Liu J 2009. A therapeutic antibody and its antigen form different complexes in serum than in phosphate-buffered saline: A study by analytical ultracentrifugation. Analytical Biochemistry 388(2):279-287.

143. Lebowitz J, Lewis MS, Schuck P 2002. Modern analytical ultracentrifugation in protein science: A tutorial review. Protein Science 11(9):2067-2079.

144. Kelly SM, Jess TJ, Price NC 2005. How to study proteins by circular dichroism. Biochimica et Biophysica Acta (BBA) - Proteins and Proteomics 1751(2):119-139.

145. Bhattacharya M, Jain N, Mukhopadhyay S 2011. Insights into the mechanism of aggregation and fibril formation from bovine serum albumin. The Journal of Physical Chemistry B 115(14):4195-4205.

146. Vetri V, D'Amico M, Foderà V, Leone M, Ponzoni A, Sberveglieri G, Militello V 2011. bovine serum albumin protofibril-like aggregates formation: Solo but not simple mechanism. Archives of Biochemistry and Biophysics 508(1):13-24.

147. d'Orlye F, Varenne A, Gareil P 2008. Determination of nanoparticle diffusion coefficients by Taylor dispersion analysis using a capillary electrophoresis instrument. Journal of Chromatography A 1204(2):226-232.

148. Cottet H, Biron J-P, Cipelletti L, Matmour R, Martin M 2010. Determination of individual diffusion coefficients in evolving binary mixtures by Taylor dispersion analysis: application to the monitoring of polymer reaction. Analytical Chemistry 82(5):1793-1802.

149. Cottet H, Martin M, Papillaud A, Souaid E, Collet H, Commeyras A 2007. Determination of dendrigraft poly-L-lysine diffusion coefficients by Taylor dispersion analysis. Biomacromolecules 8(10):3235-3243.

150. Hawe A, Hulse WL, Jiskoot W, Forbes RT 2011. Taylor dispersion analysis compared to dynamic light scattering for the size analysis of therapeutic peptides and proteins and their aggregates. Pharmaceutical Research 28(9):2302-2310.

151. Hulse W, Forbes R 2011. A Taylor dispersion analysis method for the sizing of therapeutic proteins and their aggregates using nanolitre sample quantities. International Journal of Pharmaceutics 416(1):394-397.

152. Chamieh J, Cottet H 2012. Comparison of single and double detection points Taylor dispersion analysis for monodisperse and polydisperse samples. Journal of Chromatography A 1241:123-127.

153. Pietzsch J. Horizon Symposia: Living Frontier, 2004, pp 1-4.

154. Aller SG, Yu J, Ward A, Weng Y, Chittaboina S, Zhuo R, Harrell PM, Trinh YT, Zhang Q, Urbatsch IL, Chang G 2009. Structure of P-Glycoprotein reveals a molecular basis for poly-specific drug binding. Science 323(5922):1718-1722.

155. Ambudkar SV, Kimchi-Sarfaty C, Sauna ZE, Gottesman MM 2003. P-glycoprotein: from genomics to mechanism. Oncogene 22(47):7468-7485.

156. Fromm MF 2000. P-glycoprotein: a defense mechanism limiting oral bioavailability and CNS accumulation of drugs. International journal of clinical pharmacology and therapeutics 38(2):69-74.

157. Zachbauer S, Gsur A, Brunner R, Kyrle PA, Lechner K, Pirker R 1994. P-glycoprotein expression as unfavorable prognostic factor in acute myeloid leukemia. Leukemia : official journal of the Leukemia Society of America, Leukemia Research Fund, UK 8(6):974-977.

158. Henson JW, Cordon-Cardo C, Posner JB 1992. P-glycoprotein expression in brain tumors. Journal of Neuro-Oncology 14(1):37-43.

159. Wuchter C, Leonid K, Ruppert V, Schrappe M, Buchner T, Schoch C, Haferlach T, Harbott J, Ratei R, Dorken B, Ludwig W 2000. Clinical significance of P-glycoprotein expression and function for response to induction chemotherapy, relapse rate and overall survival in acute leukemia. Haematologica 85(7):711-721.

160. Crivori P, Reinach B, Pezzetta D, Poggesi I 2005. Computational models for identifying potential p-glycoprotein substrates and inhibitors. Molecular Pharmaceutics 3(1):33-44.

161. Englund G, Hallberg P, Artursson P, Michaelsson K, Melhus H 2004. Association between the number of co-administered P-glycoprotein inhibitors and serum digoxin levels in patients on therapeutic drug monitoring. BMC Medicine 2(1):8.

162. Greiner B, Eichelbaum M, Fritz P, Kreichgauer HP, Von Richter O, Zundler J 1999. The role of intestinal P-glycoprotein in the interaction of digoxin and rifampin. Journal of Clinical Investigation 104(2):147-153.

163. Fromm MF, Kim RB, Stein CM, Wilkinson GR, Roden DM 1999. Inhibition of P-Glycoprotein–Mediated Drug Transport: A unifying mechanism to explain the interaction between digoxin and quinidine. Circulation 99(4):552-557.

164. Leahey E.B., Jr Reiffel J. A., Heissenbuttel R. H. , Drusin R. E., Lovejoy W. P., Bigger J. J 1979. Enhanced cardiac effect of digoxin during quinidine treatment. Archives of Internal Medicine 139(5):519-521.

165. Tanigawara Y, Okamura N, Hirai M, Yasuhara M, Ueda K, Kioka N, Komano T, Hori R 1992. Transport of digoxin by human P-glycoprotein expressed in a porcine kidney epithelial cell line (LLC-PK1). Journal of Pharmacology and Experimental Therapeutics 263(2):840-845.

166. Fromm MF 2003. Importance of P-glycoprotein for drug disposition in humans. European Journal of Clinical Investigation 33:6-9.

167. Leith CP, Kopecky KJ, Chen IM, Eijdems L, Slovak ML, McConnell TS, Head DR, Weick J, Grever MR, Appelbaum FR, Willman CL 1999. Frequency and clinical significance of the expression of the Multidrug Resistance Proteins MDR1/P-Glycoprotein, MRP1, and LRP in Acute Myeloid Leukemia. A southwest oncology group study. Blood 94(3):1086-1099.

168. Broxterman H, Sonneveld P, Feller N, Ossenkoppele G, Wahrer D, Eekman C, Schoester M, Lankelma J, Pinedo H, Lowenberg B, Schuurhuis G 1996. Quality control of multidrug resistance assays in adult acute leukemia: correlation between assays for P-glycoprotein expression and activity. Blood 87(11):4809-4816.

169. Lee JS, Paull K, Alvarez M, Hose C, Monks A, Grever M, Fojo AT, Bates SE 1994. Rhodamine efflux patterns predict P-glycoprotein substrates in the National Cancer Institute drug screen. Molecular Pharmacology 46(4):627-638.

170. Löscher W, Potschka H 2005. Blood-brain barrier active efflux transporters: ATP-binding cassette gene family. Neurotherapeutics 2(1):86-98.

171. Herzog CE, Trepel JB, Mickley LA, Bates SE, Fojo AT 1992. Various methods of analysis of mdr-1/p-glycoprotein in human colon cancer cell lines. Journal of the National Cancer Institute 84(9):711-716.

172. Kim RB, Fromm MF, Wandel C, Leake B, Wood AJ, Roden DM, Wilkinson GR 1998. The drug transporter P-glycoprotein limits oral absorption and brain entry of HIV-1 protease inhibitors. The Journal of Clinical Investigation 101(2):289-294.

173. Lemaire S, Van Bambeke F, Mingeot-Leclercq M-P, Tulkens PM 2007. Modulation of the cellular accumulation and intracellular activity of daptomycin towards phagocytized Staphylococcus aureus by the P-glycoprotein (MDR1) efflux transporter in human THP-1 macrophages and Madin-Darby canine kidney cells. Antimicrobial Agents and Chemotherapy 51(8):2748-2757.

174. Schaefer O, Ohtsuki S, Kawakami H, Inoue T, Liehner S, Saito A, Sakamoto A, Ishiguro N, Matsumaru T, Terasaki T, Ebner T 2012. Absolute quantification and differential expression of drug transporters, Cytochrome P450 Enzymes, and UDP-Glucuronosyltransferases in cultured primary human hepatocytes. Drug Metabolism and Disposition 40(1):93-103.

175. Cisternino S, Mercier C, Bourasset F, Roux F, Scherrmann J-M 2004. Expression, up-regulation, and transport activity of the multidrug-resistance protein Abcg2 at the mouse blood-brain barrier. Cancer Research 64(9):3296-3301.

176. Siegsmund M, Brinkmann U, SchÃ¡ffeler E, Weirich G, Schwab M, Eichelbaum M, Fritz P, Burk O, Decker J, Alken P, Rothenpieler U, Kerb R, Hoffmeyer S, Brauch H 2002. Association of the P-glycoprotein transporter MDR1C3435T polymorphism with the susceptibility to renal epithelial tumors. Journal of the American Society of Nephrology 13(7):1847-1854.

177. Miliotis T, Ali L, Palm JE, Lundqvist AJ, Ahnoff M, Andersson TB, Hilgendorf C 2011. Development of a highly sensitive method using liquid chromatography-multiple reaction monitoring to quantify membrane P-glycoprotein in biological matrices and relationship to transport function. Drug Metabolism and Disposition 39(12):2440-2449.

178. Zhang Y, Li N, Brown PW, Ozer JS, Lai Y 2011. Liquid chromatography/tandem mass spectrometry based targeted proteomics quantification of P-glycoprotein in various biological samples. Rapid Communications in Mass Spectrometry 25(12):1715-1724.

179. Tucker TGHA, Milne AM, Fournel-Gigleux S, Fenner KS, Coughtrie MWH 2011. Absolute immunoquantification of the expression of ABC transporters P-glycoprotein, breast cancer resistance protein and multidrug resistance-associated protein 2 in human liver and duodenum. Biochemical Pharmacology 83(2):279-285.

180. Héctor GP, Irene C, Isabel P, Oriol A, Stephan T 2012. Standardized relative quantification of immunofluorescence tissue staining. Nature Protocols.

181. Colombo PC, Ashton AW, Celaj S, Talreja A, Banchs JE, Dubois NB, Marinaccio M, Malla S, Lachmann J, Ware JA, Le Jemtel TH 2002. Biopsy coupled to quantitative immunofluorescence: a new method to study the human vascular endothelium. Journal of Applied Physiology 92(3):1331-1338.

182. Cordon-Cardo C, O'Brien JP, Boccia J, Casals D, Bertino JR, Melamed MR 1990. Expression of the multidrug resistance gene product (P-glycoprotein) in human normal and tumor tissues. Journal of Histochemistry & Cytochemistry 38(9):1277-1287.

183. Bogush T, Tikhomirov M, Dudko E, Sinitsyna M, Ramanauskaite R, Polotsky B, Tjulandin S, Davydov M 2012. Quantitative immunofluorescence estimation of Pgp expression in human solid tumors by flow cytometry. Moscow University Chemistry Bulletin 67(3):142-148.

184. Durr D, Stieger B, Kullak-Ublick GA, Rentsch KM, Steinert HC, Meier PJ, Fattinger K 2000. St John's Wort induces intestinal P-glycoprotein/MDR1 and intestinal and hepatic CYP3A4[ast]. Clin Pharmacol Ther 68(6):598-604.

185. Anger GJ, Cressman AM, Piquette-Miller M 2012. Expression of ABC efflux transporters in placenta from women with insulin-managed diabetes. PLoS ONE 7(4):e35027.

186. Templin MF, Stoll D, Schrenk M, Traub PC, Vöhringer CF, Joos TO 2002. Protein microarray technology. Drug Discovery Today 7(15):815-822.

187. Beck WT, Grogan TM, Willman CL, Cordon-Cardo C, Parham DM, Kuttesch JF, Andreeff M, Bates SE, Berard CW, Boyett JM, Brophy NA, Broxterman HJ, Chan HSL, Dalton WS, Dietel M, Fojo AT, Gascoyne RD, Head D, Houghton PJ, Srivastava DK, Lehnert M, Leith CP, Paietta E, Pavelic ZP, Rimsza L, Roninson IB, Sikic BI, Twentyman PR, Warnke R, Weinstein R 1996. Methods to detect P-glycoprotein-associated multidrug resistance in patients' tumors: consensus recommendations. Cancer Research 56(13):3010-3020.

188. Balimane PV, Han Y-H, Chong S 2006. Current industrial practices of assessing permeability and p-glycoprotein interaction. AAPS 8(1):E1-E13.

189. Xia CQ, Liu N, Yang D, Miwa G, Gan L-S 2005. Expression, localisation, and functional characteristics of breast cancer resistance in Caco-2 cells. Drug Metabolism and Disposition 33(5):637-643.

190. Volpe DA 2008. Variability in Caco-2 and MDCK cell-based intestinal permeability assays. Journal of pharmaceutical sciences 97(2):712-725.

191. Simmons NL 1982. Cultured monolayers of MDCK cells-A novel model system for the study of epithelial development and function. General Pharmacology 13(4):287-291.

192. Hammerle SP, Rothen-Rutishauser B, Kramer SD, Gunthert M, Wunderli-Allenspach H 2000. P-Glycoprotein in cell cultures: a combined approach to study expression, localisation, and functionality in the confocal microscope. European Journal of Pharmaceutical Sciences 12(1):69-77.

193. Irvine JD, Takahashi L, Lockhart K, Cheong J, Tolan JW, Selick HE, Grove JR 1999. MDCK (Madin-Darby canine kidney) cells: A tool for membrane permeability screening. Journal of pharmaceutical sciences 88(1):28-33.

194. Feng B, Mills JB, Davidson RE, Mireles RJ, Janiszewski JS, Troutman MD, de Morais SM 2008. *In vitro* P-glycoprotein assays to predict the *in vivo* interactions of P-glycoprotein with drugs in the central nervous system. Drug Metabolism and Disposition 36(2):268-275.

195. Anderle P, Niederer E, Rubas W, Hilgendorf C, Spahn-Langguth H, Wunderli-Allenspach H, Merkle HP, Langguth P 1998. P-glycoprotein (P-gp) mediated efflux in Caco-2 cell monolayers: The influence of culturing conditions and drug exposure on P-gp expression levels. Journal of pharmaceutical sciences 87(6):757-762.

196. Polli JW, Wring SA, Humphreys JE, Huang L, Morgan JB, Webster LO, Serabjit-Singh CS 2001. Rational use of *in vitro* P-glycoprotein assays in drug discovery. Journal of Pharmacology and Experimental Therapeutics 299(2):620-628.

197. Rautio J, Humphreys JE, Webster LO, Balakrishnan A, Keogh JP, Kunta JR, Serabjit-Singh CJ, Polli JW 2006. *In vitro* P-glycoprotein inhibition assays for assessment of clinical drug ineraction potential of new drug candidates: A recommendation for probe substrates. Drug Metabolism and Disposition 34(5):786-792.

198. Szeremy P, Pal A, Mehn D, Toth B, Fulop F, Krajcsi P, Heredi-Szabo K 2011. Comparison of three assay systems using a common probe substrate, Calcein-AM, for studying P-gp using a selected set of compounds. J Biomol Screen 16(1):112-119.

199. Seelig A 1998. A general pattern for substrate recognition by P-glycoprotein. European Journal of Biochemistry 251(1-2):252-261.

200. Tiberghien Fo, Loor F 1996. Ranking of P-glycoprotein substrates and inhibitors by a calcein-AM fluorometry screening assay. Anti-Cancer Drugs 7(5):568-578.

201. Litman T, Zeuthen T, Skovsgaard T, Stein WD 1997. Structure-activity relationships of P-glycoprotein interacting drugs: kinetic characterization of their effects on ATPase activity. Biochimica et Biophysica Acta (BBA) - Molecular Basis of Disease 1361(2):159-168.

202. Ludescher C, Thaler J, Drach D, Drach J, Spitaler M, Gattringer C, And HH, Hofmann J 1992. Detection of activity of P-glycoprotein in human tumour samples using rhodamine 123. British Journal of Haematology 82(1):161-168.

203. Rapposelli S, Coi A, Imbriani M, Bianucci AM 2012. Development of classification models for identifying "True" P-glycoprotein (P-gp) inhibitors through inhibition, ATPase activation and monolayer efflux assays. International Journal of Molecular Sciences 13(6):6924-6943.

204. Ambudkar SV, Cardarelli CO, Pashinsky I, Stein WD 1997. Relation Between the Turnover Number for Vinblastine Transport and for Vinblastine-stimulated ATP Hydrolysis by Human P-glycoprotein. Journal of Biological Chemistry 272(34):21160-21166.

205. Giacomini KM, Huang S, Tweedie DJ, Benet LZ, Brouwer KLR, Chu X, Dahlin A, Evers R, Fischer V, Hillgren KM, K.A. H, Ishikawa T, Keppler D, Kim RB, Lee C, Niemi M, Polli JW, Sugiyama Y, Swann PW, Ware JA, Wright SH, Yee SW 2010. Membrane transporters in drug development. Nat Rev Drug Discov 9(3):215-236.

206. Äänismaa P, Seelig A 2007. P-glycoprotein kinetics measured in plasma membrane vesicles and living cells. Biochemistry 46(11):3394-3404.

207. Schinkel AH, Smit JJM, van Tellingen O, Beijnen JH, Wagenaar E, van Deemter L, Mol CAAM, van der Valk MA, Robanus-Maandag EC, te Riele HPJ, Berns AJM, Borst P 1994. Disruption of the mouse mdr1a P-glycoprotein gene leads to a deficiency in the blood-brain barrier and to increased sensitivity to drugs. Cell 77(4):491-502.

208. Shen WC, Wan JS, Ekrami H 1992. Enhancement of polypeptide and protein-absorption by macromolecular carriers *via* endocytosis and transcytosis. Advanced Drug Delivery Reviews 8(1):93-113.

209. Bickel U, Yoshikawa T, Pardridge WM 2001. Delivery of peptides and proteins through the blood-brain barrier. Advanced Drug Delivery Reviews 46(1-3):247-279.

210. Simionescu M, Popov D, Sima A 2009. Endothelial transcytosis in health and disease. Cell & Tissue Research 335(1):27-40.

211. Spencer BJ, Verma IM 2007. Targeted delivery of proteins across the blood-brain barrier. Proceedings of the National Academy of Sciences of the United States of America 104(18):7594-7599.

212. Weaver M, Laske D 2003. Transferrin Receptor Ligand-Targeted Toxin Conjugate (Tf-CRM107) for Therapy of Malignant Gliomas. Journal of Neuro-Oncology 65(1):3-14.

213. Gomme PT, McCann KB 2005. Transferrin: structure, function and potential therapeutic actions. Drug Discovery Today 10(4):267-273.

214. Li HY, Qian ZM 2002. Transferrin/transferrin receptor-mediated drug delivery. Medicinal Research Reviews 22(3):225-250.

215. Daniels TR, Delgado T, Helguera G, Penichet ML 2006. The transferrin receptor part II: Targeted delivery of therapeutic agents into cancer cells. Clinical Immunology 121(2):159-176.

216. Daniels TR, Delgado T, Rodriguez JA, Helguera G, Penichet ML 2006. The transferrin receptor part I: Biology and targeting with cytotoxic antibodies for the treatment of cancer. Clinical Immunology 121(2):144-158.

217. Bleil JD, Bretscher MS 1982. Transferrin receptor and its recycling in HeLa cells Embo Journal 1(3):351-355.

218. Hughson EJ, Hopkins CR 1990. Endocytic pathways in polarized Caco-2 cells: identification of an endosomal compartment accessible from both apical and basolateral surfaces. The Journal of Cell Biology 110(2):337-348.

219. Herve F, Ghinea N, Scherrmann JM 2008. CNS Delivery *Via* Adsorptive Transcytosis. Aaps Journal 10(3):455-472.

220. Kishimoto T, Tavassoli M 1987. Transendothelial transport (transcytosis) of iron transferrin complex in the rat liver American Journal of Anatomy 178(3):241-249.

221. Pocard T, Le Bivic A, Galli T, Zurzolo C 2007. Distinct v-SNAREs regulate direct and indirect apical delivery in polarized epithelial cells. Journal of Cell Science 120:3309-3320.

222. Cogburn JN, Donovan MG, Schasteen CS 1991. A model of human small intestinal absorptive cells.1. Transport barrier. Pharmaceutical Research 8(2):210-216.

223. Heyman M, Crain AM, Nath SK, Desjeux JF 1990. Quantification of transcytosis in the human colon carcinoma cell line Gastroenterology 98(5 PART 2):A656.

224. Hughson EJ, Hopkins CR 1990. Endocytic pathways in polarized Caco-2 cells - Identification of an endosomal compartment accessible from both apical and basolateral surfaces Journal of Cell Biology 110(2):337-348.

225. Mostov KE, Cardone MH 1995. Regulation of protein traffic in polarised epithelial cells Bioessays 17(2):129-138.

226. Mostov K, Apodaca G, Aroeti B, Okamoto C 1992. Plasma membrane protein sorting in polarised epithlial cells Journal of Cell Biology 116(3):557-584.

227. Nollevaux G, Deville C, El Moualij B, Zorzi W, Deloyer P, Schneider YJ, Peulen O, Dandrifosse G 2006. Development of a serum-free co-culture of human intestinal epithelium cell-lines (Caco-2/HT29-5M21). Bmc Cell Biology 7.

228. Baumgart DC, Dignass AU 2002. Intestinal barrier function. Current Opinion in Clinical Nutrition and Metabolic Care 5(6):685-694.

229. Cheng H, Leblond CP 1974. Origin, differentiation and renewal of four main epithelial cell types in mouse small intestine .1. columnar cell. American Journal of Anatomy 141(4):461-&.

230. Lim C-J, Norouziyan F, Shen W-C 2007. Accumulation of transferrin in Caco-2 cells: A possible mechanism of intestinal transferrin absorption. Journal of Controlled Release 122(3):393-398.

231. Richardson DR, Ponka P 1997. The molecular mechanisms of the metabolism and transport of iron in normal and neoplastic cells. Biochimica Et Biophysica Acta-Reviews on Biomembranes 1331(1):1-40.

232. Zhu ZB, Makhija SK, Lu BG, Wang MH, Rivera AA, Preuss M, Zhou F, Siegal GP, Alvarez RD, Curiel DT 2004. Transport across a polarized monolayer of Caco-2 cells by transferrin receptor-mediated adenovirus transcytosis. Virology 325(1):116-128.

233. Dan N, Cutler DF 1994. Transcytosis and processing of intrinsic factor cobalamin in Caco-2 cells Journal of Biological Chemistry 269(29):18849-18855.

234. Xia CQ, Shen WC 2001. Tyrphostin-8 enhances transferrin receptor-mediated transcytosis in Caco-2 cells and increases hypoglycemic effect of orally administered insulin-transferrin conjugate in diabetic rats. Pharmaceutical Research 18(2):191-195.

235. Du W, Fan Y, Zheng N, He B, Yuan L, Zhang H, Wang X, Wang J, Zhang X, Zhang Q 2013. Transferrin receptor specific nanocarriers conjugated with functional 7peptide for oral drug delivery. Biomaterials 34(3):794-806.

Chapter 2

AIMS AND OBJECTIVES

2.1 Aims and Objectives

As highlighted in the Introduction chapter, image analysis tools currently remain underused and poorly validated for application to a wide spectrum of pharmaceutical research areas implicated in various aspects of the drug and biopharmaceutical development process. Despite the availability of a diversity of analytical approaches for the analysis of various processes of interest to pharmaceutical research (e.g. protein aggregation, transporter expression and cellular transport processes), there remains a scope for novel approaches that offer the potential to generate multiparametric data and thereby, address the challenges and shortcomings associated with available technologies.

The hypothesis pertaining to this thesis is that novel image analysis tools based on the exploitation of fluorescence intensity fluctuations can contribute to the quantification of a number of biochemical and biophysical processes that may provide novel parametric insights into pharmaceutically-relevant problems.

Thus the aims of this thesis are:

(i) To validate image analysis tools such as Raster Image Correlation Spectroscopy (RICS), Spatial Intensity Distribution Analysis (SpIDA) and Fluorescence Intensity Gaussian Mixture Model Analysis (FIGMMA).

(ii) To demonstrate that image analysis tools can unravel hidden spatiotemporal information inherent in confocal images that current commonly-utilised images analysis tools are unable to achieve.

(iii) To highlight the versatility of these tools through application to specific biological and pharmaceutical problems such as drug/protein distributions and time-dependent intracellular accumulation of ligands through passive and vesicular internalisation mechanisms.

Consequently, the specific objectives of this thesis are to:

Validate and apply RICS and SpIDA as image analysis tools for the quantification of concentration and dynamic parameters- This involves optimisation of image acquisition parameters and calibration of the confocal setup (i.e. PMT shot noise and laser beam waist measurements) followed by the performance of confocal imaging experiments.

In Chapter 3 protein concentration and ionic strength variation for a model protein, bovine serum albumin, is assessed and subsequently subjected to RICS analysis.

In Chapter 4, real-time *in situ* confocal imaging of bovine serum albumin (BSA) samples is performed to assess the formation of aggregates ranging from the oligomeric scale up to larger aggregates (i.e. microns) as a function of concentration, ionic strength and time following exposure to thermal stress at 50 °C.

In both chapters the data obtained from image analysis approaches is compared and cross-validated against dynamic light scattering and fluorescence correlation spectroscopy data.

Later these methods are applied to the assessment of intracellular ligand concentrations (e.g. Calcein and transferrin) and their dynamics (i.e. the diffusion coefficient of Cell Trace™ Calcein red-orange) in multiple cell lines.

Apply SpIDA to the quantification of protein expression and function in in vitro cell models- *In vitro* models are routinely utilised in the characterisation of transporter/receptor expression and function in the literature under physiologically-relevant conditions in an attempt to provide further insights into more complex systems (i.e. *in vivo* conditions). To assess the potential scope for application of image analysis tools for this purpose, immunofluorescence staining is performed on monolayers cultivated both on eight well chambers and Transwell® support filters.

The expression of two transmembrane proteins responsible for small molecule drug efflux (i.e. the p-glycoprotein transporter) and vesicular transport (i.e. transferrin) of endogenous proteins is assessed using this approach and the resultant data (obtained from SpIDA analysis and routine quantitative immunofluorescence) compared against previously reported expression values and observed differences in the literature.

In Chapter 5 confocal images acquired from p-glycoprotein immunofluorescence staining in MDCK-*MDR1* and MDCK-*wt* cells are subjected to both routine quantitative immunofluorescence (QIF) and SpIDA analysis. To further assess the influence of polarisation and differentiation on changes in the expression and localisation of p-glycoprotein transporters, Caco-2 monolayers cultivated on Transwell® support filters are subjected to immunofluorescence staining on days 10, 16 and 29 post-seeding. Subsequently, both two and three-dimensional images are acquired and subjected to analysis using QIF and SpIDA alongside qualitative assessment of their localisation.

Assess transporter function and inhibition- To further apply the concept of p-glycoprotein expression and function as a commonly studied phenomenon in pharmaceutical research, MDR1 inhibition by verapamil is assessed in a MDR1-transfected cell line and directly compared to the parent wild-type cell line using the routine Calcein retention assay. For this purpose, verapamil is utilised at various concentrations, co-incubated with Calcein-AM to various time points and the intracellular retention of Calcein examined through imaging cells over several fields of view for samples incubated to specified time points. Resultant images are subjected to both SpIDA analysis for each time point and concentration of verapamil to determine p-glycoprotein inhibition in both cell lines and subcellular differences in the intracellular concentration of Calcein at various times and concentration of verapamil.

Examine passive and vesicular transport mechanisms- Following on from the assessment of protein expression in *in vitro* systems, two common transport processes are studied in Chapter 6 to examine the applicability of image analysis tools in determining both the intracellular distribution and dynamics of two model drugs representing the passive and vesicular pathways, the data from which is compared against both traditional approaches and previous data in the group obtained from FCS measurements. The transcytosis of transferrin is assessed in Caco-2 and HeLa cells to assess the distribution of intracellular vesicles and their relative distribution in both cell lines. This is followed by the analysis of their relative intensities using an in-house developed Gaussian Mixture Model Analysis software (FIGMMA).

The time and concentration-dependent passive diffusion of Cell Trace™ Calcein Red-Orange AM uptake is assessed in Caco-2 and BAECS cultured on chamber slides using

a combination of RICS (intracellular dynamics), SpIDA (intracellular concentration) and routine fluorescence intensity measurements.

Chapter 3

VALIDATION OF RICS AS A NOVEL TOOL FOR THE ASSESSMENT OF PROTEIN DIFFUSIONAL BEHAVIOUR IN SOLUTION

J. Pharm. Sci., 2012, pp 2082-2093.

Research Article

Raster Image Correlation Spectroscopy as a Novel Tool for the Quantitative Assessment of Protein Diffusional Behaviour in Solution

Zahra Hamrang, [1] *Alain Pluen,* [1, 2] *Egor Zindy,* [2] *and David Clarke*[1, 2]

Received 7 November 2011; revised 27 January 2012; accepted 16 February 2012

First published online in Wiley Online Library (wileyonlinelibrary.com).

1 School of Pharmacy and Pharmaceutical Sciences, University of Manchester, UK.

2 Centre of Excellence in Biopharmaceuticals, Faculty of Life Sciences, University of Manchester, UK.

3.1 Abstract

The application of raster image correlation spectroscopy (RICS) as a tool for the characterisation of protein diffusion was assessed using a model protein, bovine serum albumin (BSA), as a function of formulation and denaturing conditions. RICS results were also validated against dynamic light scattering and fluorescence correlation spectroscopy. Results from this study demonstrate correlation between outputs obtained from the three experimental techniques.

Ionic strength-independence was observed at pH 7, and a reduction in the corresponding diffusion coefficients was noted at pH 4.5 for 1 μM BSA–Alexa Fluor® 488. Conversely, at pH 5.2, higher-concentration samples exhibited ionic strength dependency. Buffer composition, sample pre-treatment, thermal denaturation and freeze–thaw cycling were also found to influence RICS output, with a reduction in the diffusion coefficient and the number of particles observed for both pH values. In conclusion, RICS analysis of images acquired using a commercial confocal microscope offers a potential scope for application to both quantitative and qualitative characterisation of macromolecular behaviour in solution.

Keywords: Albumin; Diffusion; Microscopy; Light scattering (Dynamic); pH; Protein aggregation; Raster image correlation spectroscopy.

3.2 Introduction

With an ever-expanding interest of the pharmaceutical industry in the recruitment of biological therapies for the treatment of a multitude of pathologies, there has been a growing interest in technologies enabling the characterisation of biopharmaceutical product stability. Consequently, interest in research into formulation design and the underlying mechanisms contributing to the instability of these products during manufacture, shelf life and administration has never gained as much growth as today. Therapeutic proteins in their native state interact with the desired target, following association in a specific conformation; therefore, processes leading to structural changes or denaturation contribute to a loss of therapeutic bioactivity through immunogenicity, anaphylaxis and instability. Some of the potential routes contributing to protein biopharmaceutical structural changes during product lifetime and resultant potential implications have been summarised in Figure 3.1.

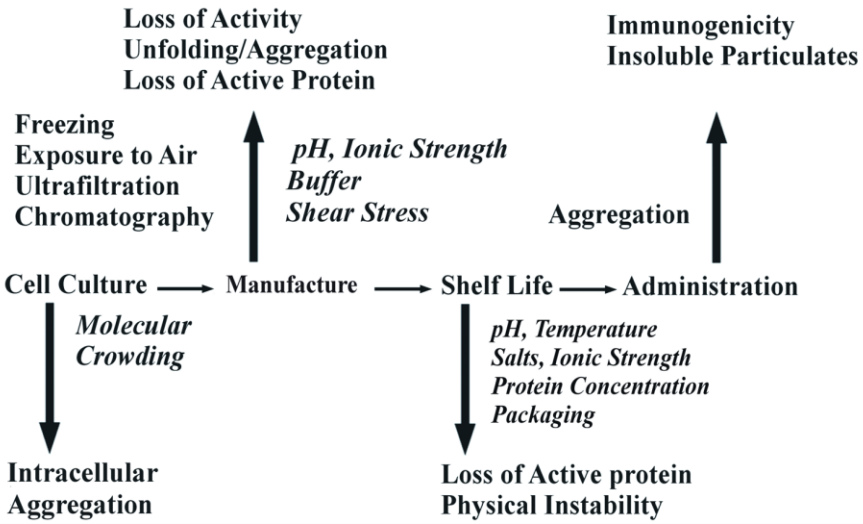

Figure 3.1 *The stages of protein biopharmaceutical development, potential contributory factors to instability and their consequences during the lifecycle of a biopharmaceutical product (adapted from literature sources).*[1, 2]

An understanding of the contributory mechanisms to the destabilisation of biopharmaceutical preparations is essential for research, development, manufacture and the quality control of products. Consequently, a careful consideration of excipient quantities, compatibility and processing techniques (utilised during manufacture, packaging and storage conditions) is crucial to ensure irreversible loss of the therapeutic protein due to denaturation, unfolding, adsorption to surfaces or covalent aggregation does not occur. Protein instability has been known to occur as a function of formulation-

related factors exemplified by pH, temperature, salt concentration and type, presence of surfactants and type of cosolvent.[3]

A range of analytical approaches are able to characterise protein behaviour in solution, all of which measure aggregation or particle size distributions (using the number of particles, diffusion time, hydrodynamic radii and enthalpies) that in some instances can lead to inconsistencies and confusion when evaluating data from multiple methodologies (e.g. differential scanning calorimetry (DSC) comparison with spectroscopies).[1] These techniques (See Table 3.1) may be utilised either in isolation or in combination with other approaches (orthogonal techniques), but bulk techniques possess disadvantages ranging from apparatus and product-related costs (e.g. size-exclusion chromatography)[2] to lack of sensitivity in detecting microscopic changes (i.e. bulk techniques) that lead to product instability and the subsequent macroscopic changes that ensue.

Table 3.1 *Some techniques previously reported for the characterisation of protein stability and an overview of their relative merits (adapted from literature sources).*[1,2]

Technique	Advantages	Disadvantages
Differential Scanning Calorimetry (DSC)[4-8]	Provides information on thermal denaturation stability	Susceptible to atmospheric changes, Requires instrument calibration, Requires larger samples
Nuclear Magnetic Resonance (NMR)[9,10]	Non-invasive, Reproducible	Sample preparation may alter aggregate structure, Requires reference spectra
Size Exclusion Chromatography (SEC)[11,12]	Accurate , Allows both sizing and quantification	Time consuming, Bulk amount of analyte required, Molecular weight not directly linked to Stoke's radius for irregular-shaped proteins
Light Scattering[12-17] ***Multi angle (MALS)***	MALS Accurate, molecular weight determination	MALS Requires refractive index, Regular calibration needed, High concentration samples for lower molecular weight proteins to yield accurate results
Dynamic Light Scattering	DLS Statistically significant results, Rapid	DLS Inappropriate for poly-disperse samples
Fluorescence Correlation Spectroscopy (FCS)[18-21]	Sensitive, rapid, Non-invasive	Single point detection, Parameter fitting is time consuming
Electrophoresis[22,23]	Accessibility, Can distinguish type of aggregate	Invasive, Denaturing, Indirect measurements, Time-consuming, Complex
FT-IR[24]	Non-destructive, Rapid	Requires regular calibration, Relatively lower sensitivity, Reference spectra
Raster Image Correlation Spectroscopy (RICS)[25,26]	Small volume/concentration samples, Provides population distribution maps, Non-invasive, Can detect a broad range of particle sizes, Multiple applications	Requires fluorescently-labelled compounds or dyes that associate with hydrophobic pockets

Hence, a thorough knowledge of the armoury of analytical techniques available is crucial when characterising a sample of unknown particle size distribution, the application of which in combination, possess the ability to detect aggregates within a diversity of size ranges. Therefore, there still remains the need for rapid, sensitive and high-throughput approaches that possess the ability to analyse smaller-volume sample sizes and detect product instability at a microscopic level. In this study we present RICS as a potential tool for the aforementioned purposes.

Raster image correlation spectroscopy, an image analysis extension initially developed by Digman *et al*.[25,27] enables the assessment of molecular mobility that can occur through exploitation of the time-related information inherent in confocal images acquired from a raster scanning laser beam in a manner similar to fluorescence correlation spectroscopy (FCS), with the added capability of spatial correlation analysis. This approach possesses the ability to determine spatial and temporal maps of fluorescence intensity fluctuations resulting from many processes exemplified by binding, aggregation and intracellular dynamics.[28] Spatial resolution at pixel level for raster images allows kinetic mapping of information contained in successive pixels (i.e. microseconds), lines (i.e. milliseconds) and frames (i.e. seconds to minutes) and consequently, detection of any present heterogeneities within a system at a microscopic level.[26,27] Reported applications of ICS extensions to date have included diffusion measurements,[29] binding to lipid membranes,[30] quantification of cell membrane receptor distributions,[31] characterisation of intracellular dynamics[26,32] and observing protein transport in cell membranes.[32]

This study reports a novel application for RICS, namely the characterisation of protein diffusion that was performed through confocal imaging of fluorescently labelled BSA samples. BSA was primarily selected because of extensive prior exploration of its characteristic behaviour in solution using numerous traditional analytical approaches, for example DLS, DSC and electrophoresis (See Table 3.1). Additionally, BSA is a commonly utilised excipient in the formulation of numerous parenteral products and performs as a multifunctional carrier. Therefore, the aggregation characteristics of fluorescently- labelled BSA that may differ from that of the native protein were examined as a function of pH, ionic strength and buffer composition. Results obtained from the analysis of confocal images were compared against that obtained from DLS and FCS.[33]

3.3 Materials and Methods

3.3.1 Materials

Bovine serum albumin–Alexa Fluor® 488 (BSA–AF488) and Rhodamine Green™ were acquired from Invitrogen (Paisley, UK). Phosphate-buffered saline (PBS; 10 mM) and guanidine hydrochloride were obtained from Sigma (Poole, UK). Sodium chloride (NaCl), hydrochloric acid, sodium hydroxide, citric acid and dibasic sodium phosphate were all obtained from Fisher Scientific Ltd. (Loughborough, UK), and ProteoStat® was obtained from Enzo Life Sciences (Exeter, UK).

3.3.2 Methods

Sample Preparation

3.3.2.1 The Influence of Ionic Strength and pH Variation

The ionic strength of 1 µM pH 7 solutions of BSA–AF488 was varied using the appropriate volume of 1 M NaCl stock solution to achieve ionic strengths in the 0–500 mM range. The buffer concentration and composition (i.e. 5 mM PBS) in the sample solutions was kept constant and the recorded pH for all samples was 7 ± 0.2. All buffers and solutions were filtered using a 0.4-µm-pore-sized Millipore syringe filter (Millipore, Watford, UK) prior to sample preparation in order to remove any particulates present in the starting materials. The diffusion of BSA (pI ~ 4.7)[34] was also assessed at pH 4.5 which was achieved by addition of 1 mM HCl and ionic strength variation using NaCl to 10, 20, 30, 50, 100, 250, 400 and 500 mM. The impact of buffer composition was also assessed using citrate–phosphate buffer (pH range 2.6–7) at pH 7 and 4.5. All experiments were carried out at room temperature in a thermostatically controlled environment (i.e. 21 °C) and the influence of sample preparation conditions such as buffer type (i.e. citrate versus PBS) and filtration effects (i.e. no filtration versus 0.2-µm-pore-size filtration) were examined following validation of RICS with DLS and FCS.

3.3.2.2 Concentration Effects

The impact of concentration and ionic strength variation was assessed at higher concentrations of BSA using the aforementioned approach for 1 μM samples. Total BSA concentrations of 10 mg/mL (i.e. 152 μM) and 40 mg/mL (i.e. 608 μM) were assessed using confocal microscopy (i.e. 1 μM BSA–AF488 was utilised, and the remainder of the sample consisted of unlabelled BSA).

3.3.2.3 Freeze–Thaw Cycling

BSA (both labelled and unlabelled) samples were frozen at −80 °C and subjected to repeated freeze–thaw cycling. Thawing at room temperature was carried out twice in 24 hours, and following further storage at −80 °C overnight, the samples were examined using confocal microscopy. A combination of high- and low-concentration samples (i.e. 1 μM) was studied using this approach. For higher-concentration samples, BSA was incubated with ProteoStat® (Enzo Life Sciences), a fluorescent hydrophobic pocket dye, for 10 min to label higher-order aggregate moieties present in the sample.[35]

3.3.2.4 Denaturation

Guanidine-induced denaturation was performed with a 6 M solution of guanidine, and the samples were subsequently stored overnight prior to confocal microscopy.[36] Results obtained from this experiment have been presented in the supplementary information section.

Thermal denaturation of BSA samples occurred through boiling samples at 80 °C for 10 min. For both denaturation experiments, a range of higher and lower concentrations (i.e. 1 and 2 μM, respectively) of BSA samples were characterised. The ionic strength and buffer composition of both the pH 7 control and denatured samples were maintained constant (i.e. 150 mM ionic strength).

3.3.2.5 Assessment of BSA Diffusion Behaviour with FCS

A Zeiss LSM 510 ConfoCor 2 setup (Zeiss, Jena, Germany) equipped with an Argon laser and a 40×/1.2NA water-immersion objective lens was utilised for the FCS measurements. The same experimental conditions as for DLS and RICS were maintained, and system calibration was performed with Rhodamine Green™ (diffusion coefficient of 2.8×10^{-6} cm^2/sec; Life Technologies)[37] in order to assess the laser beam

waist size and optimise the optical setup for further experiments. The laser beam waist was estimated using as follows:

$$\tau_D = \frac{\omega_0^2}{4D} \qquad \textit{Equation 3.1}$$

where τ_D is the diffusion time, ω_0 the laser waist beam and D is the diffusion coefficient of the species of interest.

Samples were prepared so that only 50–100 nM of fluorescently labelled BSA (i.e. BSA–AF488) was present, and in the case of 1 µM preparations, the remainder of the BSA content was unlabelled.[18] Approximately 400 µL of sample was introduced into a Lab-Tek Nunc® eight-well chamber slide (Fisher Scientific, Leicestershire, UK), and measurements were performed at 100 runs, each of 10 seconds duration, the output of which was averaged for each sample and repeated in triplicate.

Analysis of FCS Data

Single-component fits were applied to data acquired from the FCS experiments, the number of particles (N) and the diffusion time (τ_D), which is determined using the following equation:

$$G(\tau) = 1 + \frac{1}{N}\left(1 + \frac{\tau}{\tau_D}\right)^{-1}\left(1 + S^2\frac{\tau}{\tau_D}\right)^{-0.5} \qquad \textit{Equation 3.2}$$

where $G(\tau)$ is the correlation function, N is the number of particles, τ_D is the diffusion time and S is the structure parameter. Diffusion time results obtained from subsequent FCS analysis were then applied to in order to determine the diffusion coefficient of BSA–AF488 under the conditions examined.

3.3.2.6 RICS Analysis

Image analysis was carried out using in-house RICS software (ManICS). Fitting of the spatial autocorrelation curve for a square region of interest (ROI) was performed as a two-step process. Initially, a suitable coarse fit was selected using the PGSL algorithm developed by Raphael and Smith,[38] followed by a refined selection of the fitting parameters using the Levenburg–Marquardt algorithm. When the best fit was achieved (i.e. either when the maximum number of iterations reached or the incremental improvement in residual fell below a certain threshold), the number of particles (N) the diffusion coefficient (D) and R^2 of the fitted model for the ROI were derived. The principles of RICS, originally developed by Digman *et al.*,[26, 27] are based on the scan function that relates time to space (See Equation 3.3);

$$G_s(\xi,\psi) = \tau_p(\xi) + \tau_l(\psi) \qquad \textit{Equation 3.3}$$

In the scan function, τ_p is the pixel dwell time, τ_l is the line scan time, ξ is the spatial displacement in the x direction and ψ is the corresponding spatial displacement in successive lines in the y direction within a raster image. The normalized fluorescence intensity fluctuation spatial autocorrelation function, ACF, [$G_S(\xi,\psi)$] is thus

$$G_S(\xi,\psi) = G(\xi,\psi).S(\xi,\psi) = \frac{\langle \delta I(x,y)\delta I(x+\xi,y+\psi)\rangle_{x,y}}{\langle I(x,y)\rangle^2_{x,y}} \qquad \textit{Equation 3.4}$$

where I(x,y) is the fluorescence intensity detected at each pixel, and $\delta I(x,y) = I(x,y) - \langle I(x,y)\rangle x,y$ is the fluorescence intensity variation around the mean; the ACF for three-dimensional (3D) diffusion is:

$$G(\xi,\psi) = \frac{\gamma}{N}\left(1+\frac{4D(\tau_p\xi+\tau_l\psi)}{\omega_0^2}\right)^{-1}\cdot\left(1+\frac{4D(\tau_p\xi+\tau_l\psi)}{\omega_z^2}\right)^{-1/2} \qquad \textit{Equation 3.5}$$

Parameters of the ACF are $\gamma = \frac{1}{\sqrt{8}}$, accounting for the single photon illumination profile, and ω_0 and ω_z are the lateral and axial beam waist, respectively.

As RICS requires the point spread function (PSF) to extend over a certain number of pixels (approximately 4–6),[39] the scanner movement is accounted for using the $S(\xi,\psi)$ function:

$$S(\xi,\psi)=\exp\left\{-\frac{\left[\left(\frac{\xi\delta r}{\omega_0}\right)^2+\left(\frac{\psi\delta r}{\omega_0}\right)^2\right]}{1+\frac{4D\left(\tau_p\xi+\tau_l\psi\right)}{\omega_0^2}}\right\} \qquad \textit{Equation 3.6}$$

3.3.2.7 Confocal Laser Scanning Microscopy with RICS Analysis

Time series were captured for samples containing various concentrations (0.1–1 μM) of BSA–AF488 at various pixel dwell times to assess the impact of dwell time on the quality of fit and output data in order to optimise the process. The impact of the number of frames utilised for RICS analysis was assessed, and frame numbers ranging from 50 to 400 were applied. Raster scan images were acquired using a commercial Zeiss LSM510 confocal laser scanning microscope (Zeiss, Jena, Germany) equipped with a c-Apochromat 40×/NA 1.2 water-immersion objective. For imaging experiments, 400 μL of sample was added to the wells in eight-well Lab-Tek Nunc® chamber slides (Fisher Scientific, UK) and excited at 488 nm using an Argon laser (30 mW). All experiments were performed in a thermostatically controlled environment of 21 °C, and images were acquired with a pixel size of 40 nm. The pixel size was selected from the recommended values in the literature[39] and was determined from the PSF of the laser beam for the corresponding objective at 488 nm, which was determined through obtaining *z*-stacks (axial resolution) of 100 nm immobilised green beads on a coverslip and performing a time series in two dimensions (*x*–*y*) to obtain ω_0. Subsequent determination of the laser beam width was achieved through the analysis of acquired intensity profiles using ManICS.

3.3.2.8 Dynamic Light Scattering

Experiments were performed with a Nano-Zetasizer (Malvern Instruments, Worcestershire, UK) equipped with a 633 nm Helium–Neon laser (4 mW) that was set to 21 °C for all measurements. Optimal settings were applied by the instrument for each sample following a selection of 20 runs per samples and a three minute equilibration period. The measured hydrodynamic radii of the BSA–AF488 samples were applied to the determination of the diffusion coefficient using the Stokes–Einstein equation for different ionic strengths and pH experimental conditions:

$$D = \frac{kT}{6\pi\eta R}$$ *Equation 3.7*

where k is the Boltzmann constant, η is the viscosity, T is the temperature and R is the hydrodynamic radius of the characterised compound.

3.3.2.9 Statistical Analysis

Statistical assessment of all data was performed using the ANOVA two factor without replication test ($p < 0.05$) in each dataset to assess the statistical significance of any trends obtained from the analysis of RICS, FCS and DLS output.

3.4 Results

3.4.1 Calibration of RICS Analysis Using Rhodamine Green™

Raster image correlation spectroscopy analysis was calibrated using Rhodamine Green™ solution images and their autocorrelation curves, ACF (See Figure 3.2). Fitting the 2D ACF (Figure 3.2) gave a diffusion coefficient of $2.77 \pm 0.46 \times 10^{-6}$ cm^2/sec for a 0.5 µM solution of Rhodamine Green™ (Invitrogen) which is consistent with the previously reported values for this parameter for Rhodamine 6G — this assumption was made because the molecular weight of Rhodamine Green™ (i.e. 507 g/mol) is similar to that of Rhodamine 6G (i.e. 479 g/mol). Subsequently, using the above diffusion coefficient, the beam waist diameter,ω_0, was determined to be 0.363 µm (See Equation 3.1).[37] This value of the beam waist was further confirmed with that of fluorescent bead images (See Appendix 3) subjected to RICS analysis to determine the axial resolution of the 40×/NA 1.2 water immersion objective lens at 488 nm.

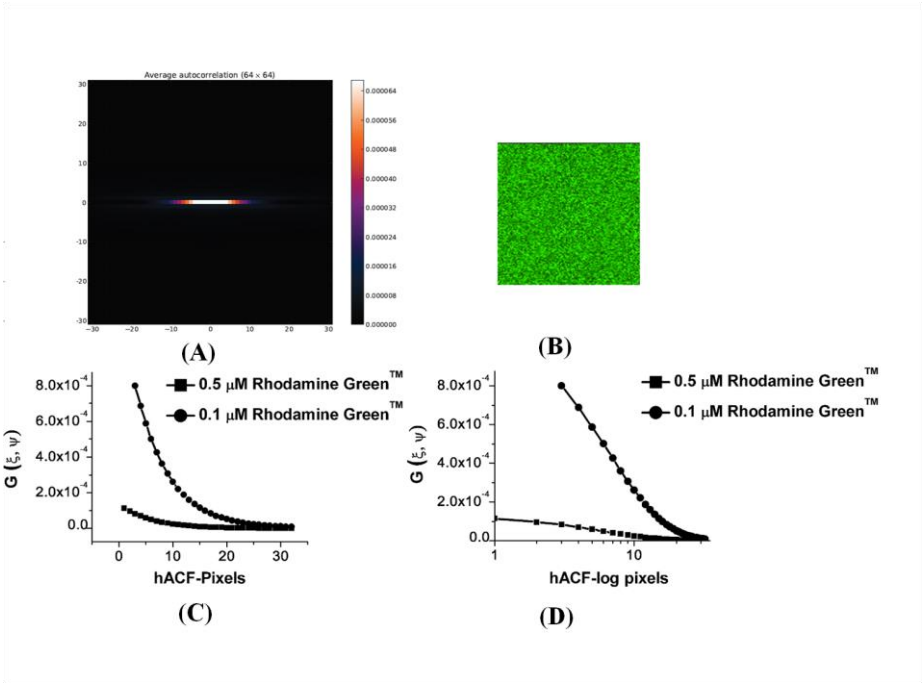

Figure 3.2 *A two-dimensional autocorrelation of 0.5 µM Rhodamine Green™ in solution.* ***(A)*** *A typical confocal image captured using a Zeiss LSM 510 confocal setup with a pixel time of 3.2 µs, a line time of 3.9 ms and a frame time of 0.039 s.* ***(B)*** *The horizontal autocorrelation function (hACF) for 0.5 and 1 µM samples of Rhodamine Green™ with a 64 × 64 pixel region of interest.* ***(C)*** *The corresponding semi-logarithmic horizontal ACF.* ***(D)***

Following calibration of Rhodamine Green™, confocal images of BSA–AF488 samples were acquired. Figure 3.3C presents an example of the raw 3D horizontal ACF for a 50 mM BSA–AF488 solution at pH 4.5 based on a 128 × 128 pixel ROI. The RICS-determined diffusion coefficient of the 50 mM BSA–AF488 sample was found to be $3.69 \pm 0.5 \times 10^{-7}$ cm^2/sec at pH 4.5 (Figure 3.3A-C). The 2D ACF for a 250 mM ionic strength sample at pH 7 is presented in Figure 3.3D, the diffusion coefficient of which was determined to be $4.4 \pm 0.68 \times 10^{-7}$ cm^2/sec.

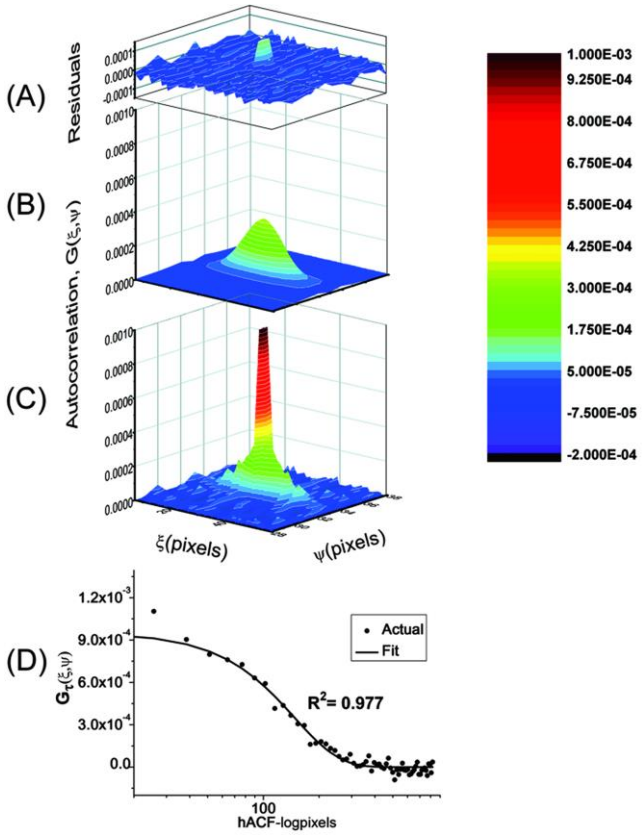

Figure 3.3 *Autocorrelation curve of a 1 µM BSA–AF488 sample of 50 mM ionic strength at pH 4.5 with* ***(A)*** *the residuals,* ***(B)*** *the fitted autocorrelation function (ACF; R^2 = 0.78),* ***(C)*** *the raw two-dimensional (2D) ACF and* ***(D)*** *a semi-logarithmic 2D horizontal ACF (hACF) for a 1 µM sample at pH 7 of 250 mM ionic strength, acquired with a pixel time of 12.8 µs, line time of 15.5 ms and a frame time of 0.0155 s.*

3.4.2 Comparison of Ionic Strength Influence on the Diffusion Data Obtained From Multiple Methodologies

3.4.2.1 Low Concentration

Following initial calibration with Rhodamine Green™, the influence of ionic strength on the diffusion of BSA–AF488 was determined at pH 7. Upon addition of 1 M NaCl stock solution, the ionic strength was modulated and its influence on BSA–AF488 diffusion was assessed over the 0–500 mM ionic strength range at pH 7 and 4.5 using FCS, DLS and RICS (See Figure 3.4 A and B).

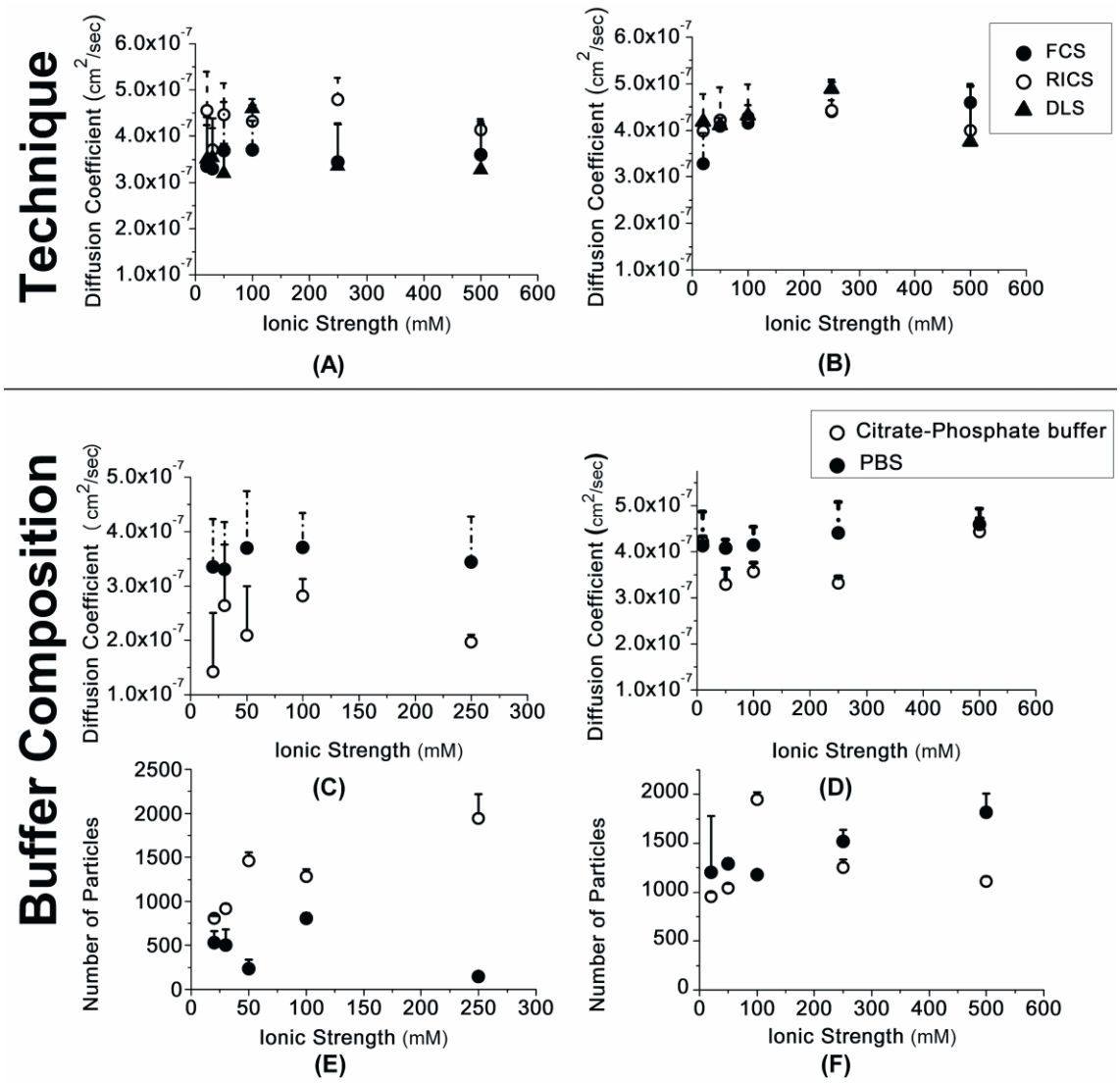

Figure 3.4 *Variation of the diffusion coefficients of BSA–AF488 as a function of the ionic strength obtained with DLS (▲), RICS (○) and FCS (•) at* ***(A)*** *pH 4.5 ± 0.2 and* ***(B)*** *pH 7 ± 0.2 in the presence of 5 mM PBS. Variation of the diffusion coefficients of BSA–AF488 as a function of ionic strength with different buffer compositions at* ***(C)*** *pH 4.5 ± 0.2 and* ***(D)*** *pH 7 ± 0.2. The number of particles associated with* ***(E)*** *pH 4.5 ± 0.2 and* ***(F)*** *pH 7 ± 0.2.*

The results demonstrate no statistically significant variation in the diffusion coefficients obtained between the different methodologies (i.e. DLS, FCS and RICS) employed following the performance of an ANOVA test ($p < 0.05$). These results are consistent with the previously published trends of ionic-strength-independent diffusion behaviour of BSA by Raj and Flygare[13] and Gaigalas *et al*.[17] at pH 7. However, at pH 4.5, a larger difference was observed between the methodologies implemented, with a greater degree of variation between the RICS and DLS output from that of FCS (i.e. statistically significant), as the diffusion coefficients determined increased over the ionic strength range studied.

As initial RICS analysis was shown to provide reliable data on BSA diffusion, the impact of filtration and centrifugation on BSA–AF488 dynamic behaviour was studied. Samples were prepared at pH 4.5 and subjected to a combination of either 0.2 or 0.4 µm filtration performed in triplicate, with centrifugation at 15,000 rpm for 20 min. These were then compared against control samples, the constituents of which were only pre-filtered. Results presented in Table 3.2 indicate that observed effects are filtration dependent and aggregates removed from 0.2-µm-filtered samples displayed a statistically significant decrease in the number of particles detected and, conversely, an increase in the diffusion coefficients. However, there was no significant statistical difference documented between the diffusion coefficient data of 0.4-µm-filtered samples and that of the untreated samples following an ANOVA test (results not shown).

Table 3.2 *The influence of sample pretreatment conditions on the diffusion coefficient (D) and number of particles (N) determined using RICS at pH 4.5 (±0.2). Values indicated in the table represent mean (± st. dev.).*

Ionic Strength (mM)		**No filtration**	**0.2 µm filtered**
20	*N*	499 ± 44.9	237 ± 6
	$D\ x10^{7}$	2.33 ± 0.82	3.72 ± 0.3
30	*N*	437 ± 30	308 ± 27
	$D\ x10^{7}$	3.48 ± 0.31	3.56 ± 0.23
50	*N*	954 ± 130	591 ± 52
	$D\ x10^{7}$	4.2 ± 0.41	4.65 ± 0.26
100	*N*	450 ± 50	256 ± 14.7
	$D\ x10^{7}$	1.93 ± 0.34	4.37 ± 0.1

3.4.2.2 High Concentrations

The influence of ionic strength variation at higher concentrations was assessed for samples prepared at pH 5.2, where the net charge of BSA is expected to be small. Parameters derived following calculation of the hydrodynamic radii (R_H) from RICS-determined diffusion coefficients as a consequence of ionic strength variation for both 10 mg/mL (152 µM) and 40 mg/mL (608 µM) BSA samples have been presented in Table 3.3.

Table 3.3 *The influence of ionic strength on the (mean ± st. dev.) hydrodynamic radii (nm), R_H, of higher-concentration BSA samples calculated using RICS-determined diffusion coefficients at pH 5.2 (±0.2). R^2 represents the quality of fit.*

		Concentration (*mg/mL*)	
Ionic strength (mM)		**10**	**40**
0	R_H	5.72 ± 0.00	6.21 ±0.00
	R^2	0.866 ±0.05	0.790 ±0.09
250	R_H	3.95 ± 0.00	4.98 ± 0.00
	R^2	0.885 ± 0.05	0.886 ±0.05
1000	R_H	3.88 ± 0.00	4.14 ± 0.00
	R^2	0.910 ± 0.02	0.85 ± 0.03

Results obtained from higher-concentration experiments indicate a decrease in the hydrodynamic radii for both concentrations with increasing ionic strengths and larger hydrodynamic radii for the 40 mg/mL (608 µM) samples as compared with that of the 10 mg/mL (152 µM) samples. Performance of a two-tailed, paired Student's *t*-test on the results indicated that the differences noted were indeed statistically significant ($P<0.05$).

3.4.2.3 Freeze–Thaw Cycling and Thermal Denaturation

Thermally denatured and freeze–thawed samples were found to exhibit diffusion coefficients of 2.35 ± 0.58 × 10^{-7} and 2.99 ± 0.50 × 10^{-7} cm^2/sec, respectively, as opposed to the control sample of the same ionic strength at pH 7, where the determined diffusion coefficient was 4.50 ± 0.10 × 10^{-7} cm^2/sec. This overall reduction in the diffusion coefficients was further depicted using a 3D contour plot of occurrences and corresponding numbers of particles for a sample boiled for 10 min at 80 °C in Figure 3.5.

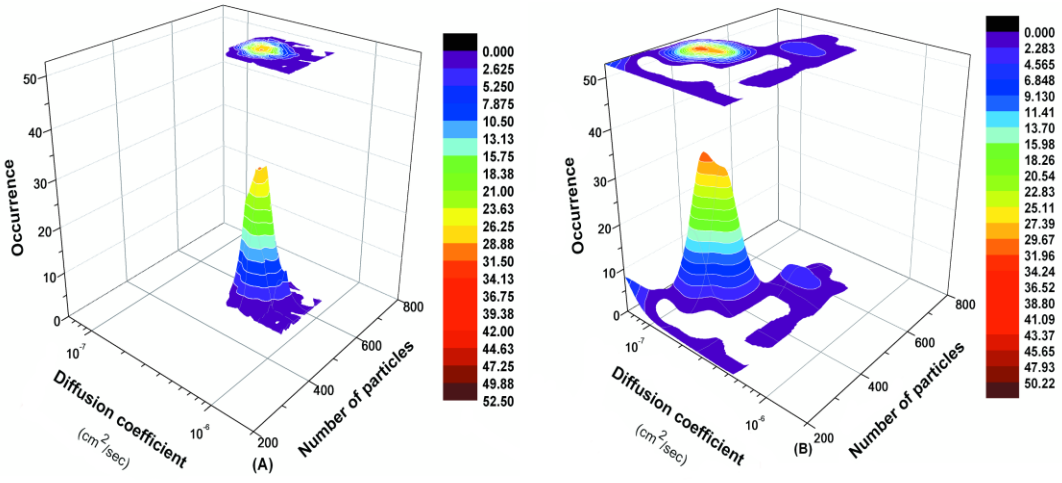

Figure 3.5 *Three-dimensional (3D) contour plot of diffusion coefficients and concentration map distributions* ***(A)*** *within a control sample of 150 mM ionic strength at pH 7 (i.e. 1 µM BSA–AF488) and* ***(B)*** *for a 1 µM sample of 150 mM ionic strength following thermal denaturation at 80 °C for 10 min, acquired with a pixel time of 12.8 µs, line time of 15.5 ms and a frame time of 15.8 s for a 1024 × 1024 resolution image. 3D contour images are based on at least 600 data points.*

Figure 3.5 presents the particle distributions following the approach described in Methods for 1 µM BSA solutions at pH 7 in the absence of thermal denaturation (Figure 3.5A) and following heat denaturation (Figure 3.5B). A relatively narrow distribution is observed in normal conditions (i.e. D ~ 4.5 × 10^{-7} cm^2/sec and N ~ 550) compared with that of a thermally denatured sample (Figure 3.5B), where two to three peaks may be observed and a broad distribution of diffusion coefficients and number of particles are present (i.e. D ~ 2.5 × 10^{-7} cm^2/sec and N ~ 400). These changes are indicative of the different populations of particles observed within the sample, the majority consisting of relatively small aggregate structures and the remainder as the native protein present in the thermally denatured sample.

3.4.2.4 The Influence of Buffer Composition on the Dynamics of BSA–AF488

The influence of buffer composition on the diffusion of BSA–AF488 was studied in the presence of citrate–phosphate buffer because citrate–phosphate buffer and PBS-influenced results have been reported in the literature.[13,17,34] RICS analysis was performed to establish any potential effects on the diffusion behaviour of BSA–AF488, number of particles and the quality of fit obtained.

Results shown in Figure 3.4C-F demonstrate a reduction in the number of particles (Figure 3.4E and F) and the diffusion coefficient (Figure 3.4C and D) following a change in buffer composition for both pH 4.5 and 7 samples, respectively. The quality of the 2D single exponential fit (Equation 3.5) assessed through the R^2 parameter was found to be consistently higher for the samples prepared in PBS as compared with that of citrate-based samples. A further ANOVA test confirmed the initial observations that the diffusion behaviour exhibits a high degree of ionic strength-independence, whereas buffer composition significantly influences the behaviour of BSA–AF488 at the same ionic strength. Overall, the results indicate that diffusion is independent of the ionic strength, but is significantly influenced by buffer composition at given ionic strengths.

3.5 Discussion

The principle objectives of this study were to examine the suitability of RICS as a tool for the quantitative assessment of protein diffusion in solution and evaluate its performance against DLS and FCS. To achieve the objectives outlined, the influences of pH, ionic strength, buffer composition, freeze–thawing and concentration effects on the indicators of aggregation (i.e. number of particles and diffusion coefficient) of BSA were examined using RICS and the aforementioned techniques. Following RICS validation, further experimentation was carried out to assess the influence of sample treatment conditions on the resultant parameters derived from RICS analysis of confocal images. Diffusion coefficients obtained at pH 7 demonstrated an overall appropriate verification of consistency in the diffusion parameters obtained from RICS, DLS and FCS. However, at pH 4.5, a statistically significant difference was noted between the DLS and RICS results upon comparison with the FCS results.

This difference could potentially be attributed to multiple factors arising from the artefacts of routine FCS application that include measurement conditions such as the use of a fixed beam and, consequently, a single confocal volume that dictates the

timescale over which data acquisition occurs and the extent to which aggregates or monomeric species are detected and quantified. This artefact has been circumvented with the introduction of the scanning FCS technique that allows the user to control the pixel dwell time and acquire data over a sampling area covering more than one confocal volume.[40]

Potential experimental errors for FCS may arise from the small immobile detection volume (i.e. within the femtolitre range) because of sampling as a point throughout the duration of the experiment, and may not reflect the overall heterogeneity of the solution (although the acquisition time should be much longer than the diffusion time to provide a correct time distribution). However, multiple exponent models allow for fitting the data and subsequent characterisation of inherent heterogeneities within the sample with the maximum entropy method. In contrast, confocal imaging with subsequent RICS analysis proceeds following definition of parameters such as pixel size range, pixel time and sampling area (i.e. ROI) by the user, thus enabling acquisition of statistically relevant data over a timescale relevant to the purposes of the experiment. In fact, it has been demonstrated that through modulation of the scan speed, it is possible to render the application of RICS more suited to the study of specific particle size ranges.[41]

Trends observed at pH 7 demonstrate no overall statistically significant difference in the diffusion coefficients and number of detected particles of BSA–AF488 across the various ionic strengths, as supported by previous studies and the statistical tests performed.[13,17] However, at pH 4.5, ionic strength dependency was evident at lower values (i.e. 10–50 mM), which is consistent with the previous reports on BSA diffusion behaviour.[13] Raj and Flygare[13] attributed this to the modulatory nature of the electrostatic interactions occurring between counterions and proteins in solution, the net charge at the corresponding pH and, consequently, the extent of Coulombic repulsion that influences the dynamics of protein diffusion in solution. At pH 4.5, BSA is known to carry a small positive charge; therefore, at lower ionic strengths (i.e. less than 0.1 M salt), there is sufficient screening provided by the counterions in solution, thus exhibiting faster diffusion coefficients.[13,17] Overall, at lower ionic strengths, the reduced diffusion coefficients were considered to be a result of the ion friction effect because of lack of screening from counterions in solution. This observation was also noted for the results obtained from pH 5.2 samples at higher concentrations owing to the small net charge of BSA within lower ionic strength ranges at this pH (See Table 3.3).[13,42]

A range of preparation techniques have been previously reported in the literature for the characterisation of BSA in solution ranging from pre-filtration of the reagents to the use of single or combination approaches utilising centrifugation and filtration prior to analysis.[13,14,24] Results (See Table 3.2) confirm that sample pre-treatment conditions indeed influence dynamics. This is consistent with the removal of larger aggregates with smaller-pore-sized filters (i.e. 0.2 μm) that lead to apparent faster diffusion coefficients and a significant reduction in particle size number when compared with untreated samples. This factor therefore requires consideration when studying heterogeneous systems containing a distribution of aggregates, often also deemed as inappropriate for sampling with bulk technologies that can only function with uniform particle size distributions and lack the sensitivity in detecting sample changes arising from filtration.

Buffers utilised for BSA sample preparation in previous studies have often entailed the use of PBS at pH 7[24,34] and citrate–phosphate buffer at pH 4.5,[13,14] and in some instances, the diffusion behaviour of BSA at pH 7 has been considered independent of the buffer composition.[13] The potential influence of the salt type and valency on the behaviour of BSA–AF488 was therefore investigated using RICS (See Figure 3.4C–E). An overall significant change in dynamics was observed that may be attributed to the ability of the ions in solution to induce aggregation and alter the stability of protein solutions through their influence on hydrodynamic parameters.[43]

Furthermore, the presence of a fluorophore eliminates the requirement for sample pre-treatment using filters or sieving, thereby preventing the probability of non-representative results being obtained from unlabelled sample characterisation. An added advantage of a fluorescently labelled sample is that it may be used at different stages, ranging from formulation testing to *in vitro* studies. Although some of the concentrations used in our study are relatively low (i.e. 1 μM BSA) in comparison with titres used in the industry, the introdicton of bright extrinsic fluorescent dyes labelling only hydrophobic pockets in aggregates should permit the use of higher concentrations coupled to a high sensitivity in the detection of trace aggregates. Thus, RICS could be potentially applied as an orthogonal technique in the deduction of aggregation.

Results obtained from the assessment of thermal denaturation effects on BSA–AF488 were presented as 3D contour plots and compared against that of a pH 7 sample of same ionic strength (See Figure 3.5). With the application of RICS analysis to a single image

time series of sufficient size, it is possible to generate statistically significant output data that may be utilised to map inherent heterogeneities in the population from a single acquired confocal image. Although in the manuscript the application of RICS analysis to smaller particle sizes was demonstrated using dyes that associate with hydrophobic pockets or bind covalently, it is possible to also characterise larger aggregates and structures of up to a few microns, in contrast to DLS that is appropriate for analysing particles/aggregates of up to 100 nm in size.

3.6 Conclusion

Raster image correlation spectroscopy can be used as a meaningful tool in the spatiotemporal interpretation of macromolecular dynamics, thereby providing a more detailed insight into the behaviour of biomolecules in comparison with DLS. The findings in this study demonstrate a novel application for RICS in the characterisation of biopharmaceutical stability, with the scope to ascertain numerous parameters ranging from the dynamics of diffusion and potential aggregation to the direct visualisation of larger structures present in confocal images. RICS only requires a commercial confocal setup, and in terms of experimental time and costs, is a rapid, direct and convenient approach as compared with the aforementioned techniques (i.e. DLS and FCS) described for the quantitative and qualitative assessment of protein behaviour in solution.

With the ever-increasing availability of commercial products that fluoresce when in association with hydrophobic pockets, particularly in the presence of aggregation, the need for fluorescent conjugation is no longer a drawback for this method, thus allowing rapid and detailed characterisation of small volume samples at a potentially high titre. Because of the nature of the experimental procedure, during early stages of biopharmaceutical product development, a very small amount or concentration of the active pharmaceutical ingredient would be required for accelerated stability tests owing to the high degree of sensitivity of the technique. Thus, time and cost issues associated with bulk synthesis of the investigated compound would be avoided. Additionally, characterisation of the stability and internalisation mechanisms of a novel product can be studied simultaneously without the need for accounting for changes in the protein behaviour following labelling.

3.7 Acknowledgements

Many thanks go to the University of Manchester Alumni Fund for supporting this project, and also to Dr Francesco Cellesi and Christopher Cadman based at the School of Pharmacy and Pharmaceutical Sciences (University of Manchester) for granting access to the Zetasizer and their valuable advice on DLS experiments. We also thank Jennifer Wedgwood and Som Jain, also based at the School of Pharmacy for providing access, training and support in the use of the viscometer.

3.8 References

1 Mahler HC, Friess W, Grauschopf U, Kiese S. 2009. Protein aggregation: pathways, induction factors and analysis. J Pharm Sci 98(9):2909–2934.

2 Cromwell MEM, Hilario E, Jacobson F. 2006. Protein aggregation and bioprocessing. AAPS J 8(3):E572–E579.

3 Chi EY, Krishnan S, Randolph TW, Carpenter JF. 2003. Physical stability of proteins in aqueous solution: Mechanism and driving forces in non-native protein aggregation. Pharm Res 20(9):1325–1336.

4 Yamasaki M, Yano H, Aoki, K. 1990. Differential scanning calorimetric studies on bovine serum albumin: I. Effects of pH and ionic strength. Int J Biol Macromol 12(4):263–268.

5 Relkin P, Mulvihill DM. 1996. Thermal unfolding of b-lactoglobulin, a-lactalbumin, and bovine serum albumin. A thermodynamic approach. Crit Rev Food Sci 36(6):565–601.

6 Michnik A, Michalik K, Drzazga Z. 2005. Stability of bovine serum albumin at different pH. J Therm Anal 80(2):399–406.

7 Gumpen S, Hegg PO, Martens H. 1979. Thermal stability of fatty acid serum albumin complexes studied by differential scanning calorimetry. Biochim Biophys Acta 574(2):189–196.

8 Giancola C, De Sena C, Fessas D, Graziano G, Barone G. 1997. DSC studies on bovine serum albumin denaturation—Effects of ionic strength and SDS concentration. Int J Biol Macromol 20(3):193–204.

9 Liu J, Song J. 2009. Insights into protein aggregation by NMR characterisation of insoluble SH3 mutants solubilised in salt-free water. PLoS ONE 4(11):e7805.

10 Valstar A, Vasilescu M, Vigouroux C, Stilbs P, Almgren M. 2001. Heat-set bovine serum albumin–sodium dodecyl sulfate gels studied by fluorescence probe methods, NMR, and light scattering. Langmuir 17(11):3208–3215.

11 Corbett RJT, Roche RS. 1984. Use of high-speed size-exclusion chromatography for the study of protein folding and stability. Biochemistry 23(8):1888–1894.

12 Hongping Y. 2006. Simultaneous determination of protein aggregation, degradation, and absolute molecular weight by size exclusion chromatography–multiangle laser light scattering. Anal Biochem 356(1):76–85.

13 Raj T, Flygare WH. 1974. Diffusion studies of bovine serum albumin by quasielastic light scattering. Biochemistry 13(16):3336–3340.

14 Li SX, Xing D, Li JF. 2004. Dynamic light scattering application to study protein interactions in electrolyte solutions. J Biol Phys 30(4):313–324.

15 Jøssang T, Feder J, Rosenqvist E. 1988. Photon correlation spectroscopy of human IgG. J Protein Chem 7(2):165–171.

16 Galantini L, Leggio C, Pavel NV. 2008. Human serum albumin unfolding: A small-angle X-ray scattering and light scattering study. J Phys Chem B 112(48):15460–15469.

17 Gaigalas AK, Hubbard JB, McCurley M, Woo S. 1992. Diffusion of bovine serum albumin in aqueous solutions. J Phys Chem 96(5):2355–2359.

18 Ghosh R, Sharma S, Chattopadhyay K. 2009. Effect of arginine on protein aggregation studied by fluorescence correlation spectroscopy and other biophysical methods. Biochemistry 48(5):1135–1143.

19 Starr TE, Thompson NL. 2002. Local diffusion and concentration of IgG near planar membranes: Measurement by total internal reflection with fluorescence correlation spectroscopy. J Phys Chem B 106(9):2365–2371.

20 Pero JK, Haas EM, Thompson NL. 2006. Size dependence of protein diffusion very close to membrane surfaces: Measurement by total internal reflection with fluorescence correlation spectroscopy. J Phys Chem B 110(22):10910–10918.

21 Földes-Papp Z, Demel U, Tilz GP. 2002. Detection of single molecules: Solution-phase single-molecule fluorescence correlation spectroscopy as an ultrasensitive, rapid and reliable system for immunological investigation. J Immunol Methods 260(1–2):117–124.

22 Seyrek E, Dubin PL, Tribet C, Gamble EA. 2003. Ionic strength dependence of protein–polyelectrolyte interactions. Biomacromolecules 4(2):273–282.

23 Ahmad AL, Hairul NAH. 2009. Protein–membrane interactions in forced-flow electrophoresis of protein solutions: Effect of initial pH and initial ionic strength. Sep Purif Technol 66(2):273–278.

24 Militello V, Casarino C, Emanuele A, Giostra A, Pullara F, Leone M. 2004. Aggregation kinetics of bovine serum albumin studied by FTIR spectroscopy and light scattering. Biophys Chem 107(2):175–187.

25 Digman MA, Gratton E. 2009. Analysis of diffusion and binding in cells using the RICS approach. Microsc Res Tech 72(4):323–332.

26 Digman MA, Brown CM, Sengupta P, Wiseman PW, Horwitz AR, Gratton E. 2005. Measuring fast dynamics in solutions and cells with a laser scanning microscope. Biophys J 89(2):1317–1327.

27 Digman MA, Sengupta P, Wiseman PW, Brown CM, Horwitz AR, Gratton E. 2005. Fluctuation correlation spectroscopy with a laser-scanning microscope: Exploiting the hidden time structure. Biophys J 88(5):L33–L36.

28 Kolin DL, Wiseman PW. 2007. Advance in imaging correlation spectroscopy: Measuring number densities, aggregation states, and dynamics of fluorescently labeled macromolecules in cells. Cell Biochem Biophys 49(3):141–164.

29 Brown CM, Dalal RB, Hebert B, Digman MA, Horwitz AR, Gratton E. 2008. Raster image correlation spectroscopy (RICS) for measuring fast protein dynamics and concentrations with a commercial laser scanning confocal microscope. J Microsc 229(1):78–91.

30 Gielen E, Smisdom N, vandeVen M, De Clercq B, Gratton E, Digman M, Rigo JM, Hofkens J, Engelborghs Y, Ameloot M. 2009. Measuring diffusion of lipid-like probes in artificial and natural membranes by raster image correlation spectroscopy (RICS): Use of a commercial laser-scanning microscope with analog detection. Langmuir 25(9):5209–5218.

31 Petersen NO, Hoddelius PL, Wiseman PW, Seger O, Magnusson KE. 1993. Quantitation of membrane receptor distributions by image correlation spectroscopy—Concept and application. Biophys J 65(3):1135–1146.

32 Gielen E, Smisdom N, De Clercq B, vandeVen M, Gijsbers R, Debyser Z, Rigo JM, Hofkens J, Engelborghs Y, Ameloot M. 2008. Diffusion of myelin oligodendrocyte glycoprotein in living OLN-93 cells investigated by raster-scanning image correlation spectroscopy (RICS). J Fluoresc 18(5):813–819.

33 Carter DC, Ho JX. 1994. Structure of serum albumin. In Advances in protein chemistry; Schumaker VN, Ed. Alabama: Academic Press, pp 153.

34 Meechai N, Jamieson AM, Blackwell J. 1999. Translational diffusion coefficients of bovine serum albumin in aqueous solution at high ionic strength. J Colloid Interface Sci 218(1):167–175.

35 FDA. 2001. Guidance for industry: Bioanalytical method validation. Rockville, Maryland: FDA, pp 7.

36 Sułkowska A, Równicka J, Bojko B, Pożycka J, Zubik-Skupień I, Sułkowski W. 2004. Effect of guanidine hydrochloride on bovine serum albumin complex with antithyroid drugs: Fluorescence study. J Mol Struct 704(1–3):291–295.

37 Rigler R, Mets U, Widengren J, Kask P. 1993. Fluorescence correlation spectroscopy with high count rate and low background—Analysis of translational diffusion. Eur Biophys J Biophys 22(3):169–175.

38 Raphael B, Smith IFC. 2003. A direct stochastic algorithm for global search. J Appl Math Comput 146(2–3):729–758.

39 Rossow MJ, Sasaki JM, Digman MA, Gratton E. 2010. Raster image correlation spectroscopy in live cells. Nat Protoc 5(11):1761–1774.

40 Petersen NO. 1986. Scanning fluorescence correlation spectroscopy. I. Theory and simulation of aggregation measurements. Biophys J 49(4):809–815.

41 Groener N, Capoulade J, Cremer C, Wachsmuth M. 2010. Measuring and imaging diffusion with multiple scan speed image correlation spectroscopy. Opt Express 18(20):21225–21237.

42 Schurr JM. 1980. A theory of electrolyte friction on translating polyelectrolytes. Chem Phys 45(1):119–132.

43 Rubin J, San Miguel A, Bommarius AS, Behrens SH. 2010. Correlating aggregation kinetics and stationary diffusion in protein–sodium salt systems observed with dynamic light scattering. J Phys Chem B 114(12):4383–4387.

44 Mueller M, Lindner B, Kusumoto S, Fukase K, Schromm AB, Seydel U 2004. Aggregates are the biologically active units of endotoxin. J Biol Chem 279(25):26307-26313.

45 Kumar Das D, Kumar Das A, Kumar Mandal A, Mondal T, Bhattacharyya K 2012. Effect of an ionic liquid on the unfolding of human serum albumin: A fluorescence correlation spectroscopy study. ChemPhysChem.13(7):1949-1955.

Chapter 4

THE APPLICATION OF IMAGE ANALYSIS TO THE QUANTIFICATION OF MONOMER LOSS AND AGGREGATION IN SOLUTION

Assessment of Aggregation Processes Using Real-time Confocal Microscopy Image Analysis and Light Scattering

Zahra Hamrang,[1] Egor Zindy,[3] Robin Curtis,[2] David Clarke [1,3] and Alain Pluen [1,3].

1. *School of Pharmacy and Pharmaceutical Sciences, University of Manchester, UK.*
2. *Manchester Interdisciplinary Biocentre, University of Manchester, UK.*
3. *Centre of Excellence in Biopharmaceuticals, University of Manchester, UK.*

4.1 Abstract

Small oligomeric species are known to contribute to aggregate and plaque formation, a process of relevance to protein aggregation in biopharmaceuticals and understanding the underlying mechanistics contributing to neurodegenerative diseases.

In this study real time confocal imaging was utilised to monitor the *in situ* loss of monomers as a function of time, concentration and ionic strength. Acquired images were subsequently analysed using Spatial Intensity Distribution Analysis (SpIDA) and Raster Image Correlation Spectroscopy (RICS) to profile monomer loss and the emergence of aggregate sub-populations. To enable characterisation of shifts in sub-populations of aggregates, resultant data were compared against that of fluorescence correlation spectroscopy and dynamic light scattering.

Reversible monomer loss was observed in purified monomeric labelled bovine serum albumin (BSA) samples for a range of concentrations and ionic strengths accompanied with the formation of larger aggregates. The combination of image analysis tools allows for both oligomeric and larger aggregate sub-type detection in contrast to conventional approaches such as dynamic light scattering that lack the ability to resolve dimers from monomeric moieties in samples containing mixed populations. The capability to monitor *in situ* oligomerisation and aggregation processes renders imaging and image analysis an attractive approach for gaining a mechanistic insight into processes contributing to the formation of larger aggregate species and sub-visible particles during the biopharmaceutical product shelf life.

Keywords: Monomer loss; Protein aggregation; Size-exclusion chromatography; Light scattering; Microscopy; Image analysis.

4.2 Introduction

Formation of small transient oligomeric intermediates has been identified as the initial step contributing to the formation of both amorphous and fibrillar structures following manufacture and purification in the production of protein-based biopharmaceutical preparations, or in processes underlying the formation of neurodegenerative amyloid plaques.[1]

Oligomeric species are often difficult to characterise owing to their reversibility as a consequence of thermodynamic unfavourability that limits their *in situ* biophysical detection and characterisation. Furthermore, heterogeneities in their formation contribute to uncertainties in the structural assessment of oligomers. In turn this has stimulated recent interest in the development of appropriate mathematical models, formation of stable irreversible oligomers and the application of novel technologies to facilitate close examination of their formation, characteristics and role in aggregation processes.[1,2]

As aforementioned, the synthesis of stable oligomeric structures has been addressed such that the synthesis of soluble oligomers was reported by Ahmad *et al*. to form at the N-terminal domain of HypF from *Escheichia coli* under conditions of high pH and low concentrations of 2,2,2-trifluoroethanol in an attempt to facilitate the assessment of aggregation and fibril formation from oligomeric species using a combination of atomic force microscopy, traditional fluorescence-based, light scattering and spectrophotometric approaches.[1] Similarly, Brummit *et al*. characterising monomer loss from IgG samples demonstrated that storage of samples on ice for a minimum of 15 minutes following treatment at elevated temperatures arrests further aggregation processes and permits the subsequent analysis of samples prepared using this approach.[3-5]

Non-native aggregation of proteins is a multistage process generally understood to be initiated by native monomer partial unfolding following an intermediate conformational transition that may render the monomer reactive to association with other unfolded monomers.

To support understanding of the underpinning stages implicated in the formation of larger aggregates, mathematical models have been developed and applied to the

determination of oligomerisation and polymerisation processes, some of which are described as follows;[6,7]

(i) The Lumry-Eyring model considers both unfolding and refolding transitions in detail whilst assembly steps implicated in aggregate formation are treated in a simplified qualitative manner.[2,7]

(ii) The extended Lumry-Eyring model considers a more detailed and sophisticated prediction of the unfolding, refolding and assembly transitions based on experimental conditions and data.[6]

(iii) Native polymerisation models treat polymerisation and aggregation processes in detail but do not consider the influence of conformational changes that ensue prior to and during self-association.[8]

(iv) Multivariate analysis of relative rates of filament or fibril growth based on primary protein structure with no emphasis on the protein secondary and tertiary structure.[9,10]

Current routine approaches utilised in the formation of oligomer species have predominantly centred around light scattering approaches (i.e. static light scattering, multi-angle light scattering and dynamic light scattering) and size exclusion chromatography (SEC), or a combination of both. However, disadvantages associated with dilution of aggregates have been deemed responsible for reversing dimers when analysing monomer loss using SEC coupled to light scattering-based detectors and dynamic light scattering does not possess the ability to resolve dimer populations from monomers.[11]

Correlation[12-14] and histogram-based[15,16] image analysis extensions introduced over the recent decade possess the ability to exploit inherent temporal fluorescence intensity fluctuations to yield meaningful parameters concerning protein diffusional behaviour and aggregation in solution. Previous reports of confocal microscopy applied to the assessment of protein aggregation have involved the validation of RICS to yield particle size distributions of monomer and aggregates for a model protein, bovine serum albumin (BSA)[17] and the application of extrinsic dyes to monoclonal antibodies in order to determine aggregate size distributions.[18-20]

Limitations in technologies enabling the real-time monitoring of kinetics of monomer loss and subsequent larger aggregate formation have posed an obstacle to real-time studies of monomer loss in protein-based samples to date. Hence, in this study SpIDA was utilised in combination with RICS to study oligomerisation and shifts in BSA diffusion coefficients in confocal image time series obtained from BSA samples subjected to thermal stress. Results obtained using these approaches were subsequently compared against dynamic light scattering and fluorescence correlation spectroscopy data to facilitate the comparison of image analysis tools with previously utilised approaches.

4.3 Materials and Methods

4.3.1 Materials

Phosphate-buffered saline (PBS), fatty acid-free Bovine Serum Albumin (BSA) and hydrochloric acid were obtained from Sigma (Poole, UK). Sodium hydroxide, citrate, sodium phosphate and sodium chloride (NaCl) were obtained from Fisher Scientific (Loughborough, UK) and Bovine Serum Albumin labelled with Alexa Fluor® 488 (BSA-AF488) was purchased from Life Technologies (Loughborough, UK).

4.3.2 Methods

4.3.2.1 Sample Preparation

2.5 mg/mL solutions of BSA-AF488 were prepared, filtered and purified to the monomeric form using size exclusion chromatography (SEC). The sample was passed through a Superdex 200 10/300 GL column with a 0.5 mg/mL flow rate. The monomer fraction was separated and collected for further analysis. The BSA concentration was determined spectrophotometrically at 280 nm assuming a molar extinction coefficient of 43,824 $M^{-1}cm^{-1}$. pH and Ionic strength adjustments with NaCl were carried out immediately prior to placement of the sample in the flow chamber at time zero and the start of image acquisition.

Similarly, stock unlabelled BSA solutions were subjected to SEC and the monomeric fraction removed for sample preparation. All solutions reported in this study were stored at 4 °C prior to experimentation. All buffers and solutions utilised were pre-filtered using a 0.2 μm pore sized filter in order to remove any potential particulates contributing to seeding.

All samples were subjected to filtration through a 0.45 µm pore-sized filter prior to analysis with confocal microscopy, dynamic light scattering and fluorescence correlation spectroscopy in order to remove larger aggregates and ensure consistency in the data obtained between the methods.

For experiments considering the RICS-derived diffusion coefficient of samples stored at 50 °C to specified time points (i.e. 30, 60, 90 and 120 minutes), samples were prepared using the method above and incubated to the desired time point on a heating block and subsequently placed on ice for 15 minutes to arrest any further aggregation prior to confocal imaging.

4.3.2.2 Real-time Confocal Imaging of Monomer Loss

Monomeric BSA-AF488 samples (i.e. 500 µL) were subsequently placed in a pre-heated flow chamber positioned in a custom stage heater pre-set to 50 °C (See Figure 4.1)

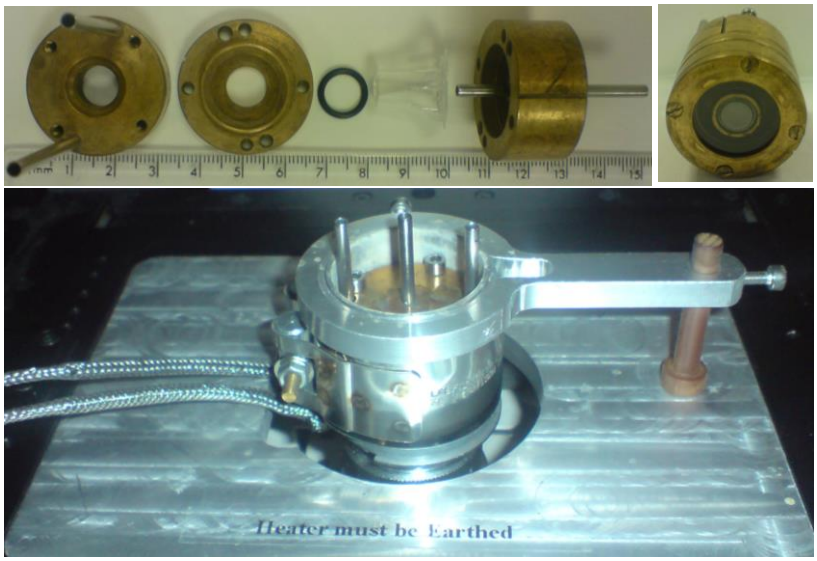

Figure 4.1 *The flow cell chamber and heating stage setup utilised in the real time characterisation of BSA-AF488 monomer loss following heating at 50 °C.*[21]

Temporal changes in monomeric samples of different BSA-AF488 concentrations (i.e. 0.4 and 1 mg/mL) at different NaCl concentrations (i.e. 50, 150 and 500 mM) were recorded at 50 °C over a period of 240 minutes as a confocal image time series. Resultant time series were analysed using SpIDA in order to evaluate the temporal evolution of BSA monomer loss and the formation of dimers and higher order

aggregates. The pre-determined monomeric quantal brightness (See Appendix 4) was utilised for histogram fitting and the subsequent calculation of monomers and dimers present within the sample.

Image time series of BSA-AF488 were acquired using a Zeiss Confocor2 LSM510 confocal microscope (Zeiss, Jena, Germany) and a c-Apochromat 40x/1.2NA water-immersion objective lens with a pixel dwell time of 6.4 μs and a corresponding pixel size of 44 nm for 1024 x 1024 pixel resolution images. Monomer loss was assessed over a period of 240 minutes using imaging and subsequent image analysis (i.e. RICS and SpIDA).

4.3.2.3 SpIDA Analysis of Confocal Images

Analysis of time series images obtained following image acquisition was performed utilising SpIDA. Fitting super-poissonian distributions of fluorescence intensity histograms determined from CLSM images forms the basis of SpIDA analysis. Parameters of quantal brightness (*QB*) and density per beam area (i.e. number of fluorescent moieties defined within a specified region) are the standard output parameters obtained using this method following the selection of a region of interest (ROI). This is achieved through the determination of the histogram of each pixel fluorescence intensity value within a specified ROI. In turn the histograms are determined from calculating all the possible configurations in which a fluorescent entity may reside in a point spread function defined region. Following weighted calculations of each configuration and its respective probability assuming a Poisson distribution for *N* particles inside the PSF, the fitting function applied to determination of the final histogram is defined as;

$$H(\varepsilon, N; \kappa) = \Sigma_n \rho^n(\varepsilon; \kappa) Poi(n, N) \quad \text{with } \rho^0(\varepsilon; \kappa) = \delta_{k,0} \qquad \textit{Equation 4.1}$$

where *H* is the histogram fitting function that is normalised so that the integral over $\acute{k}$ equals unity. ε represents the molecular quantal brightness, *N* the number of particles within the PSF, ρ^n the probability of observing an intensity of light of $\acute{k}$ (assuming proportionality to the number` of emitted photons) by *n* particles of ε brightness.[15]

Pre-requisite parameters for SpIDA analysis are the laser beam waist size and PMT shot noise, the values and method of determination of which are presented in Appendix 1.

4.3.2.4 Assessment of the Intrinsic Fluorescence of Monomeric BSA

Purified monomeric fatty acid free BSA (i.e. 4 mg/mL) was diluted in PBS and citrate-phosphate buffer (i.e. at a final concentration of 0.4 mg/mL due to detectors exhibiting saturation when recording the intrinsic fluorescence at 1 mg/mL) and the temporal intrinsic profile recorded over a period of four hours and 24 hours following initial measurements through maintenance at 50 °C on a heating block. The fluorescence intensity profile was recorded using a Cary fluorescence spectrofluorometer and the tryptophan residues excited at 280 nm (bandwidth: 5 nm) and the subsequent emission profile collected in the 285-550 nm range (bandwidth: 5 nm). This process was carried out for 0.4 mg/mL samples in PBS and citrate-phosphate buffer to compare any buffer-related effects and subsequent conformational changes following thermal stress (50 °C).

4.3.2.5 Raster Image Correlation Spectroscopy

A full description of the in-house RICS software (i.e. ManICS) is provided in the paper by Hamrang *et al.*[17] Briefly, the spatial autocorrelation curve fitting for multiple regions of interest (ROIs) was performed as a two-step process: an initial coarse fit was selected using the PGSL algorithm developed by Raphael and Smith[22] followed by a more conventional fit using the Levenburg-Marquardt algorithm. Following achievement of the best fit (i.e. either when the maximum number of iterations was reached or an incremental improvement in residual fell below a certain threshold), number of particles (N), diffusion coefficients (D) and quality of fit parameters (R^2) of the fitted model for the ROI was applied to the remainder of the ROIs in 1024 x 1024 pixel images. Subsequently, data obtained from up to 900 ROIs were exported and utilised to analyse population data. The principles of RICS, originally developed by Digman *et al.*[13,14] are based on the scan function that relates time to space:

$$S(\xi,\psi) = \tau_p(\xi) + \tau_l(\psi) \qquad \textit{Equation 4.2}$$

In the scan function τ_p is the pixel dwell time, τ_l the line scan time, ξ the spatial displacement in the x direction, and ψ the corresponding spatial displacement in successive lines in the y direction within a raster image. The normalized fluorescence intensity fluctuation spatial ACF ($G_S(\xi,\psi)$) is thus:

$$G_S(\xi,\psi) = G(\xi,\psi) \quad S(\xi,\psi) = \frac{\langle \delta I(x,y)\delta I(x+\xi, y+\psi)\rangle_{x,y}}{\langle I(x,y)\rangle^2_{x,y}} \qquad \textit{Equation 4.3}$$

Where I(x,y) is the fluorescence intensity detected at each pixel, $\delta I(x,y)=I(x,y)-\langle I(x,y)\rangle x,y$ is the fluorescence intensity variation around the mean, and the autocorrelation function for 3D diffusion is:

$$G(\xi,\psi) = \frac{\gamma}{N}\left(1+\frac{4D(\tau_p\xi+\tau_l\psi)}{\omega_0^2}\right)^{-1}\cdot\left(1+\frac{4D(\tau_p\xi+\tau_l\psi)}{\omega_z^2}\right)^{-1/2} \qquad \textit{Equation 4.4}$$

Parameters of the autocorrelation function are $\gamma = \frac{1}{\sqrt{8}}$ accounting for the single photon illumination profile, and ω_0 and ω_z, are the lateral and axial beam waist, respectively.

As RICS requires the PSF to extend over a certain number of pixels (approximately 4-6)[22], the scanner movement is accounted for using the $S(\xi, \psi)$ function:

$$S(\xi,\psi) = \exp\left[-\frac{\left(\left(\frac{\xi\delta r}{\omega_0}\right)^2+\left(\frac{\psi\delta r}{\omega_0}\right)^2\right)}{1+\frac{4D(\tau_p\xi+\tau_l\psi)}{\omega_0^2}}\right] \qquad \textit{Equation 4.5}$$

4.3.2.6 Dynamic Light Scattering

The contribution of BSA labelling with Alexa Fluor® 488 to the observed behaviour and formation of larger aggregates was assessed through the performance of dynamic light scattering experiments and subsequent comparison of the data obtained from this method with SpIDA and RICS. Purified monomeric BSA samples in citrate-phosphate buffer (i.e. pH 7) were made up to 0.4 and 1 mg/mL at 50 and 500 mM ionic strengths using 5 M pre-filtered sodium chloride (NaCl) solution. Diffusion coefficients of resultant samples were measured at room temperature (i.e. 21 °C) at the start of each experiment and profiled using a Zetasizer Nano instrument (Malvern Instruments, Worcestershire, UK) equipped with a 633 Helium-Neon laser, the number of runs of which was optimised according for the sample subjected to analysis. Subsequently the

monomeric samples were subjected to thermal stress at 50 °C and profiled at five minute time intervals for a period of up to two hours.

The measured hydrodynamic radii (from *z*-average data) of the BSA–AF488 samples were applied to the determination of the diffusion coefficient using the Stokes–Einstein equation (See Equation 4.6) for different ionic strengths and concentrations:

$$D = \frac{kT}{6\pi\eta R} \qquad \textit{Equation 4.6}$$

where k is the Boltzmann constant, η is the viscosity, T is the temperature and R is the hydrodynamic radius of the characterised compound.

4.3.2.7 Fluorescence Correlation Spectroscopy

The fluorescence correlation spectroscopy setup used in this study and underpinning principles are described elsewhere. Briefly, a Zeiss LSM 510 Confocor 2 (Zeiss, Jena, Germany) and a 40x/NA c-Apochromat water-immersion objective lens were utilised. The determination of the laser beam waist was carried out by measuring the diffusion time of Rhodamine Green™ using the 488 nm excitation wavelength (i.e. with a corresponding diffusion coefficient of 2.8 x 10^{-6} cm^2/sec)[23]. The laser beam waist was estimated using Equation 4.7;

$$\tau_D = \frac{\omega_0^2}{D} \qquad \textit{Equation 4.7}$$

Where τ_D is the diffusion time, ω_0 the laser waist beam, and D the diffusion coefficient of the species of interest.

In order to ascertain the influence of thermal stress at 50 °C on the formation of larger aggregates, representative samples were prepared from 0.013 mg/mL monomeric purified BSA-AF488 and made up to either 0.4 mg/mL or 1 mg/mL with unlabelled purified monomeric BSA in citrate-phosphate buffer (i.e. pH 7 ± 0.2) and subsequently adjusted to the desired ionic strength (i.e. 50 and 500 mM NaCl) with a 5 M NaCl stock solution. All solutions were filtered prior to sample preparation and analysis with FCS.[18] For kinetics experiments, a time delay of 300 seconds was applied between measurements and 10 runs each of 10 seconds duration performed for each time point up to 120 minutes.

Data obtained using FCS measurements was fitted using either a single or two-component fit from which the number of particles (N) and diffusion time (τ_D) was determined.

In order to achieve a single component fit the following equation was applied;

$$G(\tau) = 1 + \frac{1}{N}\left(1 + \frac{\tau}{\tau_D}\right)^{-1}\left(1 + S^2\frac{\tau}{\tau_D}\right)^{-0.5} \qquad \textit{Equation 4.8}$$

Where $G(\tau)$ is the correlation function, N is the number of particles, τ_D the diffusion time and S, the structure parameter.

The correlation function in a two-component system is determined using Equation 4.9:

$$G(\tau) = 1 + \frac{1}{N_p}\left(\frac{f_1}{\left(1 + \frac{t}{\tau_{D_i,1}}\right)\left(1 + \frac{t}{S^2\tau_{D_i,1}}\right)^{0.5}}\right) + \left(\frac{f_2}{\left(1 + \frac{t}{\tau_{D_i,2}}\right)\left(1 + \frac{t}{S^2\tau_{D_i,2}}\right)^{0.5}}\right) \qquad \textit{Equation 4.9}$$

where $\tau_{D,1}$ corresponds to the diffusion time of species 1, f_1 relates to the proportion of species 1 contribution, $\tau_{D,2}$ relates to the diffusion time from species 2, f_2 is the corresponding fraction contribution from species 2 and N is the number of particles.

Diffusion times calculated from the analysis of FCS measurements were then applied to Equation 4.7 to determine the diffusion coefficient of BSA-AF488 under the conditions examined.

4.3.2.8 Statistical Analysis

ANOVA tests ($P < 0.05$) were performed on various samples and time points to assess whether any significant statistical differences were existent within the samples.

4.4 Results

4.4.1 Assessment of the Intrinsic Fluorescence of Monomeric BSA

The influence of buffer type (i.e. salt composition) on the aggregation of BSA following thermal stress at 50 °C was assessed and the intrinsic fluorescence spectra of monomeric BSA were recorded prior to and following incubation at this temperature at the initiation of the experiment and following a 30 minute incubation at 50 °C. The results obtained from this experiment are presented in Figure 4.2;

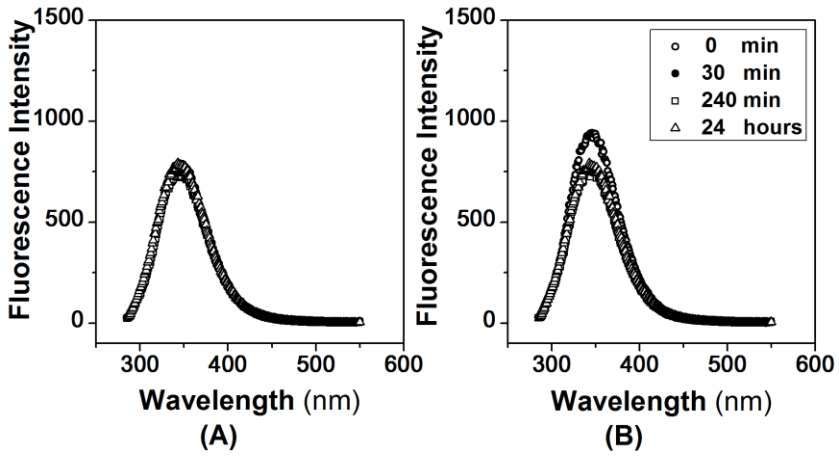

Figure 4.2 *Assessment of intrinsic fluorescence spectra changes in 0.4 mg/mL BSA samples prepared in* ***(A)*** *citrate-phosphate and* ***(B)*** *PBS buffer (pH 7 ± 0.2).*

Figure 4.2 indicates an initial low intrinsic fluorescence for the monomeric BSA sample in citrate-phosphate buffer compared to PBS. It is noteworthy, that while a reduction of the intrinsic fluorescence is observed in PBS following 30 minutes, no such change was observed with the citrate-phosphate buffer sample.

4.4.2 Real Time Quantification of Monomer Loss Using SpIDA and RICS Analysis

4.4.2.1 SpIDA Analysis

Results obtained from the monomeric control sample were subsequently applied to the SpIDA analysis of temporal changes in 0.4 and 1 mg/mL monomeric BSA-AF488 samples following incubation at 50 °C. Figure 4.3 presents the monomer (to total number of particles) temporal profile for each concentration and ionic strength examined in this study.

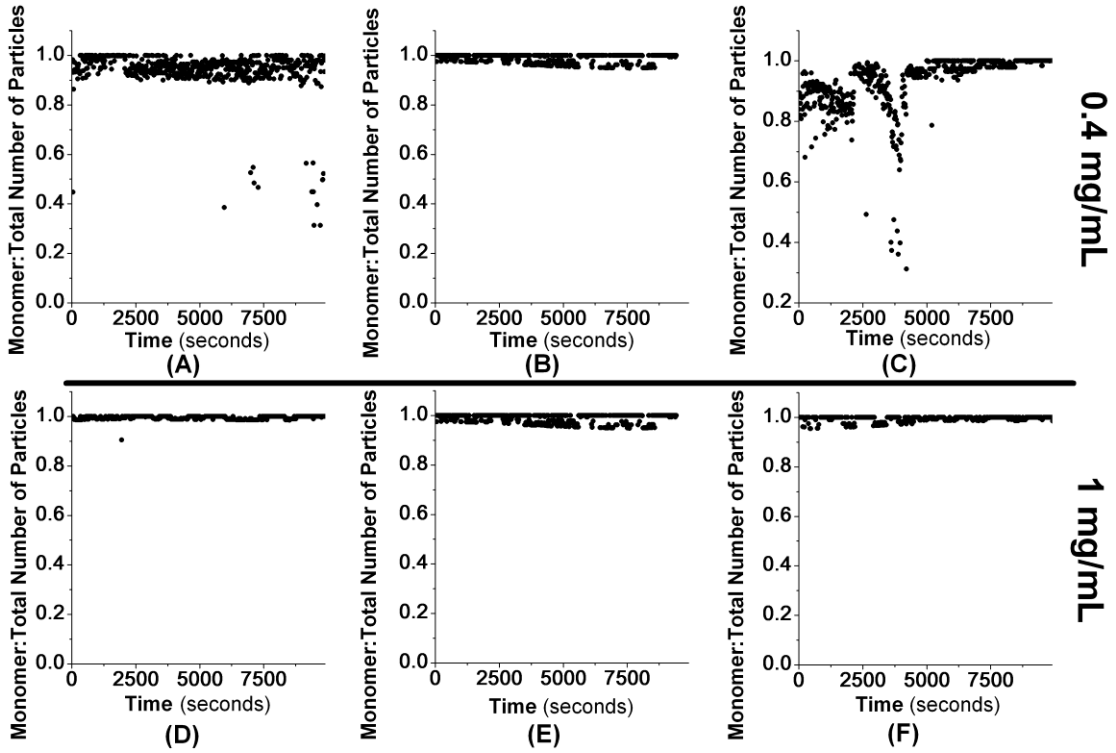

Figure 4.3 *Temporal evolution of monomer loss (relative to the total number of particles) in 0.4 (top) and 1 (bottom) mg/mL samples of monomeric BSA-AF488 (pH 7 ± 0.2) maintained at 50 °C with no agitation. Results were determined using SpIDA from a confocal image time series acquired with a pixel dwell time of 6.4 µs, resolution of 1024 pixels, pixel size of 44 nm for 50 mM* ***(A and D)*** *150 mM* ***(B and E)*** *and 500 mM* ***(C and F)*** *NaCl samples.*

These results do not indicate significant monomer loss within the observation time at all conditions examined with an apparent reversibility in monomer loss.

To normalise for monomer loss kinetics occurring on different time scales, the ratio of monomer at specified time points relative to unheated samples (t=0) were determined and plotted as a function of the time at which the monomer ratio had decreased to 0.9 (i.e. t_{90}). In order to increase clarity of the kinetic plots representative time points were selected every five minutes (See Figure 4.4).

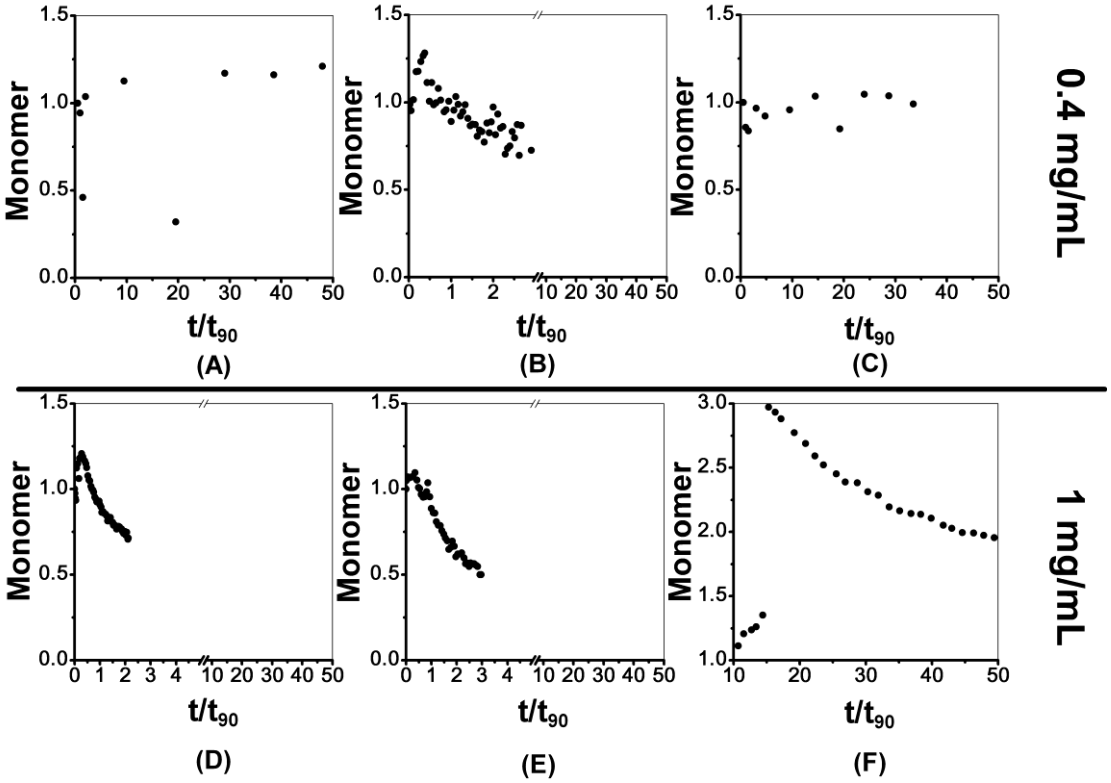

Figure 4.4 *Temporal evolution of monomer loss (relative to the monomer concentration at the start of the experiment) in a 0.4 (top) and 1 (bottom) mg/mL samples of monomeric BSA-AF488 (pH 7 ± 0.2) maintained at 50 °C with no agitation. Results were determined using SpIDA from a confocal image time series acquired with a pixel dwell time of 6.4 µs, resolution of 1024 pixels, pixel size of 44 nm for 50 mM* ***(A and D)*** *150 mM* ***(B and E)*** *and 500 mM* ***(C and F)*** *NaCl samples.*

Data presented in Figure 4.4 indicates monomer loss in all samples with a higher degree of reversibility observed in the 0.4 mg/mL samples in comparison to the 1 mg/mL samples throughout the experiment and a larger gradient of monomer loss in the first five t_{90}s in 1 mg/mL samples (with the exception of the sample containing 500 mM NaCl that demonstrated an increase in monomer concentration in the first five half-lives) in comparison to that of 0.4 mg/mL samples. For temporal dimer and trimer formation plots see Figure A4.4 and Figure A4.5 in Appendix 4, respectively. Monomer loss curve slopes were determined and applied to the analysis of monomer loss kinetic reaction order determination using the following equation from Brummitt *et al.*;[4]

$$\frac{dm}{dt} = -k_{obs}m^{\alpha} \qquad \textit{Equation 4.10}$$

Where k_{obs} represents the observed rate coefficient, m the monomer fraction at the corresponding time and α the reaction order.

Analysis of curve slopes on a log-log plot indicated that the amount of monomer decreased with the inverse of the squared root of the ratio t/t_{90}, a dependence inconsistent with the model proposed by Brummit *et al.*[4] which in turn supports the reversible dimer-monomer model.

4.4.2.2 RICS Analysis

Data presented in Table 4.1 represents the resultant diffusion coefficient determined from images acquired from BSA-AF488 subjected to thermal stress at 50 °C.

Table 4.1 *Mean diffusion coefficient x 10^7 cm^2/sec (± st. dev.) parameters obtained from the RICS analysis of 1024 x 1024 pixel images of BSA-AF488 subjected to thermal stress at 50 °C at specific time points for up to 1024 regions of interest for 0.4 mg/mL samples at indicated ionic strengths.*

	50 mM	**150 mM**	**500 mM**
Time/min	*D x 10^7 (cm^2/s)*	*D x 10^7 (cm^2/s)*	*D x 107 (cm^2/s)*
80	4.45 ± 1.00	3.82 ± 1.58	3.86 ± 0.70
160	3.96 ± 1.50	3.33 ± 1.51	4.63 ± 0.79
240	6.6 ± 1.24	4.82 ± 0.84	6.65 ± 1.25

Table 4.1 does not reveal significant differences between the diffusion coefficients obtained at 50, 150 and 500 mM NaCl for 0.4 mg/mL samples with little observed overall changes throughout the duration of the experiment.

Table 4.2 *Mean diffusion coefficient x 10^7 cm^2/sec (± st. dev.) parameters obtained from the RICS analysis of 1024 x 1024 pixel images of BSA-AF488 subjected to thermal stress at 50 °C at specific time points for up to 1024 regions of interest for 1 mg/mL samples at indicated ionic strengths.*

	50 mM	**150 mM**	**500 mM**
Time/min	*D x 10^7 (cm^2/s)*	*D x 10^7 (cm^2/s)*	*D x 10^7 (cm^2/s)*
80	5.65 ± 0.98	5.00 ± 1.37	5.40 ± 0.93
160	7.40 ± 1.34	6.10 ± 1.31	5.30 ± 0.96
240	7.37 ± 1.29	5.00 ± 1.24	4.49 ± 0.86

At 1 mg/mL a small reduction in the mean diffusion coefficient was observed for the 150 and 500 mM NaCl ionic strength-adjusted samples with time (See Table 4.2). Nevertheless, these variations did not appear statistically significant changes following the performance of ANOVA on RICS-acquired parameters.

Typical ranges obtained from the analysis of population data for diffusion coefficients are presented in Appendix 4 that indicate the presence of larger aggregates (i.e. the occurrence of slower diffusion coefficients as minimum values). Furthermore, confocal images acquired at a concentration of 1 mg/mL indicated the more frequent occurrence of larger aggregates evident in the acquired confocal micrographs examples of which have been included in Appendix 4.

4.4.3 Quantification of Monomer Loss and Aggregation at Various Time points

Larger aggregates were detected in real-time images obtained from the analysis of low ionic strength and low concentration samples. In order to assess population data in samples as a function of time, representative aliquots were removed from a 0.2 mg/mL sample (i.e. ionic strength adjusted to 50 mM NaCl) placed on a heating block and cooled on ice for 15 minutes to arrest any further aggregation. Subsequently, confocal imaging was performed on each sample and both RICS and SpIDA (See Figure 4.5) analysis performed to determine changes in sub-populations as a function of time.

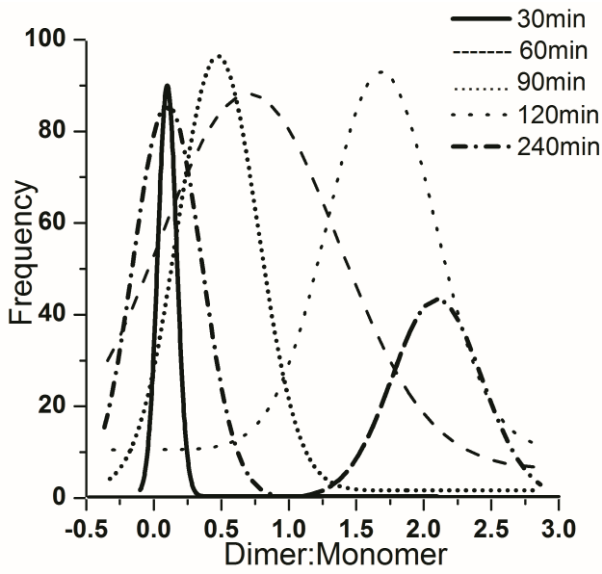

Figure 4.5 *Time-dependent Gaussian distributions of monomer populations for a 0.2 mg/mL (i.e. 50 mM ionic strength) BSA-AF488 sample heated over a period of 240 minutes. Images were acquired with a resolution of 1024 x 1024, corresponding pixel size of 44 nm and a pixel dwell time of 6.4 microseconds.*

Figure 4.5 shows an increase in the dimer:monomer populations with a broadening of the distributions over time. Importantly, a bimodal dimer: monomer distribution was observed at 240 minutes suggesting the presence of spatial heterogeneities in oligomer distributions within the sample.

Image time series acquired from samples removed at various time points were analysed using RICS and the statistical descriptors of the sub-populations of particle numbers and their corresponding diffusion coefficients determined. Figure 4.6 presents the mean ± standard deviation of the diffusion coefficients calculated from population data of samples removed at 30, 60, 90 and 120 minutes. Typical ranges obtained from the statistical analysis of population data are presented in Table A4.1 in Appendix 4.

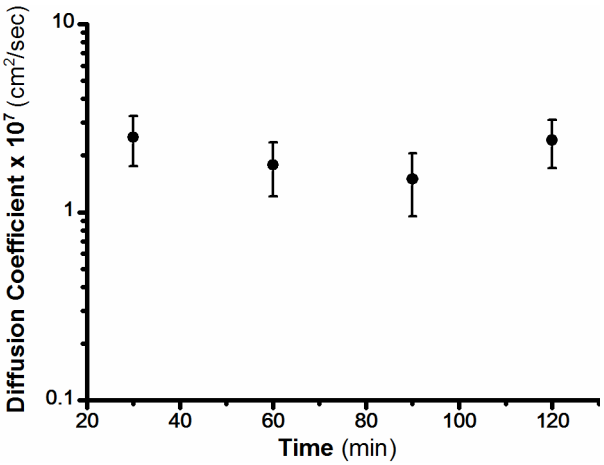

Figure 4.6 *Mean diffusion coefficients x 10^7 (cm^2/sec) ± standard deviation determined from RICS output parameters for a 0.2 mg/mL sample of 50 mM ionic strength subjected to analysis at 30, 60, 90 and 120 minutes from the same confocal image set subjected to SpIDA analysis and presented in Figure 4.5.*

Similarly, in the case of samples extracted between 30-90 minutes a decrease was observed in the median diffusion coefficients obtained from population data consistent with a reduction observed in the particle numbers in Table A4.1 and the observed minimum diffusion coefficient for samples at 50 °C (See Appendix 4). Data show in Figure 4.6 demonstrated no significant change in diffusion coefficients with time, however, further statistical interpretation of population data in Appendix 4 revealed both the occurrence of slower diffusing species and a reduction in the number of particles consistent with the formation of aggregates.

4.4.4 Dynamic Light Scattering (DLS)

The influence of thermal stress was assessed on 0.4 and 1 mg/mL unlabelled BSA samples with DLS and the *z*-average, mass distribution data and polydispersity index determined for each sample for up to two hours. Results obtained from these measurements are presented in Figure 4.7;

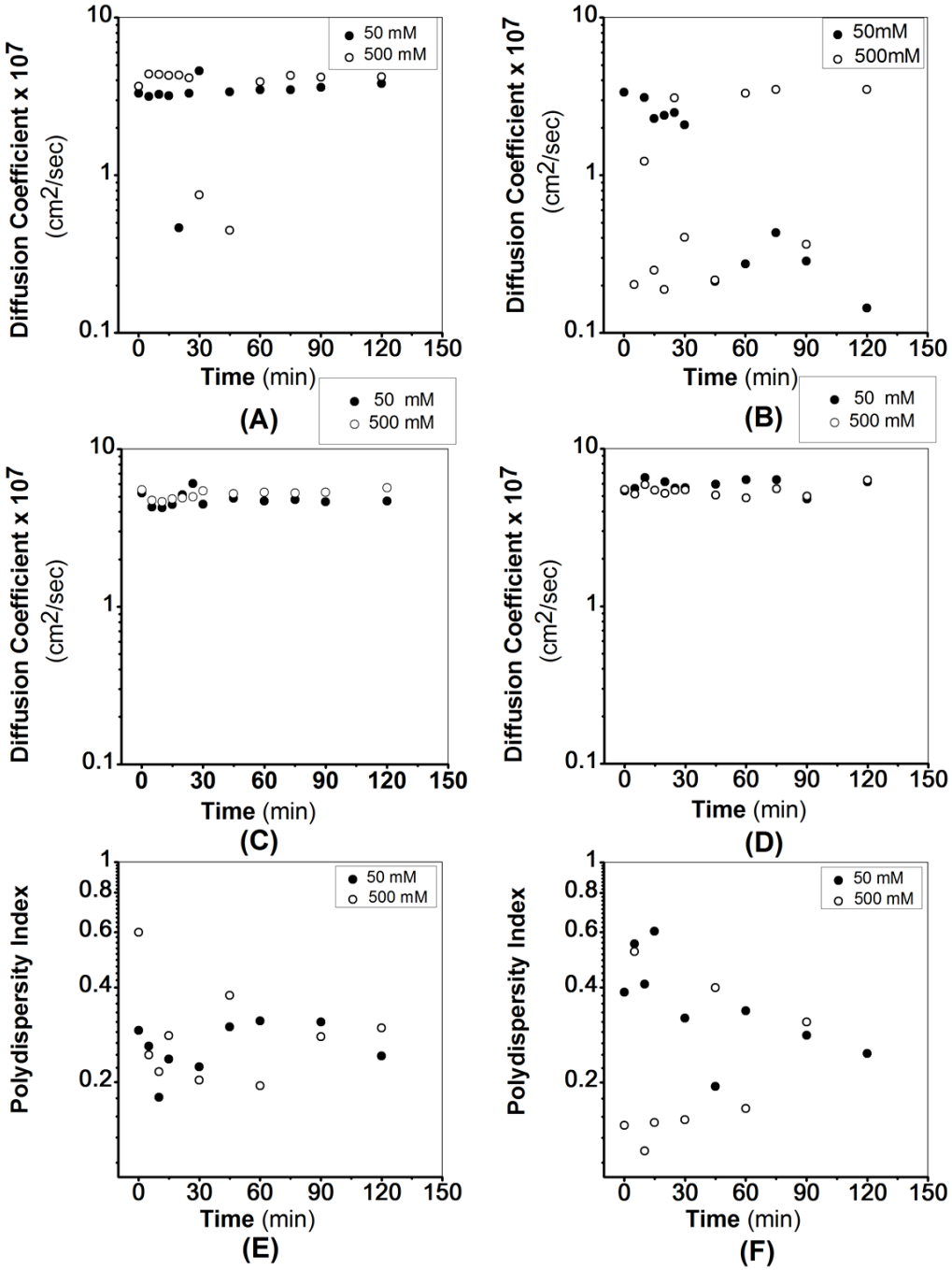

Figure 4.7 *Dynamic light scattering of BSA solutions subjected to thermal stress (i.e. 50 °C). Time-dependent diffusion coefficient variation determined from z-average for 0.4 mg/mL* ***(A)*** *and 1 mg/mL* ***(B)*** *samples heated to 50 °C, time-dependent diffusion coefficient variation calculated from the mass distribution for 0.4 mg/mL samples* ***(C)*** *and 1 mg/mL samples* ***(D)*** *and polydispersity indices determined for* ***(E)*** *0.4 mg/mL and* ***(F)*** *1 mg/mL samples in the presence of 50 and 500 mM NaCl in citrate-phosphate buffer (i.e pH 7 ± 0.2).*

Figure 4.7 illustrates a higher degree of stability and resistance to thermal stress in 1 mg/mL samples particularly in comparison to low ionic strength 0.4 mg/mL samples. Performance of the ANOVA test on the *z*-average values and polydispersity indices obtained for each condition at a 95% significance level revealed a statistically significant difference between each of the conditions of ionic strength and concentration.

Results presented in Figure 4.7 from the measurement of the mass distribution of hydrodynamic radii of BSA samples formulated in the presence of 50 and 500 mM NaCl in citrate-phosphate buffer indicate an increase in the hydrodynamic radius of BSA under these conditions at earlier time points (i.e. 0-30 minutes) with a consistently slower diffusion coefficient observed in 1 mg/mL samples at both NaCl concentrations compared to 0.4 mg/mL BSA samples.

Overall, diffusion coefficient data presented above, demonstrates a small contribution from the presence of large aggregates in mass distribution-based data in comparison to that derived from the intensity of scattered light.

4.4.5 In situ Assessment of Aggregation Using Fluorescence Correlation Spectroscopy

In order to assess the influence of thermal stress on the formation of larger aggregates, FCS measurements were performed using the method described in section 4.3.2.7. Results presented in Figure 4.8 demonstrate changes observed in the diffusion coefficients of a 1 mg/mL (i.e. 15.2 µM) BSA sample containing 50 mM NaCl in citrate-phosphate buffer (i.e. pH 7).

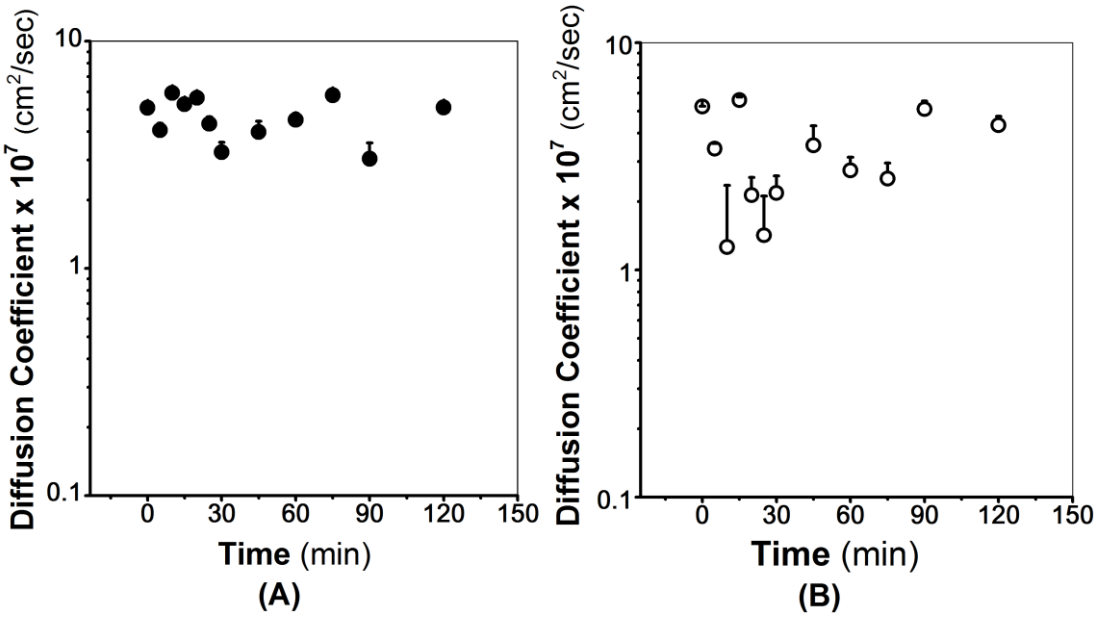

Figure 4.8 *Diffusion coefficients obtained from the FCS analysis of a 0.4 mg/mL* ***(A)*** *and a 1 mg/mL* ***(B)*** *sample in the presence of 50 mM NaCl in pH 7 citrate-phosphate buffer (n=10-15) at 50 °C. Please note that the diffusion coefficient of monomeric BSA will occur faster than 6 x* 10^{-7} cm^2*/sec at 50 °C.*

Results presented in Figure 4.8 indicate that upon heating a reduction in determined diffusion coefficients occurred in 1 mg/mL samples in comparison to 0.4 mg/mL samples formulated at the same salt concentration consistent with aggregate formation in solution. Faster diffusion coefficients (i.e. ~ 4.35 x 10^{-6} cm^2/sec) attributed to the contribution of Alexa Fluor® 488 were omitted from the output data and are not presented here. Performance of an ANOVA test with at a 95% confidence level indicated that a statistically significant difference was existent between each time point.

4.5 Discussion

Currently, only a limited number of analytical methods (e.g. SEC coupled to light scattering) are able to resolve monomeric species from dimers, and associated artefacts experienced in their use such as sample dilution and reversal of soluble oligomers, exclusion of larger aggregates following association with the column matrix and the duration of passage through the column potentially contribute to misrepresentative data as a consequence of solubilisation of reversible aggregates.[24]

For this purpose, the validation and application of tools enabling the *in situ* assessment of monomer loss with the capability to analyse broad particle size ranges is advantageous over current conventional approaches.

Hence, the application of real-time imaging and subsequent image analysis as potential tools for enabling the non-invasive assessment of samples from a monomeric state up to larger aggregate size ranges (i.e. tens of microns) constituted the objectives of this study.

Analysis of confocal image time series using SpIDA revealed the reversible formation of oligomers indicated in Figure 4.3 at both 0.4 and 1 mg/mL concentrations at all NaCl concentrations examined, consistent with previous reports on the reversibility of BSA self-association.[25] Previous reports of BSA self-association at elevated temperatures to date (< 65 °C) have considered protein concentration, incubation time and ionic strength as contributory factors to precipitating unfolding and subsequent self-association that ensues. Additionally, structural changes occurring within these temperature ranges have previously been reported as reversible for BSA.[26,27,24]

To further qualitatively assess self-association processes occurring on kinetically-distinct timescales, the monomer concentration was plotted as a function of the time at which it was reduced to 90% (See Figure 4.4). This data revealed that the rate of monomer loss was indeed lower with a higher degree of reversibility in 0.4 mg/mL samples at all ionic strengths in comparison to that of 1 mg/mL samples as would be expected upon increasing sample concentration.

Furthermore, analysis of the curve gradients indicated monomer reduction with the inverse of the squared root of t/t_{90} for 1 mg/mL samples and zero for 0.4 mg/mL BSA samples in the presence of 50 and 500 mM NaCl consistent with the formation of reversible aggregates. In comparison to previous reports of aggregate reaction order kinetic determination by Brummitt *et al.*,[4] in a system undergoing irreversible self-association (i.e. IgG non-native aggregation with a rate order of 2), data presented here indicates an insignificant and reversible loss of monomer through non-native aggregation over the timescale and conditions under which monomer loss was examined through either a zero order or inverse half-order reaction (See Figure 4.9).[4]

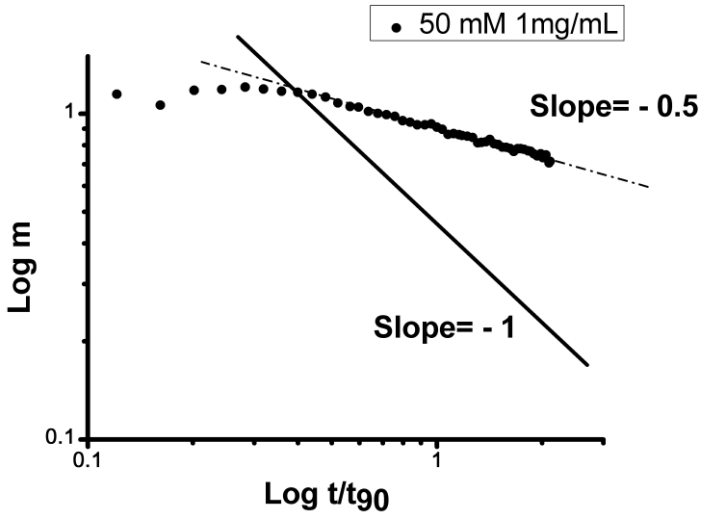

Figure 4.9 *Log-log plot of monomer loss as a function of t_{90} on a log-log scale for a 1mg/mL sample in the presence of 50 mM NaCl. The dotted line represents the slope of the monomer loss curve relative to a (solid) line possessing a slope of unity.*

The overall observed reversibility of monomer loss in Figure 4.3 and general reduction in monomers in Figure 4.4 may be attributed to an existent equilibrium between dimers and monomers, or the removal of dimers at higher concentrations from solution and rapid formation of aggregates contributing to observed higher molecular weight species in confocal micrographs (See Appendix 4). Application of SpIDA analysis to monomer loss exhibits a high degree of resistance to photobleaching effects in profiling number of particles[15] and further assessment of intensity histograms obtained from ManICS mobile fractions (See Appendix 4) revealed minimal photobleaching for RICS measurements.

The presence of larger aggregates in solution was assessed through further analysis with RICS that revealed no significant overall changes in the mean population diffusion coefficients as a function of time, thermal stress, ionic strength and BSA concentration. However, the presence of aggregates was confirmed from the analysis of population data with observed minimum diffusion coefficients occurring at a smaller order of magnitude in the majority of conditions examined (See Appendix 4) confirming the observed aggregates in confocal micrographs (See Appendix 4).

The presence of high molecular aggregates in micrographs led to the further real-time assessment of aggregation in samples formulated in citrate-phosphate buffer using dynamic light scattering, intrinsic fluorescence and fluorescence correlation spectroscopy measurements at 50 °C to determine whether the observed behaviour occurred as a function of labelling (i.e. the covalent association of BSA with Alexa

Fluor® 488), the buffer environment (i.e. salt type), ionic strength or any incompatibilities arising from interaction with the chamber (i.e. copper) used for real-time imaging.

Intrinsic fluorescence spectra presented in Figure 4.2 at ambient temperature and following thermal stress at 50 °C as a function of buffer type on protein conformation revealed a reduction in unlabelled monomeric BSA intrinsic fluorescence for samples formulated in citrate-phosphate buffer (in the presence of 50 mM NaCl) in comparison to samples prepared in PBS, indicating a reduction in the quantum yield of tryptophan and/or an environment favouring aggregation. Additionally, previous data comparing the diffusion coefficients of BSA samples formulated in citrate-phosphate buffer (pH 7) using RICS were found to consistently possess a slower diffusion coefficient and number of particles at all ionic strengths in comparison to PBS that further supports the observations in this study.[17]

Profiling particle size distributions using methods such as dynamic light scattering and fluorescence correlation spectroscopy can often present challenges in the accurate resolution of monomer loss and the formation of small soluble oligomers from the presence of larger aggregates within the analyte sample since both methods are insensitive to molecular weight changes smaller than 3-5 fold.[28]

In samples containing 500 mM NaCl small changes in the diffusion coefficients determined from the mean radii obtained from dynamic light scattering and a higher propensity for the formation of aggregates was noted by an apparent reduction in the calculated diffusion coefficients from *z*-average hydrodynamic diameters obtained from cumulant analysis and temporal changes in sample polydispersity following exposure to thermal stress (See Figure 4.7).

Furthermore, in samples containing a higher concentration of NaCl (i.e. 500 mM) in 1 mg/mL concentrations of BSA the diffusion coefficient was reduced. This may be attributed to electrostatic repulsion effects at lower ionic strengths and lack of screening from counterions in solution preventing favourable interactions leading to self-association.[29] When evaluating particle size distributions from DLS data caution must be exercised due to the apparent susceptibility of the output data to the presence of large aggregates that may significantly influence any intensity-based parameters (i.e. scattering intensity proportional to the sixth power of the particle diameter) even at low

concentrations. Hence, DLS is an appropriate qualitative indicator of large aggregate presence (up to 10 µm) and in the more precise assessment of size distributions such species must be removed through filtration or centrifugation.[30]

The broad overall heterogeneity observed in the temporal profile of higher concentration (i.e. 1 mg/mL) samples heated to 50 °C presented in Figure 4.8 was indicative of aggregate formation and the emergence of larger aggregate sub-populations within the sample.

RICS whilst permitting the accurate determination of population distributions (See Appendix 4) and dynamic information, as in the case of fluorescence correlation spectroscopy and dynamic light scattering is unable to resolve monomeric species from small oligomers (i.e. dimers) but may be applied to the determination of aggregate presence on a larger scale (i.e. trimers). Furthermore, as a correlation-based method, RICS cannot be applied to single frame images and requires the acquisition of time series for spatiotemporal mapping of aggregate sub-populations. In the context of real-time assessment of aggregation this presents a challenge to the determination of events and sub-populations at specific time points and requires aliquot removal for the analysis of aggregation at pre-defined time intervals.[15]

Fluorescence intensity histogram-based methods such as SpIDA circumvent the challenges associated with correlation-based image analysis tools (i.e. image correlation spectroscopies) and may be applied to the analysis of single confocal images, hence providing the opportunity for real-time *in situ* assessment of oligomerisation and monitoring changes in particle numbers as a function of time. However, a disadvantage associated with the application of SpIDA is the inability to yield direct dynamic information concerning aggregate formation (i.e. diffusion coefficients) and by virtue of computing oligomerisation from the direct relationship between the quantal brightness of a monomer and oligomer cannot be applied to the assessment of larger aggregate sub-populations (i.e. sub-micron particles).

In summary, image analysis tools (i.e. SpIDA and RICS) offer the potential to non-invasively analyse real-time kinetics and aggregate profiles of analyte using the same image set permitting the quantification of oligomer and particle size distributions over a broad size range. To our knowledge this study is the first report of real-time *in situ* assessment of oligomer formation with confocal imaging and offers the potential for

further exploration in unstable systems with a higher degree of propensity to form reversible soluble oligomers. Furthermore, cross-comparison of data obtained from DLS, FCS, RICS and SpIDA has demonstrated complementary data by all methods, each providing unique information on temporal sample evolution following exposure to thermal stress.

4.6 Conclusion

In this study a combination of SpIDA, RICS, FCS and DLS analysis were utilised to assess BSA aggregate formation ranging from the reversible oligomeric size range up to larger micron-sized particles (i.e. hundreds of microns). Real-time image analysis in this study indicates reversible association of monomeric BSA with a higher extent of monomer loss in higher concentration samples following the exposure of BSA-AF488 to thermal stress at 50 °C. Furthermore, lower concentration samples (i.e. 0.4 mg/mL) exhibited a higher degree of stability to thermal stresses as demonstrated by the reversibility of oligomerisation and a lower concentration of high molecular weight aggregates.

Image analysis tools provide a meaningful and non-invasive tool for the *in situ* assessment of aggregation under various conditions of formulation and environmental stresses ranging from oligomeric self-association of proteins to the formation of larger aggregates (i.e. sub-visible particles). This added advantage renders imaging an appropriate method for assessing samples possessing a broad range of particle size sub-populations in contrast to traditional approaches such as DLS that are unable to differentiate dimers from monomers and susceptible to the influence of dust and larger aggregates on output parameters.

Furthermore, the rapid acquisition of data in the form of confocal images permits the direct real-time acquisition of data in comparison to traditionally-utilised methods such as size exclusion chromatography that may distort the equilibrium of soluble aggregates through their reversal due to dilution effects or the lengthy duration of their separation.

Since oligomer formation is recognised as a principle contributory component to aggregation in biopharmaceutical preparations and neurodegenerative disorders, analysis of real-time oligomerisation with confocal microscopy may prove useful in the

interpretation of the dynamics and equilibria of oligomer formation and subsequent higher order aggregate formation over a broad concentration and particle size range.

4.7 Acknowledgements

The authors would like to thank the University of Manchester Alumni Fund for supporting this project. Many thanks to Marjorie Howard at the University of Manchester Faculty of Life Sciences facility for purification of BSA-AF488 samples.

4.8 References

1. Ahmad B, Winkelmann J, Tiribilli B, Chiti F 2010. Searching for conditions to form stable protein oligomers with amyloid-like characteristics: The unexplored basic pH. Biochimica et Biophysica Acta (BBA) - Proteins and Proteomics 1804(1):223-234.

2. Andrews JM, Roberts CJ 2007. A Lumry-Eyring nucleated polymerization model of protein aggregation kinetics: 1. Aggregation with pre-equilibrated unfolding. Journal of Physical Chemistry B 111(27):7897-7913.

3. Brummitt RK, Nesta DP, Chang L, Chase SF, Laue TM, Roberts CJ 2011. Nonnative aggregation of an IgG1 antibody in acidic conditions: Part 1. Unfolding, colloidal interactions, and formation of high-molecular-weight aggregates. Journal of Pharmaceutical Sciences 100(6):2087-2103.

4. Brummitt RK, Nesta DP, Chang L, Kroetsch AM, Roberts CJ 2011. Nonnative aggregation of an IgG1 antibody in acidic conditions, part 2: Nucleation and growth kinetics with competing growth mechanisms. Journal of Pharmaceutical Sciences 100(6):2104-2119.

5. Brummitt RK, Nesta DP, Roberts CJ 2011. Predicting accelerated aggregation rates for monoclonal antibody formulations, and challenges for low-temperature predictions. Journal of Pharmaceutical Sciences 100(10):4234-4243.

6. Roberts CJ 2003. Kinetics of irreversible protein aggregation: Analysis of extended Lumry-Eyring models and implications for predicting protein shelf life. Journal of Physical Chemistry B 107(5):1194-1207.

7. Sanchezruiz JM 1992. Theoretical analysis of Lumry-Eyring in differential scanning calorimetry Biophysical Journal 61(4):921-935.

8. Speed MA, King J, Wang DIC 1997. Polymerization mechanism of polypeptide chain aggregation. Biotechnology and Bioengineering 54(4):333-343.

9. Li Y, Mach H, Blue JT 2011. High throughput formulation screening for global aggregation behaviors of three monoclonal antibodies. Journal of Pharmaceutical Sciences 100(6):2120-2135.

10. Li Y, Ogunnaike BA, Roberts CI 2010. Multi-variate approach to global protein aggregation behavior and kinetics: Effects of pH, NaCl, and temperature for alpha-Chymotrypsinogen A. Journal of Pharmaceutical Sciences 99(2):645-662.

11. Carpenter JF, Randolph TW, Jiskoot W, Crommelin DJA, Middaugh CR, Winter G Potential inaccurate quantitation and sizing of protein aggregates by size exclusion chromatography: Essential need to use orthogonal methods to assure the quality of therapeutic protein products. Journal of Pharmaceutical Sciences 99(5):2200-2208.

12. Brown CM, Dalal RB, Hebert B, Digman MA, Horwitz AR, Gratton E 2008. Raster image correlation spectroscopy (RICS) for measuring fast protein dynamics and concentrations with a commercial laser scanning confocal microscope. Journal of Microscopy-Oxford 229(1):78-91.

13. Digman MA, Brown CM, Sengupta P, Wiseman PW, Horwitz AR, Gratton E 2005. Measuring fast dynamics in solutions and cells with a laser scanning microscope. Biophysical Journal 89(2):1317-1327.

14. Digman MA, Gratton E 2009. Analysis of diffusion and binding in cells using the RICS approach. Microscopy Research and Technique 72(4):323-332.

15. Godin AG, Costantino S, Lorenzo L-E, Swift JL, Sergeev M, Ribeiro-da-Silva A, De Koninck Y, Wiseman PW 2011. Revealing protein oligomerization and densities *in situ* using spatial intensity distribution analysis. Proceedings of the National Academy of Sciences 108(17):7010-7015.

16. Swift JL, Godin AG, Doré K, Freland L, Bouchard N, Nimmo C, Sergeev M, De Koninck Y, Wiseman PW, Beaulieu J-M 2011. Quantification of receptor tyrosine kinase transactivation through direct dimerization and surface density measurements in single cells. Proceedings of the National Academy of Sciences 108(17):7016-7021.

17. Hamrang Z, Pluen A, Zindy E, Clarke D 2012. Raster image correlation spectroscopy as a novel tool for the quantitative assessment of protein diffusional behaviour in solution. Journal of Pharmaceutical Sciences 101(6):2082-2093.

18. Demeule B, Gurny R, Arvinte T 2007. Detection and characterization of protein aggregates by fluorescence microscopy. International Journal of Pharmaceutics 329(1–2):37-45.

19. Demeule B, Lawrence MJ, Drake AF, Gurny R, Arvinte T 2007. Characterization of protein aggregation: The case of a therapeutic immunoglobulin. Biochimica et Biophysica Acta (BBA) - Proteins & Proteomics 1774(1):146-153.

20. Demeule B, Palais C, Machaidze G, Gurny R, Arvinte T 2009. New methods allowing the detection of protein aggregates A case study on trastuzumab. Mabs 1(2):142-150.

21. McGlynn H. 2009. Modelling drug delivery in *in vitro* 3D cellular assemblies School of Pharmacy and Pharmaceutical Sciences, ed., Manchester: University of Manchester. p 179.

22. Raphael B, Smith IFC 2003. A direct stochastic algorithm for global search. Journal of Applied Maths and Computing 146(2-3):729-758.

23. Rigler R, Mets U, Widengren J, Kask P 1993. Fluorescence correlation spectroscopy with high count rate and low background- Analysis of translational diffusion. European Biophysics Journal with Biophysics Letters 22(3):169-175.

24. Liu J, Andya JD, Shire SJ 2006. A critical review of analytical ultracentrifugation and field flow fractionation methods for measuring protein aggregation. Aaps Journal 8(3):E580-E589.

25. Levi V, González Flecha FL 2002. Reversible fast-dimerization of bovine serum albumin detected by fluorescence resonance energy transfer. Biochimica et Biophysica Acta (BBA) - Proteins and Proteomics 1599(1–2):141-148.

26. Yohannes G, Wiedmer SK, Elomaa M, Jussila M, Aseyev V, Riekkola M-L 2010. Thermal aggregation of bovine serum albumin studied by asymmetrical flow field-flow fractionation. Analytica Chimica Acta 675(2):191-198.

27. Lin VJC, Koenig JL 1976. Raman studies of bovine serum albumin. Biopolymers 15(1):203-218.

28. Mahler H-C, Friess W, Grauschopf U, Kiese S 2009. Protein aggregation: pathways, induction factors and analysis. Journal of Pharmaceutical Sciences 98(9):2909-2934.

29. Raj T, Flygare WH 1974. Diffusion studies of bovine serum albumin by quasielastic light scattering. Biochemistry 13(16):3336-3340.

30. Berne JB, Pecora R. 2000. Model systems of spherical molecules. In Berne JB, Pecora R, editors. Dynamic light scattering with applications to chemistry, biology and physics, ed., New York: Dover Publications.

Chapter 5

QUANTIFICATION AND ANALYSIS OF P-GLYCOPROTEIN EXPRESSION AND INHIBITION USING LIVE CELL IMAGING

Quantification and Analysis of P-glycoprotein Expression and Inhibition Using Live Cell Imaging

Zahra Hamrang,[1] Egor Zindy,[2] David Clarke[1, 2] and Alain Pluen[1]

1. *School of Pharmacy and Pharmaceutical Sciences, University of Manchester, UK*
2. *Centre of Excellence in Biopharmaceuticals, Faculty of Life Sciences, University of Manchester, UK*

5.1 Abstract

P-glycoprotein, is implicated in clinical drug resistance thus research efforts to date have focused on the quantitative analysis of its activity and expression in a diversity of samples utilising a combination of biochemical assays, proteomics and qualitative bio-imaging.

In this study, the application of image analysis tools to the assessment of p-glycoprotein expression and inhibition was investigated in multiple cell lines. Time and concentration-dependent intracellular retention of Calcein as a consequence of p-glycoprotein inhibition in the presence of verapamil was assessed in MDCK-*MDR1* cells using live cell imaging.

Intercellular heterogeneities and differences in the sub-cellular expression of the p-glycoprotein transporter between wild type and *MDR1*-transfected MDCK cell lines are indicated in this study. Furthermore, the influence of polarisation and differentiation on the expression of p-glycoprotein was assessed in Caco-2 cells demonstrating preferred apical distribution and a two-fold difference in expression from days 10 to 29 post-seeding.

In conclusion imaging possesses the ability to detect inherent intercellular heterogeneities and in conjunction with immunofluorescence staining may be applied to the analysis of biopsies providing a rapid prognostic tool. With the current ever-expanding availability of automated confocal setups the potential exists to enable high-throughput screening of p-glycoprotein inhibition using microscopic approaches, whilst performing concurrent *in vitro* assays of intracellular processes and cell viability.

Keywords: P-glycoprotein; Immunofluorescence; Calcein-AM; Spatial intensity distribution analysis; Imaging.

5.2 Introduction

P-glycoprotein, a member of the ATP-binding cassette transporter family, is a 170 kDa transmembrane protein encoded by the mdr-1 gene and by virtue of its evolutionary role in the active extrusion of xenobiotics as a protective mechanism, is responsible for the efflux of a large number of structurally and functionally diverse drug candidates. Abundant expression of p-glycoprotein in the gastrointestinal lumen epithelia[1] and endothelia of the blood-brain barrier (BBB)[2], both major target sites for drug absorption, ultimately modulates the disposition of a drug candidate. Historically, the presence of elevated p-glycoprotein expression at the BBB and in tumours has been associated with a poor clinical prognosis, necessitating further studies into the expression of this trans-membrane protein, its activity, co-administration of compounds that inhibit p-glycoprotein activity[3] and the discovery of novel therapeutics for a diverse range of pathologies.[2]

5.2.1 Quantification of P-glycoprotein Expression

To date confirmation and subsequent quantification of antigen expression in various tissues and cell lines has been performed using a number of analytical approaches ranging from western blots[4], polymerase chain reaction (PCR)[4,5], tissue microarrays[6,7], immunohistochemistry, flow cytometry[8], enzyme-linked immunosorbent assays (ELISA), and immunofluorescence staining[9,10] to variants of mass spectroscopy, in some instance coupled to chromatography and other separation technologies.[11,12,13] However, despite advances in tissue mass spectrometry and microarrays, the routine methods applied by the clinician entail standard molecular biology approaches exemplified by blotting, PCR, immunohistochemistry, flow cytometry and high quality imaging of fluorescently-stained samples extracted from tumour biopsies.

Characterisation of protein expression and localisation using quantitative immunofluorescence staining (QIF) has been reported by clinicians over recent years due to a higher degree of sensitivity and reliability coupled to direct visualisation of the protein of interest within the biopsy. Image analysis extensions exemplified by MetaMorph® and Adobe Photoshop[8,10] characterise the pixel fluorescence intensity of the labelled species of interest from acquired confocal images, as a direct link exists between the quantity of antigen expression and staining intensity of the labelled protein.[14]

5.2.2 Assays of P-glycoprotein Activity

The p-glycoprotein transporter is viewed to be responsible for various clinically relevant drug-drug interactions resulting in low bioavailability or toxicity as a consequence of efflux reversal through the inhibition of p-glycoprotein activity (e.g. quinidine and digoxin) or up-regulation of MDR1 expression (e.g. rifampin and digoxin), respectively.[15] The implication of p-glycoprotein activity in adverse effects associated with drug-drug interactions has warranted recommendations from the FDA that newly discovered drugs are categorised according to the nature of their interaction with the p-glycoprotein efflux transporter as substrates, inducers or inhibitors in order to facilitate the prediction of any potential drug-drug interactions which are of particular significance to cases where poly-pharmacy occurs.[16,17]

As the aforementioned inhibition of p-glycoprotein induced efflux has been implicated in drug-drug interactions and adverse drug reactions (toxicity) induced by intracellular accumulation, the development of approaches to determine the substrate or inhibitory activity of a multitude of xenobiotics is essential.

5.2.2.1 In vitro Assays

A range of assays have been developed over recent decades in an attempt to characterise agents as either p-glycoprotein substrates or inhibitors that enable high-throughput screening of drug candidates using either fluorimetric (i.e. the rhodamine-123 assay or Calcein-AM assay) or colorimetric approaches (i.e. the ATPase assay).[18,19] The monolayer efflux assay assessing the efflux ratio of basolaterally and apically transported drug or dye (sometimes in combination with dye-based assays) has been utilised routinely in the assessment of p-glycoprotein activity. A summary of the routine techniques and aspects concerning their application has been presented in Table 5.1.

Table 5.1 *A summary of p-glycoprotein functional assays, including the type of activity and parameter measured.*[20-22]

Assay	Activity	Analytical Requirements	Throughput
ATPase[19,23-25]	Substrate (ATPase stimulation)	Absorbance	High
Calcein-AM[25-28]	Inhibitor	Fluorescence	High
Rhodamine[29-31]	Inhibition	Fluorescence	High
Monolayer efflux[25,32]	Passage (Efflux ratio)	Fluorescence; LC-MS/MS; Radioactivity; Absorbance.	Medium to low
In vivo **(PD-PK)**[32]	Barrier penetration	Fluorescence; Absorbance; Radioactivity; LC-MS/MS.	low

Fluorometric Assays

Several studies conducted over the past few decades have reported fluorometric assays utilising either Calcein-AM[26,33] or Rhodamine 123[29,30] for the assessment of p-glycoprotein inhibition in a diversity of cell lines and in the presence of numerous inhibitors.[34] IC_{50} values have been determined from multiple p-glycoprotein inhibition assays in several human and porcine MDR-1 expressing cell models. Conflicting results in such studies concern the nature of drug interaction with the p-glycoprotein transporter and have resulted in the conclusion that no single assay or approach is appropriate for the classification of substances as substrates, inducers or inhibitors of p-glycoprotein activity.[20-22]

ATPase Assay[35] P-glycoprotein-induced substrate transport is associated with ATP hydrolysis following the recruitment of active transport pathways, when the concentration of released inorganic phosphate associated with ATPase activity can be measured colorimetrically.

Monolayer Efflux A comparison of the efflux ratio obtained from the passage of substances through monolayers of MDR1-transfected MDCK cells relative to wild-type cells is a routine approach in the determination of the modulatory role of compounds. In this approach radioactive or fluorometric assays may be used to determine the efflux of dyes or labelled tracer compounds through the monolayer model. However, monolayer studies are time consuming and high-throughput fluorometric and ATPase assays are preferred in the rapid screening of compounds. [35]

In Vivo Assays In addition to the *in vitro* assays described above, animal models have been considered to assess the impact of p-glycoprotein efflux on the pharmacokinetics of p-glycoprotein substrates in knockout animal models.[5] An account of *in vivo* p-glycoprotein assays is not within the scope of this work.

5.2.3 Spatial Intensity Distribution Analysis (SpIDA)

Reports of SpIDA were published by Godin *et al* in 2011 for application to the characterisation of protein oligomerisation densities and the software is available for download from *http://www.neurophotonics.ca/en/tools/software*.[36,37] The technique is based on the super-Poissonian fitting of fluorescence intensity histograms determined

from confocal images and yields quantitative parameters concerning the number of fluorescent moieties present (per beam area) and their corresponding molecular brightnesses. SpIDA analysis may subsequently be applied to determining local concentrations of fluorophores within a defined volume.

To this end we report the application of spatial intensity distribution analysis (SpIDA) as a novel image analysis approach. Routine quantitative immunofluorescence of p-glycoprotein transporter expression (i.e. in *MDR1*-MDCK, *wild type*-MDCK and Caco-2) was carried out by MetaMorph®.

5.3 Materials and Methods

5.3.1 Materials

Reagents and Cell Lines Goat anti-mouse IgG-Alexa Fluor® 488, DAPI, (3-(4, 5-Dimethylthiazol-2-yl)-2, 5-diphenyltetrazolium (MTT) and all cell culture reagents were obtained from Invitrogen (Paisley, UK). Verapamil, Hank's Balanced Salt Solution (HBSS), para-formaldehyde, phosphate-buffered saline (PBS) and primary monoclonal mouse anti-p-glycoprotein antibody were purchased from Sigma (Dorset, UK). Calcein-AM was purchased from Cambridge Biosciences (Cambridge, UK). Wild type (*wt*) and *MDR1*-transfected Madin-Derby Canine Kidney cells (MDCK) were obtained from the Netherlands Cancer Institute and used under terms of their material transfer agreement (Amsterdam, The Netherlands).

5.3.2 Methods

5.3.2.1 Cell Culture and Sample Preparation

MDCK-*MDR*1 (passages: 8-18), MDCK-*wt* (passages 10-20) and Caco-2 (passage 27) cells were cultivated in DMEM growth medium supplemented with 10% *v/v* Foetal Bovine Serum, HEPES buffer, 1% *v/v* L-glutamine (200 mM), and 100 *iu*/mL streptomycin and penicillin. Cells were cultivated and maintained in T-75 flasks till 70-80% confluency was achieved. Trypsinisation was performed in order to detach cells and was followed by subsequent re-cultivation or sample preparation. Fresh growth medium was added on alternate days and all cell lines were split twice weekly.

P-glycoprotein (i.e. MDR1) expression and function were assessed in MDCK-*MDR1* and MDCK-*wt* cells prior to p-glycoprotein inhibition studies. All cells were seeded onto Lab-Tek Nunc® eight-well chamber slides (Fisher Scientific, Leicestershire, UK) at a density of 10^5 cell/mL and incubated for 24 hours at 37 °C in a pre-humidified atmosphere containing 5% *v/v* CO_2.

The influence of polarisation and differentiation of Caco-2 monolayers on the quantity and localisation of MDR1 expression was assessed by seeding a density of 2.2 x 10^5 cells/cm^2 on 0.4 µm pore-sized polycarbonate filters (effective surface area of 0.33 cm^2) and the abundance of p-glycoprotein assessed on days 10, 16 and 21.

5.3.2.2 Immunofluorescence Staining

Slides and monolayers cultivated into Transwells® were rinsed three times with PBS and fixed with 4% *w/v* paraformaldehyde for 15 minutes, followed by a 10 minute incubation with ammonium chloride to saturate aldehyde reactivity. Subsequently, permeabilisation of the monolayers was performed with 0.2% *v/v* Triton X-100 in PBS for 15 minutes and blocked with a 1% *w/v* BSA in PBS solution for 30 minutes. The pre-diluted (1:250) primary antibody (Sigma, Loughborough, Leicestershire) was applied for one hour at room temperature and excess primary antibody removed with triplicate PBS rinses. Immunofluorescence samples were incubated with an anti-mouse secondary Alexa Fluor® 488-labelled IgG antibody for one hour (Molecular probes, Oregon, USA). In the case of negative controls, no primary antibody was added. Immunofluorescently stained samples were further rinsed and incubated with DAPI (i.e.

0.5 µg/mL) for 30 minutes prior to visualisation with a Zeiss LSM 510 confocal microscope (Zeiss, Jena, Germany).

5.3.2.3 Quantitative Live Cell Imaging of Intracellular Calcein Accumulation and Assessment of P-glycoprotein Expression

Live cell imaging was performed on samples seeded onto a eight-well chamber slide with a Zeiss LSM510 confocal laser scanning microscope equipped with a c-Apochromat 40 x/NA 1.2 water-immersion objective. Alexa Fluor® 488-labelled p-glycoprotein transporters and intracellular Calcein were excited using the Argon laser at 488 nm and the emitted light collected following passage through a bandpass filter (505-530 nm). Single frame and *z*-stack images were captured with a corresponding pixel size of 44 nm, a pixel time of 3.2 µs and a resolution of 1024 x 1024 pixels.

For monolayer experiments, MDCK-*MDR1* and *wt* cells were seeded onto eight well chamber slides (Fisher Scientific, Leicestershire, UK) and incubated in a pre-humidified atmosphere at 37 °C for 48 hours prior to visualisation with confocal microscopy.

All experiments were performed in a thermostatically controlled environment of 21°C over multiple fields of vision (n=10) for each sample to ensure collation of statistically significant data. Confocal imaging of immunofluorescently-labelled samples was performed using the setup described above for intracellular Calcein retention studies. In addition, DAPI was excited by a halogen lamp at 350 nm and emitted light collected at 470 nm with the same image resolution settings described above (i.e. pixel size of 44 nm and pixel dwell time of 3.2 µs).

Further information on the methodology involved in the calibration of the optical setup used here in order to correct for PMT shot noise effects and measurement of the laser beam waist are shown in Appendix 1.

5.3.2.4 SpIDA Analysis

Analysis of images with SpIDA was performed on all immunofluorescence and intracellular Calcein images using the approach described by Godin *et al* .[37] The density per beam area (of Calcein and labelled MDR1) was determined as output for all regions of interest in confocal images and applied to the determination of population distributions, intercellular heterogeneities and cross-sectional differences (i.e. along the *z*-axis) in *z*-stack images.

Fitting super-Poissonian distributions of fluorescence intensity histograms determined from confocal image pixel fluorescence intensities forms the basis of SpIDA analysis. Parameters obtained from this analysis include quantal brightness (QB) and density per beam area (i.e. number of fluorescent moieties defined within a specified region) following the selection of a region of interest (ROI). Histograms are determined from calculating all the possible configurations in which a fluorescent entity may reside in a point spread function-defined region. Following weighted calculations of each configuration and its respective probability assuming a Poisson distribution for *N* particles inside the PSF, the fitting function applied to determination of the final histogram is expressed as [37-39];

$$H(\varepsilon, N; k) = \Sigma_n \rho^n(\varepsilon; k) Poi(n, N) \text{ with } \rho^0(\varepsilon; \kappa) = \delta_{k,0} \qquad \textit{Equation 5.1}$$

Where H is the histogram fitting function that is normalised so that the integral over κ equals unity. ε represents the molecular quantal brightness, N the number of particles within the PSF, ρ^n the probability of observing an intensity of light of κ (assuming proportionality to the number of emitted photons) by n particles of ε brightness.

5.3.2.5 Quantification of the Integrated Fluorescence Intensity

Confocal images captured from immunofluorescence images were subjected to analysis of fluorescence intensity using Image J® (NIH, Bethesda) that entailed importing images into Image J® following blind three-dimensional deconvolution of *z*-stacks in AutoDeblur® (AutoQuant Inc., New York, USA). The brightest field was initially selected for analysis followed by calibration of distances, application of a median filter, thresholding of the images and subsequent analysis of the integrated fluorescence

intensity profile over a specified thresholded area. This process was performed on all images acquired to enable comparison of fluorescence intensity data.

5.3.2.6 Statistical Analysis

Unless otherwise stated all datasets were subjected to analysis of variance testing (i.e. with a $P < 0.05$).

5.4 Results

5.4.1 Confocal Images of Immunofluorescence P-glycoprotein Staining

Immunofluorescently-labelled images of MDCK-*MDR1* and MDCK-*wt* were both found to contain p-glycoprotein transporters (See Figure 5.1). Additionally, higher resolution images (i.e. 44 nm pixel size) were used to allow the determination of fluorescently-labelled p-glycoprotein densities using SpIDA analysis at a higher resolution.

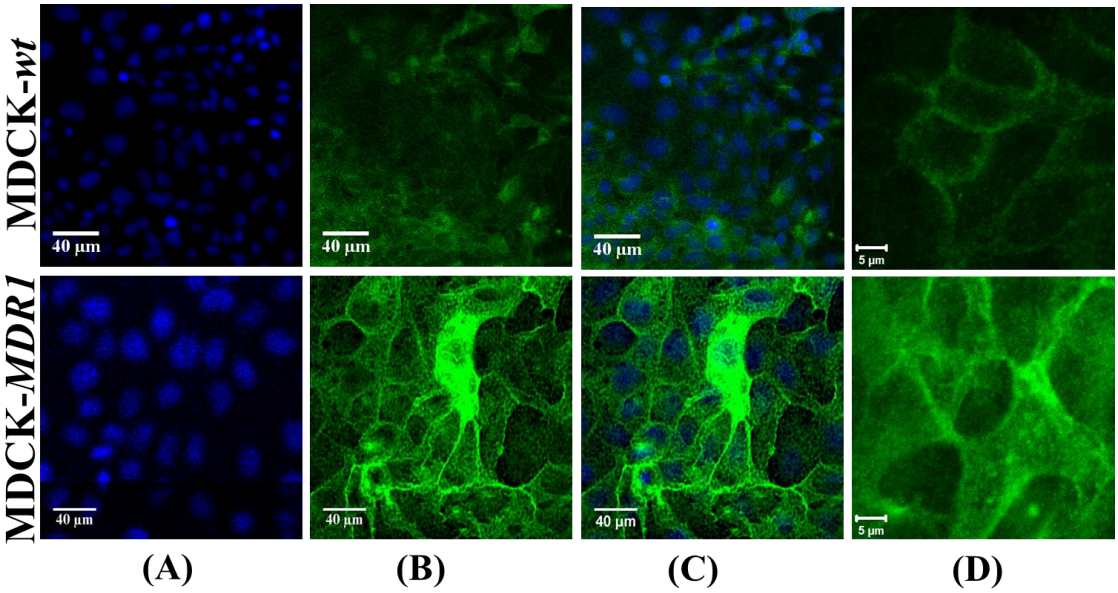

Figure 5.1 *Typical confocal images obtained from p-glycoprotein labelling* ***(A)*** *of MDCK-MDR1 and MDCK-wt cell lines counterstained with DAPI* ***(B)****, resultant composite images* ***(C)*** *and high resolution 1024 x 1024 pixel images obtained with a corresponding pixel size of 44 nm and a pixel dwell time of 3.2 µs* ***(D)****.*

P-glycoprotein (MDR1) was expressed at a higher level in the MDR1-transfected cell line in comparison to the heterogeneous expression of the wild type images (See Figure 5.1). Confocal micrographs of labelled MDR1 transporters also demonstrate the intracellular distribution of p-glycoprotein transporters in both cell lines.

The expression of p-glycoprotein was assessed in Caco-2 cells cultivated on Transwells® in order to ascertain changes in transporter expression as a function of differentiation over a 29 day period to enable comparison with the documented literature. Representative confocal images acquired from immunofluorescently-labelled samples at days 10, 16 and 29 are presented as follows;

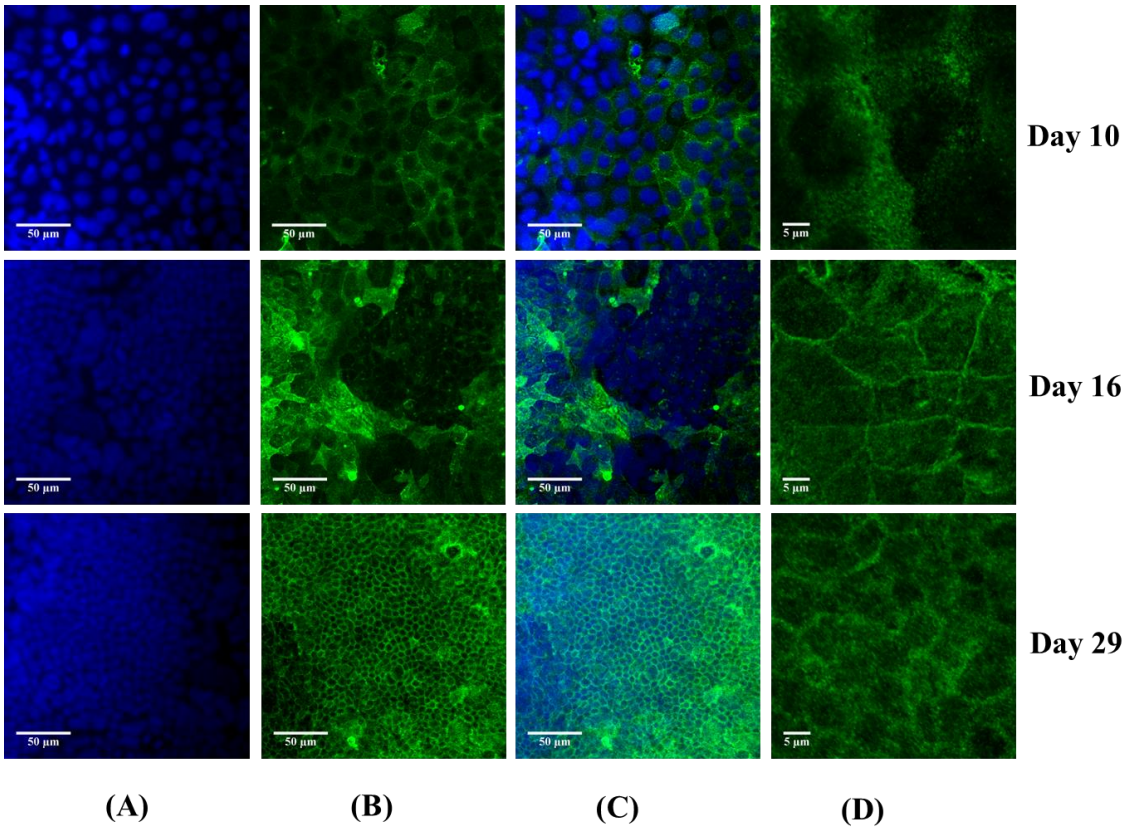

Figure 5.2 *Typical confocal images obtained from p-glycoprotein labelling Caco-2 cells with a DAPI nuclear stain* ***(A)*** *labelled p-glycoprotein transporters* ***(B)*** *resultant composite images* ***(C)*** *with a pixel size of 220 nm and high resolution 1024 x 1024 pixel images obtained with a corresponding pixel size of 44 nm and a pixel dwell time of 3.2 µs* ***(D)***.

An increase in p-glycoprotein expression with time was observed (See Figure 5.2) as Caco-2 monolayers polarise and differentiate with changes in the intracellular distribution as the cell morphology evolves (i.e. a reduction in the size of nuclei and cells). In order to assess the polarised expression of p-glycoprotein transporters, *z*-stack images of the monolayers were also acquired and subjected to both SpIDA analysis and routine quantitative immunofluorescence characterisation.

For all Caco-2, MDCK-*MDR1* and MDCK-*wt* immunofluorescence samples, negative staining was also performed to rule out possible bleeding, autofluorescence and non-

specific labelling (See Appendix 5). Results obtained from the negative staining of immunofluorescence images revealed no contributions due to autofluorescence or bleeding.

5.4.2 Quantification of P-glycoprotein Expression Using Quantitative Immunofluorescence and SpIDA Analysis

5.4.2.1 Comparison of MDCK-MDR1 and MDCK-wt Cell Lines

SpIDA analysis of high resolution images (i.e. 44 nm pixel sizes) was performed on confocal immunofluorescence images acquired from MDCK-*wt* and MDCK-*MDR1* cell lines. The subsequent probability and histogram fit obtained from analysis of cell populations is presented in Figure 5.3 below.

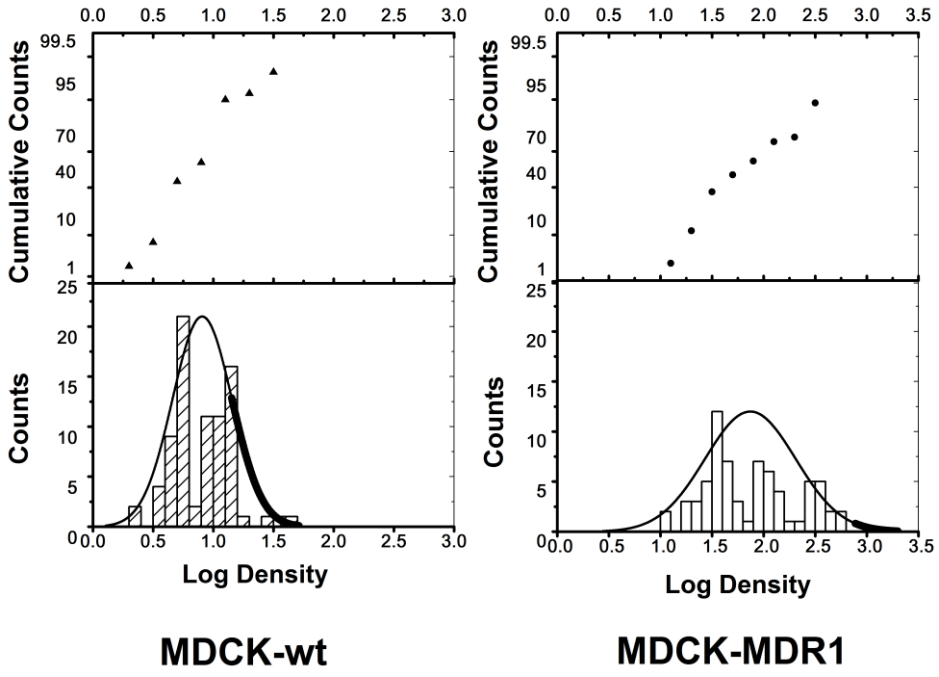

Figure 5.3 *Representative histogram and probability plot of p-glycoprotein log density values obtained from SpIDA analysis of MDCK-wt (left) and MDCK-MDR1 (right) cell lines for images with a corresponding pixel size of 44 nm and pixel dwell time of 3.2 µs. Ranges obtained from the analysis of immunofluorescence images were 5.4 < 7.9 < 12.6 and 35.5 < 74.1 < 144.5 for MDCK-wt and MDCK-MDR1 cells, respectively (n=70).*

The brightest plane in focus was selected for immunofluorescently-labelled MDCK cells when performing confocal microscopy. Probability and histogram plots demonstrate a normal distribution for the density data (i.e. labelled p-glycoprotein) such that ranges of 5.4 < 7.9 < 12.6 for MDCK-*wt* and 35.5 < 74.1 < 144.5 (log normal mean ± st. dev. MDR1 per beam area) were obtained for MDCK-*MDR1* cell lines (thick solid

lines represent data points for which there are no corresponding values on the histogram). Ranges obtained from the SpIDA analysis of both cell lines demonstrated baseline expression of p-glycoprotein in the wild-type cell line with a more widespread and higher extent of expression in the transfected cell line (i.e. MDCK-*MDR1*) as reflected by images presented in Figure 5.1 and representative population data shown in Figure 5.3. Furthermore, the performance of an ANOVA single factor test indicated a statistically significant difference between the datasets obtained from the analysis of the two cell populations ($P < 0.05$).

Standard quantitative immunofluorescence quantification in Image J® was performed using the procedure described by Hector *et al.* in *z*-stacks images through determining the number of nuclei and subsequent division of integrated density values following thresholding by the number of cells (i.e. nuclei).[40] Both SpIDA analysis and integrated fluorescence density measurements were performed in *z*-stack images acquired from immunofluorescently-labelled MDCK-*MDR1* and MDCK-*wt* cell lines. Representative data obtained from the analysis of these images are presented in Figure 5.4.

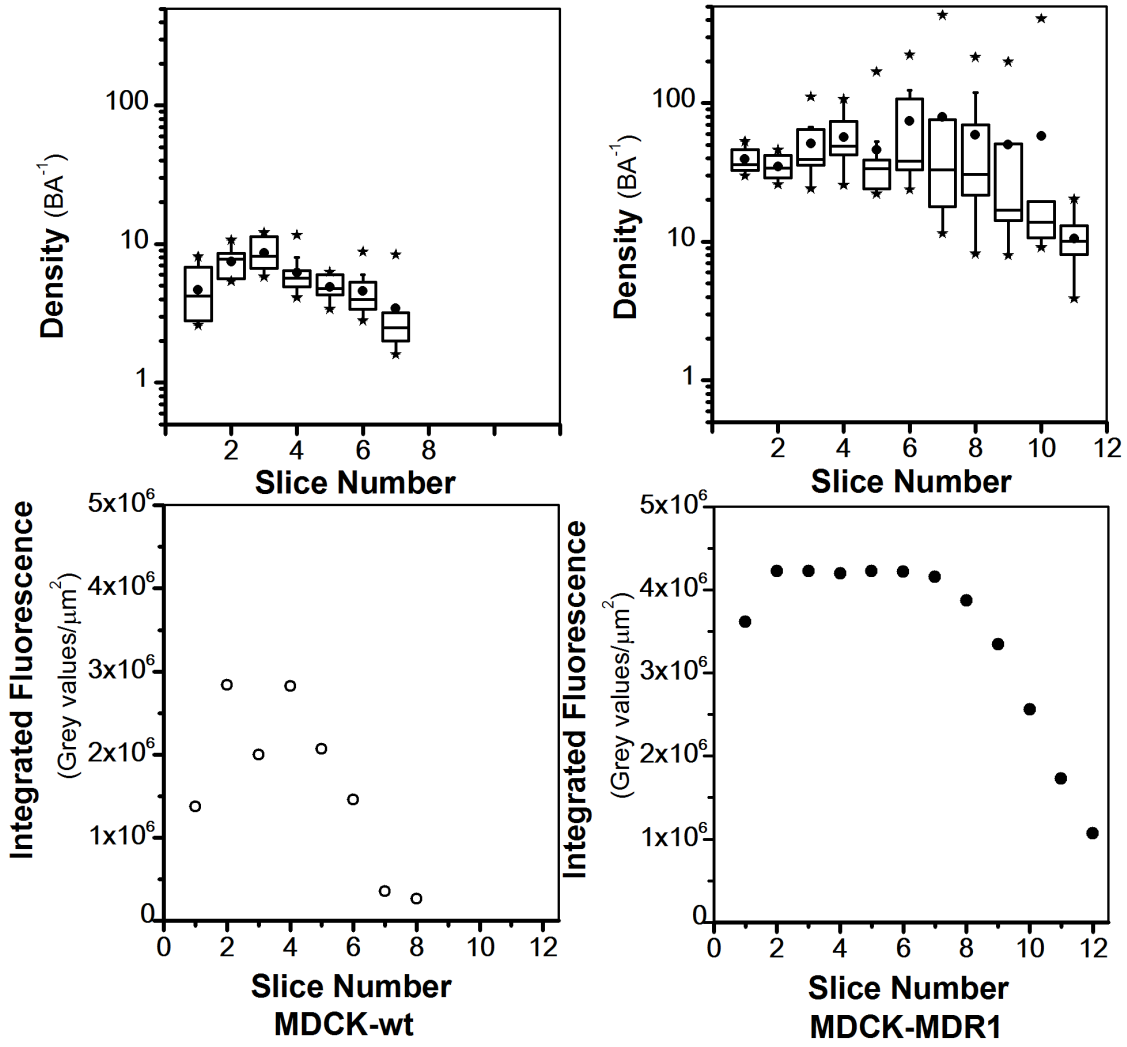

Figure 5.4 *Box and whisker plot of density data obtained from the SpIDA analysis of MDCK-wt and MDCK-MDR1 cells (top) and the corresponding corrected integrated density (Grey values per µm^2) across a z-stack image with a corresponding pixel size of 220 nm (bottom).*

Data presented in Figure 5.4 indicates a higher degree of MDCK-*MDR1* expression in comparison to MDCK-*wt* cells across the monolayer cross-section. No apparent polarity was observed in the abundance of labelled p-glycoprotein transporters following both SpIDA and routine integrated density analysis of *z*-stacks.

5.4.3 The Assessment of Changes in P-glycoprotein Expression in Caco-2 Cells with Time

The influence of polarisation and differentiation on the expression of p-glycoprotein transporters was assessed in Caco-2 cells cultivated onto Transwell® support filters. Representative samples were removed on days 10, 16 and 29 and subjected to immunofluorescence labelling. Subsequently both single and *z*-stack confocal images

were subjected to analysis using SpIDA. Representative histograms demonstrating changes in population data for each day are presented in Figure 5.5.

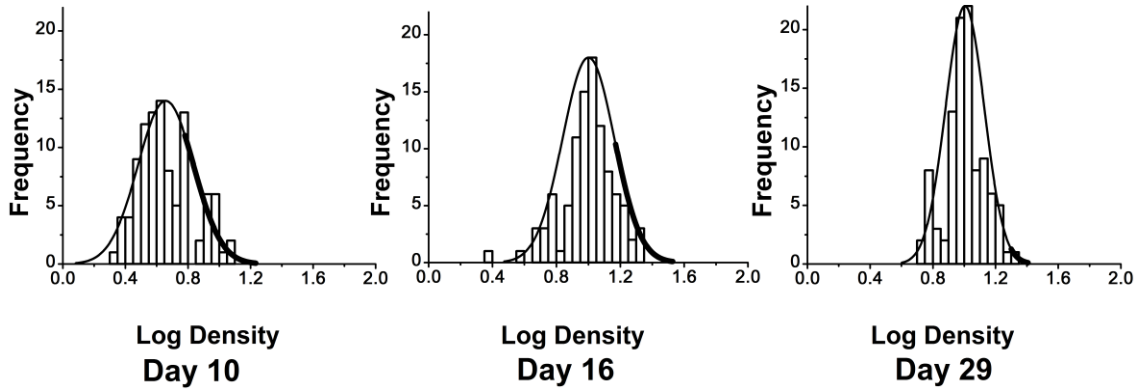

Figure 5.5 *Log Density histograms obtained of immunofluorescently-labelled MDR1 transporters following the analysis of 1024 x 1024 pixel images (pixel size 44 nm) acquired in Caco-2 monolayers cultivated on Transwells® up to 29 days. The solid line on the histogram represent regions for which there were no corresponding values.*

The histograms of MDR1 densities per beam area for two-dimensional confocal images acquired from samples stained on the specified days (i.e. 10, 16 and 29) yielded density ranges (MDR1 per beam area) of $3.5 < 4.5 < 5.9$ for day 10 samples, $8.4 < 10 < 12.5$ for day 16 samples and $8.9 < 10 < 12$ for day 29 samples. An increase in p-glycoprotein expression from day 10 to 16 was indicated, with no overall change in the determined densities up to day 29. This observation was further supported with an ANOVA test that confirmed a statistically significant difference between densities obtained at day 10 and that of days 16 and 29, however, no statistically significant difference was noted between abundances determined for days 16 and 29 ($P< 0.05$). To further probe the localisation and expression of p-glycoprotein transporters, *z*-stack images acquired from each sample were subjected to quantitative immunofluorescence and SpIDA analysis, the results of which are presented in Figure 5.6 as follows;

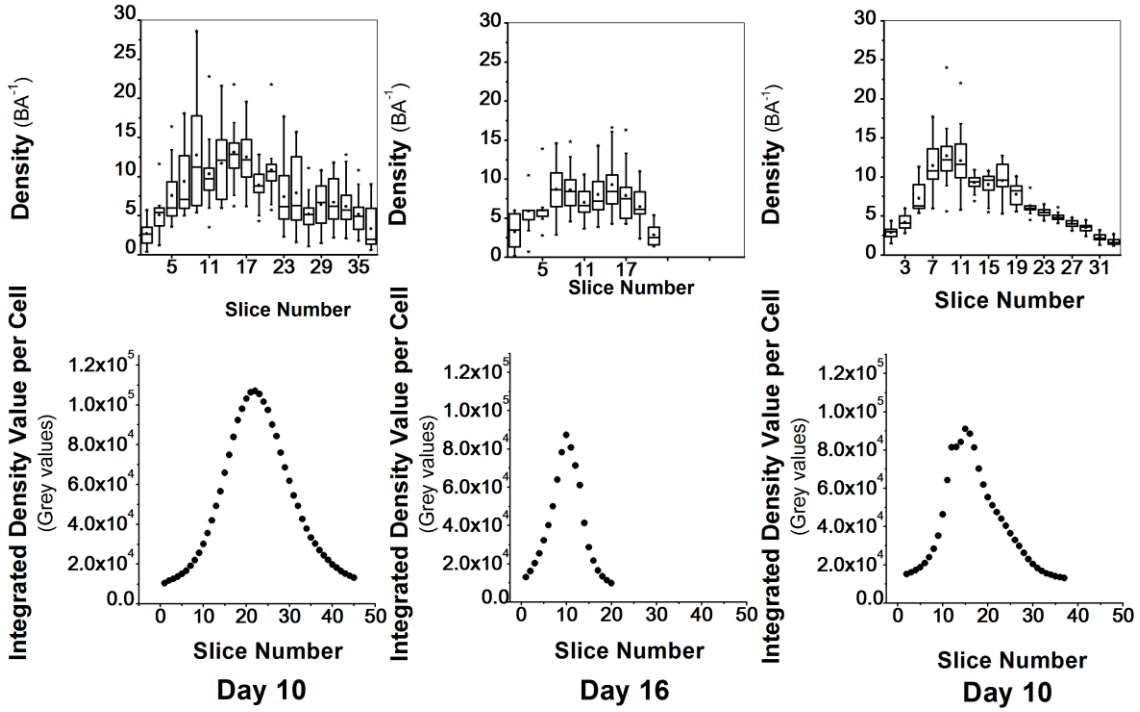

Figure 5.6 *Heterogeneity of MDR1 expression in the z-plane- Box and whisker plots of density per beam area were determined from SpIDA analysis moving from the apical to basolateral section (top) and corresponding integrated density values per cell computed using image J® (bottom) following the analysis of 1024 x 1024 pixel z-stack images of immunofluorescence images.*

Results presented in Figure 5.6 indicate a broad heterogeneity in MDR1 expression in the day 10 sample (in all slices) as reflected by the large apparent range (and error bars) in the box and whisker plot and no polarisation in the distribution of MDR1 displayed in the integrated density value plot. Later samples revealed a reduction in the density ranges and the appearance of polarity in expression with differentiation as shown by a reduction in the range displayed in the box and whisker plots and the preferred apical distribution shown in the plot of integrated density values such that by day 29 the magnitude of the error bars is significantly reduced in the basal direction (i.e. preferred apical localisation). In comparison to the data obtained from IDV analysis, box and whisker plots of MDR1 densities were able to demonstrate intercellular and cross-sectional heterogeneities in expression more clearly than routine IDV measurements.

5.4.4 Live Cell Imaging of Intracellular Calcein Retention

5.4.4.1 Changes in Intracellular Calcein As a Function of Time in the Absence of Inhibitor

Confocal micrographs shown in Figure 5.7 were captured of MDCK-*MDR1* and MDCK-*wt* cells incubated to various time point with 100 nM Calcein-AM that were subsequently rinsed and replaced with fresh HBSS prior to visualisation. Little uptake of Calcein-AM and retention in the MDCK-*MDR1* cell line was observed compared to the MDCK-*wt* cells.

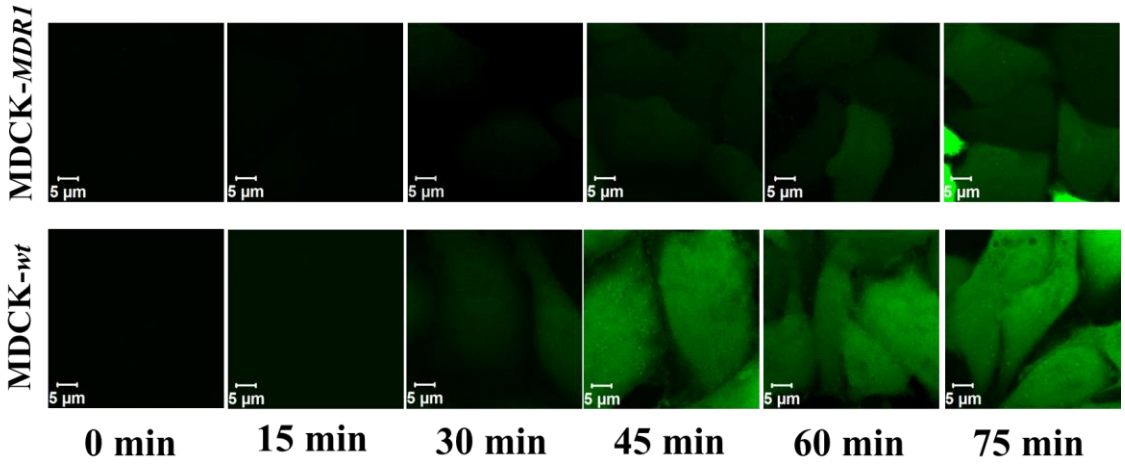

Figure 5.7 *Confocal micrographs of 1024 x 1024 pixel resolution with a corresponding pixel size of 44 nm acquired of Calcein retention in MDCK-wt (top) and MDCK-MDR1 (bottom) cells incubated to the desired time points with 100 nM Calcein-AM.*

Images presented above demonstrate little uptake of Calcein-AM and retention of Calcein in the MDCK-*MDR1* cell line in comparison to MDCK-*wt* cells. This was further assessed with quantification of fluorescence intensity data obtained from multiple fields of views and SpIDA assessment of intracellular Calcein densities.

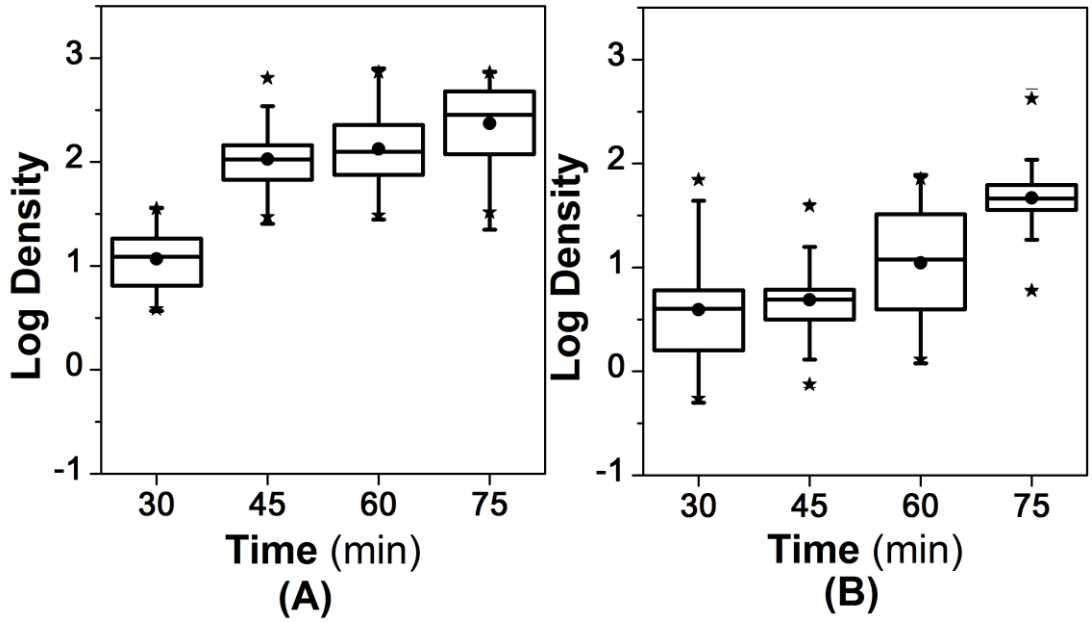

Figure 5.8 *Box and whisker plot of intracellular Calcein in MDCK-wt* ***(A)*** *and MDCK-MDR1* ***(B)*** *cells as a function of time determined from the analysis of 44 nm pixel images acquired from samples incubated with 100 nM Calcein-AM to the desired time point in the absence of inhibitor (n=10).*

Analysis of images acquired in the absence of verapamil revealed broader regional heterogeneity in MDCK-*MDR1* cells in comparison to MDCK-*wt* cells up to 75 minutes (no detectable fluorescence was observed in 15 minute samples and typical densities obtained from SpIDA analysis from subcellular regions yielded density values of zero). Performance of an ANOVA test ($P < 0.05$) indicated a statistically significant difference between the mean densities obtained at each time point and the two cell lines examined.

5.4.4.2 Intracellular Accumulation of Calcein as a Function of Time and Inhibitor Concentration

Confocal images presented in Figure 5.1 as well as quantification in Figure 5.3 indicate p-glycoprotein expression in both MDCK-*wt* and MDCK-*MDR1* cells examined with an apparent higher expression in MDR1-transfected cells and more widespread cytoplasmic localisation in comparison to MDCK-*wt* cells known to possess baseline p-glycoprotein activity. The functionality of the p-glycoprotein transporter and its inhibition in the presence of a known inhibitor (i.e. verapamil) was also assessed in confocal images obtained from both cell lines as a function of time and concentration of verapamil. Representative images obtained from the live cell imaging of Calcein retention following co-incubation with specific concentrations of inhibitor (i.e. 2.5, 5, 10, 20 and 50 μM) is presented in Figure 5.9 for MDCK-*MDR1* cells.

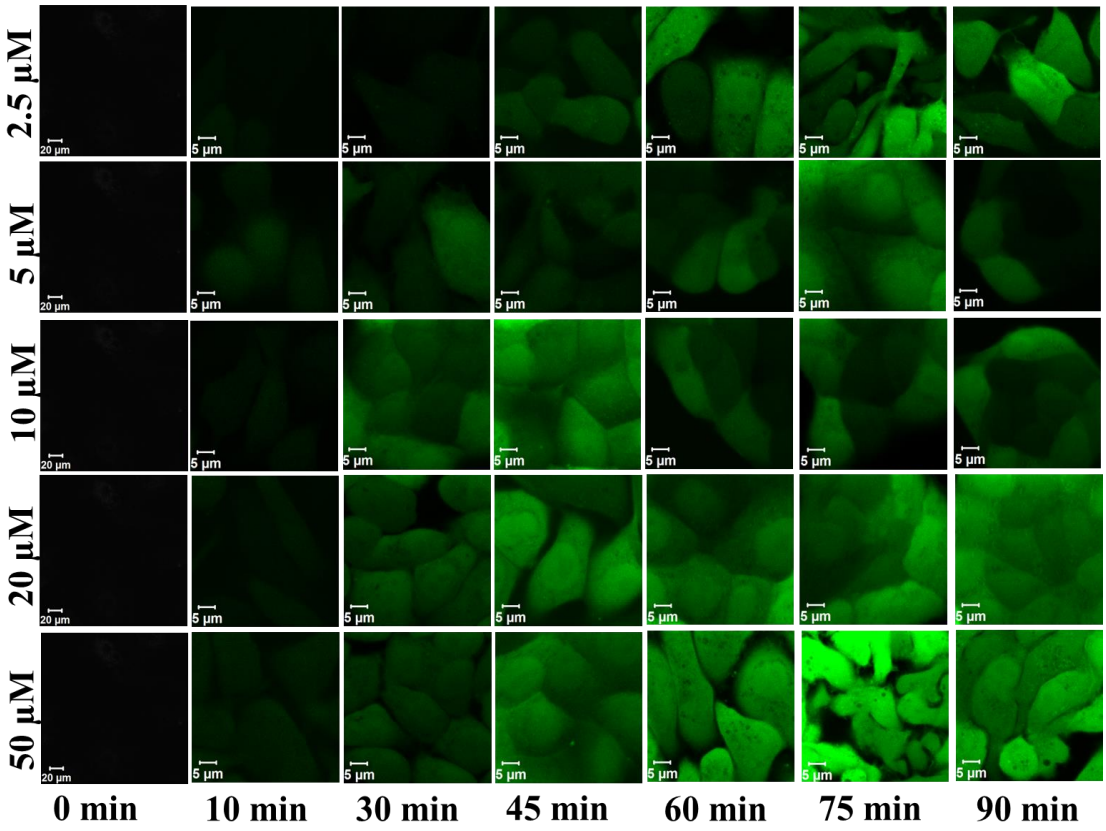

Figure 5.9 *Representative 1024 x 1024 pixel confocal images of intracellular retention of Calcein as a function of incubation time and concentration of verapamil in MDCK-MDR1 cells with a corresponding pixel size of 44 nm.*

The images presented demonstrate time-dependent uptake of Calcein-AM into *MDR1* cells and broad intercellular and subcellular heterogeneity is also apparent among cells within a field of view. Furthermore, concentration dependent behaviour was evident, such that at lower concentrations of verapamil (i.e. 2.5 and 5 µM) a lower apparent intensity was evident across all the time points with no visible fluorescence occurring till the 30 minute time point. Confocal images obtained from the intracellular retention of Calcein for the wild-type cell line are presented in Figure 5.10.

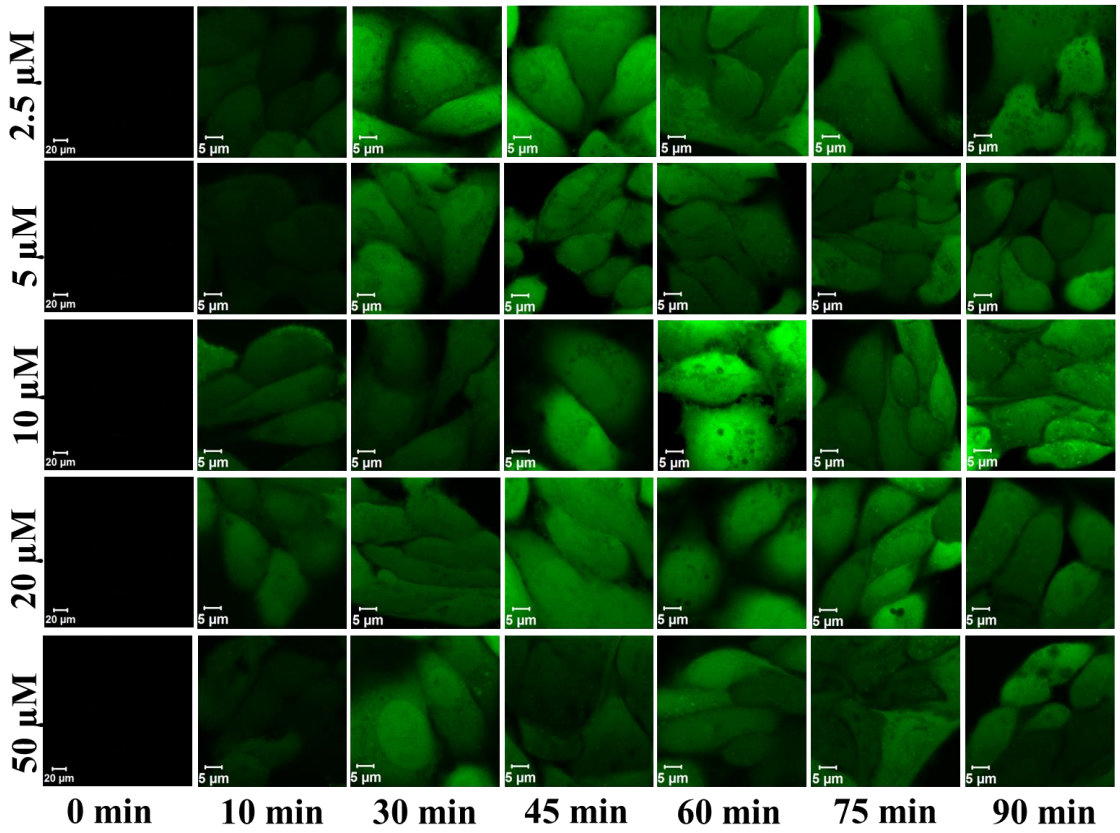

Figure 5.10 *Representative 1024 x 1024 pixel confocal images of intracellular retention of Calcein as a function of incubation time and concentration of verapamil in MDCK-wt cells with a corresponding pixel size of 44 nm.*

Similarly, in MDCK-*wt* cells time-dependent uptake of Calcein was observed across all concentrations of verapamil, but with very little differences between cell lines incubated with various concentrations of verapamil and a more rapid change in fluorescence at earlier time points.

To further examine any differences between the cell lines and within cell populations, SpIDA analysis were performed.

5.4.4.3 SpIDA Analysis of Time and Inhibitor Concentration Effects in MDCK-MDR1 and MDCK-wt Cell Lines

Intercellular and sub-cellular heterogeneities in Calcein-AM uptake and Calcein retention were assessed through the analysis of multiple ROIs (i.e. >100 beam areas in size) in high resolution (i.e. 40 nm pixel size) confocal images. Typical representative box and whisker plots obtained from the analysis of particle densities in MDCK-*MDR1* cells are represented in Figure 5.11 as follows;

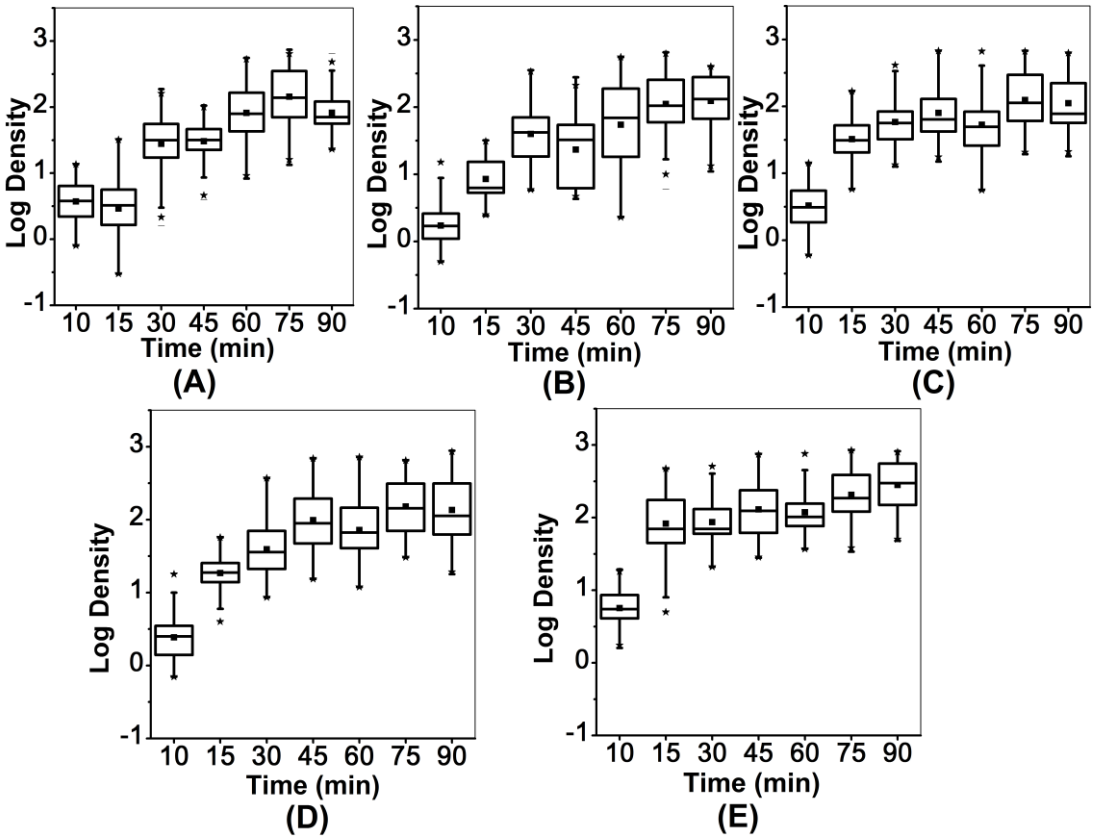

Figure 5.11 *Box and Whisker plots of log density values obtained from the SpIDA analysis of subcellular ROIs in MDCK-MDR1 cells as a function of time and verapamil concentration for 2.5 µM* ***(A)*** *5 µM* ***(B)*** *10 µM* ***(C)*** *20µM* ***(D)*** *and 50 µM* ***(E)*** *samples (n=100).*

Time-dependent behaviour was exhibited at earlier time points (i.e. up to 45 minutes) and broader regional heterogeneity at lower concentrations of verapamil (i.e. 2.5 and 5 µM) was apparent (See Figure 5.11).

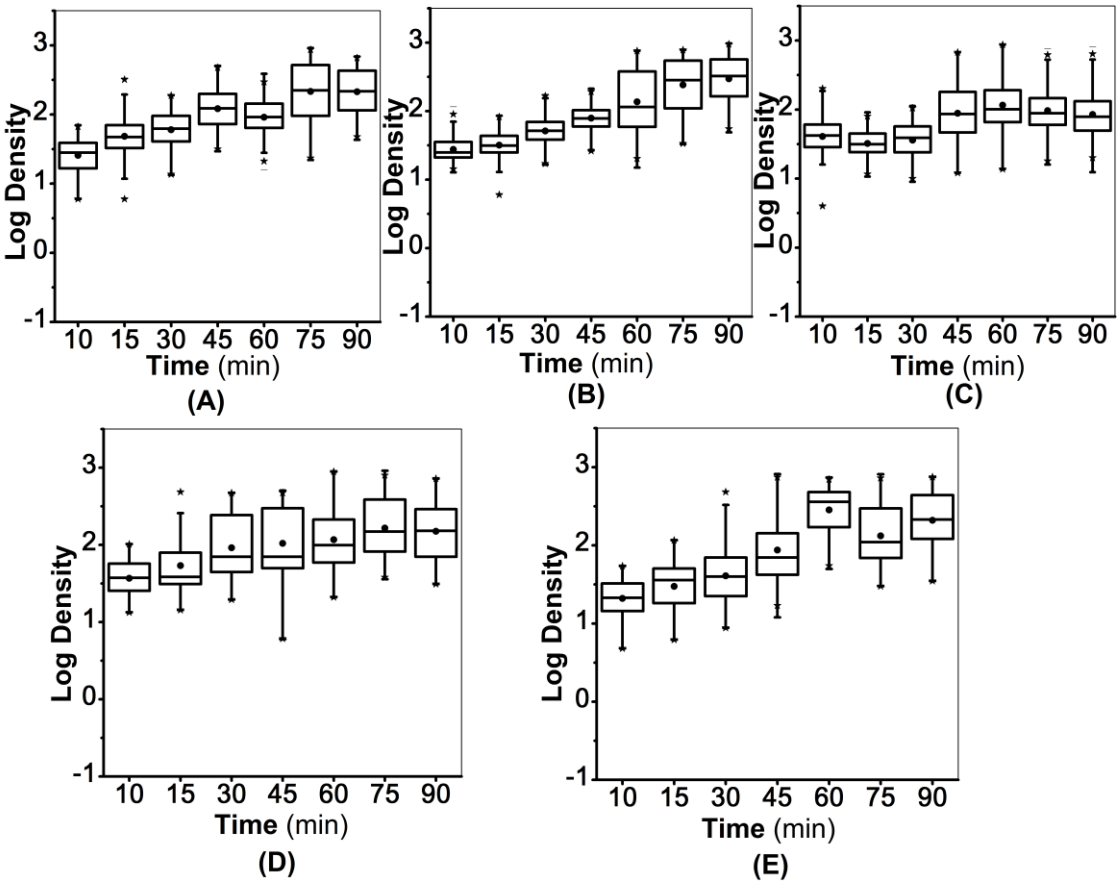

Figure 5.12 *Box and Whisker plots of log density values obtained from the SpIDA analysis of subcellular ROIs in MDCK-wt cells as a function of time and verapamil concentration for 2.5 µM* ***(A)*** *5 µM* ***(B)*** *10 µM* ***(C)*** *20µM* ***(D)*** *and 50 µM* ***(E)*** *samples (n=100).*

Statistical tests ($P < 0.05$) were performed to assess whether any significant differences were existent between time points for each concentration of verapamil, between the same time points for both cell lines and between various concentrations of verapamil.

For values obtained from the SpIDA analysis of control samples, see Figure 5.8.

5.5 Discussion

Previous reports in the literature have recommended the need for novel image analysis software that enable the quantification of fluorescently-labelled species following immunofluorescence staining. SpIDA has previously been validated and reported as a novel approach for the assessment of oligomerisation and quantification of densities in selected regions of interest. In this study a combination of SpIDA and traditional quantitative immunofluorescence were applied to profile p-glycoprotein expression in MDCK-*wt* and MDCK-*MDR1* cell lines (See Figure 5.1). Representative images and data obtained from a population of ROIs (See Figure 5.3) normalised to the sampling area appeared consistent with the baseline expression of p-glycoprotein in MDCK-*wt* cells. As would be expected, a broad intercellular and subcellular heterogeneity was observed in p-glycoprotein expression within the transfected MDR1 cell line.

Since p-glycoprotein expression was assessed in non-differentiated and polarised systems in the case of MDCK-*MDR1* and MDCK-*wt* cells (See Figure 5.4), the capability of SpIDA to analyse the polarised distribution of p-glycoprotein across Caco-2 monolayers cultivated onto Transwells® was assessed as a function of differentiation. Broad intercellular and three-dimensional heterogeneity of MDR1 expression is indicated up to day 10. However, a corresponding reduction in intercellular heterogeneities in expression was evident from day 10 to day 29 where differentiation is achieved and polarisation observed across the monolayer cross-section. Density data obtained from SpIDA analysis of samples appeared better suited for indicating the preferential apical location of p-glycoprotein transporters with smaller intercellular heterogeneity than conventional integrated density measurements per cell. These observations are consistent with previous reported literature and the evolutionary role of p-glycoprotein in the efflux of xenobiotics exposed to apical compartments in polarised tissues. Furthermore, the 2.2-fold increase observed in densities of p-glycoprotein expression determined from SpIDA analysis are consistent with reported increases observed with the LC-MRM data obtained from Miliotis *et al.* (i.e. two-fold) under identical culture conditions and very similar to the efflux ratio of digoxin reported between days 10 and 29 in the same study.[11]

The application of image analysis tools (i.e. SpIDA and quantitative immunofluorescence) in this context offers a series of advantages associated with rapid acquisition of data (i.e. imaging a large number of cells rapidly) that can be performed with any commercial confocal microscope. SpIDA provides absolute quantitative data on densities and may be applied to the assessment of three-dimensional *z*-stack images or simply two-dimensional confocal images (i.e. the brightest plane or in-focus planes) to assess cross-sectional differences in protein expression within polarised cell models, and enable comparison of multiple cell populations.

Furthermore, direct visualisation of labelled p-glycoprotein transporters allowed their localisation in the cytoplasmic region of both cell lines to be examined, consistent with the dynamic nature of the plasma membrane and existence of membrane components in intracellular vesicles. Confocal image processing permits the localisation of protein expression and quantification of their densities following immunofluorescence labelling and allows further subcellular dissection of samples. Current macroscopic methods such as mass spectrometry and western blot analysis employ whole cell lysates or transmembrane preparations and are unable to differentiate compartmentalised behaviour and membrane-associated transporters from intracellular membrane components.

Data derived in this study indicate that profiling expression in polarised cell model systems provides more insight into transporter expression in physiologically-relevant conditions allowing quantitative information on the localisation and polarised compartmentalisation, which could be lost in macroscopic methods.

Verapamil-induced inhibition of the p-glycoprotein transporter was assessed in MDCK-*wt* and MDCK-*MDR1* cells to enable direct comparison of MDR1 function between the basal activity in the wild type and MDR1-transfected cell line. The Calcein retention assay was employed to compare the functionality of p-glycoprotein in these cell lines. Representative confocal images of Calcein retention as a function of verapamil concentration and incubation time are presented in Figure 5.9 and Figure 5.10 for MDR1 and wt cells, respectively.

Initial visual assessment of confocal micrographs revealed heterogeneity across cells after various time points and concentration of verapamil. This was further investigated

through the performance of SpIDA analysis of subcellular regions (i.e. 100 regions of interest per condition) to profile intercellular heterogeneities and assess representative population data (See Figure 5.11 and Figure 5.12 for MDCK-*MDR1* and MDCK-*wt* cells, respectively). Although enabling the absolute quantification of intracellular Calcein concentrations and sampling sub-cellular regions, SpIDA could not be applied to the accurate overall analysis of sub-populations within confocal images. This has been reported by the developers of this method due to associated biasing effects in samples containing species with multiple quantal brightnesses (i.e. brighter and darker sub-regions). In the majority of cases, at both higher and lower time points a multimodal distribution was observed in the population data and the overall data did not follow a normal distribution. For this purpose, the assessment of overall heterogeneity in samples could be further analysed using analysis tools able to resolve mixtures (i.e. Gaussian mixture model analysis).

5.6 Conclusion

The assessment of p-glycoprotein expression and activity following treatment with p-glycoprotein modulators is likely to remain of interest in small molecule therapeutic design, particularly where the effects of a lead molecule on p-glycoprotein expression and substrate or inhibitor activity of a lead molecule are essential information to design more successful therapeutics and reduce the potential risk of drug-drug interactions.

This study highlighted the potential for application of image analysis tools to extract information inherent in fluorescence intensity data contained within confocal images in an attempt to yield parameters concerning the abundance of p-glycoprotein transporters and their relative localisation within polarised monolayers mimicking physiological conditions. Furthermore, the functionality of p-glycoprotein transporters was assessed using through imaging the intracellular retention of Calcein, a routinely-utilised dye in the assessment of p-glycoprotein inhibition and subsequent assessment of intercellular and regional heterogeneities in a wild type and MDR1-transfected cell line.

Given that current analytical methods utilised to assess protein expression each yield different output, direct visualisation of transporter expression coupled to quantification of their densities and relative localisation may provide a direct, rapid and convenient assay. In practice as immunochemical labelling of tumour biopsies remains a popular option, it may also be considered in prognosis determination. Additionally, microscopy

here demonstrates that the functionality of a transporter can be assessed, issues and errors associated with the application of current macroscopic methods may be avoided and the need to compare multiple methodologies minimised.

In summary, confocal imaging and image analysis tools can be applied to the non-invasive *in situ* assessment of protein expression and function in fluorescence-based assays permitting qualitative analysis of their localisation, morphology and distributions.

With the emergence of novel label-free imaging systems (i.e. stimulated Raman scattering microscopy), future label-free analysis of intracellular and membrane-associated moieties may become a reality and eliminate challenges associated with the pre-requisite for fluorophore presence in the assessment of protein expression and intracellular uptake of ligands.

5.7 Acknowledgements

We would like to acknowledge the University of Manchester Alumni Fund for supporting this project.

5.8 References

1. Dietrich CG, Geier A, Oude Elferink RPJ 2003. ABC of oral bioavailability: transporters as gatekeepers in the gut. Gut 52(12):1788-1795.

2. Löscher W, Potschka H 2005. Blood-brain barrier active efflux transporters: ATP-binding cassette gene family. Neurotherapeutics 2(1):86-98.

3. Stein WD 1997. Kinetics of the multidrug transporter (P-glycoprotein) and its reversal. Physiological Reviews 77(2):545-590.

4. Anger GJ, Cressman AM, Piquette-Miller M 2012. Expression of ABC efflux transporters in placenta from women with insulin-managed diabetes. PLoS ONE 7(4):e35027.

5. Cisternino S, Mercier C, Bourasset F, Roux F, Scherrmann J-M 2004. Expression, up-regulation, and transport activity of the multidrug-resistance protein Abcg2 at the mouse blood-brain barrier. Cancer Research 64(9):3296-3301.

6. Hu J, He X, Baggerly KA, Coombes KR, Hennessy BTJ, Mills GB 2007. Non-parametric quantification of protein lysate arrays. Bioinformatics 23(15):1986-1994.

7. Templin MF, Stoll D, Schrenk M, Traub PC, Vöhringer CF, Joos TO 2002. Protein microarray technology. Drug Discovery Today 7(15):815-822.

8. Krasznai ZT, Friedlander E, Nagy A, Szabo G, Vereb G, Goda K, Hernadi Z 2005. Quantitative and functional assay of MDR1/P170-mediated MDR in ascites cells of patients with ovarian cancer. Anticancer Research 25(2A):1187-1192.

9. Colombo PC, Ashton AW, Celaj S, Talreja A, Banchs JE, Dubois NB, Marinaccio M, Malla S, Lachmann J, Ware JA, Le Jemtel TH 2002. Biopsy coupled to quantitative immunofluorescence: a new method to study the human vascular endothelium. Journal of Applied Physiology 92(3):1331-1338.

10. Mokin M, Keifer J 2006. Quantitative analysis of immunofluorescent punctate staining of synaptically localized proteins using confocal microscopy and stereology. Journal of Neuroscience Methods 157(2):218-224.

11. Miliotis T, Ali L, Palm JE, Lundqvist AJ, Ahnoff M, Andersson TB, Hilgendorf C 2011. Development of a highly sensitive method using liquid chromatography-multiple reaction monitoring to quantify membrane P-Glycoprotein in biological matrices and relationship to transport function. Drug Metabolism and Disposition 39(12):2440-2449.

12. Hirabayashi H, Sugimoto H, Matsumoto S, Amano N, Moriwaki T 2011. Development of a quantification method for digoxin, a typical P-glycoprotein probe in clinical and non-clinical studies, using high performance liquid chromatography-tandem mass spectrometry: The usefulness of negative ionization mode to avoid competitive adduct-ion formation. Journal of Chromatography B-Analytical Technologies in the Biomedical and Life Sciences 879(32):3837-3844.

13. Kirkpatrick DS, Gerber SA, Gygi SP 2005. The absolute quantification strategy: a general procedure for the quantification of proteins and post-translational modifications. Methods 35(3):265-273.

14. Blot V, McGraw TE. 2008. Use of quantitative immunofluorescence microscopy to study intracellular trafficking. ed. p 1-20.

15. Greiner B, Eichelbaum M, Fritz P, Kreichgauer HP, Von Richter O, Zundler J 1999. The role of intestinal P-glycoprotein in the interaction of digoxin and rifampin. Journal of Clinical Investigation 104(2):147-153.

16. Seelig A 1998. A general pattern for substrate recognition by P-glycoprotein. European Journal of Biochemistry 251(1-2):252-261.

17. FDA. 2006. Drug development and drug interactions: Table of substrates, inhibitors and inducers. ed., Maryland: FDA.

18. Litman T, Zeuthen T, Skovsgaard T, Stein WD 1997. Structure-activity relationships of P-glycoprotein interacting drugs: kinetic characterization of their effects on ATPase activity. Biochimica et Biophysica Acta (BBA) - Molecular Basis of Disease 1361(2):159-168.

19. Scarborough G 1995. Drug-stimulated ATPase activity of the human P-glycoprotein. Journal of Bioenergetics and Biomembranes 27(1):37-41.

20. Schwab D, Fischer H, Tabatabaei A, Poli S, Huwyler J 2003. Comparison of in vitro P-glycoprotein screening assays: Recommendations for their use in drug discovery. Journal of Medicinal Chemistry 46(9):1716-1725.

21. Polli JW, Wring SA, Humphreys JE, Huang L, Morgan JB, Webster LO, Serabjit-Singh CS 2001. Rational use of in Vitro P-glycoprotein assays in drug discovery. Journal of Pharmacology and Experimental Therapeutics 299(2):620-628.

22. Rautio J, Humphreys JE, Webster LO, Balakrishnan A, Keogh JP, Kunta JR, Serabjit-Singh CJ, Polli JW 2006. In vitro P-glycoprotein inhibition assays for assessment of clinical

drug ineraction potential of new drug candidates: A recommendation for probe substrates. Drug Metabolism and Disposition 34(5):786-792.

23. Feng B, Mills JB, Davidson RE, Mireles RJ, Janiszewski JS, Troutman MD, de Morais SM 2008. In vitro P-glycoprotein assays to predict the in vivo interactions of P-glycoprotein with drugs in the central nervous system. Drug Metabolism and Disposition 36(2):268-275.

24. Szeremy P, Pal A, Mehn D, Toth B, Fulop F, Krajcsi P, Heredi-Szabo K 2011. Comparison of three assay systems using a common probe substrate, Calcein AM, for studying P-gp using a selected set of compounds. J Biomol Screen 16(1):112-119.

25. Simon S, Schubert R 2012. Inhibitory effect of phospholipids on P-glycoprotein: Cellular studies in Caco-2, MDCKII-mdr1 and MDCKII-wildtype cells and P-gp ATPase activity measurements. Biochim Biophys Acta Mol Cell Biol Lipids 1821(9):1211-1223.

26. Tiberghien Fo, Loor F 1996. Ranking of P-glycoprotein substrates and inhibitors by a calcein-AM fluorometry screening assay. Anti-Cancer Drugs 7(5):568-578.

27. Eneroth A, Åström E, Hoogstraate J, Schrenk D, Conrad S, Kauffmann HM, Gjellan K 2001. Evaluation of a vincristine resistant Caco-2 cell line for use in a calcein AM extrusion screening assay for P-glycoprotein interaction. European Journal of Pharmaceutical Sciences 12(3):205-214.

28. Essodaïgui M, Broxterman HJ, Garnier-Suillerot A 1998. Kinetic analysis of Calcein and Calcein−Acetoxymethylester efflux mediated by the multidrug resistance protein and P-glycoprotein. Biochemistry 37(8):2243-2250.

29. Lee JS, Paull K, Alvarez M, Hose C, Monks A, Grever M, Fojo AT, Bates SE 1994. Rhodamine efflux patterns predict P-glycoprotein substrates in the National Cancer Institute drug screen. Molecular Pharmacology 46(4):627-638.

30. Ludescher C, Thaler J, Drach D, Drach J, Spitaler M, Gattringer C, And HH, Hofmann J 1992. Detection of activity of P-glycoprotein in human tumour samples using rhodamine 123. British Journal of Haematology 82(1):161-168.

31. van der Sandt ICJ, Blom-Roosemalen MCM, de Boer AG, Breimer DD 2000. Specificity of doxorubicin versus rhodamine-123 in assessing P-glycoprotein functionality in the LLC-PK1, LLC-PK1:MDR1 and Caco-2 cell lines. European Journal of Pharmaceutical Sciences 11(3):207-214.

32. Kim RB, Fromm MF, Wandel C, Leake B, Wood AJ, Roden DM, Wilkinson GR 1998. The drug transporter P-glycoprotein limits oral absorption and brain entry of HIV-1 protease inhibitors. The Journal of Clinical Investigation 101(2):289-294.

33. Liminga G, Nygren P, Dhar S, Nilsson K, Larsson R 1995. Cytotoxic effect of calcein acetoxymethyl ester on human tumor cell lines: drug delivery by intracellular trapping. Anti-Cancer Drugs 6(4):578-585.

34. Glavinas H, von Richter O, Vojnits K, Mehn D, Wilhelm I, Nagy T, Janossy J, Krizbai I, Couraud P, Krajcsi P 2011. Calcein assay: a high-throughput method to assess P-gp inhibition. Xenobiotica 41(8):712-719.

35. Rapposelli S, Coi A, Imbriani M, Bianucci AM 2012. Development of classification models for identifying “True” P-glycoprotein (P-gp) inhibitors through inhibition, ATPase

activation and monolayer efflux assays. International Journal of Molecular Sciences 13(6):6924-6943.

36. Neurophotonics. 2010. Spatial Intensity Distribution Analysis software. ed.

37. Godin AG, Costantino S, Lorenzo L-E, Swift JL, Sergeev M, Ribeiro-da-Silva A, De Koninck Y, Wiseman PW 2011. Revealing protein oligomerization and densities in situ using spatial intensity distribution analysis. Proceedings of the National Academy of Sciences 108(17):7010-7015.

38. Sergeev M. 2010. Measurement of oligomerization states of membrane proteins via spatial fluorescence intensity fluctuation analysis. Department of Physics, ed., Montreal: McGill University. p 208.

39. Swift JL, Godin AG, Doré K, Freland L, Bouchard N, Nimmo C, Sergeev M, De Koninck Y, Wiseman PW, Beaulieu J-M 2011. Quantification of receptor tyrosine kinase transactivation through direct dimerization and surface density measurements in single cells. Proceedings of the National Academy of Sciences 108(17):7016-7021.

40. Héctor GP, Irene C, Isabel P, Oriol A, Stephan T 2012. Standardized relative quantification of immunofluorescence tissue staining. Nature Protocols.

Chapter 6

THE ASSESSMENT OF CELLULAR UPTAKE USING BIOIMAGING AND CONVENTIONAL ASSAYS

6.1 Abstract

Transcellular passage of solutes occurs in many multicellular organisms and is involved in homeostasis, selective transfer of endogenous solutes and host defence functions.

Current analytical methods for the assessment of transcellular passage of drug candidates utilise macroscopic approaches that provide little insight into cellular events. With advances in image analysis capabilities over the recent years the assessment of intracellular concentrations of molecules, their relative distributions and dynamics at both a cellular and sub-cellular level has become a possibility.

In this chapter the application of image analysis tools in the assessment of transferrin receptor expression, transferrin-Alexa Fluor® 647 transcytosis and Cell Trace™ Calcein red-orange AM uptake is studied using a combination of conventional and live cell imaging assays as examples of substances utilising the receptor-mediated and passive diffusion pathways, respectively.

Spatial Intensity Distribution Analysis and Gaussian Mixture Model Analysis have been utilised in this study to accurately quantify the intracellular concentration of fluorophores the results of which were compared to fluorescence correlation spectroscopy data previously acquired in this group. Optimal imaging settings applied to fluorescence data acquisition of ligand internalisation can be performed for cell populations in comparison to single point methods such as fluorescence correlation spectroscopy. Coupled to high content screening, this optimisation can be utilised in rapid screening of cellular uptake of a diversity of species utilising passive and vesicular transport mechanisms. Uptake of Cell Trace™ Calcein red orange AM and transferrin were found to be cell-line dependent in this study with broad intercellular heterogeneity within each cell line.

Keywords: Transcytosis; Transferrin receptor; Spatial intensity distribution analysis; Immunofluorescence.

6.2 Introduction

Transcytosis is a directional vesicular transport mechanism by which macromolecular cargo is transported across the cell. With the current interest in designing novel strategies for targeted delivery of macromolecular therapeutics, understanding the significance of transcytosis and its cellular machinery is of importance to the design and application of therapies that exploit this pathway.

Receptor-dependency has been used to distinguish between different types of transcytosis[1] the differentiation of which is based on the nature of cargo association with plasma membrane components. Receptor-dependent internalisation is highly dependent on ligand interaction with cell surface receptors. Subsequent polymerisation or conformational changes may occur following ligand association with its target receptor.[2] Components present on the vesicle membrane dictate the intracellular fate of ligands that may conclude with lysosomal degradation, interaction with intracellular receptors or exocytosis *via* sorting pathways.[3,4]

Exploitation of receptor-dependent pathways has been extensively studied over the recent decades with a particular view to developing selectively targeted therapies that when conjugated to specific ligands will selectively interact with receptors of interest.[5] However, the success of such delivery systems is limited by the extent of receptor expression at the target site encouraging further assessment of receptor-mediated transport processes and their relative significance to ligand internalisation.[6]

To date receptor-mediated mechanisms have been characterised for the uptake of low density lipoprotein (LDL),[7-9] transferrin,[10-14] insulin,[15,16] albumin,[3,17,18] and immunoglobulins (IgA and IgG) at various common cellular barriers (including the blood-brain barrier)[19,20] with the purpose of gaining an insight into the specifics of their transport and conjugation to therapeutics for targeted delivery to tissues expressing these receptors under specific pathological conditions. Such studies have primarily been founded on quantitative indirect bulk methods commonly applied to profiling membrane transport processes that yield apparent permeability (P_{app}) values for the transcellular passage of ligands. Conversely, a number of studies have focused on the direct visualisation of receptor expression and ligand transcytosis with little emphasis on quantifying vesicle numbers and their intracellular dynamics.[21]

In this study the expression of the transferrin receptor and transcytosis of fluorescently-labelled transferrin (i.e. transferrin-Alexa Fluor® 647) will be assessed as an example of receptor-mediated vesicular transport. Transferrin receptors are known to be implicated in cell iron metabolism and growth such that their expression varies between different cell lines according to nutrient and metabolic requirements.[22,23] Cells undergoing proliferation (e.g. in tissue repair and tumours) will exhibit higher transferrin receptor densities, whereas, expression remains fairly stable in non-proliferating cells.[6,23] Various combinations of molecular biology and imaging approaches have been reported for profiling transferrin receptor expression in cells and tissues. Immunofluorescence has been applied to the visualisation of membrane transferrin receptors and two-dimensional gel electrophoresis has been used for profiling both transmembrane and intracellular transferrin receptors.[24] Electron microscopy, semi-quantitative live cell imaging, immunohistochemical and immunofluorescence methods are commonly reported in the literature for the elucidation of transferrin receptor expression and vesicular transport.[24-27]

Many studies have recognised the transferrin receptor as a promising candidate for exploitation in drug delivery particularly at sites where over-expression of the transferrin receptor is evident; hence a focus on receptor-mediated transcytosis of transferrin has gained popularity.[6,23,28-30] The expression of transferrin receptors has been reported for a diversity of cell lines in the literature. Since transferrin receptor expression in HeLa (a cervical cancer cell line),[25] Caco-2[31] and endothelial cell lines[1,32] has been documented, these cell lines were selected for the assessment of transferrin receptor-mediated transcytosis as a control marker of receptor-mediated transcellular transport in this study.

The majority of research focused on studying transcytosis to date, has utilised *in vitro* cell models due to advantages associated with controlling (some) physiological parameters and the capability to study their influence on transcytosis. Parameters such as membrane pore size, seeding density, polarity index and recording tracer location throughout the time course of the experiment are factors that need to be accounted for when developing an *in vitro* model for studying transcellular transport processes.[21]

Though the majority of efforts focused to date have included the development and refinement of *in vitro* models for transcytosis, very little focus has been emphasised on

quantitative bio-imaging of these models and extracting biophysical parameters concerning the significance and contribution of specific transcytotic uptake pathways to the delivery of novel therapeutics. Furthermore, the majority of current studies rely on the recruitment of black box approaches and invasive bulk methods that whilst yielding quantitative parameters of transcellular solute passage provide little information on their intracellular distribution and concentrations.

In this study the transcellular transport mechanism (i.e. passive diffusion) and uptake of Cell Trace™ Calcein red-orange was assessed and compared to both the dynamics and extent of passive diffusion in comparison to vesicular transport due to differences in the rate and extent of diffusive processes in comparison to vesicular transport (i.e. under the same conditions diffusion may be a more rapid uptake process).

To this end, this chapter aims to assess image analysis as a tool for profiling receptor expression, characterising membrane-related transport processes namely transcellular passage of transferrin and the passive uptake of Cell Trace™ Calcein red-orange AM.

6.3 Material And Methods

6.3.1 Materials

All cell culture reagents including high glucose Dulbecco's Modified Eagle Medium (DMEM) (i.e. 4.5 g/L) supplemented with 1% *v/v* Streptomycin (10,000 µg) and penicillin G (10,000 units) solution, 1% *v/v* L-glutamine (200 mM), 10% *v/v* heat-inactivated Fetal Bovine Serum (FBS) and 1% *v/v* non-essential amino acids were acquired from Life Technologies (Paisley, UK). (3-(4, 5-Dimethylthiazol-2-yl)-2, 5-diphenyltetrazolium bromide, (MTT), transferrin-Alexa Fluor® 647, secondary goat anti-mouse IgG-Alexa Fluor® 488 and SYTO® 16 were also obtained from Life Technologies (Paisley, UK). Primary mouse anti-CD71 antibody was purchased from Santa Cruz (Santa Cruz Biotechnology, California). Dimethyl sulfoxide (DMSO), HEPES buffer, Hank's Balanced Salt Solution (HBSS) and Phosphate-Buffered Saline (PBS) were obtained from Sigma-Aldrich Ltd. (Dorset, UK). Transwell® supports and Nunc® eight well chamber slides were obtained from Fisher Scientific (Leicestershire, UK).

6.3.2 Methods

6.3.2.1 Cell Culture and Sample Preparation

Colorectal adenocarcinoma cells, Caco-2, an epithelial cell line (passages 48-58), Henrietta Lacks, HeLa, a cervical adenocarcinoma cell line (passages 15-25), bovine aortic endothelial cells, BAECs, an endothelial cell line (passages 2-12) and Madin-Derby Canine Kidney cells type II, MDCK, an epithelial cell line (passages 10-20) were seeded in T-75 flasks containing DMEM and incubated at 37 °C in a pre-humidified atmosphere containing 5% CO_2. The growth medium was replaced every 2-3 days and cell splitting was carried out when 70-80% confluency was achieved.

In order to achieve cell detachment, the medium was removed and cells were rinsed with pre-warmed sterile PBS and trypsin. This was followed by centrifugation, subsequent re-suspension of the cell pellet in DMEM medium and re-cultivation.

For monolayer studies BAECS, MDCK, Caco-2 and HeLa cells were cultivated at a seeding density of 1 x 10^5 cells/mL and incubated for 48 hours prior to visualisation with confocal microscopy. Prior to the performance of transferrin-Alexa Fluor® 647 studies, samples were pre-incubated with BSA in PBS (0.5 % *w/v*).

In addition to monolayer experiments, Caco-2 cells were seeded onto the underside of polyester Transwells® (pore size: 0.4 µm and surface area: 0.33 cm^2) with a density of 2.6 x 10^5 cells/cm^2 and incubated for 21 days with replacement of growth medium and quantification of the transcellular electrical resistance (TER) on alternate days prior to experimentation.[33]

6.3.2.2 Quantification of the Apparent Permeability of Cell Trace™ Calcein Red-Orange AM and Transferrin-Alexa Fluor® 647 Across Polarised Caco-2 Monolayers

Confluent Caco-2 monolayers cultivated onto the basolateral side of Transwell® membrane inserts (i.e. up to 21 days) were utilised to determine the transcellular passage of Cell Trace™ Calcein red-orange AM and Transferrin-Alexa Fluor® 647.

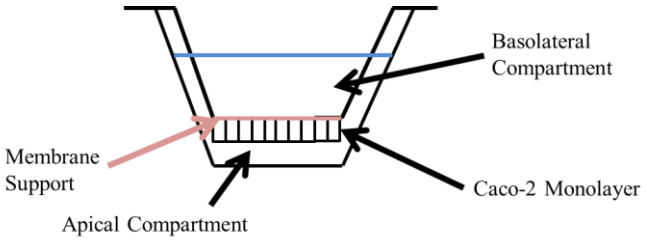

Figure 6.1 *A schematic depicting the orientation of the Caco-2 monolayers relative to the polyester Transwell® membrane. The apical face of the monolayer is in fact situated in the basolateral compartment of the well.*

All monolayers were incubated in serum-free DMEM medium 24 hours before the performance of transport experiments to avoid sudden changes in monolayer integrity (tight junction activity) and on the day of experimentation only monolayers possessing a TER in excess of 250 Ohms/cm^2 were selected for permeability assays. Prior to transport experiments the growth medium was removed, the monolayer rinsed twice in pre-warmed PBS and equilibrated with HBSS for two hours before performing transport experiments. Samples containing 5 µM Cell Trace™ Calcein red-orange AM and transferrin-Alexa Fluor® 647 were added either to the apical or basolateral chamber followed by incubation of the monolayer in a pre-humidified atmosphere at 37 °C in the presence of 5% CO_2 in separate experiments. Representative 100 µL samples were removed at 0, 15, 30, 45, 60, 90 and 120 minute time intervals respectively (from the basolateral chamber in B→A experiments- in the case of A→B experiments 40 µL was removed), and replaced with fresh HBSS. Depending on the direction of the experiment, at 120 minutes a final sample was removed from the compartment in which the starting test compound is placed. The apparent permeability coefficient, P_{app}, of both compounds was determined in both directions using the following equation adapted from Artursson *et al*:[34]

$$P_{app} = \frac{J}{AC_0} \qquad \textit{Equation 6.1}$$

Where J refers to the steady state flux (mol/seconds/cm^2), A is the surface area of the membrane (e.g. 0.33 cm^2) and C_0 the initial molar concentration of solute at the start of the experiment.

6.3.2.3 Immunofluorescence Staining

Transferrin receptor expression was assessed in MDCK and Caco-2 cells to compare expression between two cell lines. All cells were seeded onto Lab-Tek Nunc® eight-well chamber slides (Fisher Scientific, Leicestershire, UK) at a density of 1 x 10^5 cell/mL and incubated for 48 hours at 37 °C in a pre-humidified atmosphere containing 5% CO_2. Slides were rinsed in triplicate with PBS and fixed with 4% *w/v* paraformaldehyde for 15 minutes preceding a 10 minute incubation period with ammonium chloride to saturate the aldehyde functions. This was followed by permeabilisation with 0.2% *v/v* Triton X-100 in PBS for a further 15 minutes and subsequent blocking with a 1% *w/v* BSA in PBS solution for 30 minutes. The pre-diluted (1:250) primary antibody (Sigma, Poole, UK) was applied for one hour at room temperature and any excess primary antibody removed with triplicate PBS rinses. Subsequently, the samples were incubated with an anti-mouse secondary Alexa Fluor® 488-labelled IgG antibody for one hour (Molecular probes, Oregon, USA). In the case of negative controls, the addition of primary antibody was omitted. The samples were further rinsed and counter-stained with 0.5 µg/mL DAPI for 30 minutes prior to visualisation with confocal microscopy using a Zeiss LSM 510 confocal microscope (Zeiss, Jena, Germany).

6.3.2.4 Quantitative Immunofluorescence and Live Cell Imaging of Transferrin-Alexa Fluor® 647 and Cell Trace™ Calcein Red-Orange Uptake in Caco-2, HeLa and MDCK Cells

Imaging of live cells and immunofluorescently-labelled specimens was performed on samples seeded onto eight-well chamber slides with a Zeiss LSM510 confocal laser scanning microscope equipped with a c-Apochromat 40 x/NA 1.2 water-immersion objective. Alexa Fluor® 488-labelled secondary antibody was excited at 488 nm (Argon laser) and the emitted light collected at 515 nm (BP 505-530 nm). Transferrin-Alexa Fluor® 647 was excited at 633 nm (He-Ne laser) and emitted light was collected at 650 nm (LP 650). Cell Trace™ Calcein Red-Orange intracellular retention in Caco-2 cells and BAECs was excited at 543 nm (He-Ne laser) and the emitted fluorescence collected at 560 nm (BP 565-615 nm). To ensure consistency between experiments all parameters

relating to detector gain, laser transmission and amplifier gain were maintained constant. The permeant nuclear stain, DAPI, was excited at 350 nm and emitted light collected at 470 nm using a halogen lamp.

All experiments were performed in a thermostatically controlled environment of 21 °C over multiple fields of vision for each sample to ensure collation of a statistically representative number of cells.

Quantification of the Laser Beam Waist The laser beam waist, a pre-requisite parameter for SpIDA analysis was calculated using the measurements of the diffusion of Rhodamine Green™ [35] (i.e. 488 nm Argon laser) and Texas Red™ (i.e. 543 nm Helium-Neon) by Fluorescence Correlation Spectroscopy (FCS) (See Appendix 1 for a detailed account of the methodology and results).

6.3.2.5 SpIDA Analysis

Confocal Image analysis was performed on all immunofluorescence and intracellular transferrin uptake images using the method described by Godin *et al*.[36] and the analysis of uptake was carried out using the software available for download from the developer website at *http://www.neurophotonics.ca/en/tools/software*. Images were imported into the SpIDA user interface and the laser beam waist size and image pixel size inputted. The density of labelled species (per beam waist area) was determined as output for all ROIs (regions of interest) in the acquired images following corrections for white noise (i.e. background fluorescence measurements) and PMT shot noise.

Super-Poissonian fitting of fluorescence intensity histograms determined from CLSM images forms the basis of SpIDA analysis. Quantal brightness (*QB*) and the density per beam area (i.e. number of fluorescent moieties defined within a specified region) are parameters derived from SpIDA analysis achieved through determination of the fluorescence intensity histogram of each pixel fluorescence intensity value within a specified ROI. Histograms are determined from calculating all the possible configurations in which a fluorescent entity may reside in a point spread function (PSF)-defined region. Following weighted calculations of each configuration and its respective probability assuming a Poisson distribution for *N* particles inside the PSF, the fitting function applied to determination of the final histogram is:[36-38]

$$H(\varepsilon, N; k) = \Sigma_n \rho^n(\varepsilon; k) Poi(n, N) \quad \text{with } \rho^0(\varepsilon; \kappa) = \delta_{k,0} \qquad \textit{Equation 6.2}$$

where H is the histogram fitting function that is normalised so that the integral over k equals unity. ε represents the molecular quantal brightness, N the number of particles within the PSF, ρ^n the probability of observing an intensity of light of k (assuming proportionality to the number of emitted photons) by n particles of ε brightness.

6.3.2.6 FIGMMA Analysis of Acquired Images

Confocal images acquired from transferrin-Alexa Fluor® 647 uptake were subjected to analysis using an in-house Gaussian Mixture Model (FIGMMA) software. Images were imported into the graphical user interface, thresholded and subsequently masked to account only for the contribution of fluorescent moieties within confocal images and exclude extracellular regions. The optimal number of mixtures was determined through the performance of an *F*-test and comparison of various fits obtained from different numbers of mixtures (for further details see Appendix 2). The *F*-test parameters of different mixtures used for the same dataset were compared and the least complex fit with the lowest P value (i.e.< 0.05) determined from the *F*-parameter was selected as the optimum number of mixtures.

6.3.2.7 Quantification of the Integrated Fluorescence Density Values

The integrated density value per unit area of fluorescent species in confocal images was determined in monolayer and immunofluorescence images using Image J® analysis software (NIH, Bethesda, USA). Analysis of the integrated density value was carried out through importing images into Image J® following blind 3D deconvolution in AutoDeblur® (AutoQuant Inc., New York, USA) of *z*-stacks acquired from live cell imaging and acquired immunofluorescence images into Image J®. The brightest field was initially selected for analysis followed by calibration of distances, application of a median filter, thresholding images and subsequent analysis of the integrated density profile over a specific thresholded area. This process was performed on all confocal images to standardise and facilitate comparison of acquired fluorescence intensity data between various cell lines.

6.3.2.8 Statistical Analysis

Unless stated otherwise, all population samples of intracellular retention were subjected to analysis of variance (i.e. $P < 0.05$).

6.4 Results

6.4.1 Confocal Images of Immunofluorescence Transferrin Receptor Staining

Immunofluorescently-labelled images of MDCK and Caco-2 transferrin receptors (Figure 6.2) illustrate transferrin receptor expression in these cell lines. While 1024 x 1024 pixel images were acquired at a larger pixel size (i.e. 220 nm), a smaller pixel size (44 nm) was also used to allow the determination of fluorescently-labelled transferrin receptor densities using SpIDA analysis.

Typical representative images of fluorescently-labelled transferrin receptors are presented for a field of view in Figure 6.2 (A-C for MDCK and Caco-2 cells, respectively at a 220 nm pixel size) and at a higher resolution (i.e. 44 nm pixel size) (D).

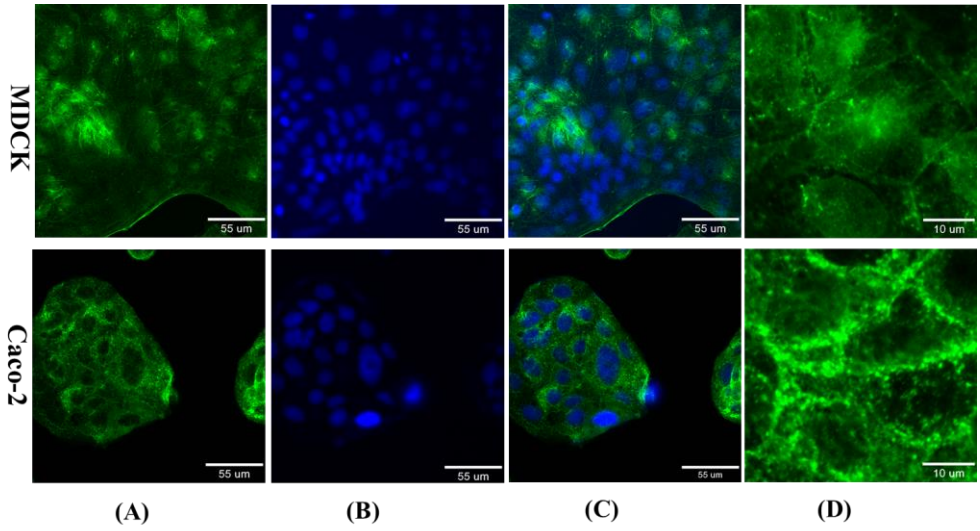

Figure 6.2 *Confocal immunofluorescence images of MDCK (top) and Caco-2 (bottom) transferrin receptors (green: **A** and **D**), counterstained nuclei (blue: **B** and **F**), composite images of DAPI and labelled transferrin receptor (**C** and **G**) and 44 nm pixel size images of labelled transferrin receptors acquired with a pixel dwell time of 3.2 microseconds.*

Figure 6.2 illustrates transferrin receptor expression in both cell lines with an apparent widespread localisation and intercellular heterogeneity in Caco-2 cells compared to MDCK cells. To confirm the distribution throughout the cells and possible differences within monolayers, *z*-stack images were also acquired.

Possible bleeding, autofluorescence and non-specific labelling were assessed with the negative stain images presented in Appendix 6. Images obtained from the negative control of MDCK cells were found to contain autofluorescence in cell borders and within the cytoplasmic region which may be attributed to autofluorescence of the membrane and cytoplasmic components.

6.4.2 Quantification of Transferrin Receptor Expression in Caco-2 and MDCK Cells Using Quantitative Immunofluorescence and SpIDA Analysis

To enable comparison of fluorescently-labelled transferrin receptors (i.e transferrin receptor expression), standard quantitative immunofluorescence quantification was performed in Image J® using the procedure described by Hector *et al*. in both *z*-stacks and single plane images (the brightest plane was selected during image acquisition) through determining the number of nuclei and subsequent division of integrated density values following thresholding by the number of cells (i.e. nuclei).[39]

6.4.3 Analysis of Transferrin Receptor Expression in Z-stack Images

Both SpIDA analysis and integrated fluorescence density measurements were performed in *z*-stack images acquired from immunofluorescently-labelled MDCK and Caco-2 cell lines. Representative data obtained from the analysis of these images are presented in Figure 6.3.

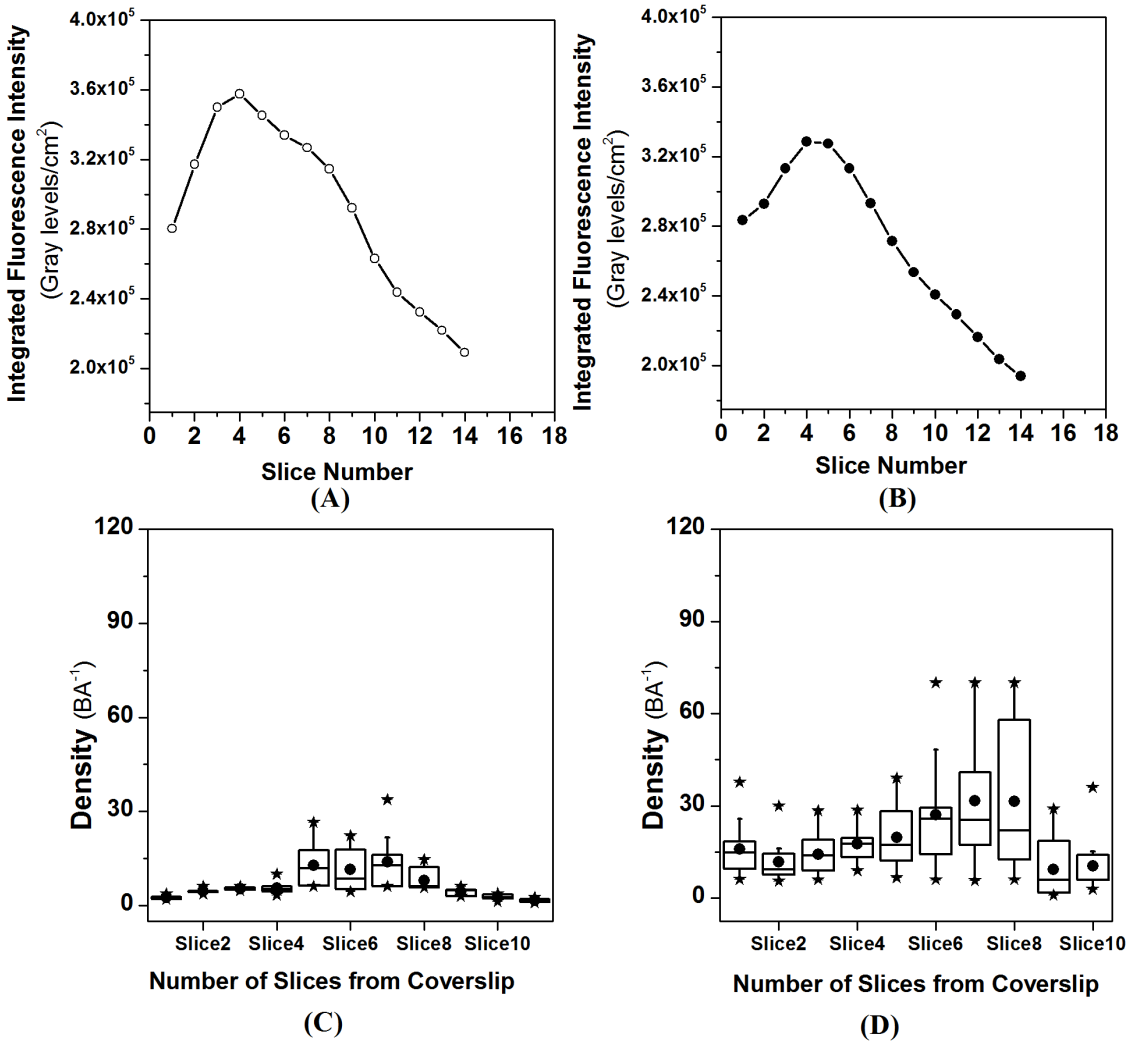

Figure 6.3 *Integrated density value per µm² of immunofluorescently-labelled transferrin receptors determined from the analysis of 1024 x 1024 pixel resolution z-stack images with a corresponding pixel size of 44 nm in Image J® - the integrated density value was determined between the first and last frames with a fluorescence signal for MDCK* ***(A)*** *and Caco-2* ***(B)*** *cells. Box and whisker plots representing density of transferrin receptors obtained following SpIDA analysis for MDCK* ***(C)*** *and Caco-2 cells* ***(D)****.*

Data obtained from both the SpIDA and integrated density measurements of transferrin receptor expression in Caco-2 and MDCK cells normalised for surface area revealed the intracellular localisation of transferrin receptors in both cell lines with a higher degree of expression observed in Caco-2 cells in comparison to MDCK cells.

6.4.4 Population Distributions in Two-Dimensional Confocal Images

Following quantitative immunofluorescence analysis, higher resolution images were subjected to SpIDA analysis in an attempt to determine intercellular and sub-cellular

heterogeneities in cell populations. Data obtained from these analyses is presented as histograms in Figure 6.4;

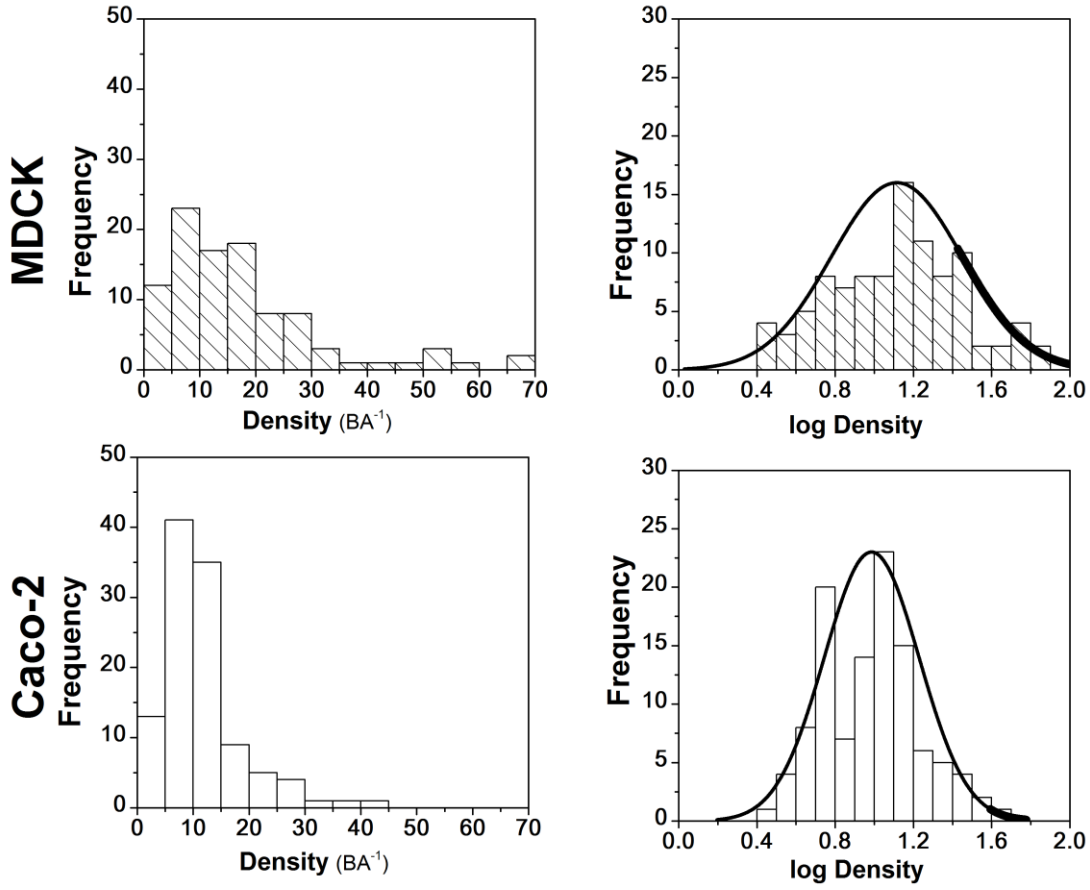

Figure 6.4 *Histograms of density distributions for labelled transferrin receptors determined from selected ROIs analysed using SpIDA (n= 80-100) in Caco-2 (bottom) and MDCK (top) cell lines with a detector gain setting of 650. Average density per beam area obtained at gain 650 is 2.8 < 9.68 < 42.3 and 2.7 < 13 < 68.5 for Caco-2 and MDCK cells, respectively (P< 0.05).*

Figure 6.4 presents the analysis of fluorescently labelled transferrin receptors at gain 650 with corresponding ranges of 2.8 < 9.68 < 42.3 and 2.7 < 13 < 68.5 for Caco-2 and MDCK cell lines. The thick lines of the histogram fit correspond to regions of the Gaussian distribution in which there are no corresponding parameters from sample data. Performance of an ANOVA test confirmed that a statistically significant difference was observed between the two sample populations (P< 0.05).

The density of labelled transferrin was also assessed at gain 600 in an attempt to establish the influence of detector gain on output parameters. Analysis of images captured at both gain settings revealed an identical profile demonstrating that following sufficient calibration of PMT shot noise and image background correction (i.e. white

noise) the outcome should be identical for images obtained from the same sample irrespective of detector gain settings utilised during image acquisition.

Performance of an ANOVA test yielded a P-value of 0.13 and 0.59 for Caco-2 and MDCK cells, respectively indicative of no significant statistical differences existent between the population data obtained with detector gain parameters of 600 and 650 ($P < 0.05$).

6.4.5 Apparent Permeability Coefficients of Transferrin-Alexa Fluor® 647 and Cell Trace™ Calcein Red-Orange AM Across Caco-2 Monolayers

Traditional apparent permeability assays were performed on Caco-2 cells cultivated in Transwell® support membranes following differentiation (i.e. day 21 post-seeding). Data obtained from the basolateral to apical passage of transferrin-Alexa Fluor® 647 and Cell Trace™ Calcein red-orange AM were used to calculate the apparent permeability coefficient P_{app} (Equation 6.1) (See Figure 6.5) .

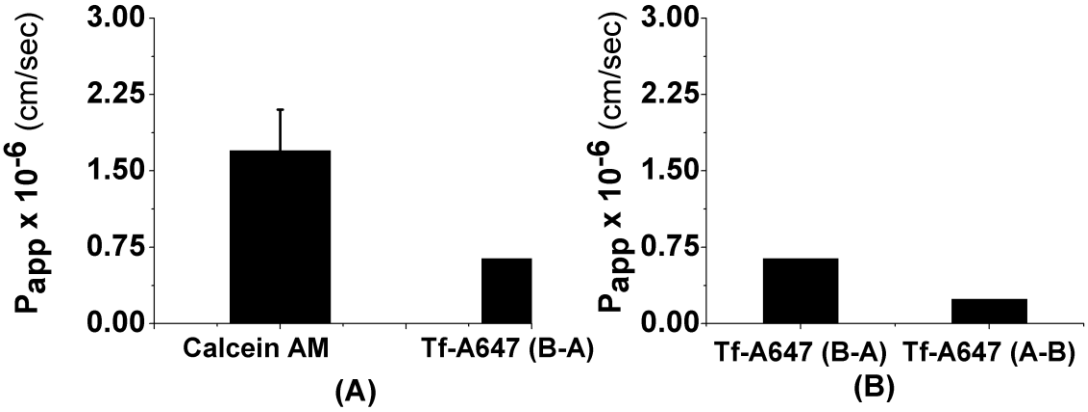

Figure 6.5 (A) *Apparent permeability coefficient, P_{app}, for the basolateral to apical (B→A) passage of Cell Trace™ Calcein red-orange AM and Transferrin-Alexa Fluor® 647* ***(B)*** *apical to basolateral (A→B) passage of Cell Trace™ Calcein red-orange AM and Transferrin-Alexa Fluor® 647 across Caco-2 monolayers. Monolayers were incubated in serum-free medium 24 hours prior to experimentation to avoid a reduction in TER values as a consequence of mechanical perturbation and sampled at 0, 10, 15, 30, 45, 60, 90 and 120 minutes (n=3).*

Figure 6.5 (A and B) show the expected polarised distribution of transferrin receptors with preferential transport of transferrin-Alexa Fluor® 647 in the basolateral to apical direction (i.e. B-A) which is in agreement with previous studies.[40] Indeed the calculated P_{app}, values i.e. 0.64×10^{-6} cm/sec for transferrin-Alexa Fluor® 647 in (basolateral to apical) and 0.24×10^{-6} cm/sec (apical to basolateral) (i.e. relative to the orientation of

the Caco-2 cell monolayer) are consistent with vesicular transport and the reported polarised heterogeneity of transferrin receptor expression in the Caco-2 cell line in the literature.[40,41]

6.4.6 Live Cell Imaging of Transferrin-Alexa Fluor® 647 Uptake

Endocytosis of transferrin-Alexa Fluor® 647 (i.e. 1 µM) was assessed in Caco-2 and HeLa cell lines following a 45 minute incubation. A combination of two-dimensional and *z*-stack images were captured to determine the intracellular distribution of transferrin-Alexa Fluor® 647 through quantification of the number of intracellular vesicles (i.e. density), their size and relative fluorescence intensities. Typical images obtained from live cell imaging of transferrin-Alexa Fluor® 647 are presented in Figure 6.6.

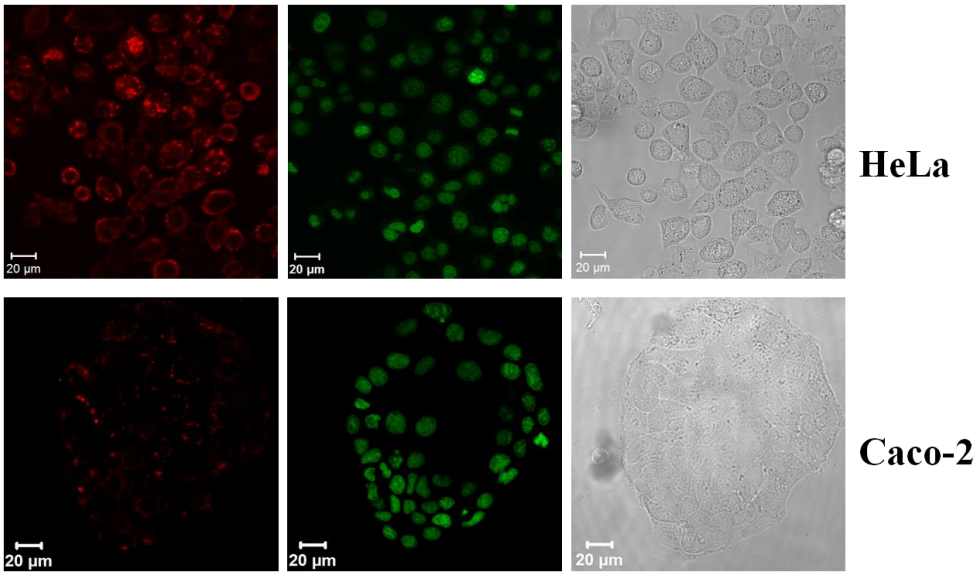

Figure 6.6 *Confocal images acquired from 1 µM transferrin-Alexa Fluor® 647 (red), Syto® 16 stain (green) and corresponding differential interference contrast images of vesicular uptake into HeLa and Caco-2 cells in HBSS with a corresponding pixel size of 0.44 µm.*

In Caco-2 cells, transferrin-Alexa Fluor® 647 fluorescence appeared both punctate and diffuse in cells. While the punctate fluorescence suggests the presence of large vesicles in cells, the observed diffuse fluorescence remains unexplained: possible reasons include the presence of a large number of small vesicles, free unconjugated Alexa Fluor® 647 dye following degradation or background noise (i.e. low SNR). In HeLa cells the uptake of transferrin appeared to have involved a greater number of large vesicles (i.e. punctate fluorescence) compared to Caco-2 cells.

Furthermore, high resolution time series images were acquired to determine the intracellular kinetics of vesicle movement for all cell lines examined (i.e. BAECs, Caco-2 and HeLa cells). Using Raster Imaging Correlation Spectroscopy (RICS) it was not possible to quantify the number of intracellular vesicles and their dynamics, due to significant photobleaching during image acquisition. Additionally, following the visual assessment of time series images no notable movement had occurred within the image acquisition time and in the dimensions examined (i.e. *x*-*y*).

Since significant bleaching was observed in the intracellular examination of transferrin-Alexa Fluor® 647 densities over time, further dynamic measurements using this approach were avoided- photobleaching is recognised to contribute to faster diffusion coefficients and lower particle numbers thereby contributing to potential misinterpretations of dynamic parameters.

6.4.7 Gaussian Mixture Model Analysis of Transferrin-Alexa Fluor® 647 Intracellular Vesicle Distributions

The intracellular density of vesicles in Caco-2 and HeLa cells was profiled using an in-house developed Gaussian Mixture Model and the best number of mixtures selected in each instance. Preliminary comparison of mixture models revealed a three mixture model to be more appropriate for the analysis of sub-populations in Caco-2 cells. In the case of HeLa cells a two mixture model was found to suffice in the majority of images analysed.

The corresponding mean obtained from the analysis of two-dimensional confocal images of Caco-2 and HeLa cells is presented in Figure 6.7.

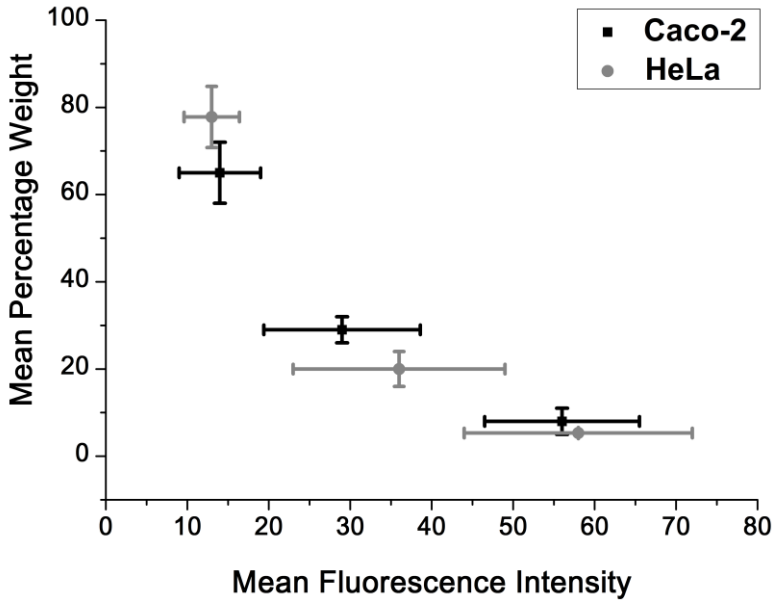

Figure 6.7 *Representative sub-population means obtained from the cluster analysis of HeLa and Caco-2 cell images with a pixel size of 0.44 µm. Bars represents the mean fluorescence intensity peaks and their corresponding weight ± st. dev. (n=100).*

At a $P < 0.05$ significance level there were no statistically significant differences observed in the population data for both HeLa and Caco-2 cells but a higher degree of heterogeneity was observed in Caco-2 cells when compared to HeLa cells as reflected by the sub-population mixture weights (Figure 6.7).

The intracellular detected fluorescence intensity of transferrin vesicles following thresholding and subsequent analysis was fairly low; hence, the mean fluorescence intensity (± *st. dev.* per μm^2) was also quantified using Image J® to confirm intensities and determined to be 79 ± 9 and 71 ± 13 for HeLa and Caco-2 cells, respectively. Therefore, intensities obtained from FIGMMA analysis were appropriate and representative of the samples analysed.

6.4.8 Live Cell Imaging of Cell Trace™ Calcein Red Orange Uptake

Time-dependency of Cell Trace™ Calcein red-orange AM uptake was assessed in BAECs and Caco-2 cells. Results in Figure 6.8 demonstrate a corresponding time and concentration-dependent increase in intracellular fluorescence intensity that is consistent with results obtained from previous research.[40]

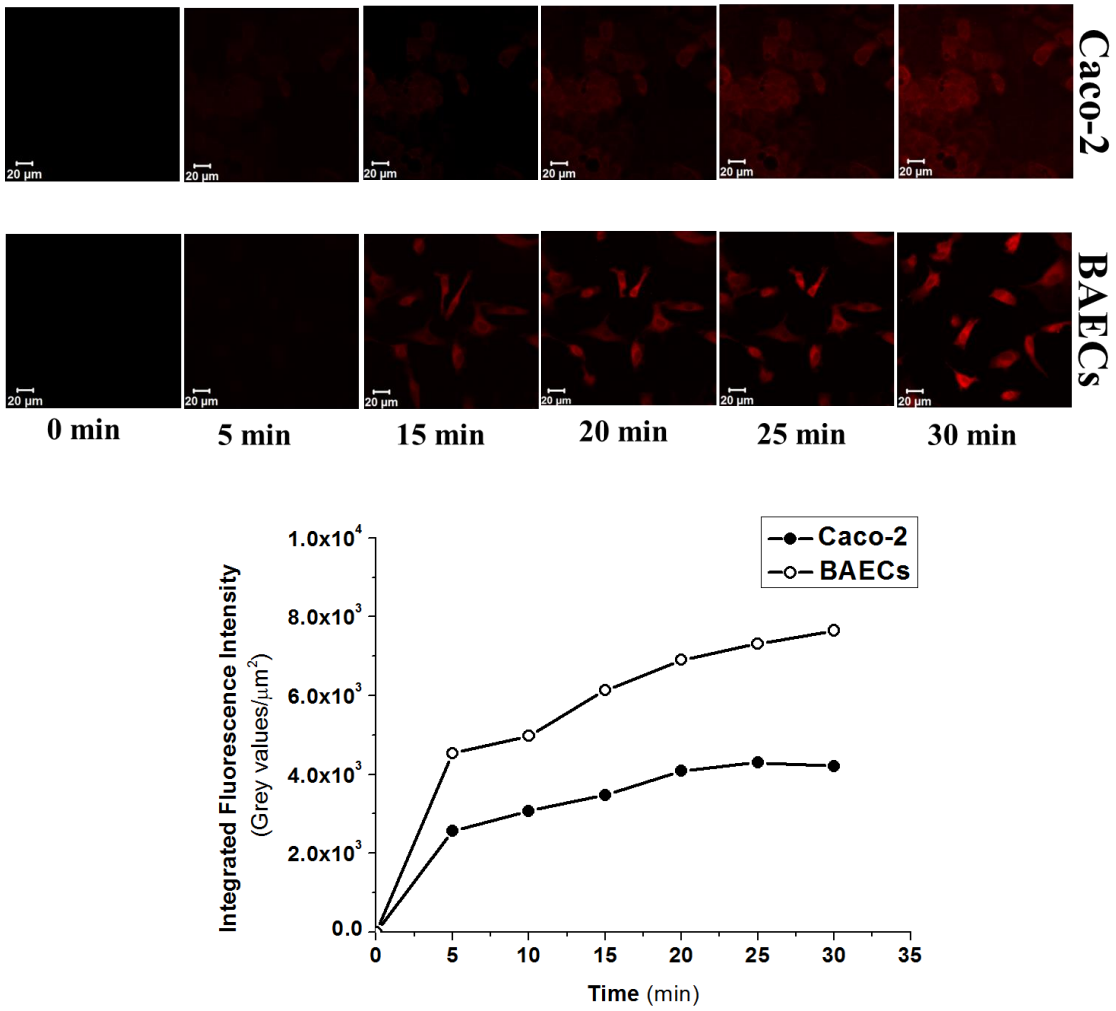

Figure 6.8 *Images representing the time-dependent accumulation of 100 nM Cell Trace™ Calcein red-orange up to 30 minutes with a corresponding pixel size of 0.44 µm for Caco-2 cells (top) and BAECs (bottom) and the corresponding integrated fluorescence intensity (Grey levels/µm²).*

To assess the intracellular concentration of Cell Trace™ Calcein red-orange, SpIDA analysis was performed on confocal images through the selection of multiple ROIs per cell in each confocal image.

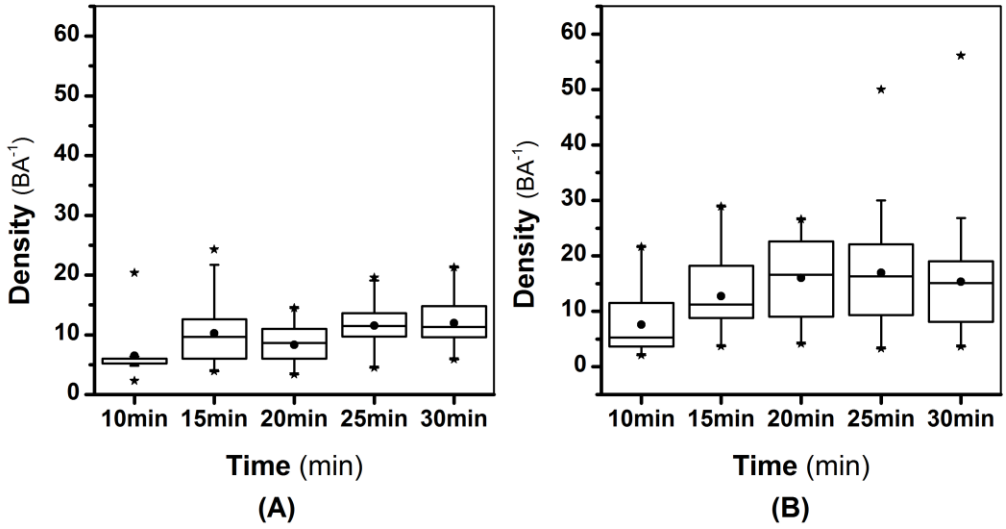

Figure 6.9 *Observed number of Cell Trace™ Calcein red-orange particles in BAECs and Caco-2 cells obtained from SpIDA analysis of live cell confocal images obtained from incubating Caco-2 cells* ***(A)*** *and BAECs* ***(B)*** *with 50 nM Calcein red-orange AM for up to 30 minutes. The mean is represented by (•) and outliers are represented by (*).*

Results obtained from the analysis of time-dependent intracellular accumulation of Cell Trace™ Calcein red-orange are presented in Figure 6.9 for both Caco-2 cells and BAECs (i.e. 50 nM) that indicated increasing densities of intracellular Cell Trace™ Calcein red-orange with time in both cell lines. Additionally, the increase in intracellular concentrations of Cell Trace™ Calcein red-orange was observed to be higher in BAECs in comparison to Caco-2 cells.

In order to further assess the ability of SpIDA analysis to determine intracellular concentrations, the retention of Cell Trace™ Calcein red-orange (50 nM) was assessed in Caco-2 cells and BAECs following 60 minute incubations. Representative confocal images, differential interference contrast and higher resolution (i.e. 70 nm pixel size) images are presented in Figure 6.10.

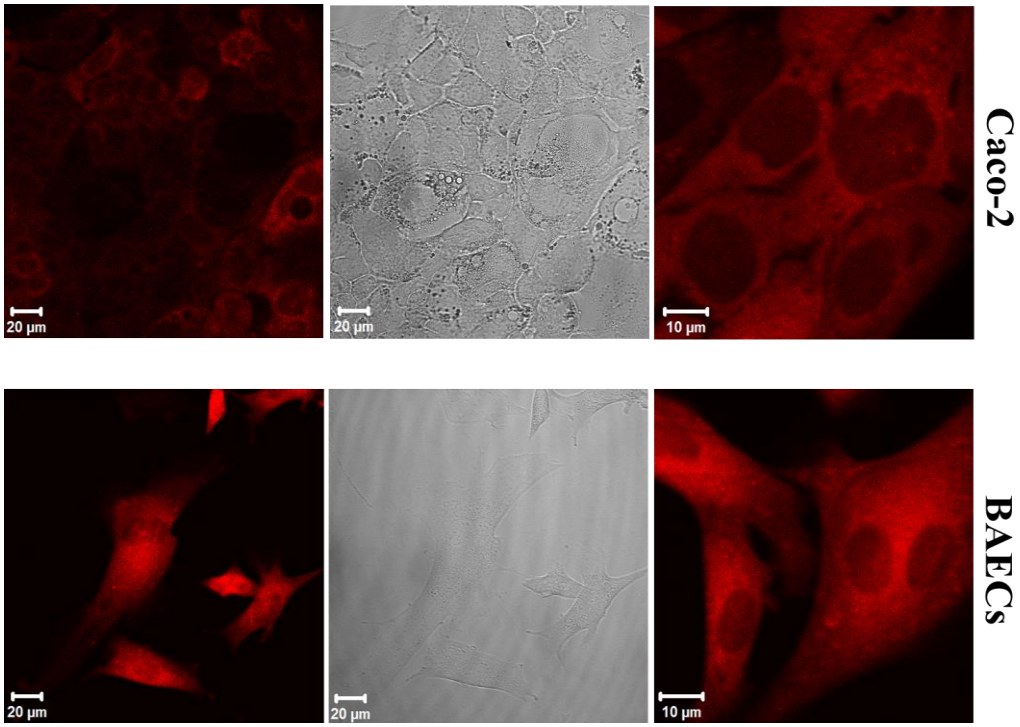

Figure 6.10 *Confocal images acquired following incubation of Caco-2 cells (top) and BAECs (bottom) with 50 nM Cell Trace™ Calcein red-orange AM for 60 minutes. Images presented are of 220 nm (left) and 70 nm (right) pixel sized images of 1024 x 1024 resolution acquired from each of the cell lines- all other image acquisition parameters were kept constant.*

In each confocal image multiple ROIs (i.e. 50-100 beam areas) were selected for analysis and the representative population mean, lower and upper quartile determined and expressed as a range for comparison against the data obtained following FCS performed in a previous project. Density per beam area population histograms and their log-normal distributions are presented in Figure 6.11.

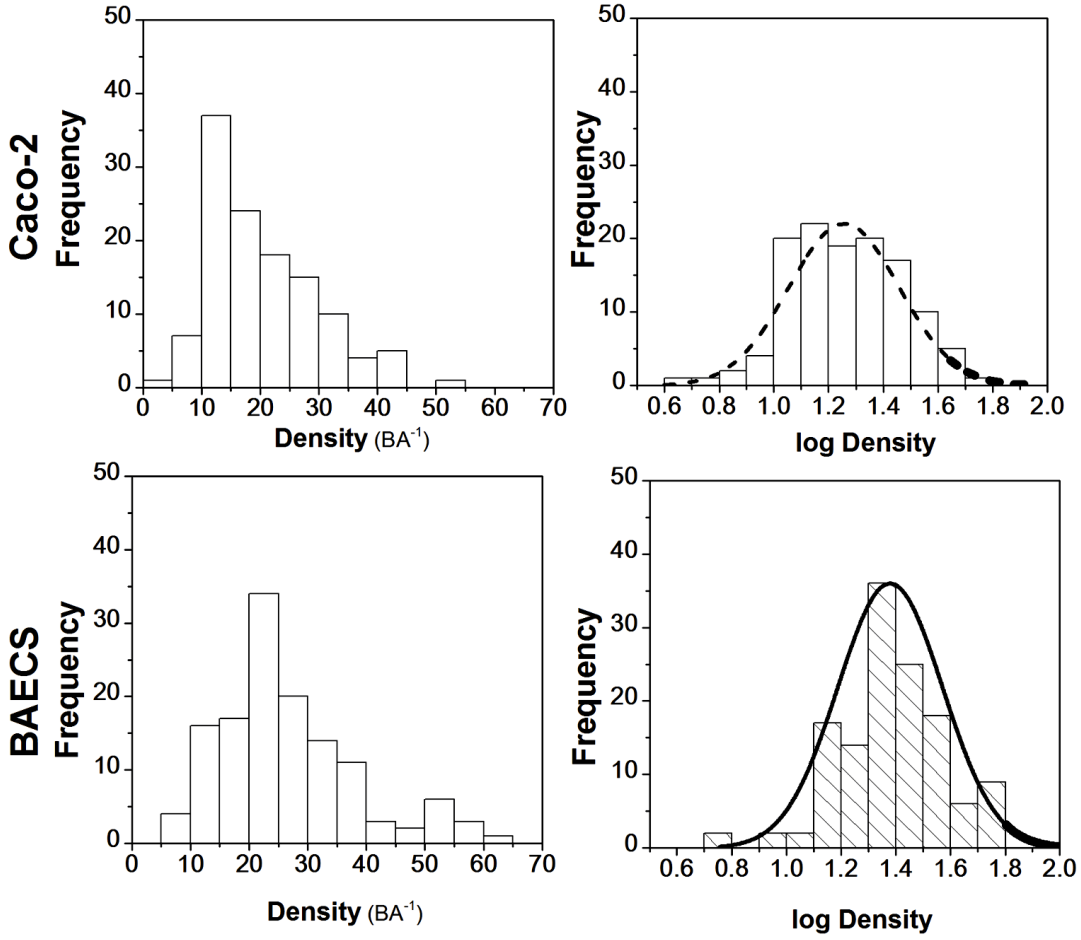

Figure 6.11 *Distributions of number of particles (Density per beam area) and Log (Density) distributions of intracellular Cell Trace™ Calcein red-orange in Caco-2 cells and BAECs. Average number of particles is 13 < 18 < 26 and 19 < 23 < 32 (Mean ± st. dev.) for Caco-2 cells and BAECs, respectively. SpIDA analysis was performed on 1024 x 1024 pixel confocal images acquired with a pixel size of 70 nm. Caco-2 cells and BAECs were seeded onto 8-well chamber slides and incubated for 24 hours prior to experimentation. 50 nM Cell Trace™ Calcein red-orange AM in HBSS was added to each well and incubated for 60 minutes at 37 °C in a pre-humidified atmosphere containing 5% CO_2. Following incubation HBSS was removed, monolayers were washed thrice with PBS and fresh HBSS added (n= 100-120). Denser lines represent ranges of the normal distribution fit in which there are no corresponding density values.*

The intracellular number of particles obtained following SpIDA analysis of samples incubated with 50 nM Cell Trace™ Calcein red-orange AM for 60 minutes was determined to be 19 < 23 < 32 and 13 < 18 < 26 in BAECs and Caco-2 cells, respectively. Hence, data obtained following the analysis of intracellular ROIs with SpIDA are in good agreement with previously reported ranges obtained from FCS measurements (i.e. 18 < 25 < 34 and 13 < 21 < 32 (log normal mean ± *st. dev.*) for BAECs and Caco-2 cells) performed under identical experimental conditions.[40] Data presented in Figure 6.10 and Figure 6.11 both indicate heterogeneity in the uptake of

Cell Trace™ Calcein red-orange AM and parameters obtained suggest cell line-dependent behaviour.

Furthermore, RICS analysis of acquired image time series indicates the intracellular diffusion time of Cell Trace™ Calcein red-orange was 396 ± 11.5 and 370 ± 32 microseconds in Caco-2 cells and BAECs, respectively. These values are consistent with previous data obtained using FCS for the quantification of the intracellular dynamics of Cell Trace™ Calcein red-orange that yielded a range of 326 < 909 < 2532 and 359 < 591 < 973 microseconds for Caco-2 cells and BAECs, respectively. The determined diffusion times obtained from RICS analysis were found to occur in the lower end of the range extracted from FCS analysis that may be attributed to photobleaching, the impact of pixel dwell time or the larger sampling area associated with RICS analysis.[40]

6.5 Discussion

Transferrin receptors are implicated in the uptake and trafficking of endogenous transferrin, hence knowledge of their expression and localisation in subcellular regions in specific cell lines are essential when studying the transcytosis of transferrin. In this chapter the expression of transferrin receptors was assessed in MDCK and Caco-2 cells to enable comparison of transferrin receptor distribution using image analysis tools such as quantitative immunofluorescence[39] and SpIDA analysis.

Analysis of images acquired in two dimensions (i.e. the *x*-*y* direction) from immunofluorescence images of transferrin using SpIDA revealed broad intercellular heterogeneity in expression between both cell lines as revealed by ranges of 2.8 < 9.68 < 42.3 and 2.7 < 13 < 68.5 for Caco-2 and MDCK cells, respectively. Both cell lines are utilised the for the assessment of transferrin transcytosis and the molecular machinery implicated in vesicular transport but currently no absolute quantitative parameters have been reported of transferrin receptor expression in these cell lines in the literature to our knowledge.[42-45]

Furthermore, examination of *z*-stack images and resultant density parameters normalised for thresholded areas obtained from routine image analysis and SpIDA revealed intracellular localisation of transferrin receptors in both cell lines consistent with the dynamic nature of vesicular transport and membrane recycling.[45] Since these

monolayers were cultivated in routine chamber slides and had not achieved differentiation, these results were solely utilised as preliminary observations of transferrin receptor expression and further assessment of expression in monolayers cultivated on Transwell® support filters would provide more detailed information on receptor expression in polarised and differentiated systems mimicking physiological conditions.

To our knowledge, there are no absolute quantitative reports of transferrin receptor expression in the literature and the majority of reported methods have semi-quantitatively profiled expression using a bulk macroscopic approach. For example, proteomic-based studies using mass spectrometric analysis rely on the preparation of lysates and provide no specific information on the localisation of receptors (or transporters) and their corresponding densities within a sample. Whilst the transferrin receptor was found to be localised intracellularly, in the case of an invasive method relying on the preparation of a cell lysate, the contribution from the cytoplasmic compartment (See Figure 6.2) would not be accounted for in determining transporter expression or would remain undifferentiated from proteins located on the plasma membrane.

Following the assessment of transferrin receptor expression, the vesicular uptake of labelled transferrin was examined through a combination live cell imaging (i.e. in Caco-2 and HeLa cells), FIGMMA and determining the integrated fluorescence intensity profiles for single confocal images. Data and images acquired from these experiments indicated differential distribution and localisation of intracellular transferrin-Alexa Fluor® 647 in the cell lines examined such that upon qualitative assessment of the images, HeLa cells appeared to have larger punctate vesicles when compared to Caco-2 cells that exhibited diffuse intracellular distribution of transferrin-Alexa Fluor® 647 (See Figure 6.6). This was further supported by the recurrent observation that a three mixture model was more appropriate for describing the intracellular vesicle sub-populations in Caco-2 cells following the performance of *F*-tests (i.e. the existence of more heterogeneity in vesicle populations in comparison to HeLa cells) (See Figure 6.7). Whilst FIGMMA analysis of transferrin vesicle images enabled the broad overall assessment of fluorescence intensity contributions from various vesicle sizes (i.e. larger vesicles of higher fluorescence intensity versus diffuse small vesicles), no quantification of vesicle sizes and their relative distribution could be inferred from this data. For this

purpose particle tracking software or granulometric analysis would enable further differentiation and categorisation of vesicles into sub-populations but both suffer from the inability to resolve smaller diffuse vesicles from background noise. Furthermore, the application of SpIDA to the analysis of vesicular compartments would result in biasing and error due to the small size of the ROIs (i.e.< 50 beam areas) selected for larger vesicles and any masking would result in the omission of data contributions from smaller intracellular particles.

In vitro models of drug absorption often rely on macroscopic (bulk) analytical approaches to quantify the amount of drug transported across cellular barriers. In this chapter the apparent permeability coefficients (P_{app}) of Cell Trace™ Calcein red-orange AM and transferrin-Alexa Fluor® 647 were assessed across Caco-2 monolayers cultivated onto the underside of Transwell® membrane inserts (See Figure 6.5). Furthermore, to aid microscopic assessment of intracellular events microscopy and image analysis were utilised to profile the temporal accumulation of Cell Trace™ Calcein red-orange (See Figure 6.8) and the vesicular transport of transferrin-Alexa Fluor® 647. Whilst macroscopic assessment enables the quantification of transported concentrations of compound to assess the solubility and permeability of a drug, microscopic assessment provides the ability to directly visualise and quantify the kinetics and extent of cellular uptake for fluorescent species and their intracellular fate at a molecular level.

In comparison to Cell Trace™ Calcein red-orange AM utilising a passive diffusion transcellular passage with a relatively similar apparent permeability coefficient in both directions, transferrin transcytosis was observed to occur more rapidly in the basolateral to apical direction (i.e. B-A). This is consistent with the directionality of detected transferrin receptors earlier in this chapter when observing a reduction in integrated density values upon moving away from the coverslip (i.e. in the apical direction). Furthermore, the observed directionality was in agreement with previous literature reporting a longer duration of intracellular retention for apically administered transferrin leading to the observed lower permeability coefficient in apically internalised transferrin in this study.[43]

A combination of monolayers cultivated on Transwells® and eight-well chamber slides were utilised for the assessment of Cell Trace™ Calcein red-orange AM uptake and

transferrin-Alexa Fluor® 647 vesicular transport in Caco-2 cells since Transwell® systems are a more physiologically relevant model despite being labour-intensive and low throughput in nature. The intracellular concentration of Cell Trace™ Calcein red-orange in Caco-2 cells (an epithelial cell line) were compared against an endothelial cell line, BAECs (See Figure 6.8 and Figure 6.9). By virtue of their role as barriers to the entry and access of xenobiotics, epithelial cells generally exhibit lower permeability to substances in comparison to endothelial cells that transport nutrients. Furthermore, differences in cell line morphologies (i.e. accessible surface area for diffusion) and membrane composition (i.e. differences in lipid constituents and transporter expression) generally influence observed differences in vesicular and passive transport processes.

Cell Trace™ Calcein red-orange, a membrane-permeable fluorescent dye, is known to enter cells rapidly under passive diffusion. The time and concentration-dependent intracellular retention of this dye was examined in BAECs and Caco-2 cells using confocal live cell imaging. Resultant integrated fluorescence intensity plots confirmed time-dependent uptake (See Figure 6.8) of Cell Trace™ Calcein red-orange into both cell lines with an apparent higher rate and extent of Cell Trace™ Calcein red-orange increase in fluorescence in BAECs when compared to Caco-2 cells.

A previous study had utilised FCS measurements to quantify the intracellular concentration and dynamics (i.e. diffusion coefficient) of Cell Trace™ Calcein red-orange in cell populations following a 60 minute exposure to this dye (See Figure 6.10). To assess the comparability of image analysis tools with FCS, data obtained from the SpIDA analysis of images acquired under identical conditions was compared for a population of cells subjected to image acquisition (i.e. 1024 x 1024 pixels with a corresponding pixel size of 44 nm). The advantages associated with the use of SpIDA analysis for profiling intracellular concentrations over RICS and FCS in this study is minimisation of photobleaching effects due to single image acquisition and rapid data collection over multiple fields of view that enables cell population profiling. Additionally, in comparison to FCS, analysis of confocal images with SpIDA does not require a specialist setup and can simply be performed with a commercial confocal microscope.

Previous ranges determined for the number of detected particles in BAECs and Caco-2 cells using FCS were $18 < 25 < 34$ and $13 < 21 < 32$ respectively, and data obtained

from SpIDA analysis of particle numbers (i.e. dye concentration) presented in Figure 6.11 yielded 19 < 23 < 32 particles for BAECs and 13 < 18 < 26 particles in Caco-2 cells, respectively. A statistically significant difference was noted between the two cell populations with an observed higher uptake of Cell Trace™ Calcein red-orange into BAECs in comparison to Caco-2 cells. Hence, the application of SpIDA analysis to the determination of intracellular concentrations with the current image acquisition parameters proved to be accurate in comparison to FCS measurements and immune to disadvantages such as phototoxicity (from a fixed laser confocal volume) and laborious data acquisition for cell populations commonly associated with FCS.

To further probe the intracellular behaviour of Cell Trace™ Calcein red-orange, RICS analysis was performed on high resolution image time series and following the achievement of the best fit resultant mean diffusion times (n=3) were found to be 396 ± 11.5 and 370 ± 32 microseconds in Caco-2 cells and BAECs that is consistent with previous FCS data for the quantification of Cell Trace™ Calcein red-orange intracellular dynamics with a corresponding range of 326 < 909 < 2532 and 359 < 591 < 973 microseconds. Whilst these values were observed to occur within the ranges determined by FCS, in both cases, a faster diffusion time was noted following RICS analysis of image time series.

RICS assessment of transferrin-Alexa Fluor® 647 vesicle dynamics in Caco-2 and HeLa cells was also performed and revealed photobleaching in the acquisition of two-dimensional image time series that limited any further analyses of vesicle dynamics and concentrations in the plane of observation. When utilising image correlation spectroscopies caution must be exercised due to the apparent susceptibility of correlation-based methods to photobleaching that result in observed lower concentrations and faster diffusion coefficients.

Photobleaching was also evident in image time series of intracellular Cell Trace™ Calcein red-orange but occurred to a lesser extent. One possible explanation for the observed differences in susceptibility to photobleaching was morphological differences in the species under examination such that Cell Trace™ Calcein red-orange images with smaller diffuse species in the cytoplasm would be less susceptible to bleaching in comparison to vesicles of a larger size and higher optical density (i.e. transferrin-Alexa Fluor® 647).

In summary, data obtained from profiling the intracellular concentration and dynamics of Cell Trace™ Calcein red-orange in this chapter demonstrated that image analysis tools (i.e. SpIDA and RICS) can indeed be utilised to generate meaningful parameters concerning the cellular uptake of molecules that can be insightful in studying the uptake of drugs in the pharmaceutical industry, determining receptor expression or profiling the intracellular fate and behaviour of compounds following entry into cells.

Imaging and subsequent analysis provide a non-invasive means of quantifying intracellular dynamics and concentrations, both at a cellular and sub-cellular level that can be applied to the assessment of internalisation mechanisms and in the case of some compounds explain the observed low apparent permeability values associated with their transcellular passage in *in vitro* systems which is not possible with current conventional bulk assays.

6.6 Conclusions

The transcytosis, transcellular passage and cellular internalisation of transferrin-Alexa Fluor® 647 and Cell Trace™ calcein red-orange AM were assessed in this chapter utilising a combination of image analysis tools and a three-dimensional *in vitro* model (i.e. a Caco-2 monolayer).

Three-dimensional *in vitro* models have been increasingly reported in the literature for predicting the uptake and subsequent fate of candidate drugs and macromolecular delivery vehicles. Till recently, simplistic *in vitro* models were utilised to determine predictors of drug absorption and bioavailability. However, such systems are unable to mimic the physiological and biomolecular complexities of an *in vivo* setting. Furthermore, analytical approaches (i.e. bulk black box methods) utilised in such studies profile transcellular transport at a macroscopic level providing little insight into events occurring at a microscopic level and the biomolecular machinery recruited in transcellular translocation.

With the current image acquisition and analysis capabilities it is possible to non-invasively probe transcellular transport at a cellular level and within polarised cell models. Rapid data acquisition from individual cells in the form of imaging provides a platform for the concomitant assessment of sub-cellular and intercellular variability in both receptor expression and the significance of vesicular transport recruitment to drug

delivery. Intracellular concentration data presented here was both reproducible between the image analysis tools implemented and in good agreement with previous experiments performed using FCS in this research group.

Though the scope of the application of image analysis tools to the assessment of transcytosis was briefly described and demonstrated in this chapter many potential avenues remain for extending bio-imaging research in this area to studying the transcellular passage of a diversity of substrates and the assessment of novel molecules that enhance vesicular transport.

6.7 Acknowledgements

We would like to thank the University of Manchester Alumni Fund for supporting this project and Dr Elena Bichenkova for granting access to the Tecan Safire platereader.

6.8 References

1. Herve F, Ghinea N, Scherrmann JM 2008. CNS Delivery *Via* Adsorptive Transcytosis. Aaps Journal 10(3):455-472.

2. Shen WC, Wan JS, Ekrami H 1992. Enhancement of polypeptide and protein-absorption by macromolecular carriers *via* endocytosis and transcytosis. Advanced Drug Delivery Reviews 8(1):93-113.

3. Bickel U, Yoshikawa T, Pardridge WM 2001. Delivery of peptides and proteins through the blood-brain barrier. Advanced Drug Delivery Reviews 46(1-3):247-279.

4. Simionescu M, Popov D, Sima A 2009. Endothelial transcytosis in health and disease. Cell & Tissue Research 335(1):27-40.

5. Spencer BJ, Verma IM 2007. Targeted delivery of proteins across the blood-brain barrier. Proceedings of the National Academy of Sciences of the United States of America 104(18):7594-7599.

6. Li HY, Qian ZM 2002. Transferrin/transferrin receptor-mediated drug delivery. Medicinal Research Reviews 22(3):225-250.

7. Simionescu M, Gafencu A, Antohe F 2002. Transcytosis of plasma macromolecules in endothelial cells: A cell biological survey. Microscopy Research and Technique 57(5):269-288.

8. Brown MS, Kovanen PT, Goldstein JL 1981. Regulation of plasma cholesterol by lipoprotein receptors. Science 212(4495):628-635.

9. Li CX, Stifani S, Schneider WJ, Poznansky MJ 1991. Low density lipoprotein receptors on epithelial cells (Madin derby canine kidney)monolayers-Asymmetric distribution correlates with functional difference. Journal of Biological Chemistry 266(14):9263-9270.

10. Aisen P 1992. Entry of iron into cells- A new role for the transferrin receptor in modulating iron release from transferrin. Annals of Neurology 32:S62-S68.

11. Klausner RD, Vanrenswoude J, Ashwell G, Kempf C, Schechter AN, Dean A, Bridges KR 1983. Receptor-mediated endocytosis of transferrin in K562 cells Journal of Biological Chemistry 258(8):4715-4724.

12. Qian ZM, Li HY, Sun HZ, Ho K 2002. Targeted drug delivery *via* the transferrin receptor-mediated endocytosis pathway. Pharmacological Reviews 54(4):561-587.

13. Trowbridge IS, Newman RA, Domingo DL, Sauvage C 1984. Transferrin receptors - Structure and function Biochemical Pharmacology 33(6):925-932.

14. Widera A, Norouziyan F, Shen WC 2003. Mechanisms of TfR-mediated transcytosis and sorting in epithelial cells and applications toward drug delivery. Advanced Drug Delivery Reviews 55(11):1439-1466.

15. King GL, Johnson SM 1985. Receptor-mediated transport of insulin across endothelial cells Science 227(4694):1583-1586.

16. Roberts RL, Sandra A 1992. Receptor-mediated endocytosis of insulin by cultured endothelial cells Tissue & Cell 24(5):603-611.

17. Schnitzer JE, Sung A, Horvat R, Bravo J 1992. Preferential interaction of albumin-binding proteins, GP30 and GP18, with conformationally modified albumins- Presence in many cells and tissues with a possible role in catabolism Journal of Biological Chemistry 267(34):24544-24553.

18. Chuang VTG, Kragh-Hansen U, Otagiri M 2002. Pharmaceutical strategies utilizing recombinant human serum albumin. Pharmaceutical Research 19(5):569-577.

19. Mostov KE 1994. Transepithelial transport of immunoglobulins. Annual Review of Immunology 12:63-84.

20. Mostov KE, Simister NE 1985. Transcytosis. Cell 43(2):389-390.

21. Tuma PL, Hubbard AL 2003. Transcytosis: Crossing cellular barriers. Physiological Reviews 83(3):871-932.

22. Huebers HA, Finch CA 1987. The physiology of transferrin and transferrin receptors. Physiological Reviews 67(2):520-582.

23. Gomme PT, McCann KB 2005. Transferrin: structure, function and potential therapeutic actions. Drug Discovery Today 10(4):267-273.

24. Gatter KC, Brown G, Trowbridge IS, Woolston RE, Mason DY 1983. Transferrin receptors in human tissues- Their distribution and possible clinical relevance Journal of Clinical Pathology 36(5):539-545.

25. Bleil JD, Bretscher MS 1982. Transferrin receptor and its recycling in HeLa cells Embo Journal 1(3):351-355.

26. Bali PK, Zak O, Aisen P 1991. A new role for the transferrin receptor in the release of iron from transferrin. Biochemistry 30(2):324-328.

27. Ghosh RN, Gelman DL, Maxfield FR 1994. Quantification of low density lipoprotein and transferrin endocytic sorting in HEP-2 cells using confocal microscopy Journal of Cell Science 107:2177-2189.

28. Daniels TR, Delgado T, Helguera G, Penichet ML 2006. The transferrin receptor part II: Targeted delivery of therapeutic agents into cancer cells. Clinical Immunology 121(2):159-176.

29. Daniels TR, Delgado T, Rodriguez JA, Helguera G, Penichet ML 2006. The transferrin receptor part I: Biology and targeting with cytotoxic antibodies for the treatment of cancer. Clinical Immunology 121(2):144-158.

30. Gan CW, Feng SS 2010. Transferrin-conjugated nanoparticles of Poly(lactide)-D-alpha-Tocopheryl polyethylene glycol succinate diblock copolymer for targeted drug delivery across the blood-brain barrier. Biomaterials 31(30):7748-7757.

31. Hughson EJ, Hopkins CR 1990. Endocytic pathways in polarized Caco-2 cells: identification of an endosomal compartment accessible from both apical and basolateral surfaces. The Journal of Cell Biology 110(2):337-348.

32. Kishimoto T, Tavassoli M 1987. Transendothelial transport (transcytosis) of iron transferrin complex in the rat liver American Journal of Anatomy 178(3):241-249.

33. Hubatsch I, Ragnarsson EGE, Artursson P 2007. Determination of drug permeability and prediction of drug absorption in Caco-2 monolayers. Nat Protocols 2(9):2111-2119.

34. Artursson P 1990. Epithelial transport of drugs in cell culture. I: A model for studying the passive diffusion of drugs over intestinal absorbtive (Caco-2) cells. Journal of Pharmaceutical Sciences 79(6):476-482.

35. Rigler R, Mets U, Widengren J, Kask P 1993. Fluorescence correlation spectroscopy with high count rate and low background- Analysis of translational diffusion. European Biophysics Journal with Biophysics Letters 22(3):169-175.

36. Godin AG, Costantino S, Lorenzo L-E, Swift JL, Sergeev M, Ribeiro-da-Silva A, De Koninck Y, Wiseman PW 2011. Revealing protein oligomerization and densities *in situ* using spatial intensity distribution analysis. Proceedings of the National Academy of Sciences 108(17):7010-7015.

37. Sergeev M. 2010. Measurement of oligomerization states of membrane proteins *via* spatial fluorescence intensity fluctuation analysis. Department of Physics, ed., Montreal: McGill University. p 208.

38. Swift JL, Godin AG, Doré K, Freland L, Bouchard N, Nimmo C, Sergeev M, De Koninck Y, Wiseman PW, Beaulieu J-M 2011. Quantification of receptor tyrosine kinase transactivation through direct dimerization and surface density measurements in single cells. Proceedings of the National Academy of Sciences 108(17):7016-7021.

39. Héctor GP, Irene C, Isabel P, Oriol A, Stephan T 2012. Standardized relative quantification of immunofluorescence tissue staining. Nature Protocols.

40. McGlynn H. 2009. Modelling Drug Delivery in *In vitro* 3D Cellular Assemblies School of Pharmacy and Pharmaceutical Sciences, ed., Manchester: University of Manchester. p 179.

41. Bur M, Huwer H, Lehr C-M, Hagen N, Guldbrandt M, Kim K-J, Ehrhardt C 2006. Assessment of transport rates of proteins and peptides across primary human alveolar epithelial cell monolayers. European Journal of Pharmaceutical Sciences 28(3):196-203.

42. Griffiths WJH, Cox TM 2003. Co-localization of the Mammalian Hemochromatosis Gene Product (HFE) and a Newly Identified Transferrin Receptor (TfR2) in Intestinal Tissue and Cells. Journal of Histochemistry & Cytochemistry 51(5):613-623.

43. Lim C-J, Norouziyan F, Shen W-C 2007. Accumulation of transferrin in Caco-2 cells: A possible mechanism of intestinal transferrin absorption. Journal of Controlled Release 122(3):393-398.

44. Zhu ZB, Makhija SK, Lu BG, Wang MH, Rivera AA, Preuss M, Zhou F, Siegal GP, Alvarez RD, Curiel DT 2004. Transport across a polarized monolayer of Caco-2 cells by transferrin receptor-mediated adenovirus transcytosis. Virology 325(1):116-128.

45. Gagescu R, Demaurex N, Parton RG, Hunziker W, Huber LA, Gruenberg J 2000. The recycling endosome of Madin-Darby canine kidney cells is a mildly acidic compartment rich in raft components. Molecular Biology of the Cell 11(8):2775-2791.

46. Gerlier D, Thomasset N 1986. Use of MTT colorimetric assay to measure cell activation. Journal of Immunological Methods 94(1-2):57-63.

47. Mosmann T 1983. Rapid colorimetric assay for cellular growth and survival: Application to proliferation and cytotoxicity assays. Journal of Immunological Methods 65(1-2):55-63.

Chapter 7

GENERAL DISCUSSION AND CONCLUSIONS

In this thesis the application of image analysis tools (i.e. RICS[1] and SpIDA[2]) to some aspects of relevance to biopharmaceutical (i.e. protein aggregation) and small molecule drug development (i.e. p-glycoprotein expression, inhibition and transcytosis) has been explored to assess their potential for providing further parametric insights into each of these processes.

Until recently, confocal fluorescence imaging entailed semi-quantitative assessment of fluorescence intensities and their distributions; however, advances in algorithms allowing spatiotemporal mapping of concentrations and dynamics have opened avenues for the application of microscopy as a quantitative tool in the elucidation of a diverse range of biophysical and biochemical parameters investigated in this thesis. To illustrate these new opportunities, three biologically and pharmaceutically-relevant problems were selected namely protein aggregation, quantification of immunofluorescently-labelled transporters and intracellular accumulation of Calcein-AM, Cell Trace™ Calcein red-orange AM and transferrin as model compounds. These research themes were characterised using RICS, SpIDA and Image J® and cross-validated against traditional assays and the literature.

Though much research effort over the recent decades has focused on profiling and preventing protein aggregation in samples and numerous analytical approaches have been validated for this purpose, each are recognised to possess caveats (i.e. analyte size ranges or sample pre-treatment requisites) necessitating the development and validation of novel approaches with improved capabilities in detecting broad particle (i.e. aggregate) size ranges.

For example- to our knowledge - RICS was applied for the first time to the quantification of protein aggregation and diffusion behaviour providing the capability to both semi-quantitatively profile aggregate sub-populations through the construction of three-dimensional contour plots of population concentrations and their corresponding diffusion coefficients, and enable statistical interpretation of aggregate sub-populations contained within samples.[3]

Image analysis approaches introduced and applied in this thesis (RICS and SpIDA) offer a potential avenue for the *in situ* assessment of small volume polydisperse (i.e. ranging from the assessment of oligomer formation to the presence of sub-micron particles) and high concentration protein samples in their native environments. These

capabilities offer the potential for continuous monitoring of temporal sample evolution without influencing the characteristics of the sample, thereby, enabling the real-time assessment of monomer loss and subsequent aggregate formation from solution. Such data can be insightful in determining the mechanism by which sub-visible aggregates are formed and further applied to assessing potential patient safety issues.

Furthermore, direct imaging of the sample provides a visual means of assessing the presence of larger aggregates in images (i.e. for particles larger than a few hundred nanometers) and the same image time series could be analysed using multiple image analysis tools (e.g. SpIDA and Image J®). The capability to monitor the evolution of particle size distributions as a function of formulation-related and environmental stresses with time render this method attractive with the potential for application to the early development profiling of novel products during early stages of the biopharmaceutical product lifecycle.

An often misconstrued disadvantage associated with labelling protein aggregates relates to the pre-requisite for fluorophore presence that with current increasing availability of extrinsic aggregate labelling dyes and imaging approaches exploiting intrinsic fluorescence emission is no longer a pitfall. In fact labelling of specific aggregate size ranges and morphologies can support the assessment of species of interest in isolation, an added advantage to the application of these approaches.[4]

Membrane-related expression and transport phenomena were studied in this thesis. Proteomics and molecular biology-based approaches have been used over the recent decades to quantify transporter and receptor expression each possessing their own relative merits. Such methods have revolved around inter-lab standardisation to drive reproducibility in the assessment of protein expression. Immunofluorescence, a commonly-utilised molecular biology tool, is a relatively simple and rapid approach to the quantification and localisation of transporters. At present, analysis of immunofluorescent labelling relies on direct comparison between the fluorescence of samples to determine the expression and consequently prognosis-related factors; hence there is a demand for image analysis tools quantifying the density of labelled species to facilitate their direct comparison.[5]

Regularly-applied bulk methods (e.g. mass spectrometry)[6] analysing cell fractions and lysates whilst providing absolute abundances of transporter expression in tissues, do not

offer the potential to visualise and locate the expression of transporters and data acquisition using these methods remains to be time-consuming. In this thesis immunofluorescence staining of the p-glycoprotein transporter was performed in multiple cell lines (i.e. control and *MDR1*-transfected) and the standard reported approach (i.e. quantitative immunofluorescence) compared to SpIDA.

Analysis of labelled p-glycoprotein transporters and transferrin receptors entailed their qualitative membrane and intracellular localisation, revealing results consistent with the dynamic nature of the plasma membrane, whilst permitting quantitative analysis of heterogeneities in expression between cell types and in various subcellular regions.

To further validate the capabilities of SpIDA in the quantification of labelled species, p-glycoprotein expression was assessed in Caco-2 monolayers as a function of confluency and polarisation, the outcome of which following immunofluorescence staining was consistent with previously reported differences in the magnitude of expression as a function of culture age (using LC-MRM) and reported digoxin efflux ratios in the literature.[7]

The novelty of this approach lies in the absolute quantification of labelled species from fluorescent confocal images combined with the direct visualisation of proteins in their native environment enabling the concomitant qualitative and quantitative analysis of cell or tissue samples in comparison to previous reports of image segmentation and the determination of integrated densities (i.e. assessment of pixel Gray values).[8-10] It is envisaged that the application of an image analysis approach robust to photobleaching and optical setup will eliminate artefacts associated with routine fluorescence measurements and offer a more reliable tool in the quantitative assessment of labelled transporters of importance to molecular biology and determination of prognoses from biopsies in the clinic.[11]

Following the application of SpIDA to the quantification of labelled p-glycoprotein transporters, to probe p-glycoprotein function, the Calcein retention assay[12] was performed in MDCK-*MDR1* and MDCK-*wt* cell lines to determine subcellular and intercellular heterogeneities as a function of incubation time with verapamil (i.e. a p-glycoprotein inhibitor) and Calcein-AM. Whilst permitting the direct microscopic examination and visualisation of Calcein retention in both cell lines, subsequent analysis with SpIDA enabled the quantification of intracellular Calcein concentrations

and intercellular heterogeneities in each image an aspect that no current method is able to address.

Membrane-related transport processes concerning the uptake of transferrin-Alexa Fluor® 647 (i.e. vesicular) and Cell Trace™ Calcein red-orange AM (i.e. passive diffusive) as drug models were assessed in both polarised Caco-2 monolayers and monolayers seeded on eight well chamber slides using the conventional apparent permeability bulk assay (i.e. spectrofluorimetric assessment) and microscopic analysis (i.e. routine fluorescence, SpIDA and FIGMAA). Data obtained from the SpIDA analysis of intracellular Cell Trace™ Calcein red-orange in cell populations was compared against that of data previously acquired in the research group using fluorescence correlation spectroscopy.

Vesicular transport of labelled transferrin was assessed in Caco-2 and HeLa cell lines through imaging and the use of routine apparent permeability assays across polarised monolayers. Results obtained from this study revealed a poor permeability and disadvantages associated with the application of bulk black box methods currently relate to the lack of insight provided by these methods into the determination of intracellular processes.

Concentration-related parameters obtained from SpIDA analysis of Cell Trace™ Calcein red-orange intracellular accumulation in cell populations were found to be consistent with previous reported data in the group, confirming both the precision and applicability of this method to the analysis of intracellular concentrations with the added advantage of rapid data acquisition over larger sampling area in comparison to fluorescence correlation spectroscopy. Additionally, image acquisition enabled the analysis of samples using more than one image analysis software such that RICS was applied to the determination of intracellular diffusion of Cell Trace™ Calcein red-orange also yielding parameters consistent with previous reports in the group.

Through the application of image analysis tools to the assessment of protein aggregation, transporter/receptor expression and cellular transport processes in this thesis, the following themes have emerged as potential areas for future exploration;

- Extending the application of imaging to the determination of foreign particulate presence using differential interference contrast imaging and development of a medium-throughput platform for image acquisition.
- The validation of high content screening systems and concomitant assessment of other intracellular processes could drive a better understanding of intercellular heterogeneities and cytotoxicity elicited as a consequence of incubation with potential drugs.
- Determining receptor oligomerisation through exploitation of the direct relationship existent between monomer quantal brightness values and aggregation, introduces the potential to examine receptor oligomerisation in sub-cellular domains when performing SpIDA. Furthermore, in systems transfected with GFP it would be a plausible means of assessing receptor oligomerisation following the association of transferrin with GFP-labelled TfR, and contribute to further quantitative elucidation of receptor-mediated transcytosis and the fate of internalised ligands.
- Optimisation of image acquisition conditions for vesicles susceptible to photobleaching and subsequent assessment of vesicular transport using live cell imaging and image analysis to further assess the significance of this route to drug delivery.
- Caco-2 polarised monolayers were used as a gastrointestinal model in this study, the principles of which may be extended to alveolar epithelia, blood-brain barrier and skin models. Furthermore, following validation of image analysis and a better understanding of transcellular vesicular transport mechanisms, such studies could eventually be extended for application to *in vivo* systems (e.g. multiphoton imaging).
- Further validation of FIGMMA (an in-house software) and identification of potential areas for application.
- The use of image analysis tools in assessing protein aggregation, transporter expression and cellular transport processes has revealed the potential scope for application of these methods to studying these phenomena and at present there remains further areas for the implementation of image analysis tools beyond this thesis ranging from the mechanistic assessment of processes contributing to the pathophysiology of neurodegenerative disorders (e.g. Alzheimer's disease) to the quantification of transporter expression and assessment of signal transduction pathways.

With current advances in imaging capabilities including high-resolution and label-free imaging (i.e. stimulated Raman scattering microscopy), the prospects of extending the

application of image analysis tools to the characterisation of a diverse range of processes is becoming a reality. It is envisaged that through the selection of relevant image acquisition techniques coupled to the appropriate image analysis tools and their validation in combination with traditional approaches, many of the current questions to the biochemist, molecular biologist, formulation scientist and biophysicist will be answered over the next few decades.

7.1 References

1. Digman MA, Brown CM, Sengupta P, Wiseman PW, Horwitz AR, Gratton E 2005. Measuring fast dynamics in solutions and cells with a laser scanning microscope. Biophysical Journal 89(2):1317-1327.

2. Godin AG, Costantino S, Lorenzo L-E, Swift JL, Sergeev M, Ribeiro-da-Silva A, De Koninck Y, Wiseman PW 2011. Revealing protein oligomerization and densities *in situ* using spatial intensity distribution analysis. Proceedings of the National Academy of Sciences 108(17):7010-7015.

3. Hamrang Z, Pluen A, Zindy E, Clarke D 2012. Raster image correlation spectroscopy as a novel tool for the quantitative assessment of protein diffusional behaviour in solution. Journal of Pharmaceutical Sciences 101(6):2082-2093.

4. Hawe A, Sutter M, Jiskoot W 2008. Extrinsic Fluorescent Dyes as Tools for Protein Characterization. Pharm Res 25(7):1487-1499.

5. Colombo PC, Ashton AW, Celaj S, Talreja A, Banchs JE, Dubois NB, Marinaccio M, Malla S, Lachmann J, Ware JA, Le Jemtel TH 2002. Biopsy coupled to quantitative immunofluorescence: a new method to study the human vascular endothelium. Journal of Applied Physiology 92(3):1331-1338.

6. Zhang Y, Li N, Brown PW, Ozer JS, Lai Y 2011. Liquid chromatography/tandem mass spectrometry based targeted proteomics quantification of P-glycoprotein in various biological samples. Rapid Communications in Mass Spectrometry 25(12):1715-1724.

7. Miliotis T, Ali L, Palm JE, Lundqvist AJ, Ahnoff M, Andersson TB, Hilgendorf C 2011. Development of a Highly Sensitive Method Using Liquid Chromatography-Multiple Reaction Monitoring to Quantify Membrane P-Glycoprotein in Biological Matrices and Relationship to Transport Function. Drug Metabolism and Disposition 39(12):2440-2449.

8. Héctor GP, Irene C, Isabel P, Oriol A, Stephan T 2012. Standardized relative quantification of immunofluorescence tissue staining. Nature Protocols.

9. McMullen RL, Bauza E, Gondran C, Oberto G, Domloge N, Farra CD, Moore DJ 2010. Image analysis to quantify histological and immunofluorescent staining of ex vivo skin and skin cell cultures. International Journal of Cosmetic Science 32(2):143-154.

10. Mertz KD, Demichelis F, Kim R, Schraml P, Storz M, Diener P-A, Moch H, Rubin MA 2007. Automated immunofluorescence analysis defines microvessel area as a prognostic parameter in clear cell renal cell cancer. Human Pathology 38(10):1454-1462.

11. Zachbauer S, Gsur A, Brunner R, Kyrle PA, Lechner K, Pirker R 1994. P-glycoprotein expression as unfavorable prognostic factor in acute myeloid leukemia. Leukemia : official journal of the Leukemia Society of America, Leukemia Research Fund, UK 8(6):974-977.

Appendix 1

QUANTIFICATION OF THE LASER BEAM WAIST AND DETERMINATION OF PMT SHOT NOISE

A1.1 Quantification of the Laser Beam Waist

The diffusion times of Rhodamine Green™ and Texas Red™ were measured with a Zeiss Confocor 2 LSM510 equipped with an Argon laser excitation source (i.e. 488 nm) and Helium-Neon laser (i.e. 543 nm) using a 40x/1.2 NA water-immersion objective lens with 30 runs each of 10 seconds duration. A single component fit was utilised to derive the diffusion time and following the application of the following equation the laser waist beam was determined;

$$\tau_D = \frac{\omega_0^2}{4D} \qquad \textit{Equation A 1.1}$$

The laser beam waist, ω_0, for the Argon and Helium-Neon excitation lasers was derived from the autocorrelation curves (ACF) obtained from Rhodamine Green™ and Texas Red™ diffusion through the confocal volume. Using previously reported diffusion coefficients of Rhodamine 6G (2.8×10^{-6} cm^2/sec)[1] and TAMRA (2.6×10^{-6} cm^2/sec)[2], the laser waist beam was determined- this assumption was made as the molecular weight of Rhodamine Green™ (507 g/mol) and Texas Red™ (625 g/mol) is similar to that of Rhodamine 6G (479 g/mol) and TAMRA (550 g/mol), respectively.[1,2] Corresponding diffusion times obtained from FCS analysis of Rhodamine Green™ and Texas red™ using the Confocor 2 LSM510 setup were 18.95±2.61 (ω_0: 0.139±0.001 µm) and 32±0.60 (ω_0: 0.194±0.001 µm) microseconds, respectively.

A1.2 Characterisation of Photomultiplier Tube (PMT) Shot Noise

Varying PMT voltage conditions and laser powers may be used to assess the conditions under which direct linearity is existent between the photoelectric current and the measured fluorescence intensity. This is significant since the derived brightness and number of particles parameters following SpIDA analysis of confocal images are strongly influenced by shot noise. In this study this measurement was performed through imaging immobilised pre-bleached beads (Zeiss, Jena, Germany) using either an Argon or Helium-Neon excitation laser and a c-Apochromat 40 x/NA 1.2 water-immersion objective. The beads were excited over a range of laser powers, at different PMT gains (i.e. 600, 650, 700 and 750), pixel dwell times and the results averaged for 1024 points (i.e. pixels).

The PMT shot noise for a 40x/1.2 NA c-Apochromat water immersion objective lens was characterised for both the Argon (i.e. 488 nm) and Helium-Neon (i.e. 543 nm) laser lines. The results obtained from these measurements at gains 600, 650 and 700 are presented as follows;

A1.2.1 The Influence of Pixel Dwell Time

Similarly, for the pixel dwell time (i.e. 6.4 μs) and gain settings (i.e. gain 700) utilised in Chapter 4 for SpIDA analysis of monomer loss the following PMT curve of shot noise was obtained;

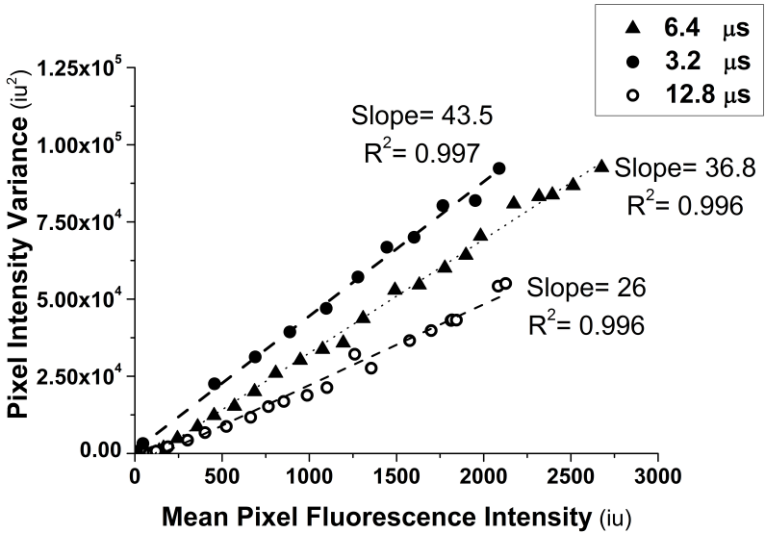

Figure A 1.1 *Plot of pixel intensity variance versus mean pixel fluorescence intensity as a function of pixel dwell time measured for a Zeiss LSM 510 setup with a corresponding detector gain of 700 (n=1024).*

The two pixel dwell times of 6.4 and 12.8 microseconds were utilised for acquiring image time series in the assessment of BSA monomer loss and subsequent assessment using SpIDA. The determined slope variance for this series of image acquisition parameters is presented above in Figure A 1.1.

A1.2.2 The Influence of Detector Gain

In chapters 4 and 5 the influence of detector gain was examined on images acquired with a pixel dwell time of 3.2 microseconds. Hence this parameter was measured for detector gains 600, 650 and 700 and is presented as follows;

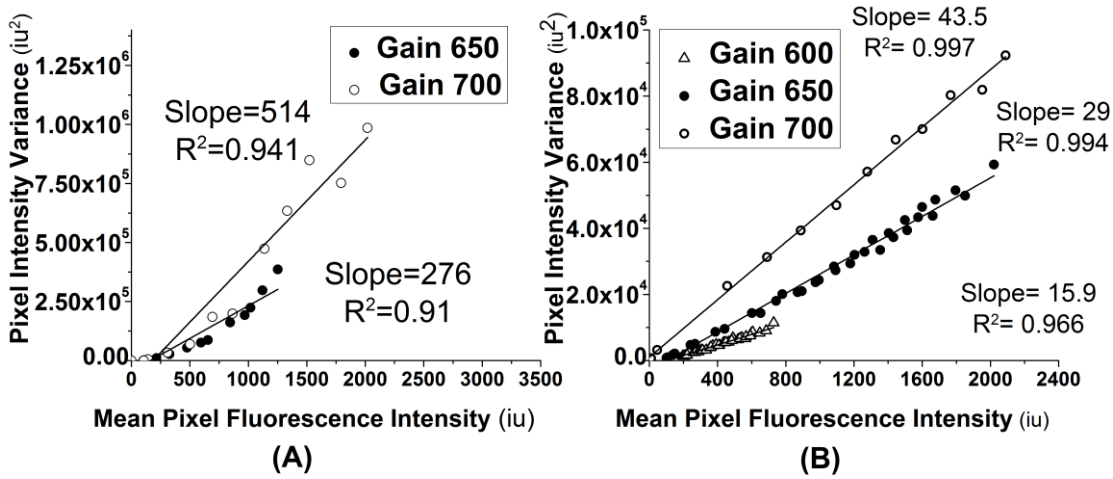

Figure A1.2 *Plots of pixel intensity variance versus mean pixel intensity for* ***(A)*** *a 543 nm Helium-Neon and* ***(B)*** *a 488 nm Argon laser for various detector gain settings (n=1024).*

The line of best fit was determined at various detector gain settings within the linear pixel intensity range.

A1.3 References

1. Schwille P, Haupts U, Maiti S, Webb WW 1999. Molecular dynamics in living cells observed by fluorescence correlation spectroscopy with one- and two-photon excitation. Biophysical Journal 77(4):2251-2265.

2. Petrasek ZK, Schwille P 2008. Precise Measurement of Diffusion Coefficients using Scanning Fluorescence Correlation Spectroscopy. Biophysical Journal 94(4):1437-1448.

Appendix 2

COMPARING GAUSSIAN MIXTURE MODELS USING THE F-TEST

The pixel brightness space *X* represents all the possible values of brightness a pixel can take.

$X = (X_1, X_2, ..., X_n)$ *Equation A2.1*

The brightness histogram of *m* pixels in an image or sub-region (i.e. region of interest) is normalised so that the total area under the histogram equals one. This is an estimation of the Probability Density Function *p(x)* of *X*, i.e. for each brightness value *x* in *X*, its estimated probability is *P(x)*.

This Probability Density Function *p(x)* is now modelled as a linear combination of *k* Gaussian distributions:

$$P(x|k) = \sum_{i=1}^{k} \frac{\omega_i}{\sigma_i \sqrt{2\pi}} e^{\frac{-(x-\mu)^2}{2\sigma_i^2}}$$ *Equation A2.2*

and each of the Gaussian distributions is defined by (μ, σ^2), as well as ω, a weight value in [*0,1*]. Hence the total number of parameters or degrees of freedom *dof|k* defining *p(x|k)* is *3k−1* as the sum of all the weights equates to 1.

The discrepancy between the probability histogram *P(x)* and the estimated Probability Density Function *p(x)* is measured using a Residual sum of squares (RSS).

$$RSS|k = \sum_{i=1}^{n} \left(P(x_i) - p(x_i|k)\right)^2$$ *Equation A2.3*

The two Probability Density Functions *p(x|k1)* and *p(x|k2)* estimated using a different number of Gaussian distributions k_1 and k_2, and $k_2 > k_1$ are subsequently compared in order assess the suitability of a more complex model over a simpler model. To do this, p(x|k2) must fit *P(X)* at least as well as $p(x|k_1)$, i.e. $RSS|k_2 \leq RSS|k_1$ and the F statistic is;

$$F = \frac{\left(\frac{RSS|k_1 - RSS|k_2}{dof|k_2 - dof|k_1}\right)}{\left(\frac{RSS|k_2}{m - dof|k_2}\right)}$$ *Equation A2.4*

The null hypothesis in this scenario is that model 2 does not provide a significantly better fit than model 1, F will have an F-distribution, with ($dof|k_2 - dof|k_1, m - dof|k_1$) degrees of freedom. The null hypothesis is rejected if the F calculated from the data is greater than the critical value of the F-distribution for some desired false-rejection probability (e.g. 0.05).[1]

A2.1 Acknowledgements

We would like to thank Dr Egor Zindy for his input and support in writing this section as the developer of FIGMMA.

A2.2 References

1. http://www.fcsxpert.com/classroom/analysis/choose_model.html, accessed on 10/10/2012.

Appendix 3

SUPPLEMENTARY INFORMATION FOR VALIDATION OF RICS AS A NOVEL TOOL FOR THE ASSESSMENT OF PROTEIN DIFFUSIONAL BEHAVIOUR IN SOLUTION

A3.1 Determination of the Point Spread Function

The PSF of the 40x/1.2 NA objective at 488 nm was measured through confocal imaging of immobilised green Fluospheres® acquired from Invitrogen (Paisley, UK) on microscope slides. In order to quantify the axial resolution, time series images (i.e. 5-200 frames) were captured of well-separated beads following manual focusing. The process was repeated for several beads and the images subjected to analysis using ManICS. Figure A3.1 presents a typical confocal image of several beads within a single frame.

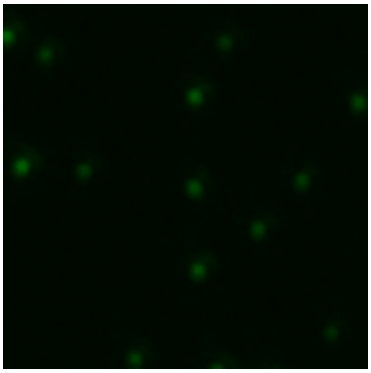

Figure A3.1 *A typical confocal micrograph of immobilised green 0.1 µm Fluospheres® in the x-y direction*

The magnitude of ω_0 determined by imaging of the immobilised beads was determined as 0.363 ± 0.013 µm same as the value obtained from the RICS analysis of 0.5 µM Rhodamine Green™. Hence a pixel size of 40 nm was selected for further measurements.

A3.2 Assessment of the Impact of Freeze-thaw Cycling in Higher Concentration Unlabelled BSA Samples

Whilst in the manuscript the application of RICS analysis to small particle/aggregate sizes, has been demonstrated, using dyes that associate with hydrophobic pockets (i.e., Proteostat®) or are covalently-bound, it is possible to also characterise larger aggregates and structures of up to a few microns (i.e. sub-visible particles). The micrograph displayed in Figure A3.2 provides a confocal image of aggregates in solution labelled with Proteostat®. Results obtained from the RICS analysis performed on 25 mg/mL BSA samples freeze-thawed and subsequently incubated with Proteostat® yielded a

diffusion coefficient of 3.29±0.50 x 10^{-8} cm^2/s. This value is in reasonable agreement with the estimated diffusion coefficient calculated from the Stoke-Einstein equation for a particle with similar dimensions deduced from a confocal micrograph (i.e. ~2.5x10^{-8} cm^2/s) possessing aggregates with similar dimensions and appearance to that of Figure A3.2.

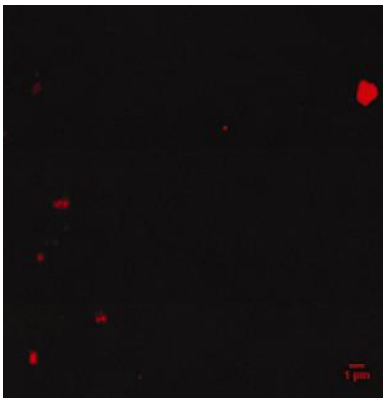

Figure A3.2 *Confocal micrograph of aggregates labelled with Proteostat® in a 1mg/mL BSA sample following 48 hours of freeze-thaw treatment.*

The added capability of RICS to specifically characterise and study aggregates or sub-visible particles could potentially be of great importance in the exclusive characterisation of such small fractions in biopharmaceutical preparations and their subsequent contribution to immunogenicity,[2] an area where there still remains a need for novel technologies.[1] Given the multi-functionality of RICS analysis, it would be possible using the same approach/images to characterise the interaction of aggregates with immune cells in conjunction with other novel image analysis tools (i.e. Spatial Intensity Distribution Analysis, etc).

A3.3 The Influence of Guanidine-Induced Denaturation on Derived RICS Parameters

Guanidine-induced denaturation was performed with a 6 M solution of guanidine (Gdn.HCl) and the subsequent overnight storage of the samples prior to characterisation with confocal microscopy and FCS.

Figure A3.3 presents the 3D population distribution obtained from RICS analysis of **(A)** a pH 7 control sample and **(B)** a sample following overnight storage with 6 M guanidine of the same ionic strength (i.e. 150 mM).

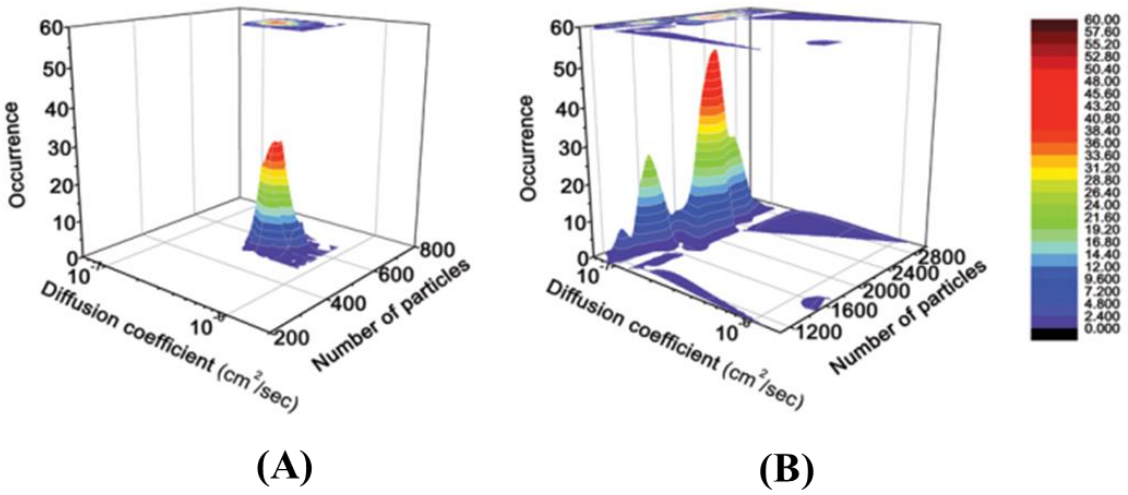

Figure A3.3 *A 3D contour plot of map distributions obtained from a 1 µM BSA-AF488 sample of* ***(A)*** *150 mM ionic strength (pH 7) as a control and* ***(B)*** *following overnight incubation with 6 M guanidine hydrochloride. A time series of confocal images of 1024 x 1024 resolution were acquired with a pixel time of 12.8 microseconds, line time of 15.5 milliseconds and a frame time of 0.0155 seconds.*

The different distributions obtained from 1 µM BSA-AF488 in normal conditions **(A)** and in presence of 6 M guanidine **(B)** are easily observed. There is a sharp decrease in the diffusion coefficient in presence of 6 M guanidine. These results are comparable to the study of BSA with FCS by Ghosh *et al*.[3] Interestingly, the apparent number of particles increases sharply but does not follow theoretical calculations of the expected number of particles for a 1 µM sample (i.e. ~550). Hence, the 6 M guanidine denatured sample was tested using a spectrofluorimeter and the results obtained from FCS experiments (Confocor 2, Zeiss): both exhibited a similar increase in fluorescence intensity (values) and in the number of particles. These observations were noted in by Das Kumar *et al*.[4] considering the interaction of human serum albumin with charged ionic species.

A3.4 The Influence of Sample Preparation Conditions on the Diffusion of BSA-AF488

A3.4.1 Buffer Composition

Results of the R^2 of optimal fits obtained from RICS analyses following variation of the buffer composition is presented in Figure A3.4;

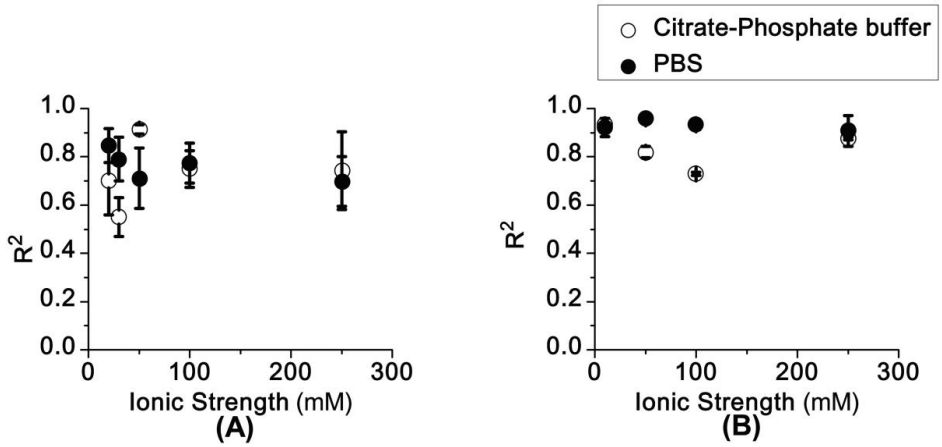

Figure A3.4 *The goodness of fit for data fitted using ManICS in Figures 2.4C-F following variation of buffer composition.*

Results indicate a consistently higher R^2 values from the fits performed on the PBS data (not statistically significant).

A3.4.2 Sample Filtration Treatment

The quality of the fit obtained from the comparison of non-filtered and 0.4 µm filtered data with that of 0.2 µm filtered samples has been presented in Figure A3.5. Filtered samples were found to consistently posses a higher R^2, also an indicator of homogeneity or aggregation in a system, compared to non-filtered and 0.4 µm pore-sized filters.

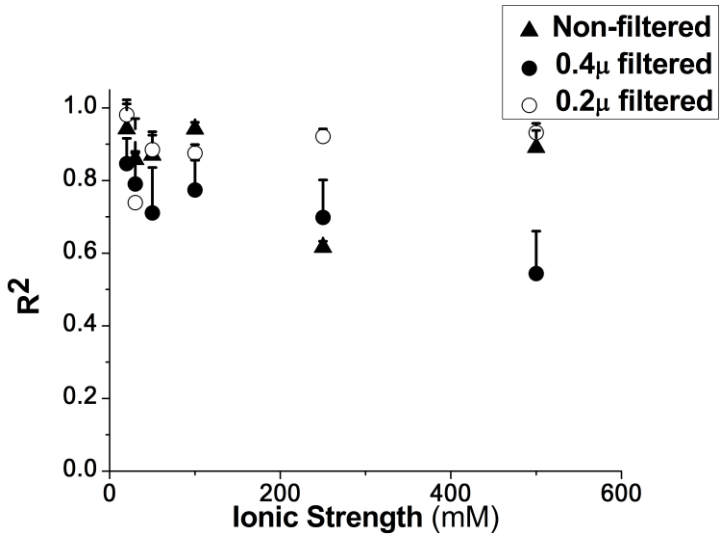

Figure A3.5 *Parameters of the goodness of fit obtained from the fitting of non-filtered (▲), 0.4 μm filtered (●), and 0.2 μm filtered (○) confocal images in ManICS.*

A3.5 References

1. Mueller M, Lindner B, Kusumoto S, Fukase K, Schromm AB, Seydel U 2004. Aggregates are the biologically active units of endotoxin. Journal of Biological Chemistry 279(25):26307-26313.

2. Mahler H-C, Friess W, Grauschopf U, Kiese S 2009. Protein aggregation: pathways, induction factors and analysis. Journal of Pharmaceutical Sciences 98(9):2909-2934.

3. Ghosh R, Sharma S, Chattopadhyay K 2009. Effect of arginine on protein aggregation studied by fluorescence correlation spectroscopy and other biophysical methods†. Biochemistry 48(5):1135-1143.

4. Kumar Das D, Kumar Das A, Kumar Mandal A, Mondal T, Bhattacharyya K 2012. Effect of an Ionic liquid on the Unfolding of Human Serum Albumin: A Fluorescence Correlation Spectroscopy Study. ChemPhysChem 13(7):1949-1955.

Appendix 4

SUPPLEMENTARY INFORMATION FOR THE APPLICATION OF IMAGE ANALYSIS TO THE QUANTIFICATION OF MONOMER LOSS AND AGGREGATION IN SOLUTION

A4.1 Assessment of White Noise Contribution

The contribution of citrate-phosphate buffer (i.e. pH 7) to background noise was assessed using confocal microscopy. A sample of citrate-phosphate buffer was placed in an eight well chamber slide and representative confocal images of the buffer acquired at the same pixel dwell time (i.e. 6.4 µs) and resolution (i.e. 44 nm) as the image time series. Representative images obtained from imaging citrate-phosphate buffer are presented in Figure A4.1.

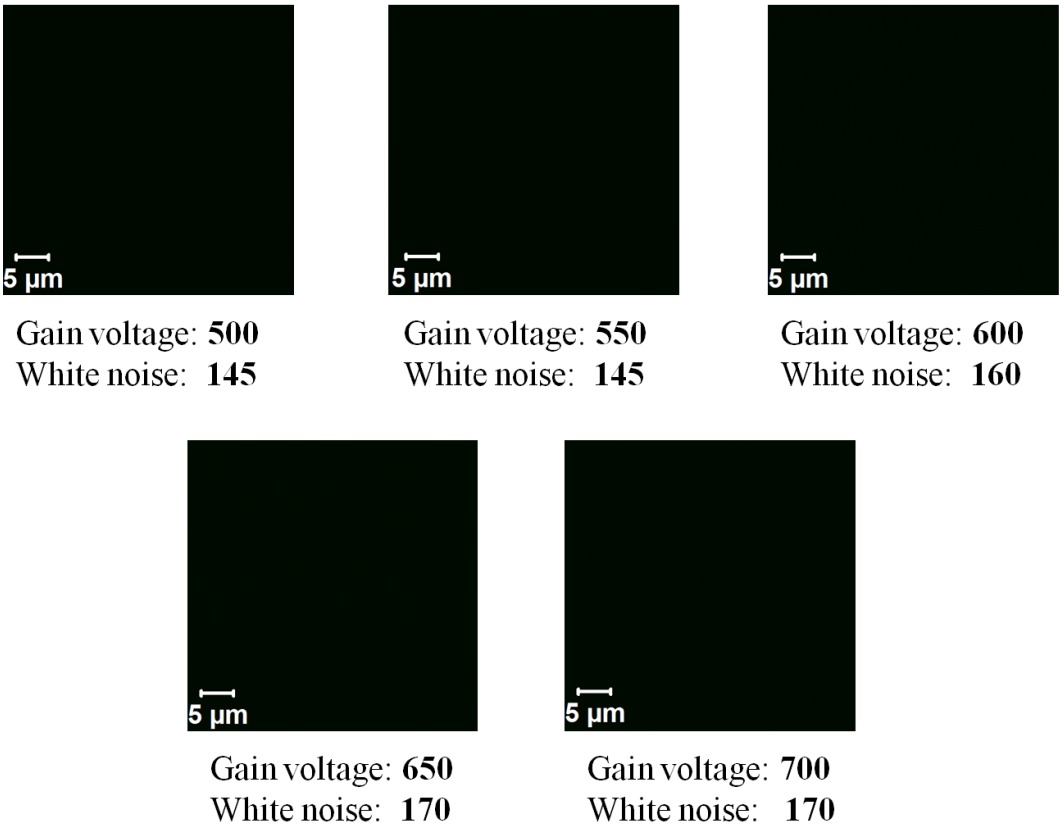

Figure A4.1 *Confocal image of citrate-phosphate buffer solution acquired with a pixel dwell time of 6.4 µs and pixel size of 44 nm for a 1024 x 1024 pixel image.*

Subsequently citrate-phosphate buffer images were subjected to analysis using Image J® and the fluorescence intensity determined for the image determined as white noise. This parameter was inputted into the SpIDA user interface for all analysed image time series experiments.

A4.2 Quantification of the Quantal Brightness of Monomeric BSA-Alexa Fluor®488

As aforementioned in the introduction of this thesis, it is possible to exploit the direct relationship between the quantal brightness of a monomeric entity and a dimer ($\varepsilon = 2\varepsilon_0$) in order to determine the spatiotemporal evolution of subpopulations in samples (i.e. image time series) consistent with aggregation.

When two fluorescent populations with different molecular quantal brightnesses are present within a sample (i.e. a confocal image) and not spatially segregated, or in the presence of autofluorescence, the total histogram becomes a convolution of the two distributions obtained from each species;

$$H(\varepsilon_1, N_1, \varepsilon_2, N_2, A; k) = H(\varepsilon_1, N_1; k) \otimes H(\varepsilon_2, N_2; k) \qquad \textit{Equation A4.1}$$

Where A_i represents the number of pixels, N_i represents the number of particles and ε_i represents the molecular quantal brightness for the *n*th population.

Application of a one-population model in a mixed sample will yield a resultant ε intermediate between the present species in the sample, whilst following performance of a monomeric ε control test it is possible to extract information about the present populations using a two-population (i.e. monomer-oligomer) model. Thereby, through appropriate knowledge of monomeric ε it is possible to determine spatiotemporal aggregation profiles from confocal image time series.

Hence, the brightness of monomeric BSA-AF488 obtained from size exclusion chromatography with a final concentration of 1.5 mg/ml (i.e. 22.5 μM) was diluted to 1 μM and subjected to confocal microscopy. Resultant images were analysed using SpIDA over 100 frames and the population data and corresponding quantal brightness were determined. The determined quantal brightness was applied to all further measurement of aggregation.

The determined molecular quantal brightness for the monomeric form of BSA-AF488 from an images time series was 1.4 ± 0.2.

A4.3 Descriptive Statistics of BSA-AF488 Samples Subjected to Analysis with RICS

To further profile the particle size distributions in monomeric BSA samples to SpIDA analysis and gain quantitative dynamic information of diffusion, RICS analysis was performed on image time series acquired from each time point. Representative number of particles data for each time point is presented in Table A4.1 as follows;

Table A4.1 *A summary of the temporal evolution of diffusion coefficients ($cm^2/sec \times 10^7$) and number of particles obtained from the analysis of image time series at specific time points (n=900) following RICS analysis ($P < 0.05$) where LQR and UQR represent the lower and upper quartile range of diffusion coefficients, respectively.*

Time/min	Parameter	Mean	Median	St. dev.	Min	Max	LQR	UQR
30	$D \times 10^7$	2.50	2.61	0.74	1.03	8.35	2.10	3.00
	N	1717	1745	155	1215	2130	1636	1827
60	$D \times 10^7$	1.78	1.67	0.57	1.03	5.34	1.47	1.93
	N	626	605	84	548	1080	594	622
90	$D \times 10^7$	1.50	1.40	0.55	0.95	5.70	1.20	1.60
	N	600	591	55	490	937	572	612
120	$D \times 10^7$	2.41	2.48	0.69	0.73	4.69	1.98	2.97
	N	1252	1265	86.	715	1461	1230	1300

Representative diffusion coefficients determined from RICS analysis of image time series at each time point demonstrate a reduction in the diffusion coefficient consistent with the formation of larger aggregate moieties in the sample. A reduction in the number of particles is associated with the formation of aggregates and this phenomenon was observed with images acquired from samples between 30-90 minutes.

A4.4 Real-time Samples

Confocal image time series of 150 frames were acquired for real-time experiments providing number of particle and diffusion coefficients at various time points. Representative parameters obtained from the statistical analysis of these image time series with RICS are presented in Tables A4.2-A4.4 for 0.4 mg/mL samples as follows;

Table A4.2 *Representative statistical parameters obtained from the RICS analysis of a BSA-AF488 sample in the presence of 50 mM NaCl subjected to thermal stress at 50 °C where LQR and UQR represent the lower and upper quartile range, respectively.*

Time/min		Mean	Median	St. Dev.	Min	Max	LQR	UQR
80	$D \times 10^7$	4.45	4.86	0.64	0.64	7.97	3.55	5.47
	N	531	529	51	476	1582	516	544
160	$D \times 10^7$	3.96	4.75	1.50	0.82	7.97	3.24	5.70
	N	530	524	94	504	1675	513	535
240	$D \times 10^7$	6.60	6.78	1.24	1.00	9.90	6.19	7.49
	N	504	495	117	481	1911	487	507

Data presented in Table A4.2 above indicates the presence of larger aggregates in the sample as observed with lower diffusion coefficients for the minima (e.g. 8.2 x 10^{-8} cm^2/sec at 160 minutes). Data presented indicates a reduction in number of particles with time consistent with aggregation.

Table A4.3 *Representative statistical parameters obtained from the RICS analysis of a BSA-AF488 sample in the presence of 150 mM NaCl subjected to thermal stress at 50 °C where LQR and UQR represent the lower and upper quartile range, respectively.*

Time/min		Mean	Median	St. Dev.	Min	Max	LQR	UQR
80	$D \times 10^7$	3.82	4.72	1.58	0.73	7.97	2.96	5.33
	N	535	525	106	490	1627	514	535
160	$D \times 10^7$	3.33	4.29	1.51	0.59	7.97	2.48	4.86
	N	529	527	69	477	1585	513	541
240	$D \times 10^7$	4.82	4.86	0.84	1.64	9.20	4.38	5.37
	N	680	682	33	489	794	660	701

Data presented in Table A4.3 above indicates the presence of larger aggregates in the sample as observed with lower diffusion coefficients for the minima (e.g. 8.2×10^{-8} cm^2/sec at 160 minutes). Furthermore, an initial reduction in particle numbers is observed consistent with the formation of aggregates at these time points.

Table A4.4 *Representative statistical parameters obtained from the RICS analysis of a BSA-AF488 sample in the presence of 500 mM NaCl subjected to thermal stress at 50 °C where LQR and UQR represent the lower and upper quartile range, respectively.*

Time/min		Mean	Median	St. Dev.	Min	Max	LQR	UQR
80	$D \times 10^7$	3.86	3.93	7.00	0.48	6.85	3.58	4.28
	N	1007	1006	36.2	884	1138	983	1030
160	$D \times 10^7$	4.63	4.62	7.86	1.31	8.13	4.26	5.10
	N	721	720	16	674	780	711	731
240	$D \times 10^7$	6.65	6.60	1.25	1.40	9.90	5.87	7.56
	N	591	593	24	491	659	580	606

Data presented in Table A4.4 above indicates the presence of larger aggregates in the sample as observed with lower diffusion coefficients for the minima (e.g. 4.8 x 10^{-8} cm^2/sec at 80 minutes). Despite an increase in the diffusion coefficient from 80 to 240 minutes, the corresponding number of particles was reduced in this experiment consistent with the formation of aggregates.

Representative parameters obtained from the statistical analysis of these image time series with RICS are presented in Tables A4.5-A4.7 for 1 mg/mL samples as follows;

Table A4.5 *Representative statistical parameters obtained from the RICS analysis of a BSA-AF488 sample in the presence of 50 mM NaCl subjected to thermal stress at 50 °C where LQR and UQR represent the lower and upper quartile range, respectively.*

Time/min		Mean	Median	St. Dev.	Min	Max	LQR	UQR
80	$D \times 10^7$	5.65	5.71	0.98	0.8	9.8	5.22	6.29
	N	1267	1269	38	1097	1379	1244	1293
160	$D \times 10^7$	7.4	7.54	1.34	0.35	9.98	6.6	8.46
	N	1469	1483	83	1061	1706	1433	1526
240	$D \times 10^7$	7.37	7.51	1.29	0.36	9.9	6.67	8.4
	N	1830	1845	111	1332	2137	1779	1905

Data presented in Table A4.5 above indicates the presence of larger aggregates in the sample as observed with lower diffusion coefficients for the minima (e.g. 8×10^{-8} cm^2/sec at 80 minutes). No reduction in the number of particles was observed within the experiment timescale, hence this parameter was not further utilised for any analyses.

Table A4.6 *Representative statistical parameters obtained from the RICS analysis of a BSA-AF488 sample in the presence of 150 mM NaCl subjected to thermal stress at 50 °C where LQR and UQR represent the lower and upper quartile range, respectively.*

Time/min		Mean	Median	St. Dev.	Min	Max	LQR	UQR
80	$D \times 10^7$	5.00	5.35	1.37	0.28	9.81	4.57	6.10
	N	2698	2738	215	1636	5697	2625	2823
160	$D \times 10^7$	6.10	6.36	1.31	0.23	9.83	5.68	7.00
	N	2604	2592	364	1711	5592	2521	2658
240	$D \times 10^7$	5.00	5.33	1.24	0.24	8.69	4.67	6.00
	N	2902	2922	295	1828	6438	2838	3000

Data presented in Table A4.6 above indicates the presence of larger aggregates in the sample as observed with lower diffusion coefficients for the minima (e.g. 2.8×10^{-8} cm^2/sec at 80 minutes). No reduction in the number of particles was observed within the experiment timescale, hence this parameter was not further utilised for any analyses.

Table A4.7 *Representative statistical parameters obtained from the RICS analysis of a BSA Alexa Fluor® 488 sample in the presence of 500 mM NaCl subjected to thermal stress at 50 °C where LQR and UQR represent the lower and upper quartile range, respectively.*

Time/min		Mean	Median	St. Dev.	Min	Max	LQR	UQR
80	$D \times 10^7$	5.40	5.50	0.93	0.62	8.80	5.00	6.00
	N	3142	3161	206	2378	6715	3071	3235
160	$D \times 10^7$	5.30	5.40	0.96	0.41	9.65	4.87	5.98
	N	3488	3510	136	2550	3816	3419	3579
240	$D \times 10^7$	4.49	4.58	0.86	0.43	9.31	4.11	5.10
	N	3750	3747	107	3399	4534	3680	3827

Data presented in Table A4.7 above indicates the presence of larger aggregates in the sample as observed with lower diffusion coefficients for the minima (e.g. 6.2 x 10^{-8} cm^2/sec at 80 minutes). No reduction in the number of particles was observed within the experiment timescale, hence this parameter was not further utilised for any analyses.

A4.5 Fluorescence Intensity Histograms of Confocal Image Time Series

In order to rule out the influence of photobleaching on the observed reduction in monomer numbers, the intensity histogram obtained from confocal image time series were investigated over the observation time.

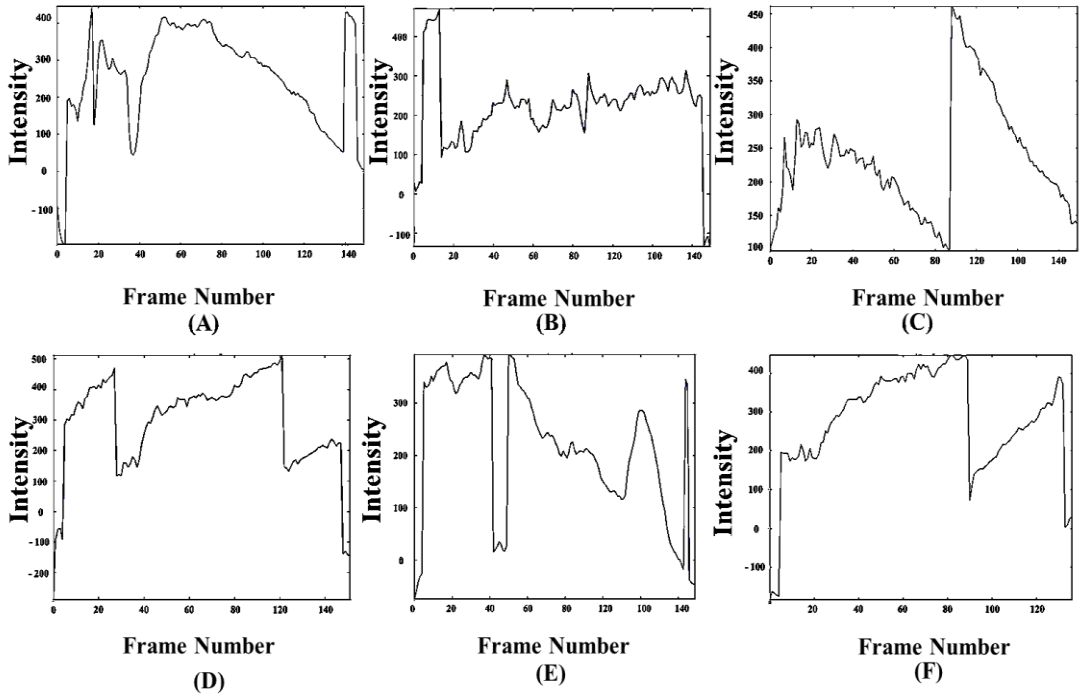

Figure A4.2 *Intensity histograms obtained for mobile components of confocal image time series for a* ***(A)*** *50 mM ionic strength 1 mg/mL* ***(B)*** *150 mM ionic strength 1 mg/mL* ***(C)*** *500 mM ionic strength 1 mg/mL* ***(D)*** *50 mM ionic strength 0.4 mg/mL* ***(E)*** *150 mM ionic strength 0.4 - mg/mL and* ***(F)*** *500 mM ionic strength 1 mg/mL sample of BSA-AF488 heated to 50 °C.*

As aforementioned, whilst RICS measurements are amenable to the effects of photobleaching SpIDA has previously been reported to be robust to the effects of photobleaching with little or no effect on output density parameters following bleaching. Images displayed in Figure A4.2 demonstrate no significant and constant decay for the samples with time; however, fitting of the autocorrelation was only performed within frame ranges where the fluorescence had stabilised.

A4.6 Confocal Micrographs of Aggregate Presence in BSA-AF488 Samples

To illustrate the presence of aggregates following exposure of labelled BSA samples to thermal stress at early time points (i.e.< 5 minutes), representative images were extracted from time series and presented in **Figure A4.3**.

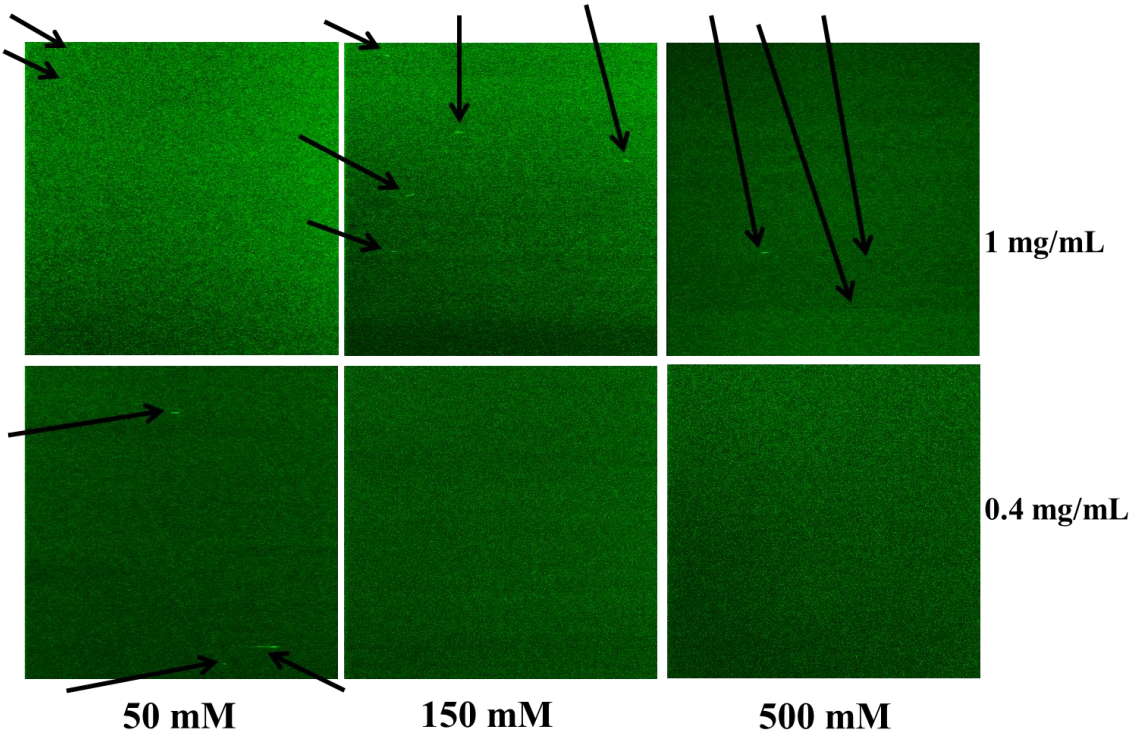

Figure A4.3 *Confocal micrographs (pixel size 44 nm) extracted from image time series experiments to display the presence of large aggregates for 1024 x 1024 pixel images of 1 mg/mL (top) and 0.4 mg/mL samples of BSA-AF488 at various ionic strengths.*

Please note that the image contrast and brightness has been adjusted to ease visualisation of the aggregates to the reader.

A4.7 The Real-time Assessment of Oligomer Formation

Time-dependent changes in oligomer formation were monitored using confocal microscopy followed by analysis with SpIDA. Plots representing the temporal evolution of BSA-AF488 samples as a function of thermal stress at 50 °C are presented in Figure A4.4 as follows;

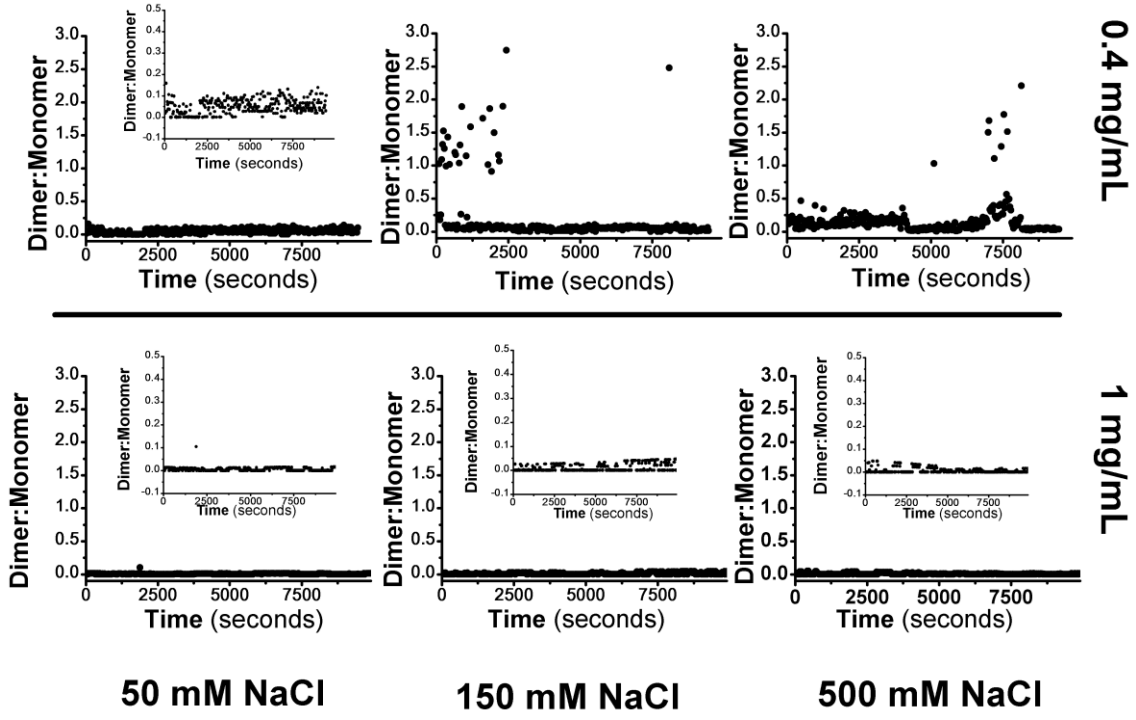

Figure A4.4 *The real-time temporal evolution of dimer formation expressed as dimer to monomer ratio for 44 nm pixel sized images of 0.4 (top) and 1 mg/mL (bottom) BSA-AF488 subjected to thermal stress at 50 °C and subsequent analysis with SpIDA at indicated ionic strengths.*

Data presented in Figure A4.4 indicates the reversible formation of dimers under the conditions examined and within the experimental timescale at all ionic strengths. To assess the formation of trimers, further analysis of confocal image time series was performed the results of which are presented as follows;

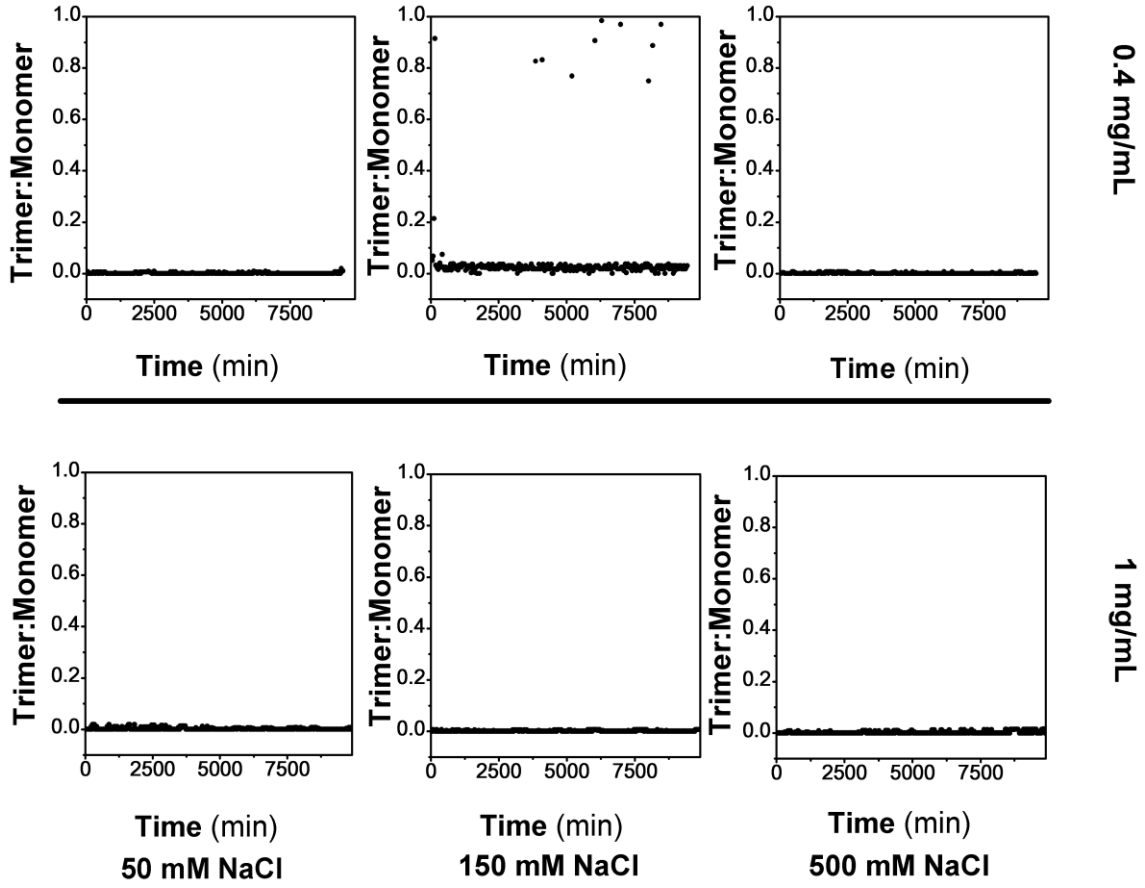

Figure A4.5 *The real-time temporal evolution of trimer formation expressed as trimer to monomer ratio for 44 nm pixel sized images of 0.4 (top) and 1 mg/mL (bottom) BSA-AF488 subjected to thermal stress at 50 °C and subsequent analysis with SpIDA at indicated ionic strengths.*

Data presented in Figure A4.5 indicates minimal and reversible trimer formation in all samples further supporting the proposed reversibility of dimer formation observed previously in Figure A4.4.

Appendix 5

SUPPLEMENTARY INFORMATION FOR THE QUANTIFICATION AND ANALYSIS OF P-GLYCOPROTEIN EXPRESSION AND INHIBITION USING LIVE CELL IMAGING

PART A

A5.1 Negative Staining of Immunofluorescence Images

MDCK-*MDR1* and MDCK-*wt* cells utilised in this study were subjected to immunofluorescence staining in order to quantify p-gp expression. In order to rule out non-specific staining monolayers were stained in the absence of primary antibody. Confocal images acquired from the negative control samples are presented as follows;

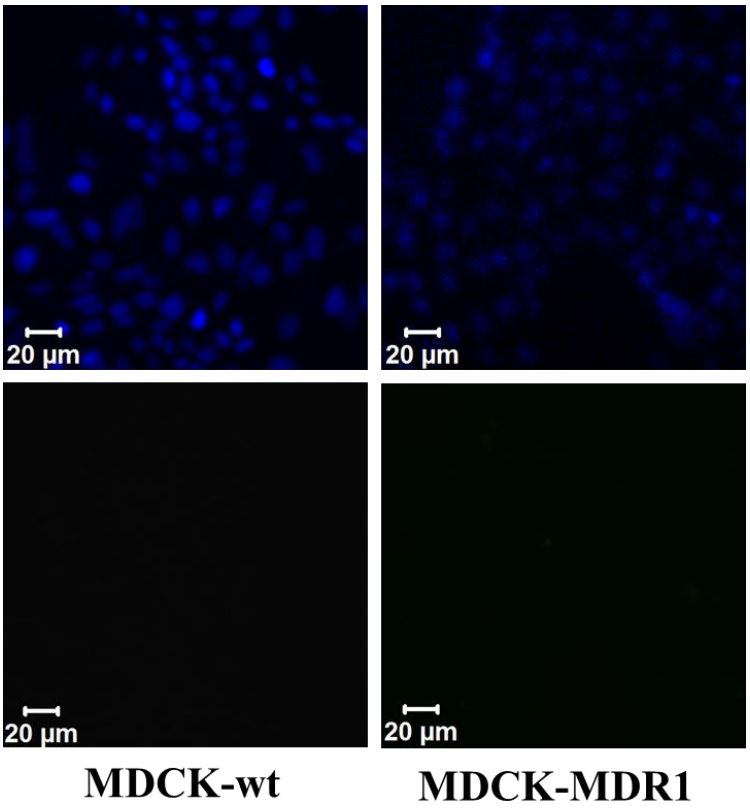

Figure A5.1 *Blue DAPI counterstain (top) and negative stain of MDCK-wt (left) and MDCK-MDR1 (right) for p-glycoprotein expression (bottom) for images with a resolution of 1024 x 1024 pixels and corresponding pixel size of 220 nm.*

Images obtained from negative controls of immunofluorescently stained samples indicate the absence of autofluorescence and non-specific labelling following incubation with secondary labelled antibody.

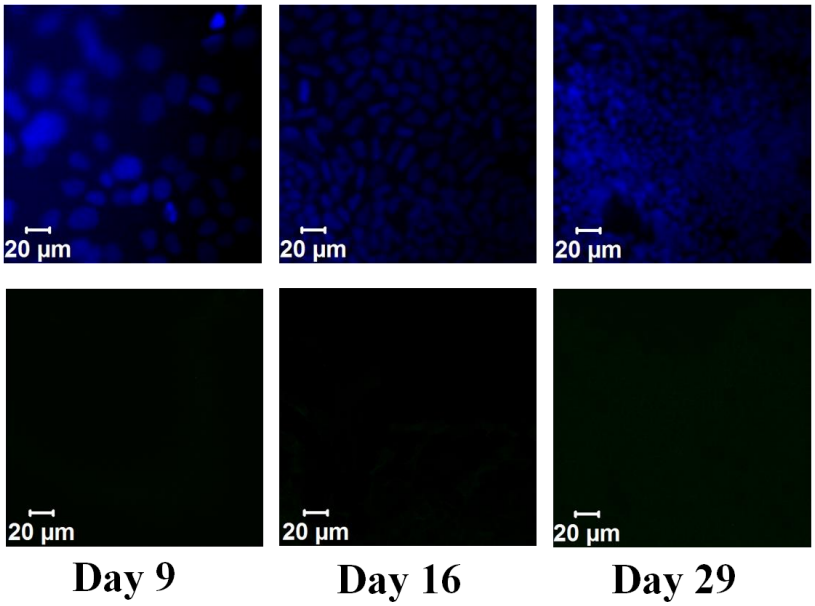

Figure A5.2 *Blue DAPI counterstain (top) and negative stain of MDCK-wt (left) and MDCK-MDR1 (right) for p-glycoprotein expression (bottom) for images with a resolution of 1024 x 1024 pixels and corresponding pixel size of 220 nm.*

Negative immunofluorescence images presented above for Caco-2 monolayers indicated the presence of minor autofluorescence in images.

A5.2 Cell Line Viability Using the MTT Assay

The MTT assay was used to assess the effect of incubation up to 90 minutes with verapamil and Calcein-AM and the performance of experiments at room temperature on the *via*bility of MDCK (*wt* and *MDR1* cells). The MTT assay was carried out in MDCK-*wt* and *MDR1* cells using the method described in Appendix 6. The results obtained from performance of MTT assays has been presented as percentage viability relative to the control (i.e. in the absence of verapamil and Calcein-AM) are compared in Figure A5.3.

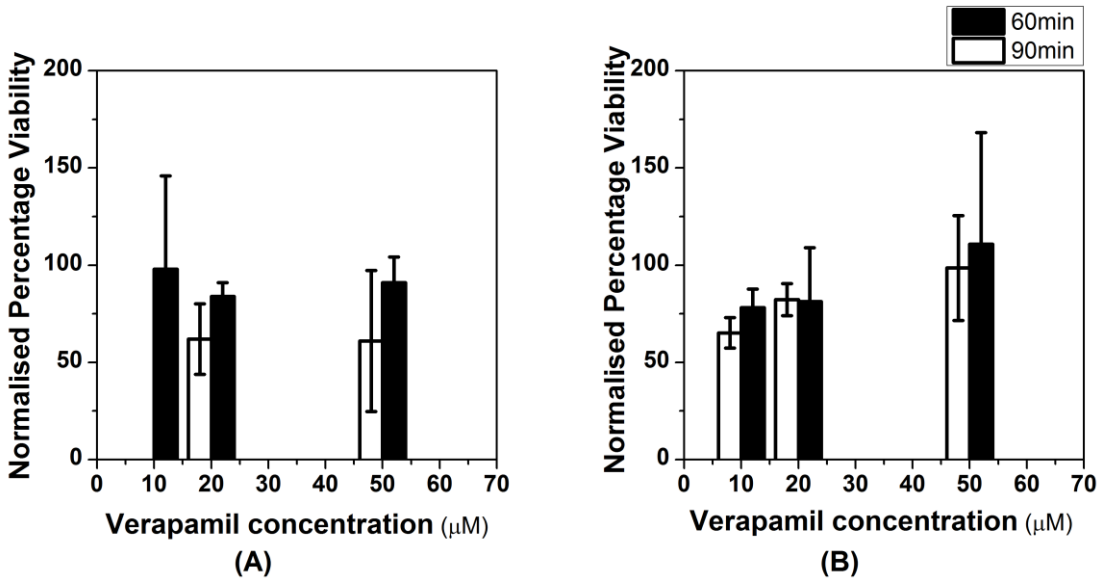

Figure A5.3 *Bar charts representing percentage change in cell viability following incubation of MDCK-wt* ***(A)*** *and MDCK-MDR1* ***(B)*** *cell lines with varying concentrations of verapamil up to 90 minutes and exposure to room temperature for two hours (n=3).*

A reduction in cell viability was observed at higher concentrations of verapamil incubated up to 90 minutes (i.e. 63 and 62% relative to control for 20 and 50 µM verapamil, respectively). Reduced viability was also inferred from microscopy where cells exhibited a more spherical morphology in each field of view during image acquisition.

A5.3 SpIDA Analysis of Intracellular Calcein Retention

Images acquired from the intracellular retention of Calcein as a function of time and verapamil concentration were subjected to SpIDA analysis and the population statistics determined for each concentration and time point in both MDCK-*MDR1* and MDCK-*wt* cell lines.

The descriptive statistics and corresponding probability and histogram plot for each concentration and time point in MDCK-*MDR1* and MDCK-*wt* cells are presented as follows;

Table A5.1 *Statistical parameters derived from the analysis of intracellular Calcein in MDR1 cells co-incubated with 2.5 µM verapamil.*

Time(min)	Mean	Median	Stdev	Min	Max	LQR	UQR
10	3.7	3.9	2.0	0.8	12.6	2.2	6.8
15	2.9	3.2	2.4	0.3	32.4	1.7	5.7
30	27.5	30.9	2.7	1.6	186.2	15.8	50.1
45	30.2	31.6	1.8	4.0	104.7	22.4	46.8
60	81.3	79.4	2.8	8.3	549.5	43.7	158.5
75	158.5	72.4	2.7	12.6	741.3	72.4	631.0
90	81.3	70.8	1.9	22.9	645.7	56.2	120.2

To assess the normality of the distribution obtained at this concentration, representative histogram and probability plots were constructed for each time point and typical plots are presented as follows;

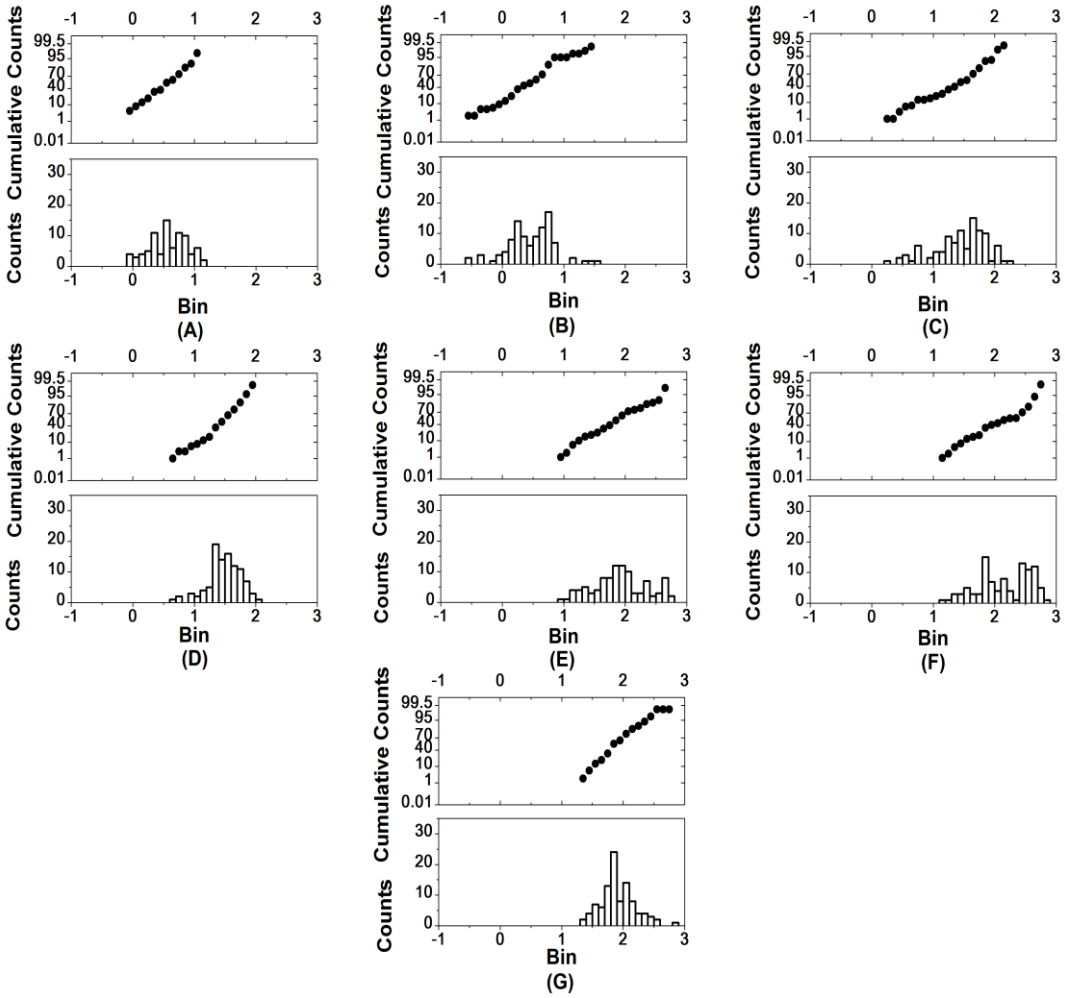

Figure A5.4 *Representative probability and histogram plots of intracellular Calcein obtained from MDCK-MDR1 cells at* ***(A)*** *10 minutes* ***(B)*** *15 minutes* ***(C)*** *30 minutes* ***(D)*** *45 minutes* ***(E)*** *60 minutes* ***(F)*** *75 minutes and* ***(G)*** *90 minutes at a 2.5 µM concentration of verapamil.*

MDCK-*MDR1* cells exhibited a normal distribution upon incubation with 2.5 µM verapamil over various time periods (i.e. 10, 45, 60 and 90 minutes). However, a lack of linearity of the probability histogram fits at some points was evident, which is consistent with the presence of more than one sub-population (i.e. a bimodal distribution) within the data as indicated above in the case of 15, 30 and 75 minute incubations.

A summary of descriptive statistics derived from the analysis of samples incubated with 5 µM verapamil is presented in Table A5.2 as follows;

Table A5.2 *Statistical parameters derived from the analysis of intracellular Calcein in MDR1 cells co-incubated with 5 µM verapamil.*

Time(min)	Mean	Median	Stdev	Min	Max	LQR	UQR
10	1.7	1.7	2.1	0.5	15.8	1.1	2.7
15	8.5	6.3	2.0	2.4	31.6	5.4	15.8
30	39.8	41.7	2.5	5.8	354.8	18.2	72.4
45	25.1	31.6	2.8	4.3	251.2	6.3	55.0
60	55.0	69.2	4.3	2.3	251.2	18.6	199.5
75	100.0	100.0	2.7	6.0	660.7	60.3	263.0
90	125.9	131.8	2.5	10.0	407.4	69.2	281.8

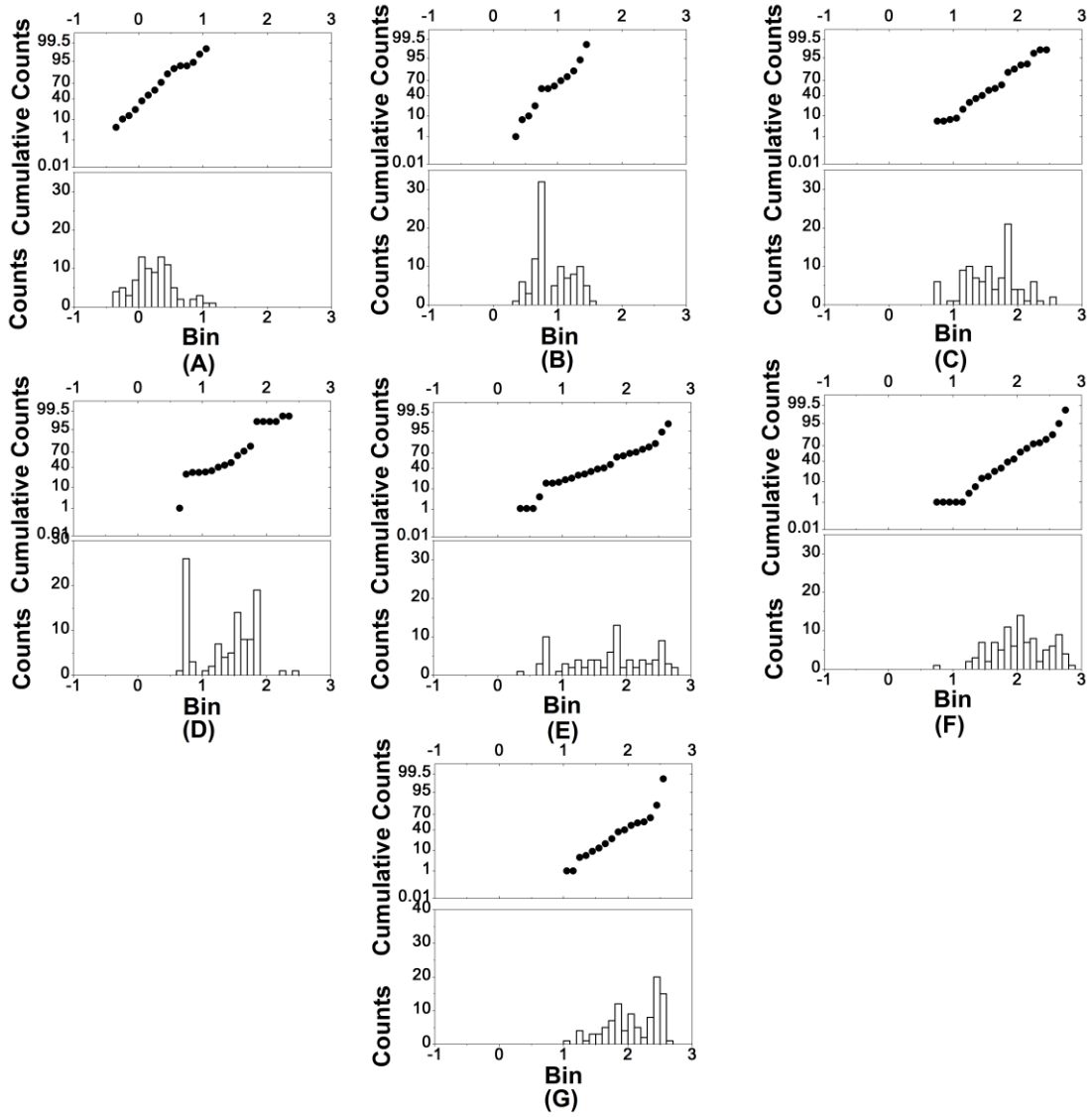

Figure A5.5 *Representative probability and histogram plots of intracellular Calcein obtained from MDCK-MDR1 cells at* ***(A)*** *10 minutes* ***(B)*** *15 minutes* ***(C)*** *30 minutes* ***(D)*** *45 minutes* ***(E)*** *60 minutes* ***(F)*** *75 minutes and* ***(G)*** *90 minutes at a 5 µM concentration of verapamil.*

Histogram and probability fits indicated multimodal distributions and the presence of more than one sub-population after periods of incubation with verapamil. For example, MDCK-*MDR1* cells displayed multimodal distributions due to the lack of linearity of the probability plots.

A summary of descriptive statistics derived from the analysis of MDR1 samples incubated with 5 µM verapamil is presented in Table A5.3 below;

Table A5.3 *Statistical parameters derived from the analysis of intracellular Calcein in MDR1 cells co-incubated with 10 µM verapamil.*

Time/min	Mean	Median	Stdev	Min	Max	LQR	UQR
10	3.3	3.1	2.2	0.6	14.1	1.9	5.5
15	31.6	31.6	1.9	5.8	158.5	20.4	52.5
30	58.9	56.2	2.2	12.6	426.6	32.4	83.2
45	79.4	63.1	2.5	15.8	676.1	39.8	125.9
60	63.1	50.1	2.8	5.6	691.8	15.8	83.2
75	125.9	125.9	2.5	20.0	676.1	63.1	295.1
90	109.6	74.1	2.5	18.2	631.0	56.2	218.8

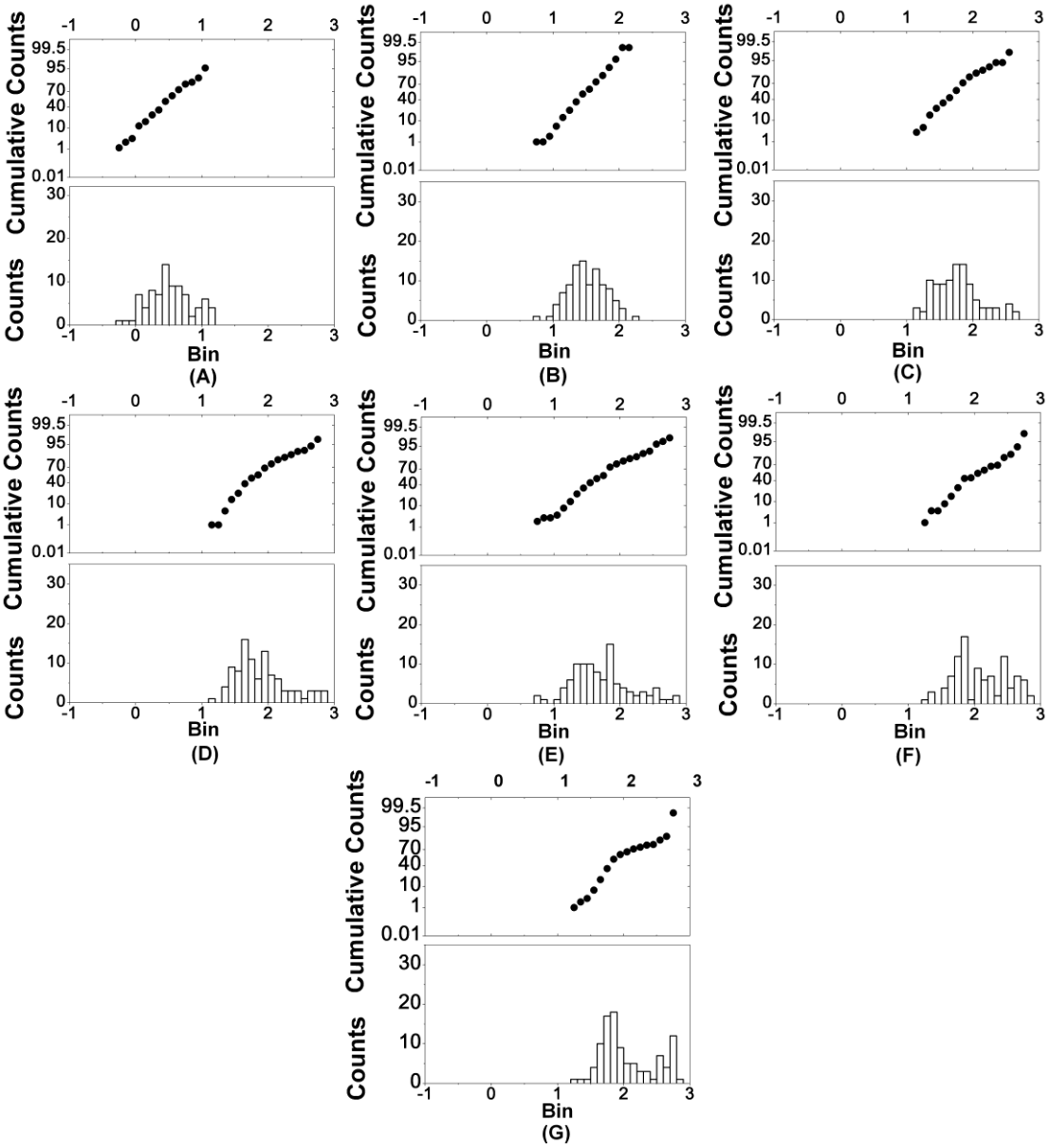

Figure A5.6 *Representative probability and histogram plots of intracellular Calcein obtained from MDCK-MDR1 cells at* ***(A)*** *10 minutes* ***(B)*** *15 minutes* ***(C)*** *30 minutes* ***(D)*** *45 minutes* ***(E)*** *60 minutes* ***(F)*** *75 minutes and* ***(G)*** *90 minutes at a 10 µM concentration of verapamil.*

After shorter incubation periods, a normal distribution was observed for MDCK-*MDR1* cell populations co-incubated with verapamil and Calcein-AM.

In Table A5.4 a summary of descriptive statistics derived from the analysis of samples incubated with 20 µM verapamil is presented;

Table A5.4 *Statistical parameters derived from the analysis of intracellular Calcein in MDR1 cells co-incubated with 20 µM verapamil.*

Time(min)	Mean	Median	Stdev	Min	Max	LQR	UQR
10	2.5	2.5	1.9	0.7	18.2	1.5	3.5
15	18.6	18.6	1.6	4.0	57.5	12.6	25.1
30	38.9	36.3	2.2	7.9	398.1	21.9	69.2
45	97.7	89.1	2.5	15.5	691.8	46.8	199.5
60	79.4	66.1	3.2	31.6	724.4	40.7	158.5
75	158.5	158.5	2.3	30.2	645.7	70.8	316.2
90	134.9	125.9	2.8	17.8	891.3	97.7	158.5

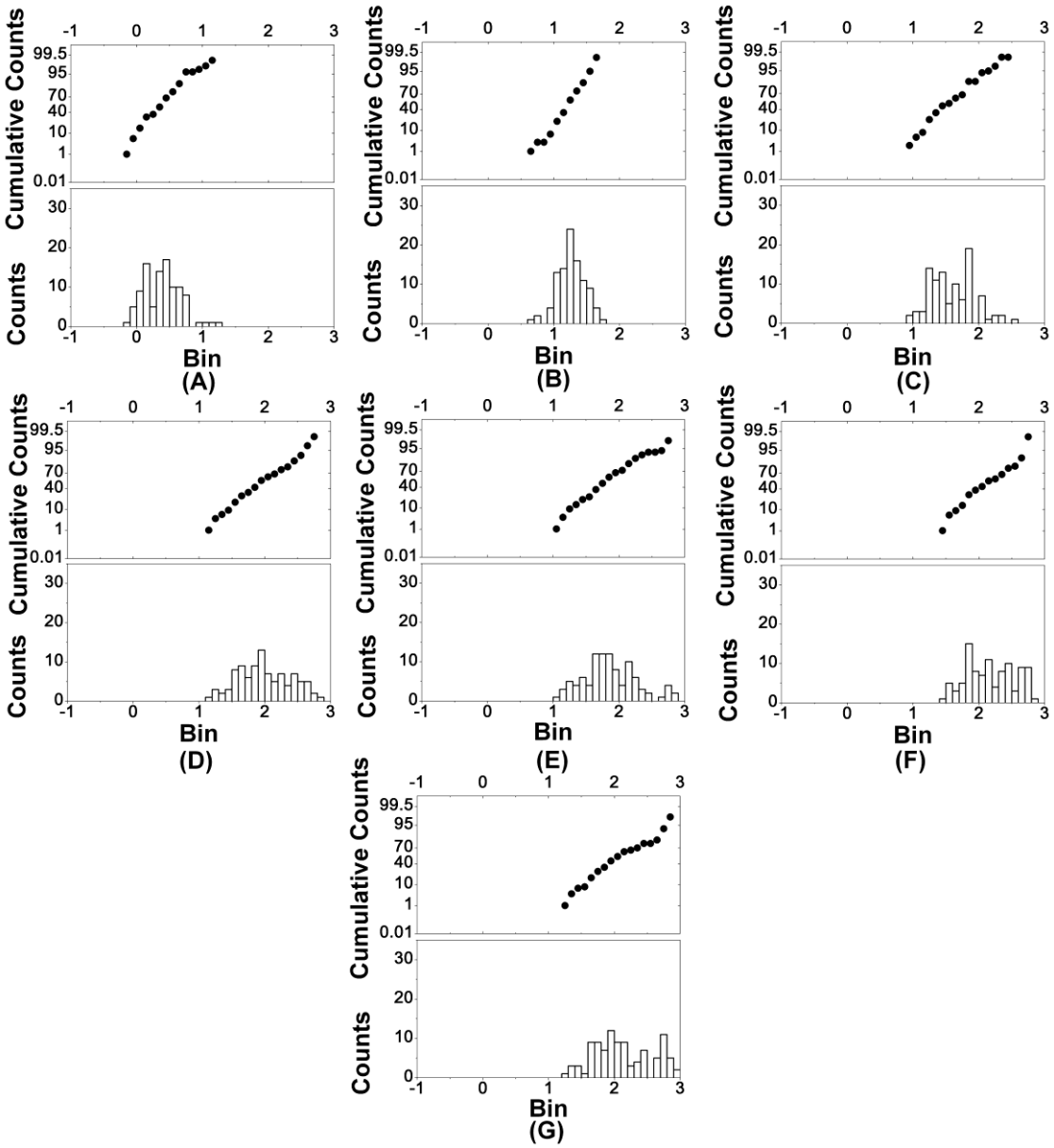

Figure A5.7 *Representative probability and histogram plots of intracellular Calcein obtained from MDCK-MDR1 cells at* ***(A)*** *10 minutes* ***(B)*** *15 minutes* ***(C)*** *30 minutes* ***(D)*** *45 minutes* ***(E)*** *60 minutes* ***(F)*** *75 minutes and* ***(G)*** *90 minutes at a 20 µM concentration of verapamil.*

Histogram and probability plots derived from samples incubated with 20 µM verapamil indicate normal distributions at earlier time points (i.e. 10, 15, 30 and 45 minutes) and the emergence of more than one sub-population at later time points.

A summary of descriptive statistics derived from the analysis of *MDR1* cell samples incubated with 50 µM verapamil is presented in Table A5.5;

Table A5.5 *Statistical parameters derived from the analysis of intracellular Calcein in MDR1 cells co-incubated with 50 µM verapamil.*

Time/min	Mean	Median	Stdev	Min	Max	LQR	UQR
10	5.8	5.5	1.7	1.6	19.5	4.2	8.7
15	83.2	70.8	2.7	4.9	501.2	44.7	158.5
30	87.1	70.8	2.0	20.9	512.9	63.1	128.8
45	131.8	125.9	2.4	27.5	758.6	61.7	239.9
60	125.9	100.0	1.9	37.2	794.3	77.6	158.5
75	199.5	186.2	2.2	33.9	851.1	120.2	389.0
90	158.5	631.0	2.1	47.9	831.8	158.5	631.0

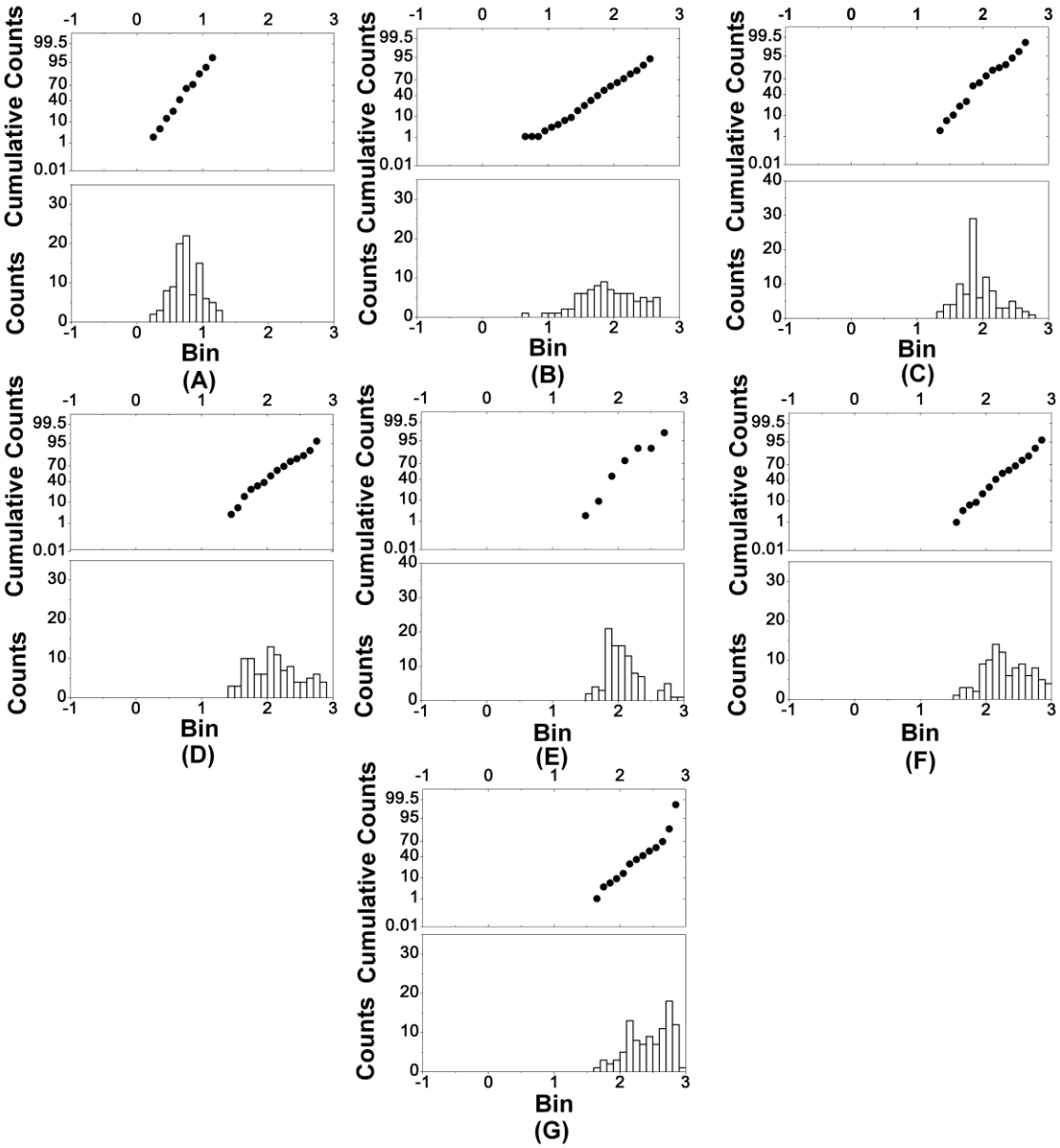

Figure A5.8 *Representative probability and histogram plots of intracellular Calcein obtained from MDCK-MDR1 cells at* ***(A)*** *10 minutes* ***(B)*** *15 minutes* ***(C)*** *30 minutes* ***(D)*** *45 minutes* ***(E)*** *60 minutes* ***(F)*** *75 minutes and* ***(G)*** *90 minutes at a 50 µM concentration of verapamil.*

With the exception of 60 minute and 90 minute incubation times, a normal distribution of intracellular Calcein retention was observed.

Table A5.6 a summarises representative descriptive statistics derived from the analysis of *wt* samples incubated with 2.5 µM verapamil.

Table A5.6 *Statistical parameters derived from the analysis of intracellular Calcein in wt cells co-incubated with 2.5 µM verapamil.*

Time/min	Mean	Median	Stdev	Min	Max	LQR	UQR
10	25.7	28.2	1.7	6.0	70.8	17.0	38.9
15	49.0	46.8	2.3	6.0	338.8	33.9	70.8
30	60.3	63.1	1.8	13.2	190.5	40.7	95.5
45	120.2	123.0	1.9	29.5	501.2	74.1	199.5
60	91.2	91.2	1.8	15.8	389.0	64.6	158.5
75	213.8	223.9	2.7	21.9	912.0	100.0	524.8
90	213.8	218.8	2.1	42.7	691.8	114.8	436.5

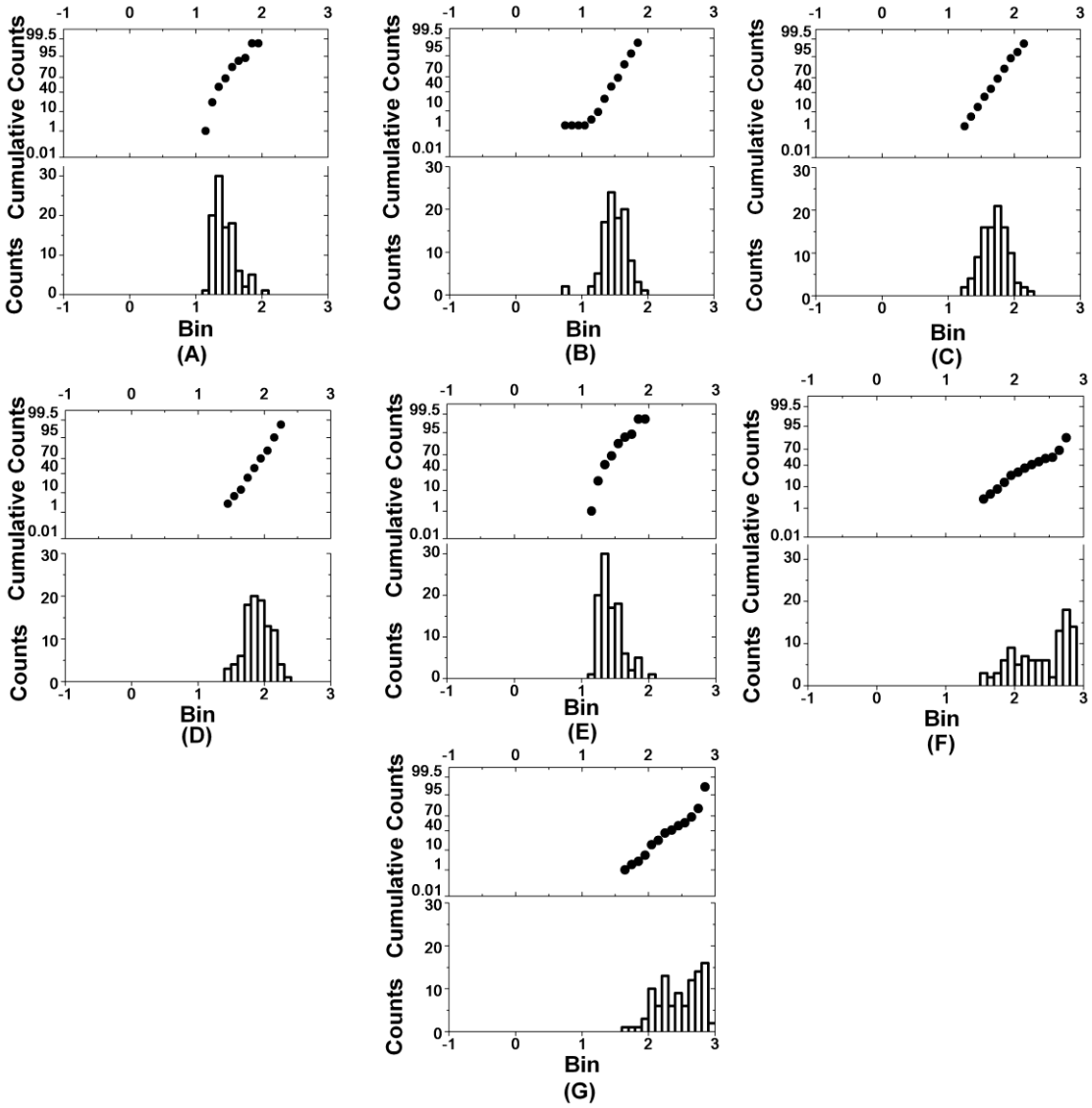

Figure A5.9 *Representative probability and histogram plots of intracellular Calcein obtained from MDCK-wt cells at* ***(A)*** *10 minutes* ***(B)*** *15 minutes* ***(C)*** *30 minutes* ***(D)*** *45 minutes* ***(E)*** *60 minutes* ***(F)*** *75 minutes and* ***(G)*** *90 minutes at a 2.5 µM concentration of verapamil.*

Descriptive statistics derived from analysis of MDCK-*wt* samples incubated with 5 µM verapamil are summarised below in Table A5.7;

Table A5.7 *Statistical parameters derived from the analysis of intracellular Calcein in wt cells co-incubated with 5 µM verapamil.*

Time/min	Mean	Median	Stdev	Min	Max	LQR	UQR
10	27.5	25.1	1.5	12.6	125.9	20.9	35.5
15	31.6	31.6	1.5	6.0	85.1	24.5	43.7
30	50.1	51.3	1.6	15.8	177.8	38.9	70.8
45	79.4	70.8	1.6	25.7	213.8	58.9	104.7
60	134.9	114.8	2.8	15.1	758.6	60.3	389.0
75	239.9	281.8	2.5	33.1	776.2	112.2	549.5
90	295.1	323.6	2.1	49.0	977.2	166.0	575.4

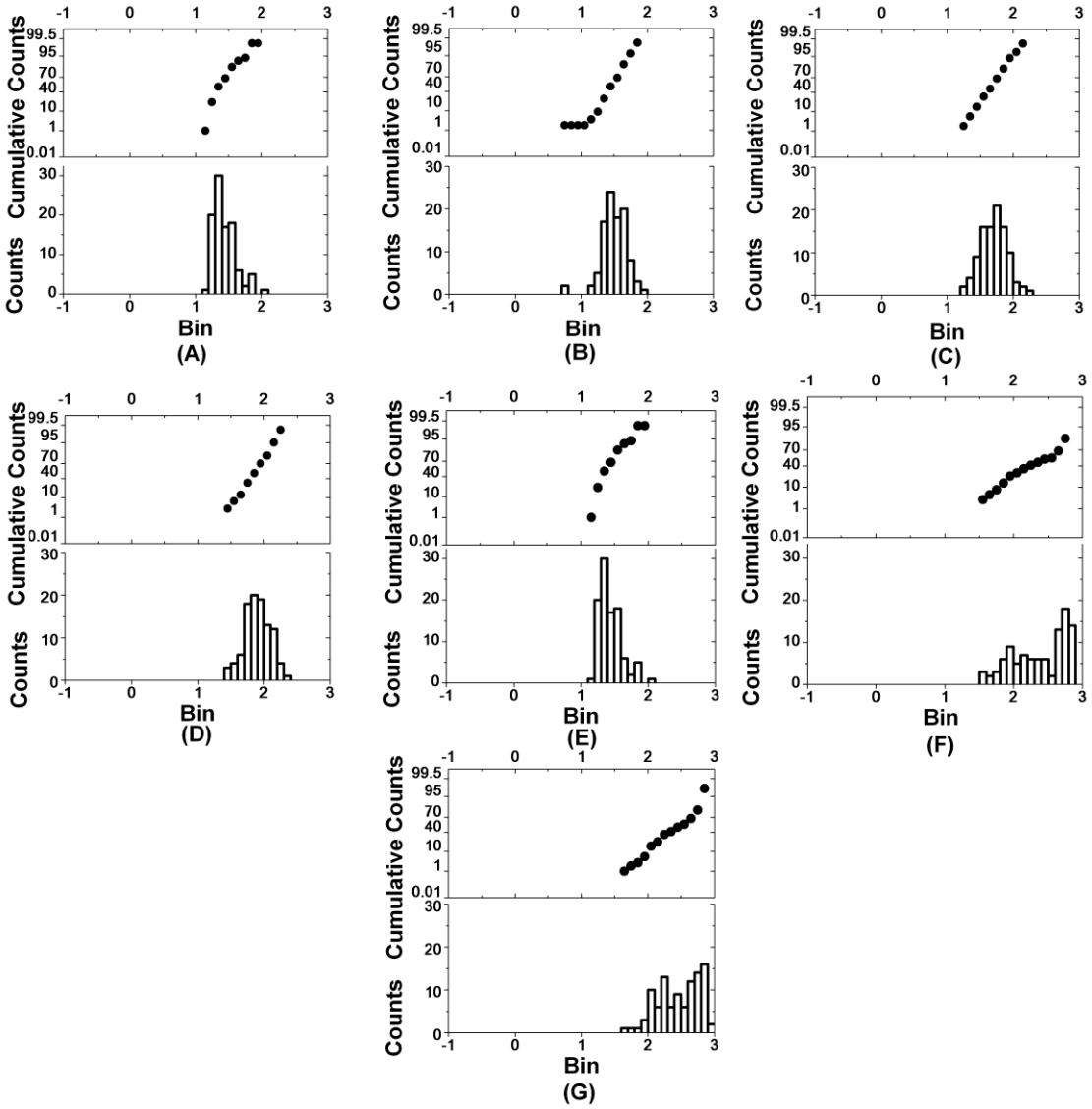

Figure A5.10 *Representative probability and histogram plots of intracellular Calcein obtained from MDCK-wt cells at* ***(A)*** *10 minutes* ***(B)*** *15 minutes* ***(C)*** *30 minutes* ***(D)*** *45 minutes* ***(E)*** *60 minutes* ***(F)*** *75 minutes and* ***(G)*** *90 minutes at a 5 µM concentration of verapamil.*

Descriptive statistics derived from the analysis of MDCK-*wt* samples incubated with 10 µM verapamil are presented in Table A5.8;

Table A5.8 *Statistical parameters derived from the analysis of intracellular Calcein in wt cells co-incubated with 10 µM verapamil.*

Time/min	Mean	Median	Stdev	Min	Max	LQR	UQR
10	39.8	41.7	1.9	4.0	199.5	25.1	50.1
15	31.6	30.9	1.7	10.5	91.2	23.4	45.7
30	36.3	39.8	1.8	8.9	112.2	24.0	58.9
45	89.1	85.1	2.8	12.6	660.7	46.8	182.0
60	125.9	100.0	2.6	12.6	851.1	66.1	190.5
75	95.5	91.2	2.2	15.8	758.6	63.1	158.5
90	85.1	79.4	2.2	12.6	812.8	50.1	125.9

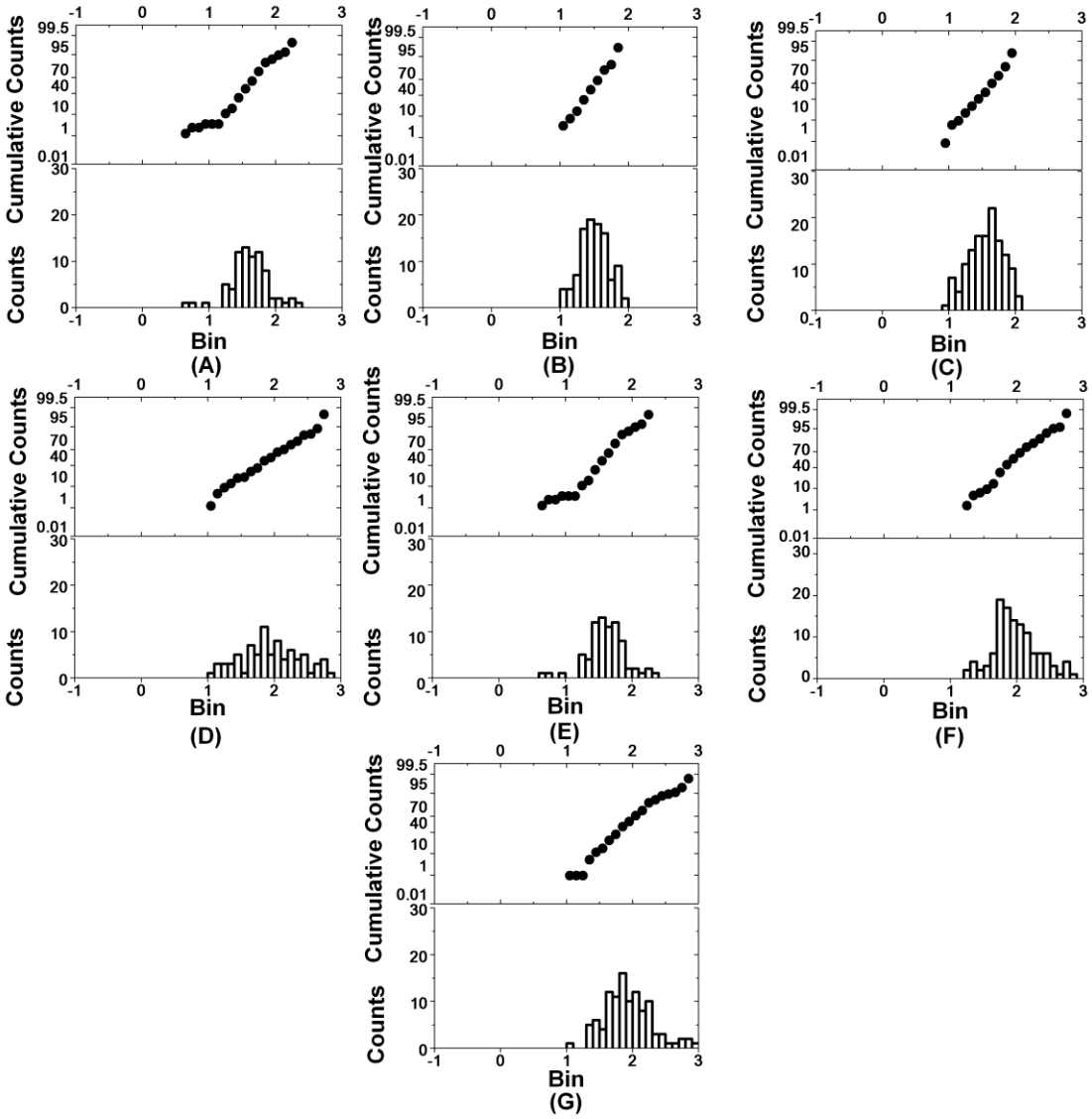

Figure A5.11 *Representative probability and histogram plots of intracellular Calcein obtained from MDCK-wt cells at* ***(A)*** *10 minutes* ***(B)*** *15 minutes* ***(C)*** *30 minutes* ***(D)*** *45 minutes* ***(E)*** *60 minutes* ***(F)*** *75 minutes and* ***(G)*** *90 minutes at a 10 µM concentration of verapamil.*

A summary of descriptive statistics derived from the analysis of MDCK-*wt* samples incubated with 20 µM verapamil is presented in Table A5.9;

Table A5.9 *Statistical parameters derived from the analysis of intracellular Calcein in wt cells co-incubated with 20 µM verapamil.*

Time	Mean	Median	Stdev	Min	Max	LQR	UQR
10	36.3	37.2	1.7	13.2	100.0	25.7	56.2
15	53.7	38.9	2.3	14.5	478.6	30.9	89.1
30	91.2	70.8	2.5	19.5	467.7	43.7	245.5
45	100.0	70.8	2.8	6.0	501.2	50.1	302.0
60	117.5	100.0	2.7	20.9	891.3	58.9	208.9
75	166.0	147.9	2.5	35.5	912.0	93.3	380.2
90	158.5	151.4	2.5	30.9	724.4	74.1	288.4

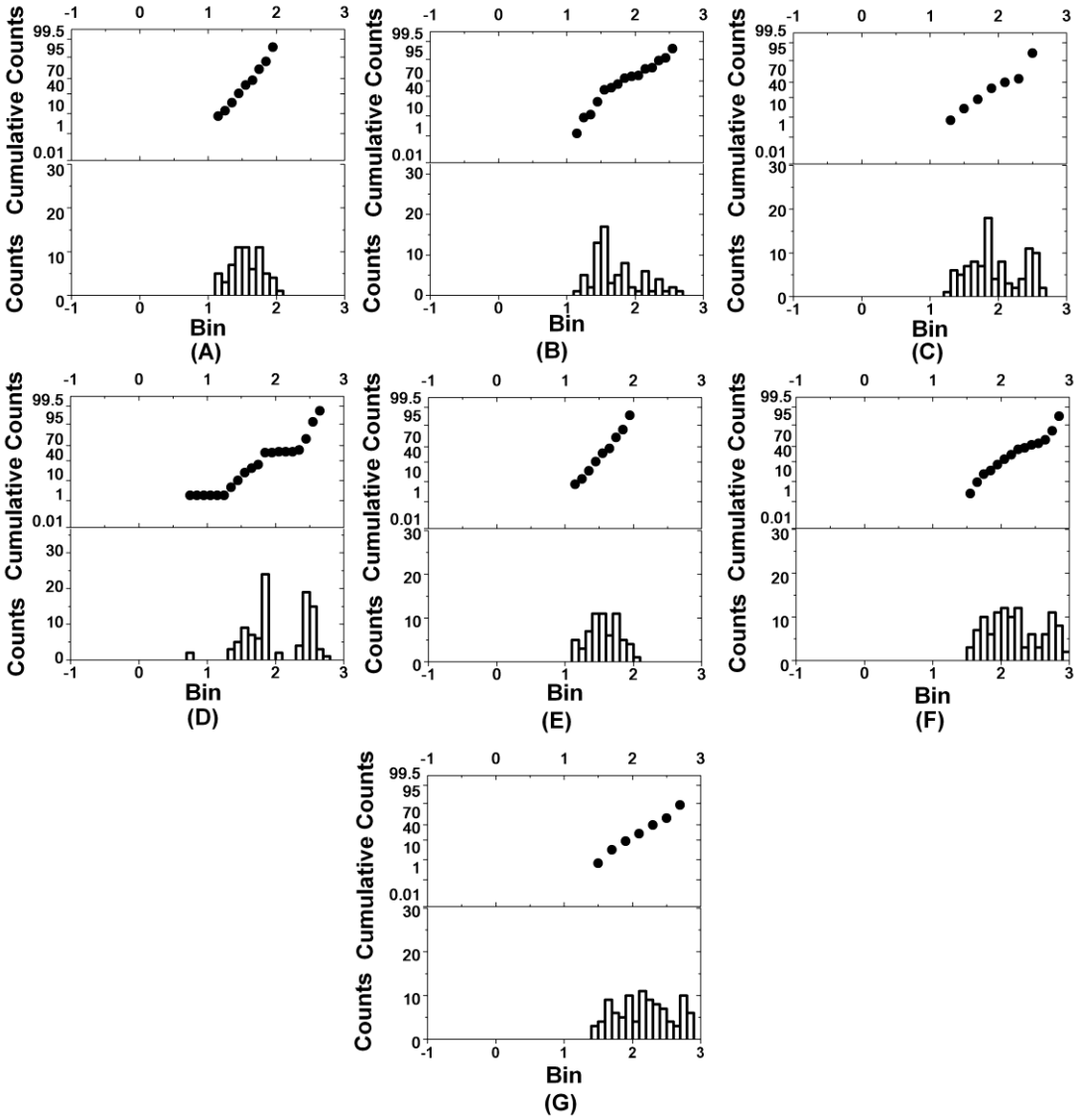

Figure A5.12 *Representative probability and histogram plots of intracellular Calcein obtained from MDCK-wt cells at* ***(A)*** *10 minutes* ***(B)*** *15 minutes* ***(C)*** *30 minutes* ***(D)*** *45 minutes* ***(E)*** *60 minutes* ***(F)*** *75 minutes and* ***(G)*** *90 minutes at a 20 µM concentration of verapamil.*

Descriptive statistics from analysis of MDCK-*wt* data incubated with 50 µM verapamil are similarly presented in Table A5.10;

Table A5.10 *Statistical parameters derived from the analysis of intracellular Calcein in wt cells co-incubated with 50 µM verapamil.*

Time/min	Mean	Median	Stdev	Min	Max	LQR	UQR
10	20.9	21.4	1.8	4.8	53.7	14.5	33.9
15	29.5	36.3	1.9	6.2	114.8	18.2	50.1
30	40.7	39.8	2.3	8.7	478.6	22.4	70.8
45	87.1	70.8	2.6	10.0	812.8	50.1	158.5
60	251.2	316.2	1.9	39.8	724.4	158.5	501.2
75	131.8	125.9	2.4	30.2	831.8	70.8	302.0
90	208.9	213.8	2.2	34.7	741.3	125.9	436.5

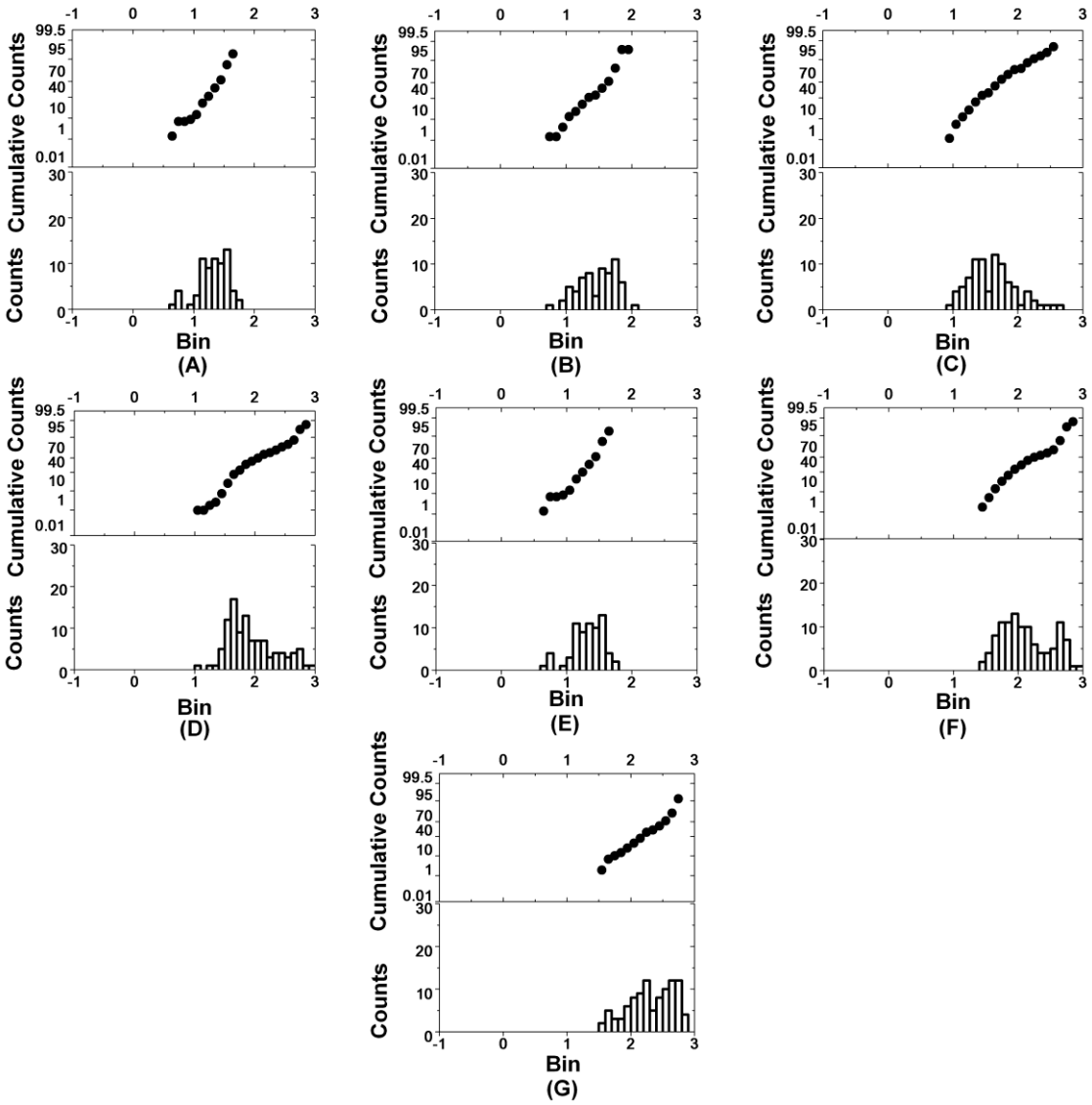

Figure A5.13 *Representative probability and histogram plots of intracellular Calcein obtained from MDCK-wt cells at* ***(A)*** *10 minutes* ***(B)*** *15 minutes* ***(C)*** *30 minutes* ***(D)*** *45 minutes* ***(E)*** *60 minutes* ***(F)*** *75 minutes and* ***(G)*** *90 minutes at a 50 µM concentration of verapamil.*

All samples followed a normal distribution, with the exception of the 75 minute incubations.

Note: All representative high resolution images obtained for MDCK-*MDR1* and MDCK-*wt* cell lines have been included on a CD as **Appendix 5B** and **Appendix 5C**, respectively.

Appendix 6

SUPPLEMENTARY INFORMATION FOR THE ASSESSMENT OF CELLULAR UPTAKE USING BIOIMAGING AND CONVENTIONAL ASSAYS

A6.1 Performance of the MTT Assay to Determine Cell Viability Under Experimental Conditions

The influence of agents utilised throughout the duration of live cell imaging experiments (i.e. 2 hours) on cell viability was assessed using the MTT viability assay. The MTT assay quantifies cell proliferation, and conversely cell death due to apoptosis or necrosis, both of which result in a reduction in cell viability. MTT is bioreduced by mitochondrial dehydrogenases in metabolically active cells to an insoluble formazan product characterised by a purple precipitate that is soluble in growth medium, the absorbance of which may be quantified at 570 nm using a plate reader.[1,2]

In order to determine the calibration curve and an ideal seeding density for the MTT assay, BAECs, Caco-2 and HeLa cells were seeded onto 96-well plates (surface area: 0.32 cm^2/well, Nunc™, Fisher, Leicestershire, UK) at various seeding densities and incubated for 48 hours (in a pre-humidified atmosphere containing 5% CO_2) to select for the optimal seeding density with a corresponding absorbance in the linear range. A 100 µL aliquot of cell suspension was transferred to each well. This was followed by removal of the DMEM growth medium, addition of 200 µL of (pre-filtered) MTT solution in HBSS (0.5 mg/mL), and incubation of the cells in a pre-humidified atmosphere containing 5% CO_2 for a period of 3-4 hours.

Confirmation of the presence of purple precipitate by light microscopy was followed by removal of the MTT solution and addition of 200 µL of DMSO to each well. The plate was agitated prior to storage in the dark for two hours and the absorbance at 570 nm measured using a Tecan Safire microplate reader (Tecan Safire, Reading, UK). The background at 670 nm was subtracted from the corresponding absorbance values.

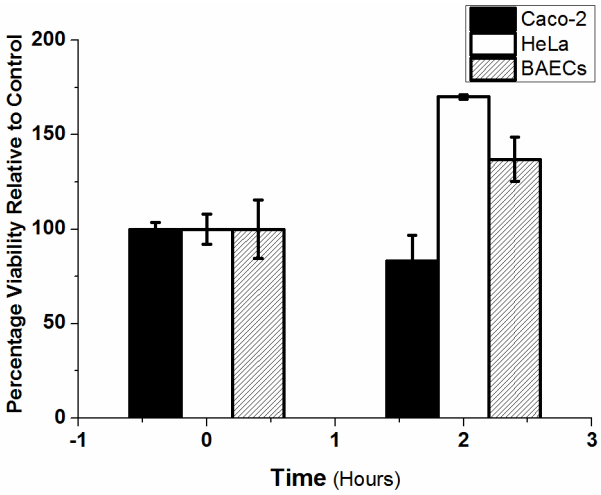

Figure A6.1 *Bar chart displaying the mean percentage change in cell viability relative to the control (n=4, ± st.dev.) for Caco-2 (left) and BAEC cells (right) with a seeding density of 2 x* 10^5 *cells/mL following exposure to room temperature (i.e. 21 °C) for two hours.*

A6.2 Calibration Curves for Fluorophores Dissolved in OptiMEM® Transport Medium

In order to determine the concentration of transferrin-Alexa Fluor® 647 and Cell Trace™ Calcein Red-Orange AM during monolayer permeability transport experiments, the fluorescence intensity of each was measured as a function of concentration using a Tecan Safire multifunctional plate reader the results of which are presented as follows;

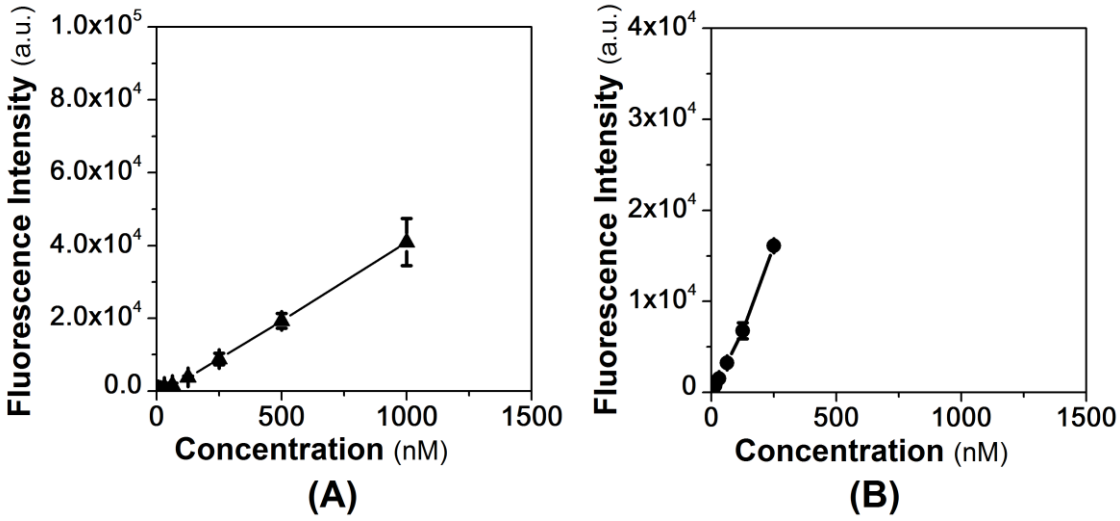

Figure A6.2 *Calibration plot of mean fluorescence intensity ± st. dev. measured using a fluorescence plate reader as a function of concentration measured for Cell Trace™ Calcein Red-Orange AM excited at 537 and emission collected at 617 nm* ***(A)*** *and transferrin-Alexa Fluor® 647 excited at 650 nm and emission collected at 680 nm* ***(B)*** *(n=4).*

Parameters obtained from the calibration slope were subsequently applied to the determination of concentrations retrieved from apical and basal chambers during permeability assay data analysis.

A6.3 The TER Profile of Caco-2 Cell Lines Cultivated on the Basolateral Face of Transwell® Membranes

Results obtained from the TER profile of Caco-2 cells seeded onto the underside of the Transwell® membrane supports demonstrated the achievement of confluency between days 5-7 post-seeding and differentiation occurred within observed samples following the 12-15 days range displayed as follows;

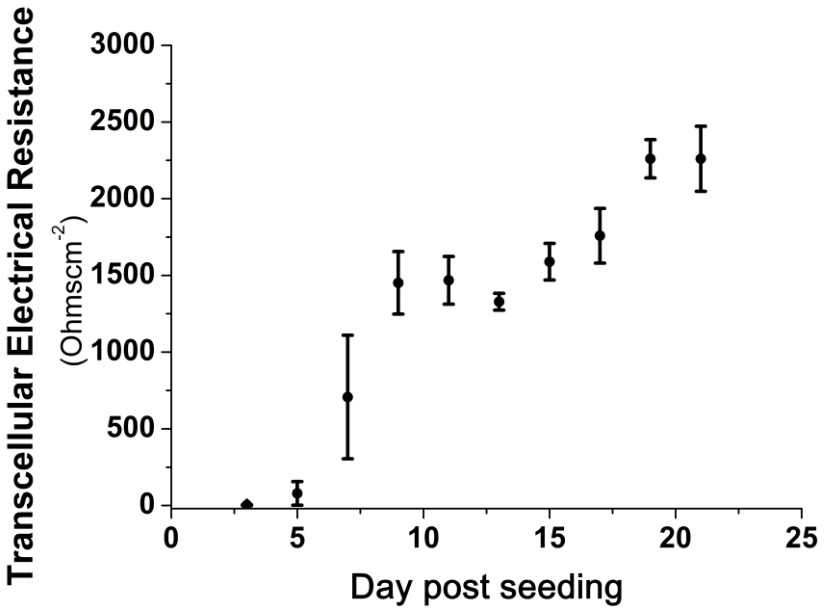

Figure A6.3 *Mean TER values (n=4, ± st.dev.) characterised for Caco-2 monolayers cultivated on the underside of Transwell® polyester membrane support filters (seeding density: 8.6 x 10^4 cells/filter) with a pore size of 0.4 µm and corresponding surface area of 0.33 cm^2. TER values were recorded from day 3 post-seeding and up to day 21 on alternate days.*

A6.4 Retention of Tight Junction Activity Following Permeability Experiments in Transwells®

In some experiments a significant reduction in the measured TER was observed following pre-incubation with BSA solution and subsequent incubation in HBSS or serum-free medium for transferrin-Alexa Fluor® 647 experiments. However, data from the Lucifer yellow rejection assay performed on the same Transwells® indicated a 99% or more exclusion rate (i.e. P_{app}~ 1.33 x 10^{-10} cm/sec) similar to that of the control Transwell® following a 60 minute incubation with 300 µM Lucifer yellow.

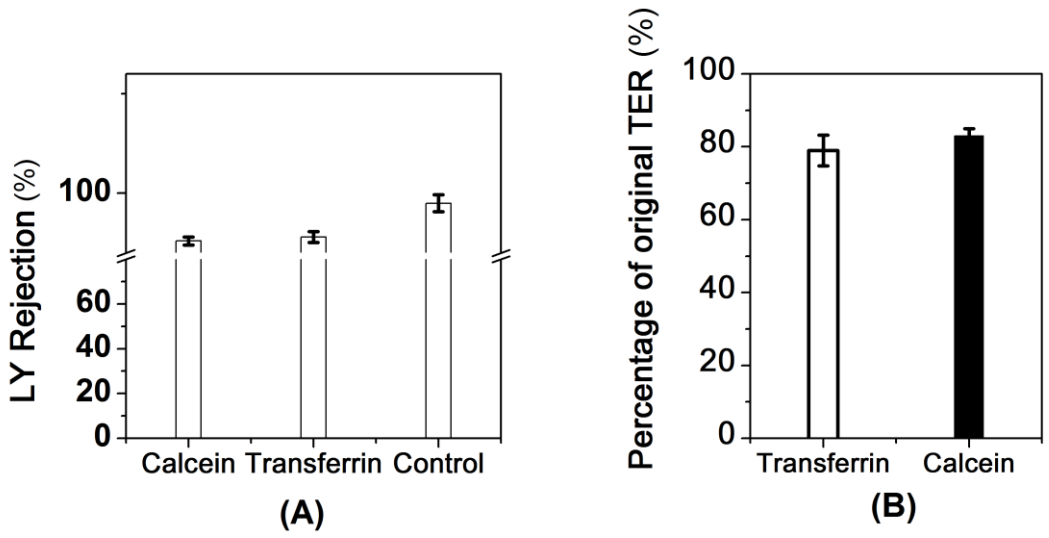

Figure A6.4 *Percentage Lucifer yellow rejection (i.e. %LY rejection) for a control compared to those incubated with transferrin-Alexa Fluor® 647 and Cell Trace™ Calcein red-orange AM* ***(A)*** *and Bar chart displaying the TER of Caco-2 cell monolayers following serum deprivation and the addition of transferrin-Alexa Fluor® 647* ***(B)****. Percentages displayed are that of post experimental readings relative to the original TER recorded prior to experimentation and incubation with transferrin-Alexa Fluor® 647and Cell Trace™ Calcein red-orange AM (n=3).*

A6.5 Negative Controls of Immunofluorescence Stains

In order to rule out issues relating to bleeding, autofluorescence and non-specific binding of IgG-Alexa Fluor® 488, negative controls were performed (i.e. in the absence of incubation with the primary antibody and utilising PBS as a control).

A6.5.1 Caco-2 Cells

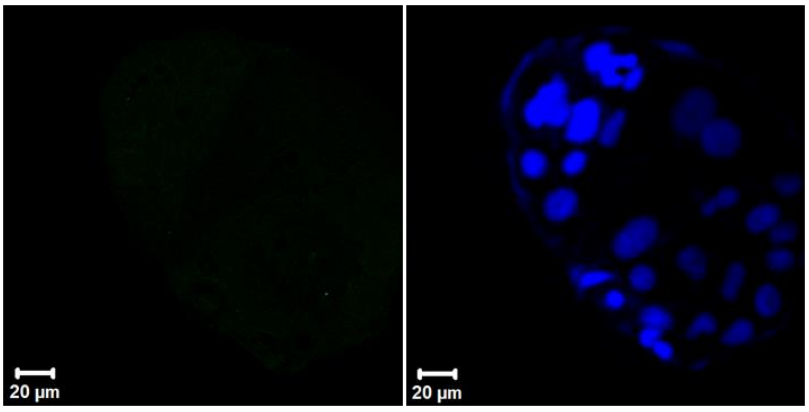

Figure A6.5 *Negative immunofluorescence stain of Caco-2 cells (left) and blue DAPI nuclear counterstain (right) for an image with a resolution of 1024 x 1024 pixels and corresponding pixel size of 220 nm.*

Results obtained from the negative stain of Caco-2 cells demonstrate no non-specific binding and limited autofluorescence following incubation with the secondary antibody

permitting further analysis of images acquired from the fluorescently-labelled transferrin receptors.

A6.5.2 MDCK Cells

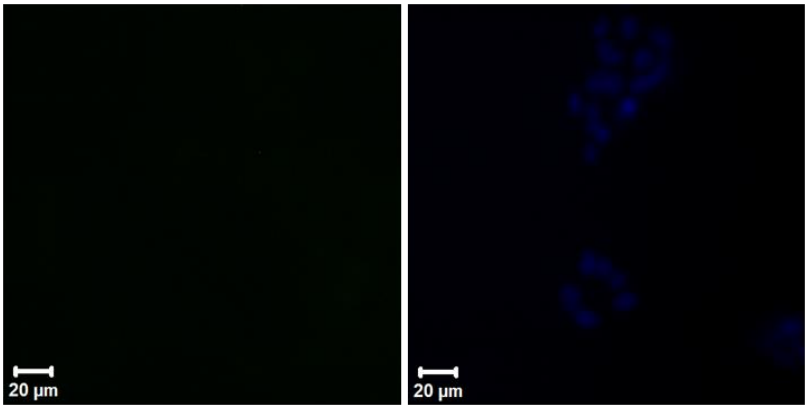

Figure A6.6 *Negative immunofluorescence stain of MDCK cells (left) and blue DAPI counterstain (right) with a resolution of 1024 x 1024 pixels and corresponding pixel size of 220 nm.*

In MDCK cells a small amount of fluorescence was observed in negative control images that appeared to be consistent with the autofluorescence of membrane and cytoplasmic components. In performing further SpIDA, the relative contribution of this fluorescence was quantified and accounted for as a white noise contribution in further analyses.

A6.6 SpIDA Analysis

To investigate the influence of bias associated with visibly heterogeneous images containing brighter and darker regions, homogenous regions were selected and subjected to SpIDA analysis following white noise correction and the selection of the PMT shot noise appropriate to the detector gain value selected. A screenshot of the graphical user interface is included in Figure A6.7.

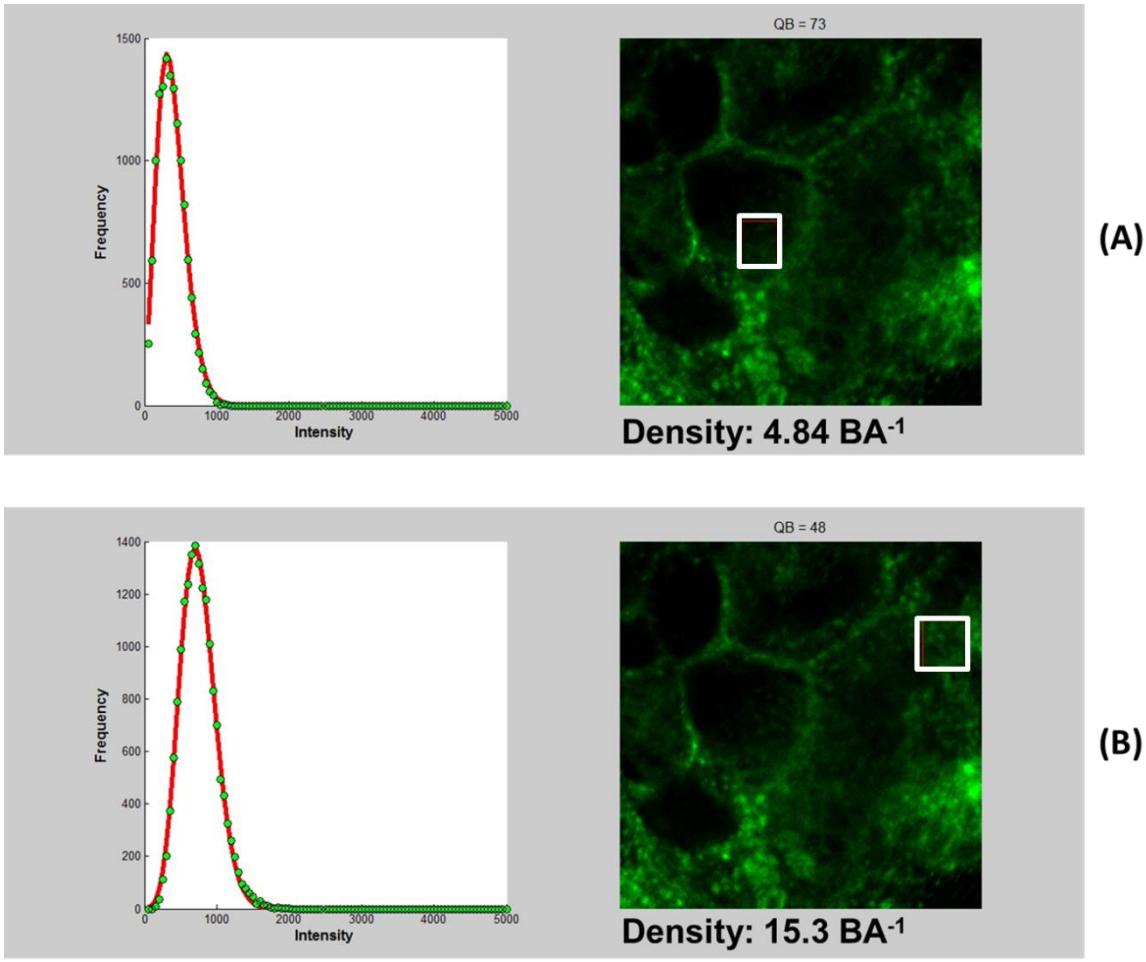

Figure A6.7 *Typical histogram fits obtained following the analysis of regions of interests selected in an image of immunofluorescently- labelled transferrin receptors for a visibly darker region* ***(A)*** *and a brighter region* ***(B)*** *of 1024 x 1024 pixel resolution and a pixel size of 44 nm.*

A6.7 The Influence of Detector Gain Settings on Output Parameters

In Chapter 6, distributions of labelled transferrin receptor number densities obtained from the analysis of confocal images were presented in Figure 6.4. Representative histograms of labelled transferrin receptors for images captured at a detector gain of 600 are presented in Figure A6.8.

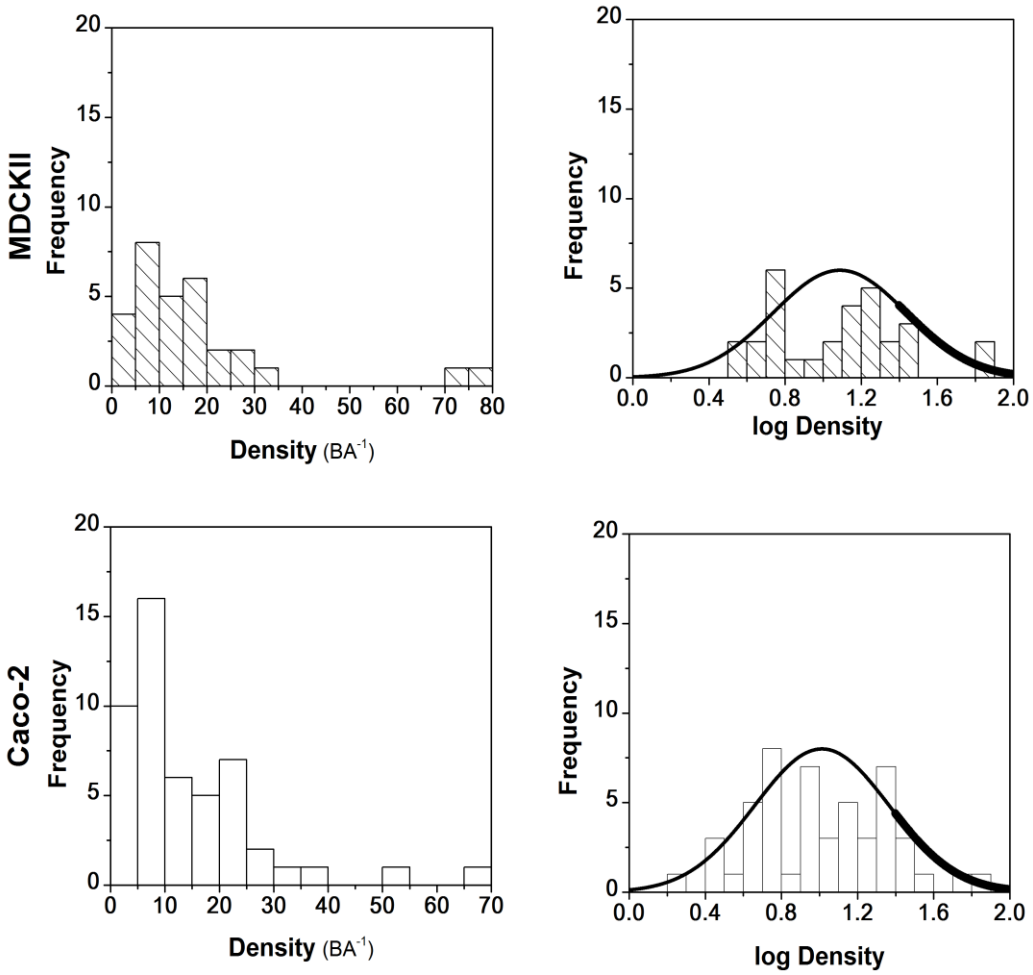

Figure A6.8 *Representative histograms of labelled transferrin receptors analysed from 50-60 regions of interest in Caco-2 (top) and MDCK (bottom) cells with a detector gain setting of 600 and corresponding mean density per beam area of 6 <14 < 20 and 6< 17< 19 for labelled transferrin receptors in Caco-2 and MDCK cells (P< 0.05).*

In order to assess the influence of detector gain settings in Caco-2 and MDCK cell lines, the population size range determined under both gain settings were compared (See Table A6.1).

Table A6.1 *Corresponding densities obtained per beam area from the analysis of MDCK and Caco-2 cell immunofluorescence images acquired with a detector gain setting of 600 and 650 ($P < 0.05$).*

Cell Line	Detector Gain	Density (BA^{-1})
MDCK	600	6< 17< 19
	650	7< 12< 22
Caco-2	600	7< 17< 22
	650	6< 11< 13

Density parameters obtained from these regions were found to differ significantly ($P < 0.05$) following ANOVA statistical analysis of the population data ($P = 4.9 \times 10^{-6}$) and should be accounted for when selecting specific ROIs for SpIDA analysis. Hence, multiple regions were selected for analysis of receptor expression densities.

A6.8 Control Confocal Images of Cell Trace™ Calcein Red-Orange AM

In order to rule out the contribution of background fluorescence, leaching or autofluorescence to acquired images fluorescence confocal images and corresponding differential interference contrast images were captured at 0 minutes for both Caco-2 cells and BAECs presented in Figure A6.9.

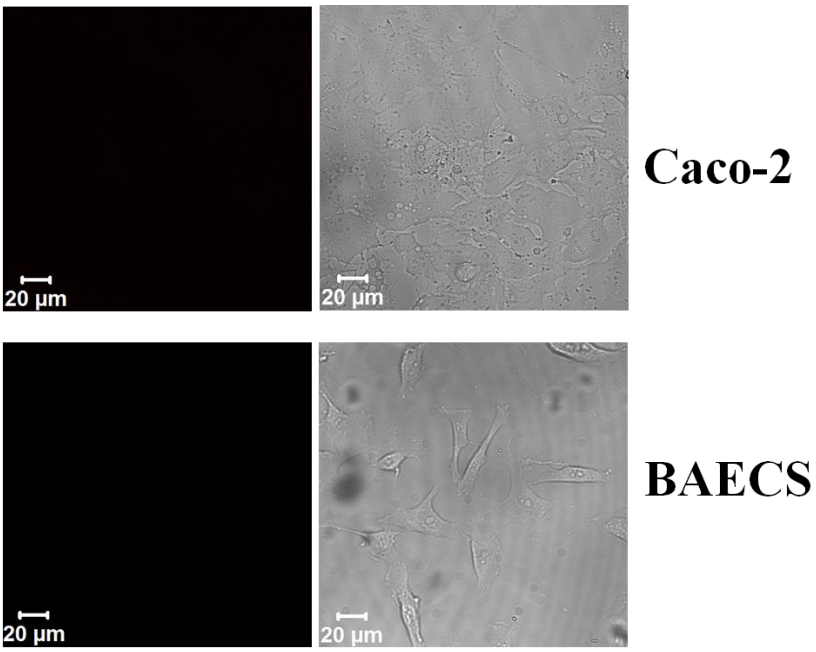

Figure A6.9 *Confocal images of Caco-2 cells (top) and BAECs (bottom) at time zero without Cell Trace™ Calcein red-orange AM and the corresponding differential interference contrast images for 512 x 512 pixel resolution images with a corresponding pixel size of 440 nm.*

Control confocal images indicate the absence of any background contributions (i.e. autofluorescence) to the acquired images in regions of the image where cells are present.

A6.9 Raster Image Correlation Spectroscopy Analysis of Vesicle Dynamics

RICS was utilised to assess the Transferrin-Alexa Fluor® 647 vesicular dynamics in Caco-2 and HeLa cell lines at a higher pixel resolution (i.e. 44 nm pixel size). Time series images were acquired for these cell lines at various pixel dwell times (i.e. 3.2 and 6.4 microseconds) all of which were observed to contribute to photobleaching. A typical representative fluorescence intensity histogram obtained in the RICS user interface is presented as follows;

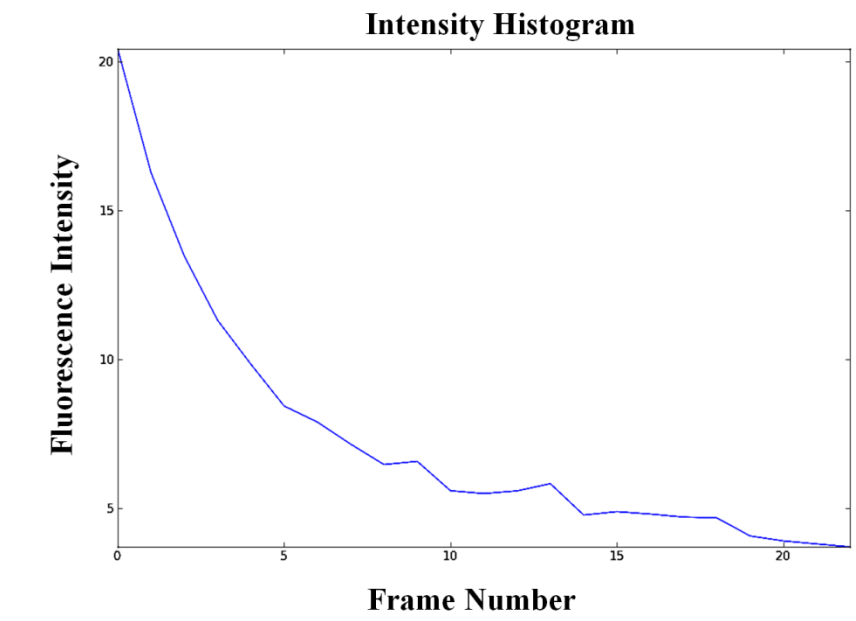

Figure A6.10 *A representative fluorescence intensity histogram profile obtained for a 512 x 512 pixel resolution image time series (i.e. 23 frames) of HeLa cells with a corresponding pixel size of 44 nm, pixel dwell time of 3.2 microseconds.*

Despite variation of pixel dwell times and distance of the objective from the coverslip, no improvements were observed in the fluorescence intensity of all image time series utilised in this study with little or no observed recovery in the fluorescence following bleaching. Future options to explore in this area may be the use of anti-fading media or alternative fluorophores though Alexa Fluor® 647 is recognised as being a photostable fluorophore.

A6.10 References

1. Gerlier D, Thomasset N 1986. Use of MTT colorimetric assay to measure cell activation. Journal of Immunological Methods 94(1-2):57-63.

2. Mosmann T 1983. Rapid colorimetric assay for cellular growth and survival: Application to proliferation and cytotoxicity assays. Journal of Immunological Methods 65(1-2):55-63.